University of Naples Federico II

Polytechnic and Basic Sciences School

Department of Chemical Sciences

Ph.D. in Chemical Sciences

Complex bioinspired organic systems and hybrids: green chemistry solutions for surface functionalization, biomedicine, and nanotechnology

Rita Argenziano

Advisor
Prof. Alessandra Napolitano

Examiner
Prof. Finizia Auriemma

XXXV Cycle 2019-2022

Coordinator: prof. Angela Lombardi

Index

ABSTRACT.....1

LIST OF PUBLICATIONS.....5

MANUSCRIPTS IN PREPARATION.....7

1 INTRODUCTION.....8

1.1 Phenol compounds 10
1.1.1 Phenolic acids 12

1.2 Polyphenols 18
1.2.1 Eumelanins as natural phenolic pigments 18
1.2.2 Tannins as naturally occurring phenolic compounds.....21
1.2.3 The second most abundant phenolic polymers on the earth: the lignin 24

1.3 Agri food by-products as a source of phenolic compounds 26
1.3.1 Fruit by-products 27
1.3.2 Lignocellulosic by-products.....31
1.3.3 Vegetable by-products.....34

1.4 Green Extraction Techniques for the recovery of phenolic compounds 36

1.5 Complex organic biopolymers-inorganic hybrid materials..... 38
1.5.1 Synthesis of metal nanoparticles embedded into organic compounds.....41
1.5.2 Hybrid systems based on graphene materials 43

1.6 Aims of the PhD project..... 45

2 5,6-DIHYDROXYINDOLE COMPOUNDS AND EUMELANIN PRECURSORS FOR SURFACE FUNCTIONALIZATION AND BIOMEDICAL APPLICATIONS.....47

2.1 Spectroelectrochemical reverse engineering as a top-down approach to evaluate the effect of metal binding on DHI and DHICA melanins redox properties 50
2.1.1 Redox activity of DHI and DHICA melanin.....50

2.1.2 The effect of metal binding on the radical scavenging activity of DHI and DHICA melanins 59

2.2 Non-covalent interaction in redox-active films generated from a eumelanin precursor in the presence of HMDA 69

2.2.1 Investigation of the key factors driving film deposition from MeDHICA/HMDA ..69

2.2.2 Morphological, structural, and electrochemical characterization of MeDHICA/HMDA film 72

2.2.3 Computational studies 77

2.2.4 Chemical characterization of the film components 77

2.2.5 Chemical, kinetic and morphological analysis of the MeDHICA/HMDA film 80

2.2.6 Antioxidant properties of the MeDHICA/HMDA films and cell protection effects 83

2.2.7 Proposed model for MeDHICA-HMDA film deposition 86

2.3 Melanin pigments from 5,6-dihydroxyindole carboxamides: properties evaluation for assessment of the potential for dermocosmetic applications 90

2.3.1 Oxidation of DHICA amides: pigment formation and properties characterization 96

2.3.2 *N*-butane-5,6-dihydroxy-1*H*-indole-2-carboxamide and its melanin for dermocosmetic application 98

2.4 Experimental section 107

3 NATURAL AND SYNTHETIC DERIVATIVES OF PHENOLIC COMPOUNDS AS TYROSINASE INHIBITOR FOR THE TREATMENT OF PIGMENTARY DISORDERS 117

3.1 Preparation of extracts from selected agri-food by-products 120

3.1.1 Inhibition of mushroom tyrosinase activity by natural phenolic compounds extracts from agri-food by-products 122

3.1.2 Inhibition of enzymatic browning in fruit smoothies by natural phenolic compounds extracts from agri-food by-products 126

3.2 Preparation of 2-S-lipoylcaffeic acid butanamide 134

3.2.1 Synthesis of the amide derivative of coumaric acid 134

3.2.2 Synthesis of the 2-S-lipoylcaffeic acid butanamide 138

3.2.3 Inhibition of mushroom tyrosinase activity by 2-S-lipoylcaffeic acid butanamide 140

3.3 Experimental section 141

4 MUSSEL INSPIRED BIOADHESIVES FROM WASTE PROTEINS AND PLANT DERIVED PHENOLIC COMPOUNDS FOR BIOMEDICAL APPLICATIONS 146

4.1 Bio adhesives from soy proteins and plant derived polyphenols 149
4.1.1 Preparation of SPI/polyphenols hydrogels 149
4.1.2 Mechanical properties of SPI/polyphenols hydrogels 151
4.1.3 Characterization of SPI/polyphenols hydrogels 153
4.1.4 SPI/agarose/polyphenols hydrogels 160
4.1.5 Cytocompatibility and wound healing properties 163
4.1.6 Hemocompatibility 166
4.1.7 Antibacterial evaluation 168

4.2 Bioadhesives from whey proteins and extracts from agri-food by-products ... 172
4.2.1 Preparation of WPI/polyphenols hydrogels 172
4.2.2 Properties of WPI/polyphenols hydrogels 173

4.3 Experimental section 177

5 GREEN METHODOLOGIES FOR THE RECOVERY OF LOW AND HIGH MOLECULAR WEIGHT PHENOLIC COMPOUNDS FROM AGRI-FOOD BY-PRODUCTS 185

5.1 Lignin extraction from nut shells 187
5.1.1 Structural Characterization of Nut shell Lignin 188
5.1.2 Antioxidant Properties of the Nut Shell-Derived Lignin 196

5.2 Extraction of low and high molecular weight phenolic compounds from defatted Spent Coffee Ground (dSCG) 200
5.2.1 Extraction of low molecular weight phenolic compounds from dSCG 201
5.2.2 Green extraction of lignin of solid residue from dSCG hydroalcoholic treatment 205
5.2.3 Antioxidant properties of dSCG extracts 207

5.3 Recovery of low and high molecular weight phenolic compounds from other agri-food by-products by a sequential two-steps protocol 208
5.3.1 Evaluation of the antioxidant properties of low molecular weight phenolic compounds recovered from different agri-food by-products 208
5.3.2 Extraction and characterization of low molecular weight phenolic compounds from pomegranate peel and seeds by-products 210

5.3.3 Extraction and characterization of high molecular weight phenolic compounds from ethanol solid residue of pomegranate by-products 214

5.4 Experimental Section 219

6 THE YIN (ORGANIC) AND YANG (INORGANIC) HYBRID SYSTEMS FOR BIOMEDICAL AND ELECTRONIC APPLICATIONS

225

6.1 Pecan Nut Shell-mediated synthesis of silver nanoparticles *via* mechanochemistry: a green approach to a multifunctional material with photocatalytic, antibacterial and antioxidant properties 227

6.1.1 Silver ion reduction by Pecan Nut Shell: wet-chemical *versus* mechanochemical approach 227

6.1.2 Morphological and structural characterization of AgNP-PNS 230

6.1.3 Antioxidant properties of AgNP-PNS 233

6.1.4 Photocatalytic properties of AgNP-PNS 234

6.1.5 Antibacterial and antibiofilm activity of AgNP-PNS 236

6.2 Lignin from chestnut shells as a potent reducing agent for the preparation of silver nanoparticles and implementation of high antioxidant and antibacterial poly (lactic acid) electrospun fibers 241

6.2.1 Synthesis of AgNP-CLN following a green procedure 241

6.2.2 Incorporation of AgNP-CLN into poly(lactic acid) electrospun fibers containing cellulose nanocrystals or chitosan films and evaluation of their antioxidant and antibacterial properties 241

6.3 Electron flow characterization of catechol-graphene composite hydrogels for charge storage application 250

6.3.1 Structural characterization of catechol-graphene hydrogel 250

6.3.2 Mechanisms for charge-storage and electron-transfer without mediators 256

6.3.3 Mechanisms for charge-storage and electron-transfer with mediators 263

6.4 Experimental section 276

7 *CONCLUSIONS* 285

8 REFERENCES 290

LIST OF ABBREVIATIONS 321

Abstract

The core of this PhD thesis is the exploitation, the manipulation, and the mimicking of natural phenolic systems as functional biocompatible components for use in hydrogels, sensors, surface coating, underwater adhesion, drug delivery and interfaces in technological and biomedical applications. Use of green chemistry methodologies, based on mechanochemical treatments, solvent free reaction, deep eutectic solvents, for preparation/manipulation of these materials or their extraction from natural sources represents a main approach pursued in this research activity. The synergistic effect stemming from combination of these compounds, exhibiting unique intrinsic features, with inorganic materials, resulting in tuning of their chemical, optical, and even electrical properties was also investigated.

In detail, the main outcomes of this PhD research activity can be summarized as follows:

- A versatile dip-coating technology widely applied in the case of polydopamine (PDA) for surface functionalization of various materials was applied to the methyl ester of the melanin precursor 5,6-dihydroxyindole-2-carboxylic acid (DHICA) in combination with hexamethylenediamine (HMDA) capable of imparting adhesive properties. For the investigation of the redox activity and morphology of the resulting film, voltammetric and AFM/SEM techniques were used. Chemical characterization was performed using HPLC, MALDI-MS, and ^{1}H-NMR. Using chemical assays and a model of UV-stressed human immortalized keratinocytes (HaCat) cells, the film reducing activity was assessed and compared to PDA based film. The hypothesized film deposition mechanism is the spontaneous assembly of self-organized networks held together primarily by electrostatic

interactions of MeDHICA in the anion form and HMDA as the dication. The film exhibited considerable oxidative stress protection on HaCaT cells and showed strong reducing properties.

- The synthesis of new eumelanin precursors such as the amide/diamide derivatives of 5,6-dihydroxyindole-2-carboxylic acid was developed, based on the use of N-[(dimethylamino)-1H-1,2,3-triazolo-[4,5-b] pyridin-1-ylmethylene]-N-methylmethanaminium hexafluorophosphate N-oxide (HATU) as coupling agent and requiring the protection of the catechol function by easily removable acetyl groups. Satisfactorily high yields (>85%) were obtained for all amides. The melanin-like pigments prepared by the amide derivatives by oxidative polymerization in air in aqueous buffer at pH 9, exhibited chromophores resembling those of DHICA-derived pigments. In the case of the carboxybutanamide, analysis of the pigment by EPR, ATR FT IR and MALDI MS indicated a substantial structural similarity to DHICA melanin, while investigation of the early intermediates confirmed unchanged regiochemistry of the oxidative coupling. The pigment exhibited a UVA-visible absorption even more intense than that of DHICA melanin, and a noticeable solubility in polar solvents of dermocosmetic relevance together with optimum antioxidant and lipid peroxidation inhibition properties.
- Phenolic compounds deriving from agri-food by-products or synthetic conjugates of caffeic acid such as 2-*S*-lipoylcaffeic acid butanamide were exploited as active compounds for the inhibition of tyrosinase. Preliminary analysis of these compounds on dopa or tyrosine oxidase activity of mushroom tyrosinase showed potent inhibitory effects. Overall, these results hint to the use of these compounds as a valuable option in the treatment of pigmentation disorders associated with an overproduction of melanin by the action of tyrosinase.

- An alternative strategy for the implementation of bio-inspired glues by proper combination of polyphenols or waste materials including proteins with *in-situ* generated catechol polymers was developed. The hydrogels proved to be biocompatible, hemocompatible, not harmful to skin, displayed durable adhesiveness and exhibited good water vapour permeability. Additionally, they demonstrated excellent contact-active antibacterial properties and in some cases a favourable wound healing activity on dermal fibroblasts.
- A green deep eutectic solvent (DES) based protocol coupled with a ball milling pre-treatment for the recovery of lignins from edible nuts was developed. In particular, the extracted materials were recovered in satisfactory yields (19-27% w/w). A completely spectroscopic and chromatographic characterization allowed to conclude that the majority of the samples consisted of lignins with remarkable antioxidant properties.
- A low-cost, scalable and straightforward solid-state mechanochemical protocol for the synthesis of silver nanoparticles (AgNP) based on the use of the highly reducing agri-food by-product Pecan Nut Shell (PNS) or lignin was developed. In addition, lignin or mechanochemical prepared Lignin/AgNPs were incorporated into poly (lactic acid) electrospun fibers, providing materials with enhanced antioxidant and antimicrobial properties for use in the biomedical sector.

Finally, as part of the PhD project carried out during a training period carried out at the Institute of Bioscience and Biotechnology, University of Maryland (College Park, USA) under the supervision of Professor Gregory Payne the following research activities were developed:

- A top-down reverse engineering mediators-based approach for the study of a chitosan hydrogel embedded with 5,6-dihydroxyindole (DHI) and the corresponding carboxyl acid (DHICA) melanins was implemented.

This approach coupled with a spectroelectrochemical analysis highlighted the change in terms of antioxidant activity of DHICA and DHI melanin before and after metal binding.

- A *facile* reverse engineering method was applied to fully characterize new functional hybrids catechol-graphene composite hydrogels, showing synergistic properties such as metal-like conductivity, redox activity and charge-storage through an electrical double as demonstrated by spectroelectrochemical measurements. Conducting and redox-active components enable distinctly different mechanisms for charge-storage and electron-transfer; these components act synergistically, and mediators provide unique opportunities to extend the capabilities of electronic materials.

List of publications

Argenziano, R.; Alfieri, M.L.; Arntz, Y.; Castaldo, R.; Liberti, D.; Monti, D.M.; Gentile, G.; Panzella, L.; Crescenzi, O.; Ball, V.; Napolitano, A.; d'ischia, M., Non-covalent small molecule partnership for redox-active films: Beyond polydopamine technology. *Journal of Colloid and Interface Science*, **2022**, *624*, 400-422; doi: 10.1016/j.jcis.2022.05.123.

Argenziano, R.; Della Greca, M.; Panzella, L.; Napolitano, A., A Straightforward Access to New Amides of the MelaninPrecursor 5,6-Dihydroxyindole-2-carboxylic Acid and Characterization of the Properties of the Pigments Thereof. *Molecules*, **2022**, *27*(15); 4816, doi: 10.3390/molecules27154816.

Argenziano, R.; Moccia, F.; Esposito, R.; D'errico, G.; Panzella, L.; Napolitano, A., Recovery of Lignins with Potent Antioxidant Properties from Shells of Edible Nuts by a Green Ball Milling/Deep Eutectic Solvent (DES)-Based Protocol. *Antioxidant*, **2022**, *11*(10), 1860; doi:10.3390/antiox11101860.

Kim, E.; **Argenziano, R.**; Zhao, Z.; Chen, C.; Shen, M.; Bentley, W.E.; Napolitano, A.; Payne, F.G., Characterizing Electron Flow through Catechol-Graphene Composite Hydrogels. *Advanced Materials Interfaces*, **2022**, *9*(35); doi:10.1002/admi.202202021.

Argenziano, R.; Salazar, S.; Panaro, A.; Calarco, A.; Di Sallec, A.; Aprea, P.; Cerruti, P.; Panzella, L.; Napolitano, A., Combining the Potent Reducing Properties of Pecan Nutshell with a Solvent-Free Mechanochemical Approach for Synthesizing High Ag^0 Content-Silver Nanoparticles: An Eco-Friendly Route to an Efficient Multifunctional Photocatalytic, Antibacterial, and Antioxidant Material. *Nanomaterials*, **2023**, *13(5)*, 821; doi:10.3390/nano13050821.

Argenziano, R.; Alfieri, M.L.; Gallucci, N.; D'Errico, G.; Panzella, L.; Napolitano, A., A model eumelanin from 5,6-dihydroxyindole-2-carboxybutanamide combining remarkable antioxidant and photoprotective properties with a favourable solubility profile for dermo-cosmetic applications. *International Journal Molecular Sciences,* **2023**, *24(4),* 4241; doi:10.3390/ijms24044241.

Manuscripts in preparation

Argenziano, R.; Viggiano, S.; Esposito, R.; Schibeci, M.; Gaglione, R.; Castaldo, R.; Fusaro, L.; Boccafoschi, F.; Arciello, A.; Della Greca, M.; Gentile, G.; Cerruti, P.; D'errico, G.; Panzella, L.; Napolitano, A., All-natural mussel-inspired bioadhesives from soy proteins and plant derived polyphenols with marked water-resistance and favourable antibacterial profile for wound treatment applications. Submitted.

Chapter 1

Introduction

Phenols and polyphenols provide the core reactive unit in several bioactive compounds and biopolymers, including catecholamines, flavonoids, estrogens, melanins and other plant occurring heterogeneous polymers like tannins and lignins [1]. Phenolic compounds have been increasingly investigated for their well-known antioxidant properties and exploited as functional biocompatible components for hydrogels, sensors and other functional systems [2]. Natural phenol polymers such as lignins, tannins have received considerable attention for the design of functional materials for technological and biomedical applications, thanks to their peculiar chemical-physical properties [3,4]. Eumelanins and related phenolic polymers, particularly polydopamine, have attracted growing interest for surface coating, antifouling, underwater adhesion, drug delivery, biosensing and as interfaces in bioelectronics [5–7]. The exploitation or the mimicking of natural phenolic systems may allow to translate their UV-absorbing, photoconductive, redox and free radical scavenging properties into new functional soft, robust, adhesive, multifunctional and biocompatible materials and molecular systems for various biomedical applications [8]. Moreover, in *o*-diphenolic systems, the ready conversion to the reactive *o*-quinone system allows for chemical functionalization, polymerization, and interactions with a variety of systems such as polysaccharides, proteins, or with metals and other inorganic surfaces, creating hybrid systems [9–11]. This affordable approach can be used for the manipulation of polyphenols, creating interesting and complex network structures or functionalized surfaces for nanotechnology or biomedical

applications. Moreover, the use of green chemistry methodologies including solvent free conditions and mechanochemistry for functionalization, manipulation, activation of polyphenol or their extraction from natural sources such as agri-food wastes represent the central strategy to improve/potentiate their activities for various applications (Figure 1.1) [12,13].

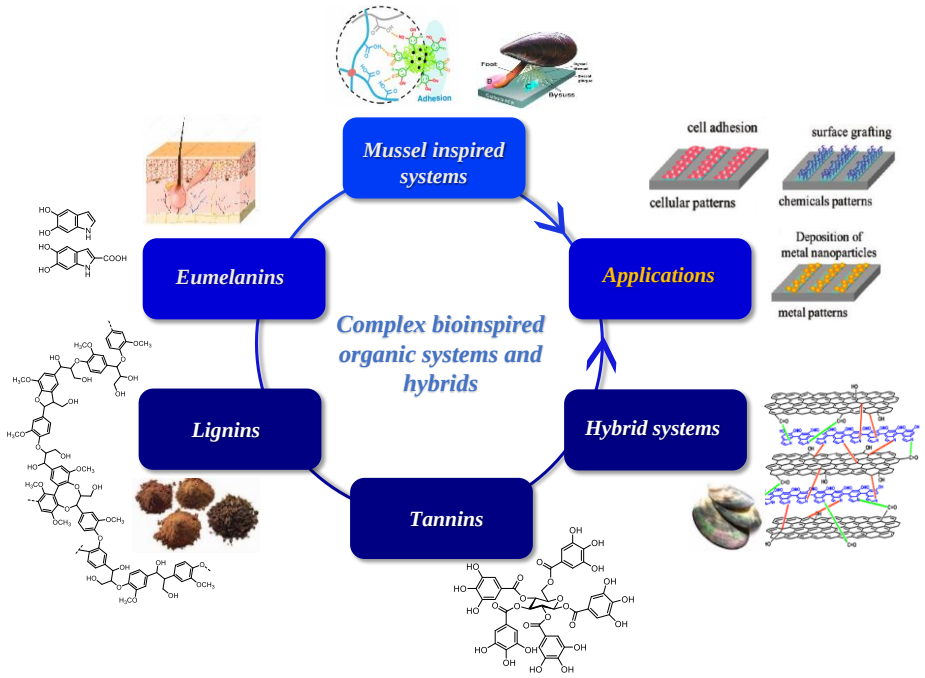

Figure 1.1. State of art.

1.1 Phenol compounds

Almost 2000 years ago Hippocrates said: "Let food be your medicine, and medicine be your food". Since that time the beneficial effects of natural products have been explored for many purposes [1]. Among natural products, there are phenolic compounds, a prominent family of ubiquitous compounds widely distributed in plants and/or marine organism with fascinating inherent biocompatible, bioadhesive, antioxidant, and antibacterial properties [2,14]. In fact, they represent a huge group of naturally occurring phytochemicals, with well-known nutritional and therapeutic dietary skills that are able to alleviate degenerative diseases and skin conditions connected to cumulative oxidative damage. The unique structure of these compounds, consisting of one or more phenol structural units, allow the formation of strong non-covalent interactions (e.g., electrostatic, cation – π interactions, multiple hydrogen bonding) as well as covalent interactions (e.g., Michael addition/Schiff-base reaction, radical coupling reaction, coordination with metal ions) [15] (Figure 1.2).

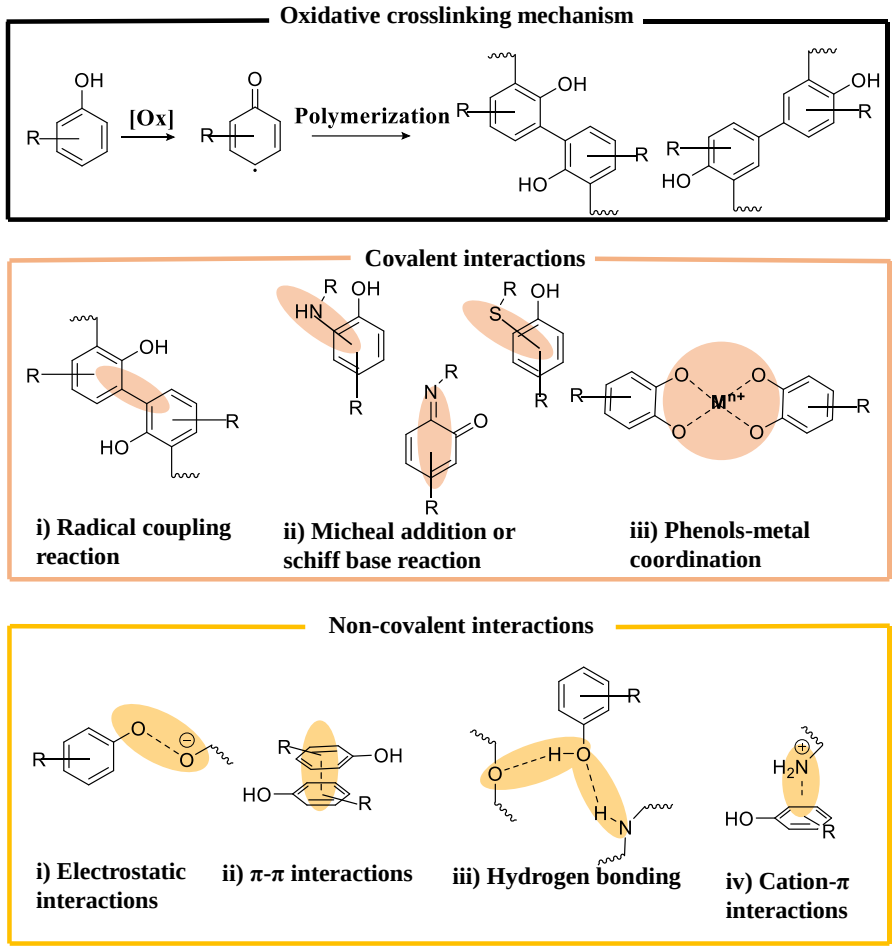

Figure 1.2. Oxidative crosslinking and other mechanism of interaction of phenols.

In addition, as result of the variety of phenol scaffolds and of their several possible combinations, these compounds exhibit various physical, chemical and biological properties. More than 8000 kinds of compounds with phenolic structures have been identified and extracted from different natural sources, mostly from plants [16–18]. Among these, phenolic acids, lignins, tannins and melanins have attracted increasing interest for surface coating, functionalization, sensors, and hydrogels in biomedical and nanotechnology fields, not only as monomers (phenolic acids) or as biopolymers (melanins, tannins, lignin,

polydopamine), but also combined with other type of materials such as inorganic compounds [8,16–19].

1.1.1 Phenolic acids

Phenolic acids represent one of the simplest structural classes belonging to phenols family. These compounds are generally classified in two main subgroups namely as the hydroxybenzoic acids and the hydroxycinnamic acids. The first one is characterized by a C6-C1 structure, and they include p-hydroxybenzoic, protocatechuic, vanillic, syringic, and gallic acids. On the other hand, the hydroxycinnamic acids, characterized by a three-carbon side chain, are caffeic, ferulic, p-coumaric, and sinapic acids (Figure 1.3) [20].

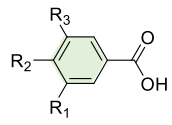

Hydroxybenzoic acid

Acid	R_1	R_2	R_3
p- Hydroxybenzoic	H	OH	H
Protocatechuic	OH	OH	H
Vanillic	OCH_3	OH	H
Syringic	OCH_3	OH	OCH_3
Gallic	OH	OH	OH

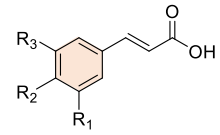

Hydroxycinnamic acid

Acid	R_1	R_2	R_3
p-Coumaric	H	OH	H
Ferulic	OH	OH	H
Caffeic	OCH_3	OH	H
Sinapic	OH	OH	OCH_3

Figure 1.3. Chemical structures of most abundant naturally occurring phenolic acids.

These compounds are widespread in nature, particularly in berries, cereals, legumes, fruit and oilseeds, where the highest amount of phenolic acids is frequently found as esters, glycosides, or amides [21], rarely as free water insoluble or saccharide-conjugated soluble forms [22]. These compounds exhibit a wide range of unique intrinsic properties [23]. They show marked antioxidant properties against reactive nitrogen species (RNS) and reactive oxygen species (ROS) due to the presence of hydroxyl group on the aromatic ring [24,25].

Reactive oxygen species are by-products of numerous metabolic processes in living systems [26]. DNA, RNA, proteins and lipids are damaged by RNS and ROS, and ROS and RNS imbalance leads to oxidative stress in cells. Several phenolic acids widely distributed in nuts, fruits and vegetables can counteract ROS and RNS induced damages by providing free radical scavenging activity and upregulation of the enzymes that detoxify ROS and RNS. They also have the capacity to increase the levels of endogenous antioxidant enzymes, resulting in a beneficial effect against cancer development, cardiovascular diseases, inflammatory diseases and other disorders. Exposure to UV radiation can lead to skin cancer and accelerated aging of the skin by causing sunburn, DNA damage, and connective tissue degeneration. Given the damaging effects of species generated by irradiations such as reactive oxygen species (ROS) in the skin, including superoxide ion ($O_2^{\cdot-}$), hydroxyl radical ($OH^{\cdot}$), and peroxyl radical ($ROO^{\cdot}$), numerous studies have been devoted to the study of antioxidant compounds to enhance the endogenous cutaneous defense system against these oxidative stress-mediated diseases [27]. In addition to the antioxidant property, common to almost all phenolic compounds, phenolic acids possess other potentially clinically relevant properties such as chemo-preventive activity against gastric ulcers, long-term diabetes complications, diabetic neuropathy, kidney dysfunction and retinopathy [28]. For example, lettuce, potatoes, apples, berries and coffee beans, with high levels of phenolic compounds, are anti-mutagenic, so able to prevent cancer [29,30]. They can ease cardiovascular complications such as cardiomyopathy and inhibit enzymes involved in Alzheimer's disease. Phenolic acids have also shown in vitro marked antibacterial activity against several pathogenic strains (Figure 1.4) [31,32].

On these bases, more attention has been focused on the incorporation of phenolic acids as active components in various matrix to make the most of their extraordinary properties [33].

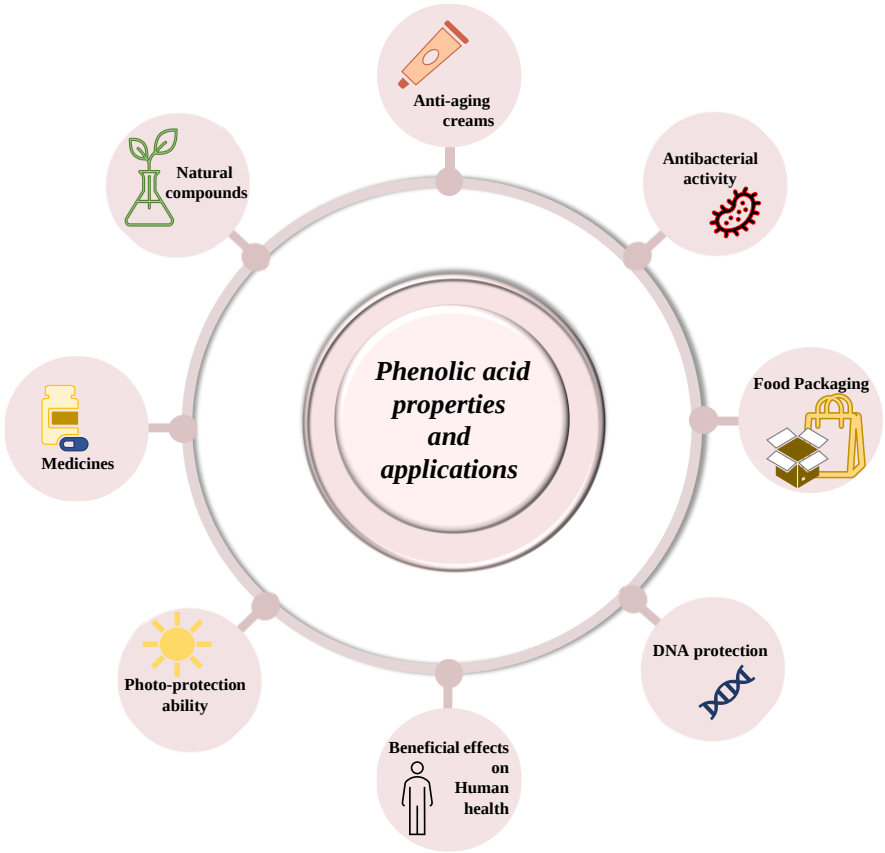

Figure 1.4. Representative scheme of phenolic acid properties and applications.

1.1.1.1 Incorporation of phenolic acid into biopolymers

In this context, many studies have been devoted to the exploitation of naturally occurring phenolic acids for various applications in different fields [34].

For example, to reduce the excessive use of disposable plastics and their negative impact on the environment, in the last decade alternative materials were developed for food packaging applications. With this aim, the development of biobased polymers as a method of replacing petroleum-based synthetic plastics has been extensively investigated [35]. In particular, the addition of active chemicals into the biodegradable polymer matrix is emerging as a low-cost method for enhancing food preservation. On the other hand, the *facile*

incorporation of phenolic acids into the polymers make this an affordable strategy, that adds value to biodegradable materials for both stabilization or/and functionalization purposes [27].

Recently, great interest has been devoted to starch, one of the most naturally occurring polymers, recovered from several plant sources, including potato, corn, and cassava. In fact, it has been demonstrated that this affordable material can be improved when combined with other biodegradable polymers [37]. For instance, when starch is combined with other polysaccharides, such xanthan or gellan gum, its mechanical limitations are easily overcome. Derivatives of cellulose such as methylcellulose (MC), hydroxypropyl methylcellulose (HPMC), and carboxymethylcellulose, have demonstrated outstanding film-forming capacity, giving films with superior hydrophobic compound barrier capabilities and high mechanical performance when incorporated into starch.

Other materials from natural sources such as proteins have been widely investigated for use in food packaging [38]. Of relevance are caseinate, whey protein, soy protein, gluten, and gelatin. Due to their distinctive structure, protein films offer greater mechanical characteristics than polysaccharide films [39]. However, the high-water vapor permeability remains one of their major limitations, that can be easily overcome in presence of high amounts of phenolic acids. The interaction of phenolic compounds, particularly phenolic acids, with proteins, including gelatin, whey, and egg proteins, can dramatically change the structural, physicochemical, and biological characteristics of proteins and increase their potential uses, including hydrogels, biocompatible and biomimetic glues, nanostructures for drug delivery and other devices for biomedicine and organic electronics [40]. In fact, it is well known that structural modifications can significantly enhance the functional properties of proteins. To modify proteins, three main methods are frequently used: physical, enzymatic modifications, and chemical modifications [41].

Non-covalent physical interactions between phenolic chemicals and proteins can result in phenolic-protein complexes (*e.g.*, electrostatic, hydrophobic, van der Waals and hydrogen bonding). On the other hand, phenolic substances can be linked to proteins through covalent bonds [42]. Notably, although either modification may change the characteristics of proteins, phenolic-protein conjugates are more stable than non-covalent phenolic-protein complexes. While in the past decade most studies were focused on these latter that are easier to obtain than covalent phenolic-protein conjugates, more recently attention has been directed to crosslinked systems, with the development of new strategies to create phenolic-protein conjugates such as alkaline, free radical-mediated grafting, enzyme-catalysed grafting, and chemical coupling techniques.

1.1.1.2 Mussel inspired catechol-protein strategies

As expected, the nature has already discovered the extraordinary network that protein/polysaccharides and phenolic acids are able to create. Various sessile marine organisms, including marine plants and animal organisms, have developed their own strategies to adhere to a variety of surfaces using this lattice structure. The underwater adhesion of brown algae is due to polyphenols/alginates lattice linked also by calcium ions. The phenolic compounds and alginate are secreted separately, and only subsequently cross-linked together to form the final adhesive. The remarkable property of this network structure is of great interest for biomedical and tissue engineering applications [43–47].

Another system that has represented a great source of inspiration are the proteins of byssus. These proteins, such as *Mytilus edulis* foot proteins-3 and -5 (Mfp-3 and -5), located in the distal portion of the mussel byssus where the byssal foot engages the substrate surface. The key feature is the high content of lysine residues and of 3,4-dihydroxy-L-phenylalanine (DOPA), a compound belonging to the *o*-diphenol or catechol class. These latter are susceptible to oxidation,

giving rise to *o*-quinones highly electrophilic species capable of establishing covalent or non-covalent interactions.

Based on this knowledge, an interplay of several chemical factors has been proposed to explain the excellent adhesion (between different materials) and cohesion (between different parts of the same material) properties of byssus proteins, such as H-bonding, electrostatic, hydrophobic, coordination and π-cation interactions.

Among the various approaches that can be used to modify material surfaces, the most convenient in terms of time and easily accessible are those based on wet adhesion technologies inspired by nature.

In 2007 following inspiration from the robust adhesion properties of mussel byssus proteins, a new material has been described: polydopamine (PDA) [48–52].

This latter is a black, insoluble, eumelanin-like substance generated by the alkaline oxidative polymerization of dopamine. The combination of the functional groups of the aminoacids lysine and DOPA of byssus proteins allows dopamine (Figure 1.5) to form polymeric films that can be easily deposited at the interface of different materials, including metals, oxides, inorganic semiconductors, ceramics, and polymers, can bind cells, biomolecules, and metal ions, and can be used to control or modify the hydrophobicity of a variety of interfaces [53–56].

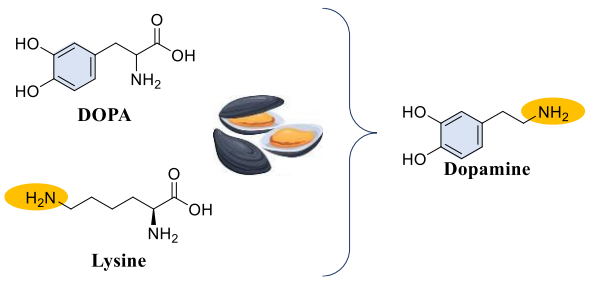

Figure 1.5. Mussel Inspired PDA.

PDA film properties, including hydrophilicity and thickness, can be finely tuned by a variety of experimental parameters including dopamine concentration, nature of the buffer, oxidant, and pH. Polydopamine also displays many properties in common with naturally occurring melanin, including optical, paramagnetic and electrical properties, and, most importantly, it exhibits excellent biocompatibility. Another valuable feature lies in its chemical structure that incorporates many functional groups such as catechol, amine, and imine. These functional groups can serve both as the starting points for covalent modification with desired molecules and as the anchors for the loading of transition metal ions, which can give rise to diverse hybrid materials by virtue of its powerful reducing capability toward these metal ions under basic conditions. With these benefits, the use of polydopamine is not restricted to surface coating and has been rapidly extended to a wide range of applications across the chemical, biological, medical, and materials sciences, as well as in technology and engineering fields [57,58]. However, despite their growing relevance in materials science, the control, optimization, and tailoring of surface and mechanical characteristics are currently limited. As a result, the development of a PDA-based technology is constrained. In one of the most plausible currently accepted theories, the polydopamine oxidation pathway shares many characteristics with melanin biosynthesis. It includes an oxidative reaction pathway, which transforms dopamine into 5,6-dihydroxyindole (DHI), one of the main eumelanin precursors, followed by further polymerization steps [59].

1.2 Polyphenols

1.2.1 Eumelanins as natural phenolic pigments

Melanins occupy a prominent position among biopolymers of polyphenol type. These latter are an important class of phenolic pigments deriving from the oxidative metabolism of tyrosine, responsible for the brown colour of skin, hair,

hair and eyes of humans and mammals. They are mainly divided into two varieties: eumelanins (black or brown) and pheomelanins (yellow-red). Eumelanins have an absorption spectrum of the broad electromagnetic spectrum and excellent antioxidant properties, characteristics of great importance for photoprotective applications, helping to prevent sunburn, DNA damage and skin cancer. Instead pheomelanins, typical of individuals with red hair, light skin and eyes and freckles, are known for their photosensitizing properties, causing a higher proness to skin tumors in individuals with the red phenotype [60–62].

Melanins are generated in melanocytes, highly specialized cells located between the epidermis and the dermis. The synthesis of melanins begins with the oxidation of the amino acid L-tyrosine by tyrosinase, followed by a series of spontaneous reactions that depend on various factors such as the presence of thiols, the pH, the presence of ions such as zinc and copper, and oxygen. After the first enzymatic step of oxidation of L-tyrosine (or L-DOPA) to dopaquinone, a common precursor to eumelanins and pheomelanins, the prevalence of one or the other metabolic pathway depends on the levels of the amino acid cysteine which can intercept the dopaquinone. In fact, dopaquinone is an *o*-quinone and therefore particularly reactive towards thiols. In the absence or at low concentrations of cysteine, the intramolecular addition of dopaquinone by the amino group prevails with the formation of leudopachrome. This can be oxidized again in a redox reaction with the same dopaquinone giving dopachrome, which can subsequently rearrange with or without decarboxylation to generate the two monomers from which the eumelanins are composed, 5,6-dihydroxyindole (DHI) and 5,6-dihydroxyindole-2-carboxylic acid (DHICA) [63]. In vivo the formation of DHICA is favored by an enzymatic action of dopachrome tautomerase (Dct or Tyrosinase-related protein 2, Tyrp-2) or by the presence of transition metal ions such as Cu^{2+} or Zn^{2+}[64]. For this reason, natural melanins contain over 50% DHICA (Figure 1.6) [65].

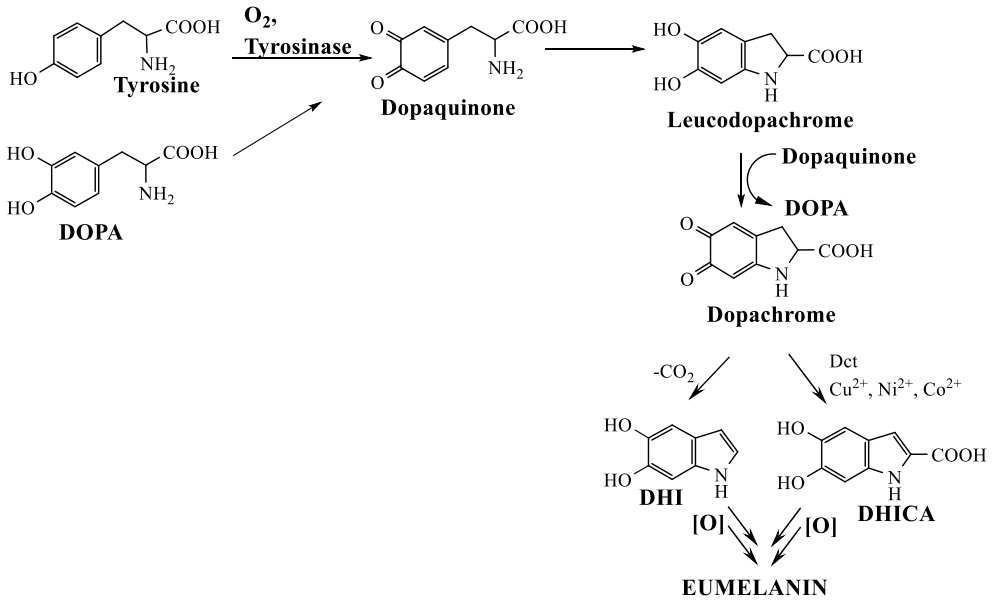

Figure 1.6. Eumelanin biosynthetic pathway.

Thanks to their many unique properties, in the last decade eumelanins have attracted great interest for potential applications as a biocompatible functional material for electronic and bioelectronic components, functionalization of surfaces, photoprotection of the skin and other applications in the field of cosmetics. In fact, these pigments, thanks to the peculiar catechol structure, can bind metal ions and some organic compounds such as drugs and toxins, and so they have been widely used in various fields such as optical biomimetics, cosmetics, UV protective lenses, food colorants, anti-melanoma therapy, and the preparation of metallic nanoparticles [66–68]. Melanin and melanin-like compounds have also been used as coating materials in electronics, sunscreens, energy storage, biofilms, drug delivery systems, and a variety of biomedical applications including bioimaging, diagnostic, tissue engineering, biosensors, photoacoustic imaging, phototherapy and therapeutic use [69]. A multitude of biopolymer-based materials including inorganic surfaces have been reinforced

or given extra functionality by the addition of melanin nanoparticles (MNP) or melanin-like nanoparticles (MLNP) [69].

1.2.2 Tannins as naturally occurring phenolic compounds

The term "tannin," which comes from the French term "tanin" and the latin Tannum “oak bark”, is used to describe a variety of naturally occurring phenolic compounds [70]. Tannins are divided in two main groups: condensed tannins and hydrolysable tannins [71]. Condensed tannins are oligomeric and polymeric species that cannot be hydrolysed, whereas the identification of many tannins as "hydrolysable tannins" resulted from the discovery that many of them may be hydrolytically divided into their constituents. These latter have as main component a monosaccharide, often D-glucose, whose hydroxy groups are esterified with phenolic substances like ellagic acid (EA) or gallic acid to produce, respectively, gallotannins and ellagitannins (Figure 1.7) [71]. These latter classes of tannins are abundant in oak wood (Quercus robur, Quercus petraea, and Quercus alba) [72], chestnut (Castanea sativa) [72–74], and myrobalan, galls (Quercus infectoria and Rhus semialata) [74–76], sumac fruits (Rhus coriaria [74,77] and Terminalia chebula) [74,78].

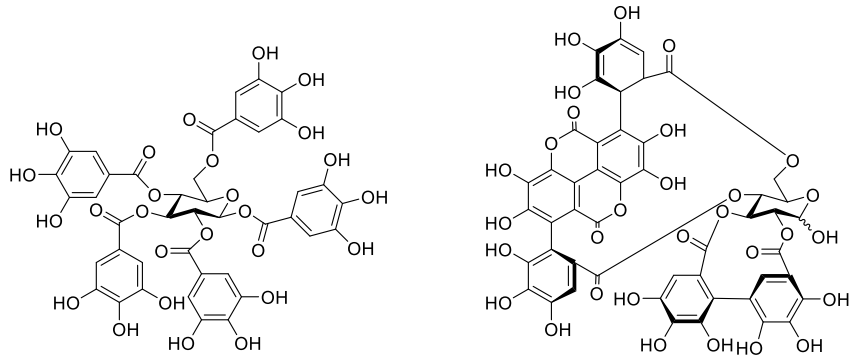

Figure 1.7. General structure of hydrolyzable tannins: a) gallotannin and b) ellagitannin.

On the other hand, condensed tannins represent the other major class of tannins. They are polymeric flavonoids, and their most common structural units are derivatives of the flavanols (+)-catechin, (-)-epicatechin, (+)-gallocatechin, (-)-epigallocatechin and (-)-epigallocatehin gallate, shown in Figure 1.8 [71].

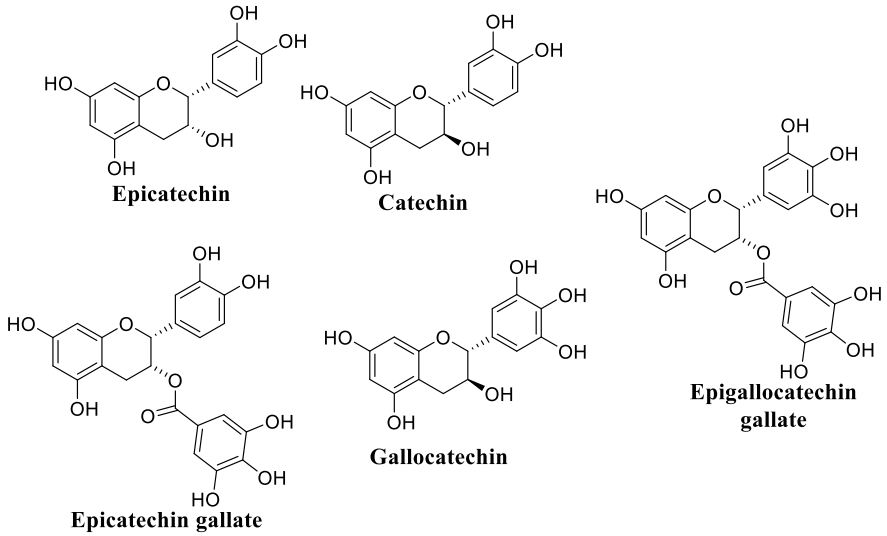

Figure 1.8. Structures of catechin, (-)-epicatechin, (+)-gallocatechin, (-)-epigallocatechin and (-)-epigallocatehin gallate.

They are characterized by a wide structural diversity due to possible O-methylation, C-and O-glycosylation, and O-galloylation. In addition, condensed tannins can be further distinguished into procyanidins and profisetinidins. Procyanidins can be classified in a dimeric B-type and trimeric C-type form, linked by single bond between units, usually between the C4 and the C6 or C8 of the flavanol units, or the A-type, characterized by an additional bond between C-2 and 7 or 5-OH (Figure 1.9) [79]. Profisetinidins, mainly found in some type of wood, such as quebracho (*Schinopsis lorentzii*) e mimosa (*Acacia mollissima*) [80], differ from the procyanidins by the absence of a hydroxyl group at C5 position of the A ring [71]. They can contain up to 10 units of monomers, with a molecular weight varying from 500 to over 20,000 Da [81].

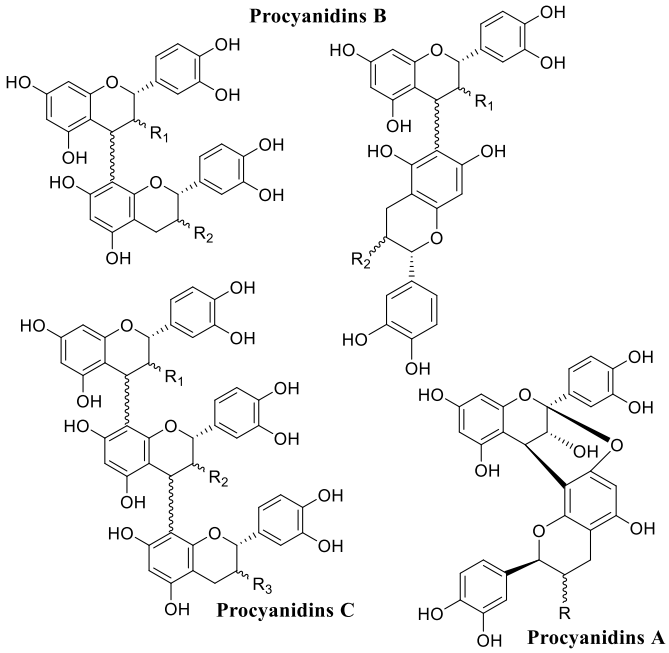

Figure 1.9. General structures of a) and b) B-type c) C-type and d) A-type procyanidins.

Among other naturally occurring phenolic compounds, tannins stand out thanks to their exceptional antioxidant, antibacterial, and anticancer properties [82–84]. The beneficial effects of these compounds were already discovered in the ancient societies, where the animal brain and fat, rich in tannins, were commonly used to protect animal skins. Nowadays, tannins have been associated to anticancer properties and to minimize the ability of a variety mutagens to cause mutations [85]. In fact, oxygen-free radicals are produced by several mutagens and/or carcinogens, able to interact with biological macromolecules causing different diseases. The antioxidative characteristic of tannins, which is crucial in preventing cellular oxidative damage, including lipid peroxidation, may be connected to their anticarcinogenic and antimutagenic potentials. In addition to these properties, tannins antibacterial activity is also widely known. Tannins can inhibit the growth of numerous fungi, viruses, bacteria, and yeasts. As result, tannins present in different fruits act as barrier

against microbial diseases and can be utilized in food processing to extend the shelf life of some foods.

1.2.3 The second most abundant phenolic polymers on the earth: the lignin

Another class of compounds belonging to the phenolic family is lignin. Lignin is an irregular, water-insoluble, high molecular mass biopolymer (600-15000 kDa), and after cellulose, is the second most abundant naturally occurring complex organic material of polyphenol type on the earth, accounting for approximately 30% of the organic carbon on the planet. Its main precursors are different hydroxycinnamyl alcohol monomers, such as coniferyl, sinapyl and *p*-coumaryl alcohols, which differ from each other in the degree of methoxylation [86]. The ratios of these precursors are variable depending on the plants considered. For instance, in lignin from softwood, the coniferyl alcohol content is often 90-95%, whereas from hardwood normally the coniferyl and sinapyl alcohol content is around 25-50% and 50-75%, respectively. Lignin from grass typically includes all three components. After oxidative coupling steps, these compounds give rise to the formation of guaiacyl (G), syringyl (S), and *p*-hydroxyphenyl (H) lignin units [86]. Typically, lignin polymer forms ether or ester bonds with other molecules present in nature such as cellulose. Consequently, the resulting natural polymers, named lignocellulose, is a complex and useful material. Different sources of lignocellulose contain different ratios of these constructive polymers. [87] Hardwood stem typically contains 24-40% of hemicellulose, 40-55 % of cellulose, and 18-25% of lignin, whereas the softwood stem contains 45-50% cellulose, 25-35% of hemicellulose and 25-35% of lignin. The most frequent inter-unit bond is the β-O-4-aryl ether linkage but β-5-phenylcoumaran, 5,5-biphenil, 4-O-5-biphenil ether, β-1-(1,2-

diarylpropane), β-β-pinoresinol and α-O-4-aryl ether can be also found (Figure 1.10) [4,88].

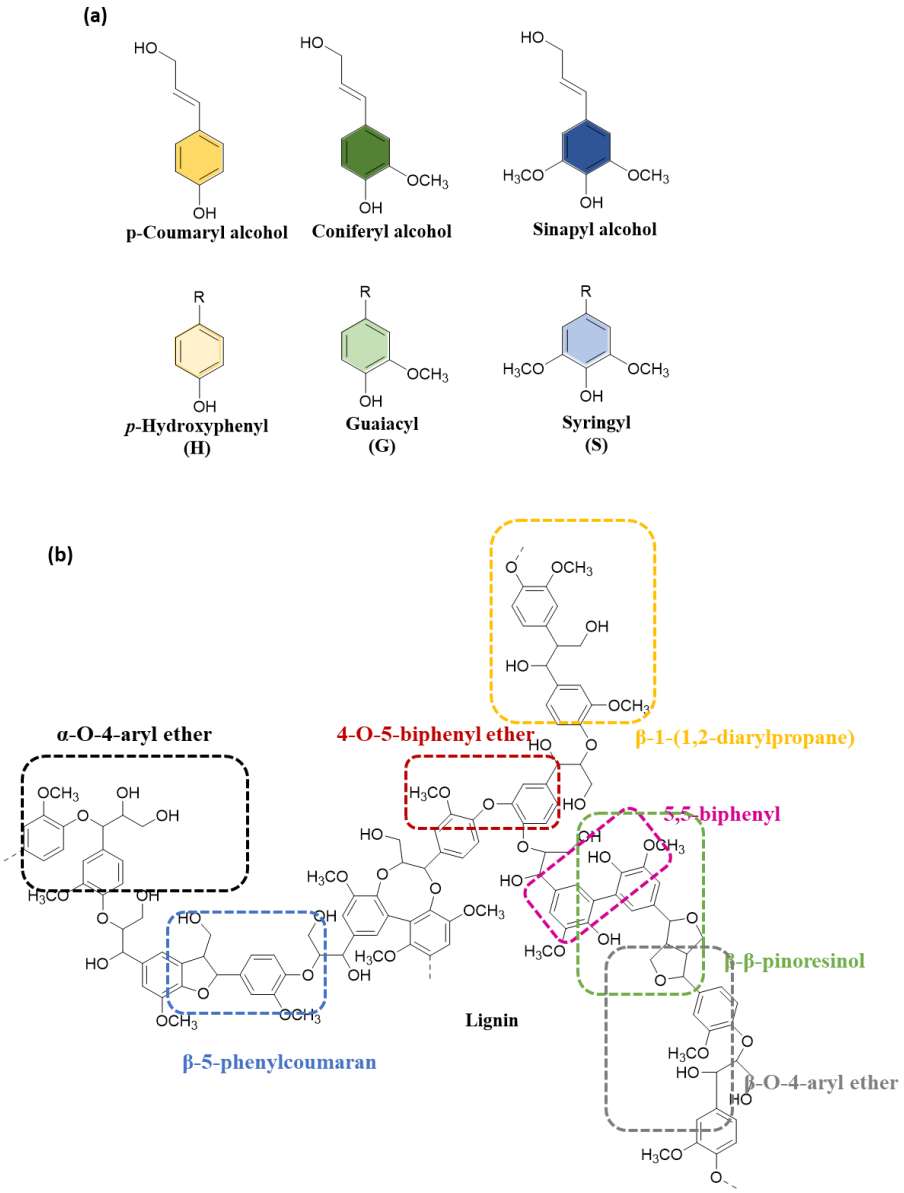

Figure 1.10. Chemical structures of a) lignin monomers and the corresponding structure in lignin b) lignin scaffold [89].

All these structures are related to the extraordinary properties of these important biopolymers. Lignin exhibits many biological functions in plants [90]. In fact, this polymer provides strength and hydrophobicity to the plant cell walls and at the same time protects the polysaccharides from microbial degradation. However, the enormous success of this complex biopolymer is also due to the beneficial effects on humans and other organisms such as antioxidant, antimicrobial, antibiotic ability and the prevention against cancer [91,92]. In addition, other relevant properties for this polymer during the last years has been described including the ability to reduce coronary heart disease, control diabetes, obesity, and Alzheimer's disease [93]. Natural lignin polymer protects plants from UV damage by shielding UV rays, characteristic of great interest for dermocosmetic, agricultural or food packaging applications [94,95]. In addition, lignins have generally been found to be non-toxic (in reasonable concentrations) by in vitro or in vivo toxicological assessment. One of the main factors driving the increased attention on lignin research and applications is the enormous amount of lignin produced as a by-product by many industrial sectors, still not fully exploited.

1.3 Agri food by-products as a source of phenolic compounds

The accessibility of phenolic compounds in several natural sources, including fruits, vegetables, and lignocellulosic biomasses, has inspired vigorous research into their characteristics and potential uses.

Recently, there has been a rise in interest using agri-food by-products as readily available, sustainable sources of phenolic chemicals [96]. A reasonable approximation of 1.3 billion tons of food is wasted globally every year as a result of procedures that occur along the whole supply chain [97]. In particular, the agri-food sector is in responsible for producing large amounts of organic biomass, of which a sizeable portion is designated as food waste and is composed of leaves, roots, stalks, bark, bagasse, straw remnants, seeds, wood,

and animal by-products [98]. Disposal of these by-products represents a cost to the food processor and has a negative impact on the environment. According to calculations, 50-110 m^3 of CO_2 and 90-140 m^3 of methane are released into the environment when one metric ton of organic solid waste decomposes [99]. Additionally, organic wastes may be the cause of phytotoxicity events such as water degradation and pollution, the death of marine organism, the suppression of seed germination, and digestive diseases in animals [100]. On the other hand, these materials might be seen as a widely accessible, reasonably source of value-valuable opportunity [97].

1.3.1 Fruit by-products

About 44% of all waste produced worldwide is made up of waste from fruits and vegetables (Figure 1.11). Most fruit by-products have phenolic chemicals in equal or higher concentrations than the fruit itself. The following is a list of the primary fruit by-products.

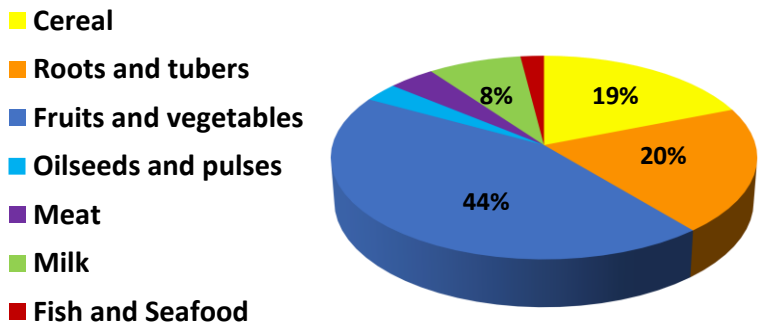

Figure 1.11. Graphic representative of waste produced worldwide.

Grape and wine by-products. The greatest fruit crop in the world is grape, which is mostly used to make table grapes, raisins, juices, and most importantly, wine [101]. Each year approximately 9 million tons of waste are produced by the wine and winery sectors worldwide, which is equivalent to 20% weight-for-

weight of the total grapes used to make wine [102]. The remaining pulp, peel, stems, and roughly 20-26% of the grape seeds make up most of the grape by-product known as grape pomace [103]. Grape pomace contains a variety of phenolic compounds, including (+)-catechin, quercetin, (-)-epicatechin, EA, hydroxytyrosol, myricetin, and trans-resveratrol, as well as phenolic acids like caffeic, gallic, 4-hydroxybenzoic, and syringic acid (Figure 1.12), which are well known for their positive effects on human health [103]. Another significant type of polyphenols found in grape pomace is condensed tannins. Oenological tannins, which are frequently employed as additives in the food and beverage industries, are in fact among the most significant high-value chemicals found in this by-product [36]. These tannins are also employed as feed additives and can regulate the metabolism of fat and glucose. Lastly, grape by-products have a lignin percentage of around 16-24% w/w [104].

Orange and lemon by-products. *Citrus sinensis* (orange), *Citrus reticulata* (mandarin), *Citrus tangerine* (tangerine), *Citrus aurantifulia* (lime), *Citrus limon* (lemon), *Citrus limetta* (sweet lime), and *Citrus paradisi* (grapefruit) are only a few of the fruits that belong to the citrus family [105]. Since around one-third of citrus fruits are used to make fresh juice or drinks, and since the output of citrus juice accounts for about half the fruit's weight, a substantial quantity of waste, up to 15 million tons annually, is generated worldwide (mostly from peel, seeds, and pulp). Citrus peels, together with the seeds and pulp, are a significant source of flavonoids, particularly flavanone glycosides (hesperidin, naringin, and narirutin), flavanones (hesperetin and naringenin), and flavone aglycons (sinensetin, nobiletin, luteolin, and tangeretin) (Figure 1.12) [96,102,103]. Citrus by-product extracts have been proposed as antioxidant, antibacterial, and antimicrobial agents, or as food additives, to give food and beverages a bitter flavor [106]. Polyphenols are present in significant concentrations in citrus residues, and citrus peels have a 15% greater total phenol content than the peeled fruit.

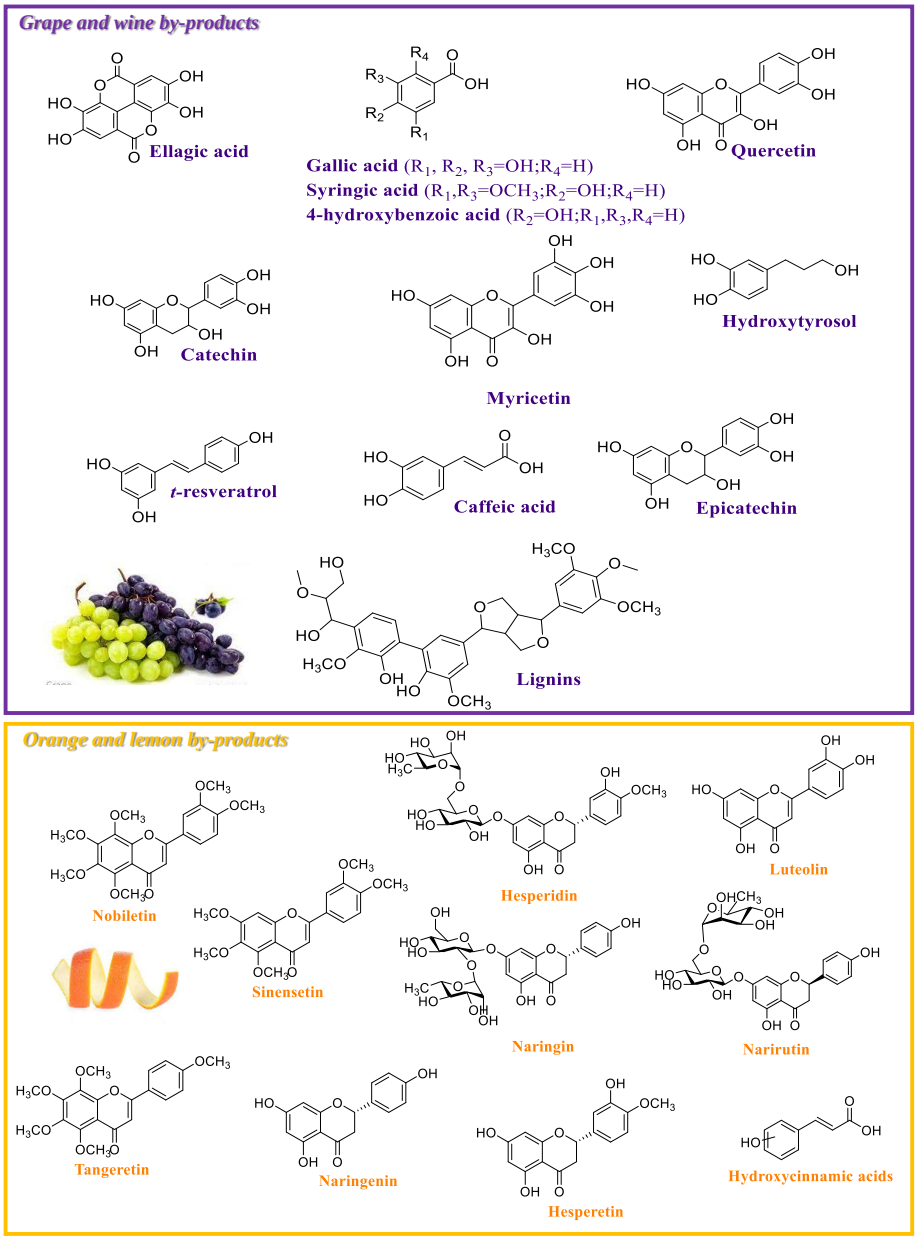

Figure 1.12. Main phenolic components of grape, orange and lemon by-products.

Pomegranate by-products. Pomegranate, also known as *Punica granatum L.*, is widely used in the juice industry. Nine tons of by-products are created for every ton of pomegranate juice produced [102]. The primary components of

pomegranate by-products are peels, pomace, and seeds, which have a 10-fold higher phenolic content than the pulp and make this waste material one of the most intriguing industrial by-products [102]. Different polyphenols, including anthocyanins, flavonoids, as well as ellagitannins, punicalagin and punicalin, are abundant in pomegranate by-products, contributing to their strong antioxidant activity (Figure 1.13) [36,102,103,107]. Pomegranate by-products have been shown in several studies to have health-promoting properties, including anticancer and antibacterial properties [108–111].

Apple by-products. The primary by-products of the apple business are apple pomace, peels, and seeds, which are also a cheap source of phenolic chemicals. Quercetin glycosides, kaempferol, catechin, procyanidins, and particularly the dihydrochalcone phlorizin are among those that have a significant impact. There are also other polyphenols such anthocyanins and phenolic acids, primarily chlorogenic and caffeic acids [96,102,103]. By-products from apples show antibacterial, antitumor, and cardioprotective properties (Figure 1.13) [112,113].

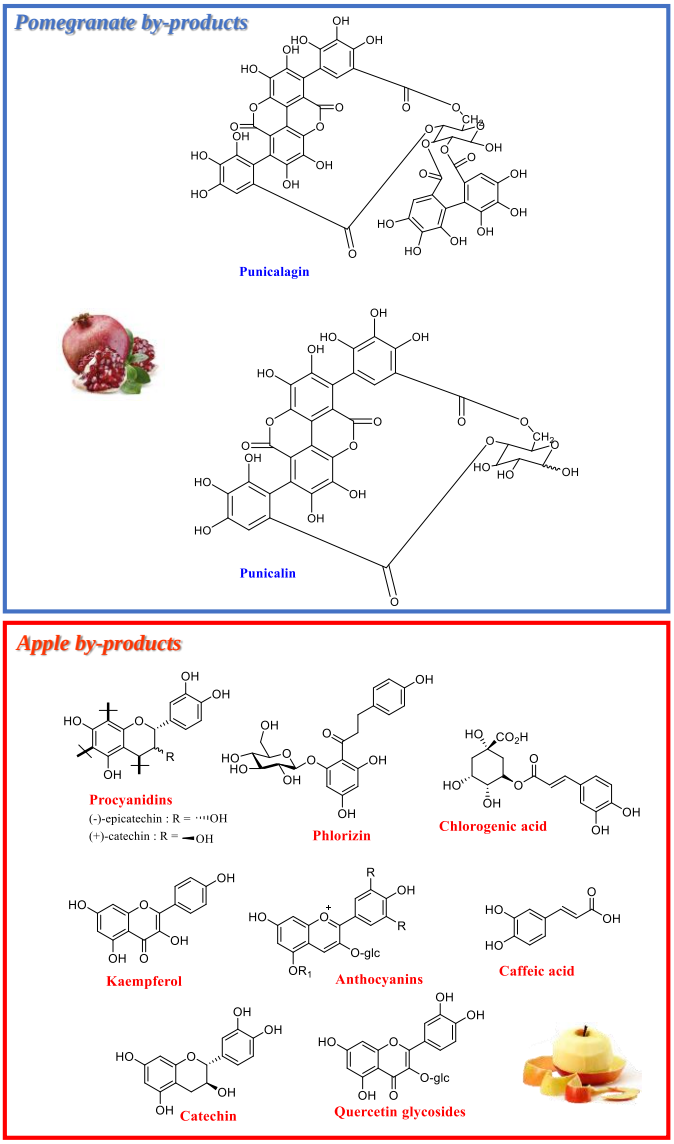

Figure 1.13. Main phenolic components of apple and pomegranate by-products.

1.3.2 Lignocellulosic by-products

Lignocellulosic agri-food by-products like wheat straw, wheat bran, and distiller's grain, spent coffee grounds from the industrial production of soluble

coffee, sawdust, nut shells and other wastes from the wood industry have been widely described as a clean source of phenolic compounds.

Coffee by-products. With a global output of over 105 million tons per year, coffee is one of the most consumed drinks [114]. Coffee is industrially processed into several by-products, including Spent Coffee Grounds (SCG) and coffee silverskin (CS), which together account for more than half of the dry weight of the coffee fruit. A total of six million tons of SCG are produced globally each year in the preparation of soluble coffee or espresso drinks [36], whereas CS is the residue left over after the bean roasting process [115]. These by-products have attracted growing interest as potential active ingredients to be used in many industries, due to their availability and their main components.

The three primary components of SCG are proteins (8%), melanoidins (25%) and carbohydrates (38-42%) [116,117]. Significant levels of phenolic acids, including flavonoids, caffeic acid, protocatechuic acids, and chlorogenic acid and its isomers and derivatives, have also been discovered in SCG [118–122]. Additionally, SCG has a lignin percentage of 20-26% and a low condensed tannin content [123]. Monosaccharides, proteins, and phenolic chemicals like chlorogenic acid and its isomers make up most of the polysaccharides in CS (Figure 1.14) [124,125]. High levels of health-promoting qualities are exhibited by SCG and CS, including, for example, protection against gastrointestinal and cardiovascular disorders as well as anti-inflammatory, anticarcinogenic, and antibacterial activity [124,126–131].

In the design of materials for packaging, coffee by-products have been recently used as thermo- and photo-oxidative stabilizers [117].

Nut fruit by-products. Considerable volumes of wastes are generated by pistachio, peanut, pecan, hazelnut, and chestnut shells. In the following section the main components of these by-products are described.

A significant commercial crop is pistachio. The fruit consists of a lignified shell and an edible seed. The edible seeds are separated from the shell, which is the

waste product, based on their intended usage. Besides cellulose (30–55%), hemicelluloses (20–32%), and lignin (12–38%) [132], pistachio shells also contain phenolic chemicals, including gallic acid, protocatechuic acid, catechin, epicatechin, rutin, naringin, luteolin, eriodictyol, quercetin, and naringenin [133,134].

Another common and affordable by-product is peanut shell, which is produced in China alone in around 5 million tonnes annually [135]. In addition, cellulose (48%), hemicellulose (3%), and lignin (28%), [136] while luteolin and eriodictyol have also been found, are present in this waste material [135].

The chestnut business also produces a significant number of by-products, mostly the inner and outer shells, which account for 10% to 15% of the total weight of the chestnut [137]. Lignin, cellulose, and hemicelluloses are abundant in chestnut by-products. Like the waste from other nut fruits, chestnut waste also contains flavonoids (quercetin, rutin, catechin, and epicatechin), phenolic acids (primarily gallic acid and protocatechuic acid), and hydrolyzable tannins (vescalagin, castalagin and gallocatechin) [138]. Both the interior and exterior shells of chestnuts contain significant amounts of EA [139].

Another significant agricultural crop of various South American countries is pecan nuts. Up to 49% of the pecan nut is made up of the nutshell, which is inedible [140]. This by-product includes many phenolic compounds, such as gallic acid, EA, p-hydroxybenzoic acid, protocatechuic acid, and epigallocatechin gallate [141], as well as large levels of condensed tannins.

More than half of all nuts weigh in as shell, which is also the main by-product of the hazelnut industry's manufacturing. A number of bioactive compounds, including catechin, epicatechin gallate, and gallic acid, have also been discovered in hazelnut shells, which are made up of around 30% hemicelluloses, 27% celluloses, and 43% lignin (Figure 1.14) [142].

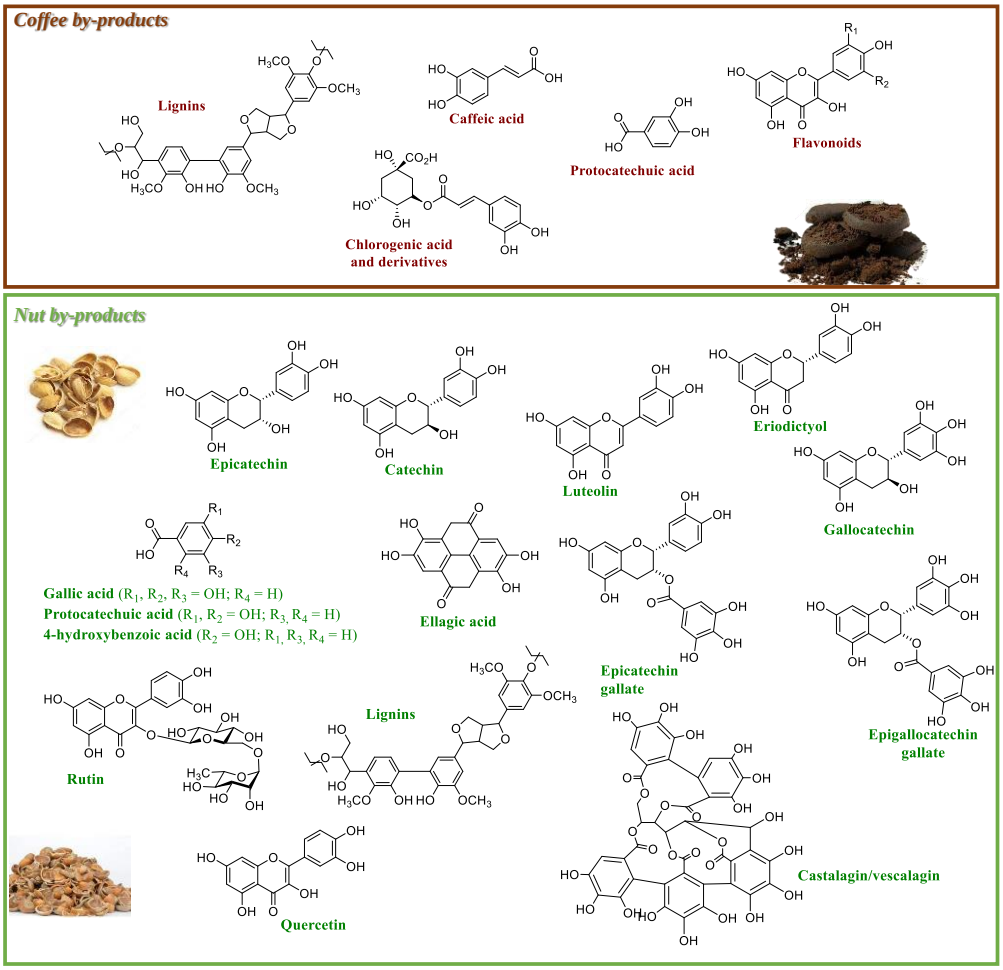

Figure 1.14. Main phenolic constituents of coffee and nut by-products.

1.3.3 Vegetable by-products

Similar to fruit by-products, the vegetable sector generates large volumes of waste that may have similar health benefits with respect to the starting material [96].

By-products from tomatoes. One of the most significant crops in the world is the tomato. However, during industrial processing, around one-third of the weight is lost as skin and seeds. Bioactive chemicals, particularly carotenoids

like lycopene and -carotene, but also phenolic substances, are abundant in tomato residues. Flavonols, primarily quercetin, rutin, and kaempferol glycoside derivatives, as well as flavanones such naringenin glycosylated derivatives are present in the peels and seeds. Also hydroxycinnamic acids as caffeic, ferulic, chlorogenic, and *p*-coumaric acids are present (Figure 1.15) [143]. By-products from tomatoes have been shown to be effective antibacterial and antioxidant agents [144].

By-products from onions. The skin, outer fleshy leaves, top and bottom bulbs, which are generated in more than 450,000 tons just in Europe, are the main by-products of industrial onion peeling. These include very high concentrations of flavonoids like quercetin and kaempferol glycosides. Red onions also contain anthocyanins (Figure 1.15) [145,146].

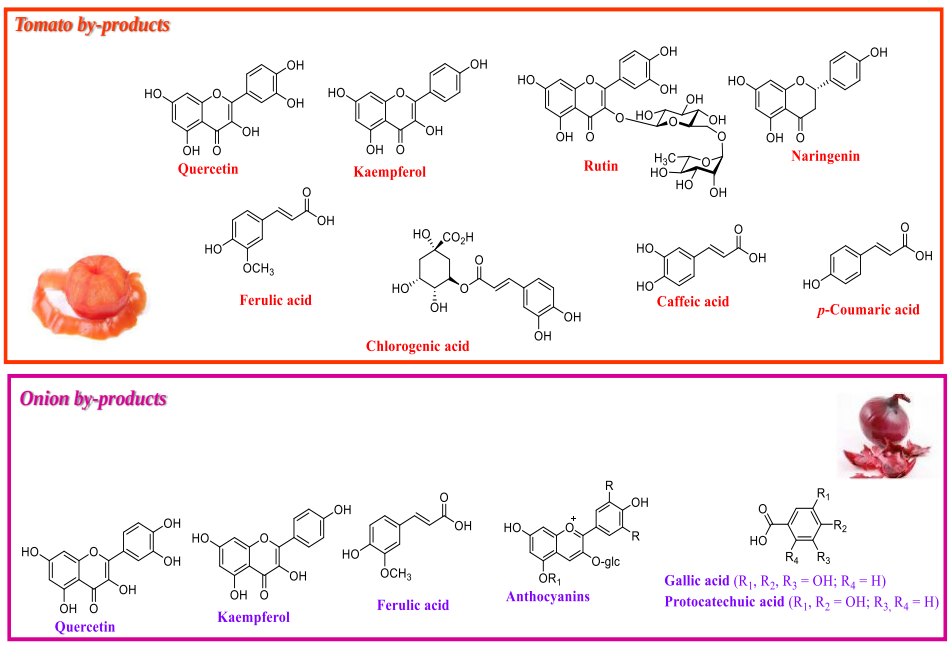

Figure 1.15. Main phenolic constituents of tomato and onion by-products.

1.4 Green Extraction Techniques for the recovery of phenolic compounds

In addition to the research of sustainable and green sources of phenolic compounds, several research efforts have been directed to the implementation of extraction methodologies in agreement with the green chemistry principles.

Microwave Assisted Extraction. Among emerging green techniques, Microwave Assisted Extraction (MAE) has recently found increasing applications for several purposes [147]. This technique can be classified as a green extraction technique since it minimizes the extraction time and reduces the consumption of solvent. Dielectric heating, which is the process by which microwave electromagnetic radiation warms a dielectric material by causing the polar components of the matrix to rotate into molecular dipoles, serves as the foundation for MAE [148]. Several parameters should be optimized to improve the MAE process such as microwave power, extraction temperature, time, and solvent content. In this regard, only two solvents are commonly used in combination or alone such as water and ethanol, due to their ability to absorb the microwave energy and to solubilize phenolic compounds [149].

Ultrasound Assisted Extraction. Similarly to MAE, Ultrasound Assisted Extraction (UAE), enable you to decrease the amount of time and solvent consumption necessary to effectively extract phenolic chemicals from agri-food wastes [149]. This green extraction technique is very common and widespread as it only requires the use of ultrasonic bath. The method is based on the cavitation process that occurs when ultrasonic waves with a frequency between 20 kHz and 100 MHz travel through the sample in cycles of compression and expansion [150].

Mechanical treatment. Mechanochemical reactions are those that are initiated by mechanical methods (milling, grinding, compression) and are carried out either solvent-free or with catalytic quantities of solvent. In particular, ball

milling mechanochemistry has emerged as a generally applicable approach to solvent-free synthesis, which can be cleaner, faster, and simpler than conventional routes. When compared to conventional extraction processes, this type of treatment significantly reduces processing time, increases extraction yields, reduces solvent use, and eliminates noise and radiation. With well specified parameters for maximizing reactivity, such as frequency, medium-to-sample weight ratio, etc., it provides an enclosed solvent-free reaction environment [151].

Deep Eutectic Solvent. One of the methods most frequently used to extract phenolic chemicals from agri-food wastes, is solid-liquid extraction [152]. Although this approach often uses organic solvents, that have several intrinsic disadvantages, *e.g.,* low boiling points, flammability, toxicity, and non-biodegradability [153]; it also has extrinsic disadvantages such as long extraction times, high prices and low yields. Of course, a valid green and available alternative is represented by water, limited by its solubilizing properties only useful as an extraction solvent for polar and hydrophilic molecules. As a result, there is a significant need for green solvents that have the same outstanding extraction qualities as organic solvents but are less expensive and have a less negative impact on the environment. Recently, deep eutectic solvent (DES), a novel class of environmental and green solvents, have been discovered and used in the extraction of phenolic chemicals [154,155]. Abbott et al. provided the first description of DES preparation. These compounds can be made quickly by combining a hydrogen bond acceptor (HBA) and a hydrogen bond donor (HBD) at an appropriate temperature [155–157]. DES has various benefits over typical organic solvents, including affordability, simplicity of production, and accessibility. Also, most of them have extremely low toxicity and are biodegradable. The usual formula for DES is Cat^+X^-zY, where Cat^+ is generally ammonium, sulfonium, or phosphonium, X^- is a Lewis base that is typically a halide, Y is a Lewis or Bronsted acid that forms a "complex" with X^-,

and z is the quantity of Y molecules that interact with the anion [158]. Due to these interactions, an eutectic mixture is created, which has a lower melting point than its component alone. The most often utilized component in the manufacturing of DES, well known for the affordability and non-toxicity, is the choline chloride (ChCl) salt. In addition to alcohols, amino acids, carboxylic acids, and sugars, the most common HBD are urea, ethylene glycol, and glycerol [159,160]. In fact, DES have only recently been created by combining primary metabolites with biodegradable starting components. These "natural deep eutectic solvents" were created by mixing substances that are widely found in nature and have significant functions in the solubilization, storage, or transportation of metabolites in living cells and animals [161,162]. The physicochemical properties of DES, such as their freezing point, conductivity, density, viscosity, and polarity, often rely on the composition of the material; as a result, changes in the HBD and HBA components or their content could affect these properties [163]. DES typically show a higher density with respect to that observed for both water and for the sum of its components. Additionally, most of DES show a significant viscosity (> 100 cP) at room temperature, as result of the hydrogen bond network between the components. This phenomenon could be attributed to the large number of ion size and electrostatic or van der Waals interactions between the constituents. Due of their high viscosity, DES usually exhibit poor conductivity. The protons and electrons that DES can donate and accept, as well as the capacity to form hydrogen bonds, collocate them in first position as dissolving solvents toward phenolic chemicals in complex matrix [164].

1.5 Complex organic biopolymers-inorganic hybrid materials

The recent introduction of hybrid systems has expanded the scope of phenolic compound to a variety of different materials, applications, and deposition techniques [165].

The field of organic-inorganic hybrid materials has experienced a significant growth over the last 20 years and is now unquestionably one of the most important and intriguing areas of study in many important fields, including sensors, electronics, optics, lightning, medicine, catalysis, energy storage, and energy conversion [166]. In general, hybrid organic-inorganic materials are the natural intersection of two worlds, each of which has significantly advanced the field of materials science [95]. Hybrid materials research has both potential and problems [167]. The goal of hybrid systems is to create novel materials with improved properties. The hybrid system enhances the synergistic effect of the distinct capabilities of each material, allowing for the creation of fine-tuned nanomaterials by modifying their chemical, optical, and even electrical properties. The advantages of these hybrid systems include (i) overcoming the limitations of each system, (ii) being easily designable into a diverse composite, and (iii) being broadly applicable in the fields of biological/chemical sensors, drug delivery, and therapeutic agents due to their multifunctionality [166,168]. In fact, hybrid materials commonly combine elements that have been extensively studied in their separate areas, but, becoming a part of a hybrid compound, they offer a new aspect to their characteristics.

Nowadays, various hybrid systems have been created and used. Inorganic elements such as metal oxide nanoparticles, graphene, carbon nanotubes, silica, and polymers can be used to create polymer-hybrid nanoparticles [169]. Blending organic substances (phospholipids, proteins, and lipids) with natural or synthetic polymers, on the other hand, can result in innovative hybrid nanosystems capable of combining the benefits of these biomacromolecules with those of tailor-made synthetic polymers. In the recent decade, the development of novel methodologies centred on the discovery of biocompatible hybrid materials has resulted in amazing advances in the biomedical area, with an emphasis on the manufacturing of new drug carriers capable of accessing particular locations such as cancer sites [170,171]. For instance, the strategy of

covalently attach small initiator molecules to surfaces of natural polymers or inorganic biocompatible materials and grafting polymers in situ from these surfaces - the so-called "grafting-from" - has enabled the preparation of hybrid systems with a wide range of properties [172,173]. It is important to highlight the responsive hybrid systems that can respond to environmental signals such as temperature and pH while still maintaining biological activity. Materials developed using these methodologies have emerged as strong contenders for the next-generation platform of systems employed in this industry. On the other hand, the creation of lipid polymer hybrid nanostructures looks to be a viable drug delivery platform [174–176]. Such systems may be configured in a variety of ways and are customizable in terms of release characteristics and long-term behaviour in vivo. Among all the possible interesting research lines, nanoparticles and grafted graphene systems are in depth described in the following paragraphs (Figure 1.16).

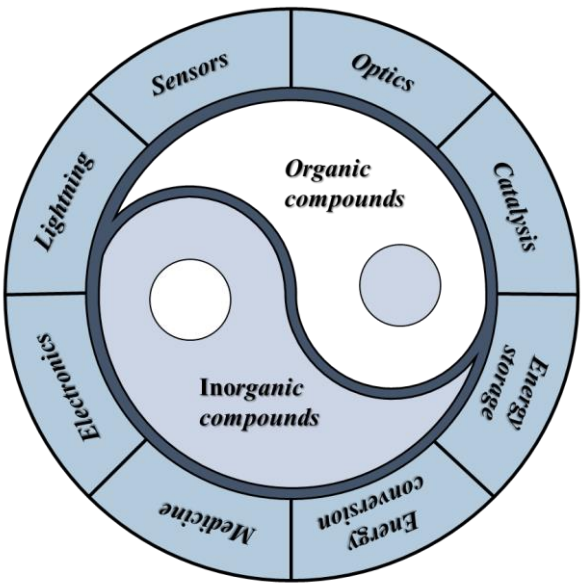

Figure 1.16. Synergistic effect of organic and inorganic materials.

1.5.1 Synthesis of metal nanoparticles embedded into organic compounds

The hybridization of nanostructured systems or biocompatible polymers has been highlighted due to its biological and physicochemical properties [168]. In fact, nanotechnology represents one of the most promising areas of research, concerning the creation and application of materials with nanoscale dimensions [177]. Due to its high surface-to-volume ratio and other advantageous features, the nanoscale offers extraordinary applications in many branches of research. As a result, the creation and application of nanomaterials constitute the main focus of contemporary research [178]. Among the nanomaterials, metal oxide nanoparticles have attracted increasing interest due to their wide range of uses in many fields, such as electrochemical applications, dye degradation, catalysis, and their reputation as extraordinary agents in the struggle against various infections [179,180].

Among the diverse nanostructured materials of transition metal oxides, TiO_2 obtained a favourable position as common nanomaterial that is used commercially in many different sectors because of its intrinsic characteristic such as low cost and photostability. In spite of these excellent properties, recent studies revealed that TiO_2NPs are quite toxic [181,182]. When TiO_2 was used as a photocatalyst by Fujishima and Honda to photolyze water, the potential of this material was first generally recognized. Importantly, pressure and temperature from the surrounding environment during the procedure impact the structure of TiO_2NPs, determining their functional properties and uses. Materials based on titanium oxide have found extensive use in the sectors of electronics, energy conversion, and environment. Nowadays, all the processes described for the synthesis of these metal oxide nanoparticles uses a lot of harmful chemicals [183].

In this context, the need to investigate on the production of metal oxide nanomaterials using eco-friendly, greener, and non-toxic approaches is becoming urgent [184]. Thus, numerous green approaches are used to create metal oxide NPs by utilizing diverse greener, cheaper, and eco-friendly sources such as plant extracts, bacteria, fungus, and other biological entities [185,186]. Natural phenolic compounds have been extensively investigated as reducing and stabilizing agents for the environmentally friendly preparation of metal nanoparticles, resulting in materials that are finding more and more applications in various fields, mostly because of their potent antioxidant properties as well as their well-known antimicrobial activity [187,188].

Due to their wide range of uses as for example in antibacterial dressings, antimicrobial and anti-cancer medications, proteasome inhibitors, sunscreen, and anti-aging agents, gold nanoparticles (AuNPs) have attracted considerable attention. AuNPS produced using a peach aqueous extract have demonstrated strong antibacterial synergistic activity when combined with various antibiotics and a potent anticandidal activity, in addition to optimal antioxidant properties as expected by the presence of phenolic compounds [189]. According to a different study, AuNPs prepared following a green procedure based on the use of extracted phenolic compounds from Punica granatum juice have been suggested as boosters for enhancing the Sun Protection Factor (SPF) in commercial sunscreen formulations, taking into account the lack of toxic effects on human microvascular endothelial cells and dermal fibroblasts [190]. In addition, other type of AuNPs were prepared using a Panax ginseng berry extract or onion peels. [191][192].

Furthermore, silver nanoparticles (AgNPs) have been frequently used in the cosmetics and biomedical industries. For instance, AgNPs were obtained by a ginseng berry extract, used as a reducing agent. The resulting AgNPs proved more antioxidant-active than the pure ginseng berry extract, inhibited mushroom tyrosinase, had antibacterial activity against Escherichia coli and

Staphylococcus aureus, and caused the death of murine melanoma cell lines [193]. Moreover, various extract by root of plants such as *Coleus forskohlii* [194] or by an *Achillea vermucularis* have been used for the synthesis of AgNPs [195]. AgNPs produced by use of orange peel aqueous extracts were similarly shown to have potent antibacterial and antioxidant effects. Another natural reducing and stabilizing ingredient that is frequently used to produce AgNPs is lignin [196]. Additionally, a green AgNPs production method based on spent coffee grounds and the potential antibacterial activity displayed by chitosan films functionalized with the substance have recently been described [197].

1.5.2 Hybrid systems based on graphene materials

In 2004, two physicists from the University of Manchester isolated for the first time a material with the thickness of a single atom: graphene [198]. Graphene is composed of sp^2 carbon atoms organized in a hexagonal honeycomb geometry; this fundamental unit is repeated to form a planar crystalline structure called "sheet". Above and below the top are the conjugated double bonds, responsible together with the structural perfection, of the properties of the material [199,200]. In recent years graphene and its derivatives have attracted enormous interest and focused scientific research on their possible applications [201]. In particular, graphene oxide, which is a material based on the structure of graphene, but enriched with oxygenated functional groups, is gaining considerable interest [202]. In fact, graphene oxide is a key component of the graphene family that has been shown to be an efficient reinforcement in hydrogel systems and to be easily dissolved in water and other organic solvents due to the presence of oxygen groups. Furthermore, graphene oxide can be reduced, theoretically restoring the graphene structure [203]. However, the presence of defects in the starting compound and the formation of defects due to

the transformation processes like reduction produce a material with intermediate characteristics called reduced graphene oxide (rGO). Several chemical reducing agents have been investigated to create reduced graphene oxide sheets [203,204]. Functionalization of graphene used in the delivery GO that has excellent processability has become a promising functional nano reinforcing material for various biomedical applications. Employing the covalent or noncovalent method named “graft” or “load”, GO can be modified with other nanoparticles (NPs) or biomolecules to expand its biomedical applications [205]. Nanohybrids offers several advantages giving rise to a material characterized by the peculiar properties of each counterpart. In addition, as already described in paragraph 1.1.1.2, dopamine is quite simple to self-polymerize into adherent polydopamine (PDA) and has a high binding affinity to a wide range of nanomaterials. This affinity allows the uniform dispersion of nanofillers in the hydrogel network, resulting in unique hydrogel systems. Previous research found that simultaneous surface functionalization and reduction of graphene oxide occurred during the oxidative polymerization of dopamine [206]. Furthermore, an artificial nacre based on graphene oxide sheets cross-linked by dopamine via evaporation-induced assembly process was developed, characterized by a hierarchical nano/microscale structure of the natural nacre and its excellent integration of mechanical properties [207]. The tensile strength and toughness of this synthetic nacre are respectively 1.5 and 2 times greater those of the natural nacre, and also the electrical conductivity proved higher. Applications for this kind of robust integrated artificial nacre include flexible supercapacitor electrodes, artificial muscle, and tissue engineering. Han et al. created a composite hydrogel using partly reduced graphene oxide by regulating the extent of reduction during dopamine self-polymerization [208]. This created a hydrogel had high adhesiveness and conductivity, but with low mechanical strength.

1.6 Aims of the PhD project

Within the context briefly described in the previous paragraphs, this PhD work was aimed mainly at the exploitation, manipulation, and functionalization of phenolic compounds as active components for surface coating, functional and hybrid materials in nanotechnology and biomedical applications.

In particular, the following goals were pursued, and the results achieved are described in detail in the following chapters:

a. Study of the structure/property relationship in model eumelanins of 5,6-dihydroxyindole (DHI) and the corresponding carboxyl acid (DHICA), before and after metal binding with the aid of a mediators-based cyclic voltammetry technique;

b. Development of innovative and versatile dip-coating technologies for surface functionalization following the extraordinary wet adhesion properties of polydopamine, imparting adhesive properties to the methyl ester of DHICA by use of hexamethylenediamine and investigating the mechanisms underlying film deposition from non-adhesive melanin-type polymers;

c. Synthesis of new eumelanin precursors as amide/diamide derivatives of 5,6-dihydroxyindole-2-carboxylic acid and dimers for preparation of model pigments by oxidative polymerization and study of their absorption properties, antioxidant activity and solubility in various solvent of relevance for dermocosmetic applications;

d. Evaluation of conjugates of caffeic acid derivatives with dihydrolipoic acid *ad hoc* synthesized and of natural compounds extracted from agri-food by-products as inhibitors of tyrosinase in the perspective of their dermocosmetic applications for the treatment of skin disorders;

e. Development of bio-inspired hydrogels by proper combination of soy protein or whey protein with selected phenolic acids such as caffeic acid,

chlorogenic acid and gallic acid or extracts from different agri-food by-products;

f. Development of eco-friendly extraction protocol to recover value-added compounds (phenolics and lignins) from selected agri-food by-products and their exploitation as active components in hybrids nanostructured materials such as AgNPs;

g. Implementation of new functional hybrids catechol-graphene composite hydrogels.

Part of the work described under the research lines a) g) were performed during a four-month visit at Institute of Bioscience and Biotechnology, University of Maryland (College Park, USA) under the supervision of Professor Gregory Payne.

Chapter 2

5,6-dihydroxyindole compounds and eumelanin precursors for surface functionalization and biomedical applications

As illustrated in the Introduction section, eumelanin represents a family of heterogeneous and polymeric catechol pigments, ubiquitously found in nature. These pigments provide to mammals a wide *spectrum* of interesting properties with a broad variety of functionality, such as radical scavenging, pigmentation, thermal regulation, and radiation protection [209]. In particular, they derive from the oxidative polymerization of two catechol systems, 5,6-dihydroxyindole (DHI) and 5,6-dihydroxyindole-2-carboxylic acid (DHICA), isolated for the first time from black eumelanin by Raper et al. in 1927 [210]. Although these eumelanin precursors are apparently similar, the presence of a carboxylic group dramatically affects the chemical properties and biological activity of the related melanins, which are still not clarified and that purportedly hold the key to the actual physiological significance of melanogenesis.

To better understand the structural-functional relationships and the biological activity of these natural pigments, synthetic DHI or DHICA melanins have been prepared by an easily biomimetic oxidation procedure. In particular, DHICA melanin have shown highest free radical scavenging capabilities and antioxidant activity compared to DHI melanin [211].

The poor solubility of melanins including the model pigments obtained by oxidation of DHI and DHICA under biomimetic conditions has limited the full characterization of their properties that may hold the key of their biological role and allow for a rational exploitation in different fields [212]. This holds

particularly for the redox properties that are difficult to investigate on insoluble materials with a variable morphology and particle size as is the case of model synthetic melanins from DHI and DHICA, moreover making any comparison between these pigments and other systems of biological relevance meaningless.

To circumvent the problems raising from the poor solubility and allow for a better exploitation of the remarkable antioxidant activity of the melanins from DHICA research work has been directed to derivatives of DHICA that might afford melanin related pigments with more favourable properties. Synthetic eumelanin from the methyl ester of DHICA (MeDHICA) has shown remarkable antioxidant properties by conventional chemical assays [213], optimum lipid peroxidation activity together with an improved solubility profile with respect to DHICA melanin, and good cytocompatibility toward HaCaT cells [213,214].

These pigments exhibit various and different favourable properties, thanks to their ability to give rise to multiple interactions including covalent and hydrogen bonding, cation-π and aromatic interactions, or bind different metals. This opens new perspectives for their use in biomedical, technology applications and surface functionalization [209].

In this last case, new opportunities in PDA based surface chemistry have derived from the discovery that hexamethylenediamine (HMDA) markedly enhances film deposition from the polymerization of dopamine and a variety of catechol substrates [57], including the key eumelanin precursor DHI, leading to films with attractive properties in terms of morphology and functionalities [59]. In all these studies, it has been widely hypothesized that HMDA causes intermolecular amine-quinone condensation reactions that result in strongly cross-linked oligomer formations. However, the detailed mechanism by which HMDA can mediate film deposition by catechol polymerization has remained so far little understood.

Another field where the properties of DHICA melanin might be usefully exploited is the development of dermocosmetic formulations for

photoprotection. Yet, this function could not expectedly be played by the melanins from MeDHICA as these pigments are light in colour (pale yellow) with null absorption in the visible region. Therefore, the search for other derivatives of DHICA that may afford soluble pigments with a significant covering of the Uv-Vis region as typical of melanin pigments represents a research goal of interest [213].

In this context are framed the research work described herein focused onto the study of these pigments, their exploitation and improvement of their properties for biomedical and functional applications.

In particular, described in this Chapter are results that have led to:

- implementation of a spectroelectrochemical reverse engineering approach for the study of the metal binding effect on redox and radical scavenging properties of DHI and DHICA melanins;
- development of film deposition promoted by HMDA from DHICA derivatives, investigation of the main film components and study of the adhesion mechanism;
- synthesis of novel amides of DHICA and study of the antioxidant properties, solubility profile and inhibition of lipid peroxidation of the melanins thereof.

Results and Discussion

2.1 Spectroelectrochemical reverse engineering as a top-down approach to evaluate the effect of metal binding on DHI and DHICA melanins redox properties

2.1.1 Redox activity of DHI and DHICA melanin

This part of the PhD research work was performed during a training period spent at the Institute for Bioscience and Biotechnology Research and Fischell Department of Bioengineering of University of Maryland (U.S.A.) under the supervision of Prof. G. Payne and Dr. E. Kim.

The investigation of the function of biological systems usually starts by characterization of their structure using conventional techniques. However, this approach is very difficult to apply to complex organic systems such as eumelanin primarily because of the low solubility that hampers the application of conventional methods of structural investigation. Recently, alternative top-down methods based on an electrochemical reverse engineering methodology were developed [215–217].

In this study, this innovative approach was applied to probe the redox properties of synthetic DHI and DHICA melanins. To this aim, DHI and DHICA melanins were prepared by an enzymatic promoted oxidation. Both monomers were dissolved in 0.1 M phosphate buffer at pH 7. Subsequently, to the resulting solution, 15 u/mL of a peroxidase solution was added, followed by 1.2 eqs. of H_2O_2 solution (30% w/w) [218].

Based on previous studies [215,216], in a first series of experiments an electrochemical methodology was slightly adapted and applied to these samples. As shown in Figure 2.1, this approach uses a solid melanin sample, entrapped in a non-conducting chitosan film, and deposited on a gold electrode. In particular, DHI or DHICA melanins prepared as described before, were dissolved at final

concentration 5 mg/mL in a chitosan water solution (1% w/w, pH 5.5) and sonicated for 30 minutes. 20 μL of the resulting solution was dropped on a gold bare electrode surface and dried in a vacuum oven for 20 min. To neutralize the coated film, the electrode was dipped in a 0.1 M phosphate buffer (PB) solution at pH 7 for 20 minutes.

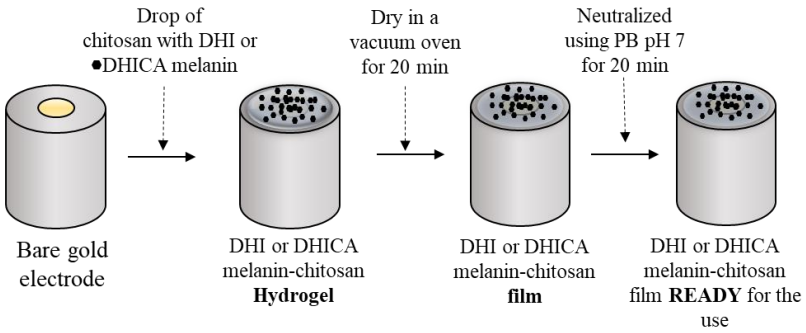

Figure 2.1. Schematic representation of the procedure for the deposition of chitosan-DHI or DHICA melanin film coated on gold electrode.

As mentioned before, eumelanin are insoluble pigments and therefore their major limitation during an electrochemical analysis is their poor solubility, making difficult the exchange of electrons with the electrode surface. Consequently, the use of soluble mediators able to transfer electrons between melanin and the underlying electrode was crucial, providing redox connectivity between the melanin sample and the electrode (Figure 2.2). In particular, after applying a controlled input voltage, the resulting potential is transmitted to the melanin entrapped into the chitosan film through the soluble mediators, acting as electrons shuttles. The output currents are detected, and the redox activities of the melanin are evaluated.

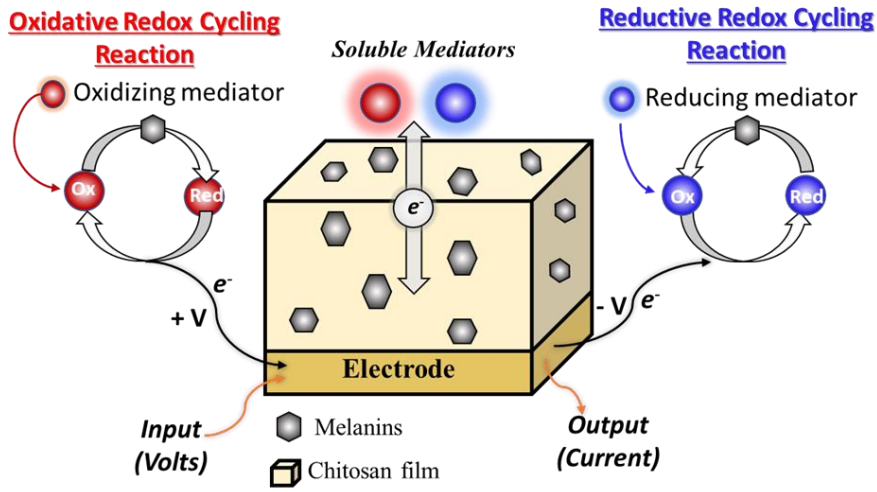

Figure 2.2. Schematic representation of the redox connectivity established between chitosan-DHI or DHICA melanin film and a gold electrode using soluble mediators.

To obtain useful output signals, initial measurements were devoted to the choice of mediators and their concentrations. Several mediators such as Ir^{+3}, Ru^{+3}, Ir^{+4}, Fe^{+3} at different ratios and concentration were tried. The optimal conditions were observed in the case of 1,1'-ferrocenedimethanol (Fc) and Phenazine-1-carboxylic acid (PCA). Subsequently, DHI and DHICA melanins as film-coated on electrodes were dipped into a 0.1 M phosphate buffer solution, containing the two selected soluble mediators (50 µM Fc and 50 µM PCA). A cyclic potential between -0.7 V and +0.5 V was applied at a scan rate 2 mV/s. In control experiments, the same experiment on chitosan-coated electrode, without entrapped melanin were performed.

In the potential range from 0 V to -0.7 V *vs* Ag/AgCl, the eumelanin reduction occurs, and the electrode act as an electron source. Under these conditions, the mediator PCA is reduced to PCA^{2-}, producing a positive (reducing) current. As shown in Figure 2.3, in the case of chitosan, a minimal reducing current was observed, likely due to the electrochemical reduction of PCA ions that diffuse

through the film to the electrode, whereas a considerable amplification of the reducing currents for both melanin-chitosan films was detected.

On the contrary, in the potential range from 0.5 V to 0 V *vs* Ag/AgCl, the eumelanin oxidation occurs, and the electrode acts as an acceptor of electrons. Under these experimental conditions, Fc is oxidized to Fc^{+}, producing a negative (oxidizing) current.

In Figure 2.3 panel a, the current response of melanin-chitosan films as a standard cyclic voltammogram (CV) are reported, whereas in Figure 2.3b the results are expressed as the output current response of current *vs* time. It is evident that both amplifications appear nearly "steady" over time: specifically, the CV curves are approximately superimposable, and the output curves appear to be similar for each consecutive cycle. Overall, these results suggested that compared to the chitosan control, the cyclic voltammetry of melanin-chitosan film shows a considerable amplification, the paired amplification in oxidation and reduction currents provides evidence that both melanins are redox-active and can repeatedly exchange electrons with the mediators.

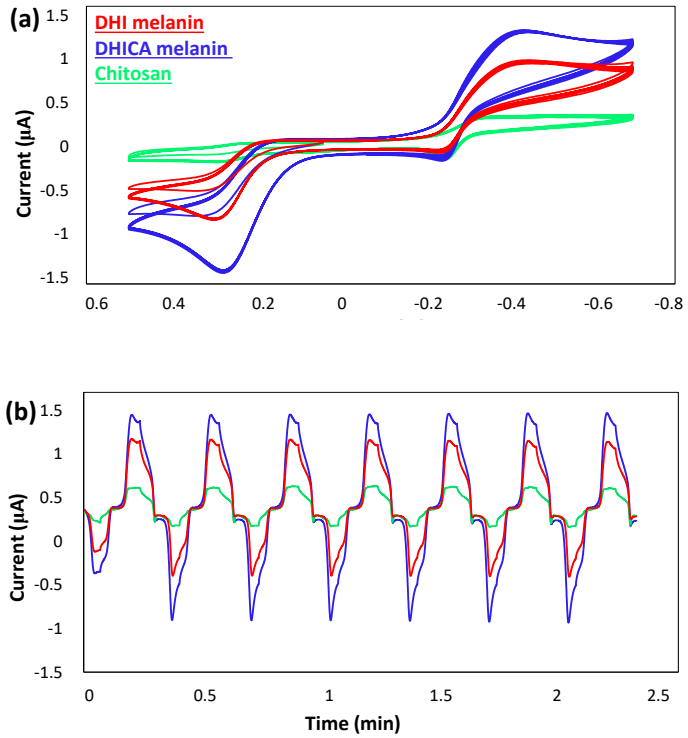

Figure 2.3. (a) Cyclic voltammograms of films containing melanin samples (scan rate of 2 mV/s) in the presence of the two selected mediators; (b) output current response of current *vs* time of films containing melanin samples (scan rate of 2 mV/s) in the presence of the two mediators.

This amplification can be explained by the reductive redox-cycling mechanism (Figure 2.4). Briefly, after the reduction of PCA, the reduced PCA^{2-} can diffuse into the melanin-chitosan film and transfer electrons to melanin. As result, some oxidized melanin moieties are converted into their reduced states and oxidized PCA is generated again, ready to start another redox cycle.

On the other hand, in the case of oxidative redox-cycling mechanism, Fc is oxidized to Fc^{+}, the oxidized Fc^{+} can diffuse into the melanin-chitosan film and accepts electrons from melanin. Consequently, some reduced melanin moieties are converted into their oxidized states and reduced Fc is generated again.

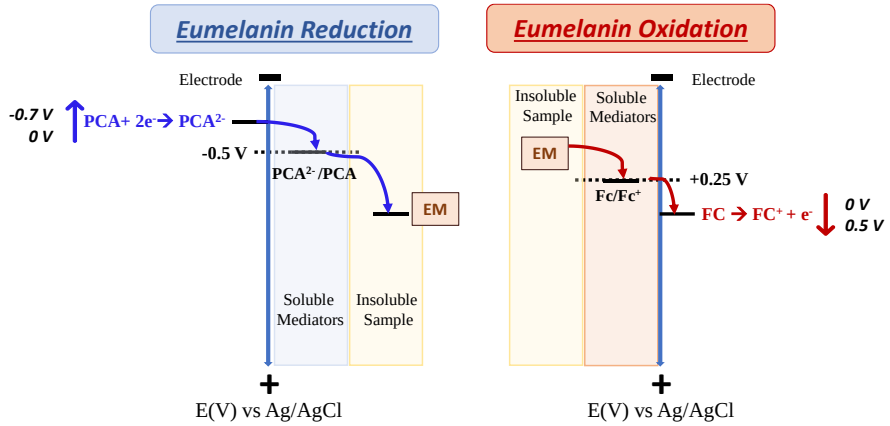

Figure 2.4. Reductive redox-cycling mechanism of melanin-chitosan film with mediators.

Survey of the electrochemical studies of melanin reported in literature shows that electrodeposition represents a widely explored alternative to conventional cyclic voltammetry for the redox study of insoluble compounds or coatings. In fact, applying a constant potential it is possible to obtain the electrodeposition of compounds on the electrode surface. In particular, under the above-described conditions, DHI or DHICA monomer formed a coating onto the electrode, as a result of their oxidation and consequently polymerization on its surface. However, using this methodology it is very difficult to control the film thickness and to establish a straightforward comparison of the two melanin films, since they have very different kinetic polymerization rate and also the final aggregates are quite different [219].

To get additional information, the charge transferred during the oxidation and reduction of CVs, was calculated integrating the current over time ($Q=\int i \cdot dt$). In addition, the ratio between the charge for the melanin-chitosan films and for the control chitosan film, allow to calculate the reductive and the oxidative Amplification Ratio (*AR*) (Figure 2.5).

$$AR_{Red} = \frac{{Q_{Red}}^{Mel-Chit}}{{Q_{Red}}^{Chit}} \qquad AR_{Ox} = \frac{{Q_{Ox}}^{Mel-Chit}}{{Q_{Ox}}^{Chit}}$$

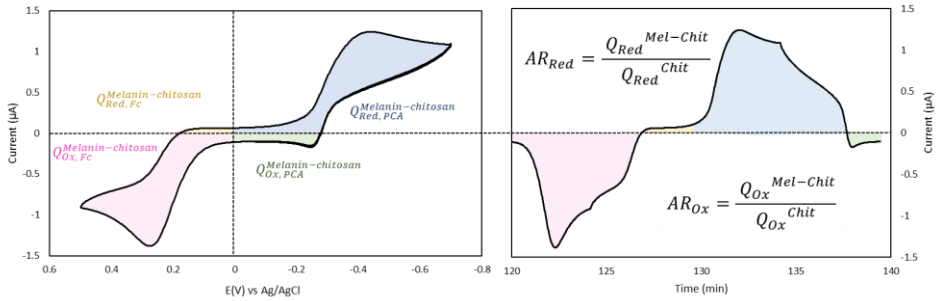

Figure 2.5. Schematic representation of output curves to quantify charge transferred (Q) and amplification ratios (ARs).

Moreover, a Rectification Ratio (RR), that compares the response of the oxidized and reduced portions, was also calculated as follows:

$$RR = \frac{Q_{Red}{}^{Film}}{Q_{Ox}{}^{Film}}$$

With regards to ARs, the denominator represents the charge of the control experiment (chitosan film), reflecting the diffusion of mediators to the electrode, whereas the numerator represents the charge of the melanin-chitosan film and so reflects the diffusion of the mediator but also their redox activity. As illustrated in Figure 2.6, in the case of DHICA melanin a higher Amplification Ratio was observed with respect to DHI melanin, indicating that DHICA melanin are more redox active or that the redox active sites are more accessible to mediators. This finding can be related to the supramolecular structure of melanin. In fact, as already reported in literature DHI melanin are probably characterized by a more compact structure, held together by π-π stacking interactions. In addition, for the two melanin-chitosan films and the chitosan control, the RR approaches to 1, suggesting that the oxidized and reduced fractions are quantitively similar.

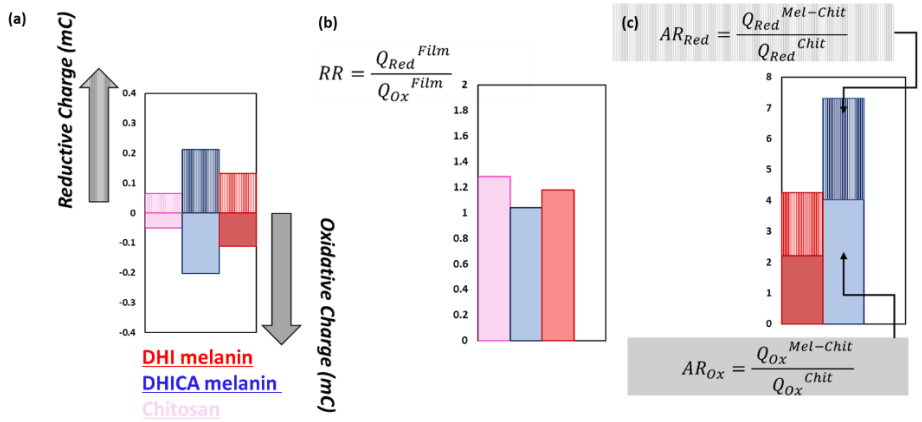

Figure 2.6. Graphic representation of the (a) oxidative and reductive charge, (b) Rectification Ratio (*RR*) and (c) Amplification Ratio (*AR*), blue bar for DHICA, red bar for DHI and pink bar for chitosan.

In another series of experiments, a dynamic analysis, commonly used for reverse engineer technological systems, was performed. Firstly, the melanin-chitosan films were dipped into a 0.1 M phosphate buffer solution, containing the two selected soluble mediators (50 µM Fc and 50 µM PCA). Then a variation of the frequency, using a scan rate from 2 to 1000 mV/s of the imposed oscillating potential input from −0.7 V to + 0.5 V, was applied. As illustrated in Figure 2.7, the frequency used controls the depth of the film region probed by the mediators redox-cycling.

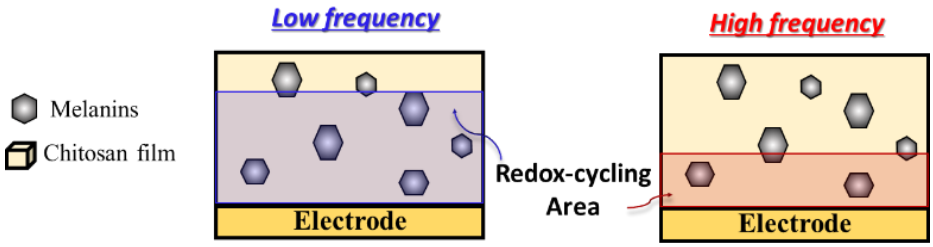

Figure 2.7. Schematic representation of the scan rate effect on the depth of mediator penetration into the film and into the core of melanin particles.

As shown in Figure 2.8, the charge transferred to the electrode significantly decreases at higher scan speeds, probably due to the shorter time the mediators have to cross the film and exchange electrons with the electrode. In fact, in all cases the AR is higher at slower scan speeds while this ratio decreases significantly at higher scan speeds.

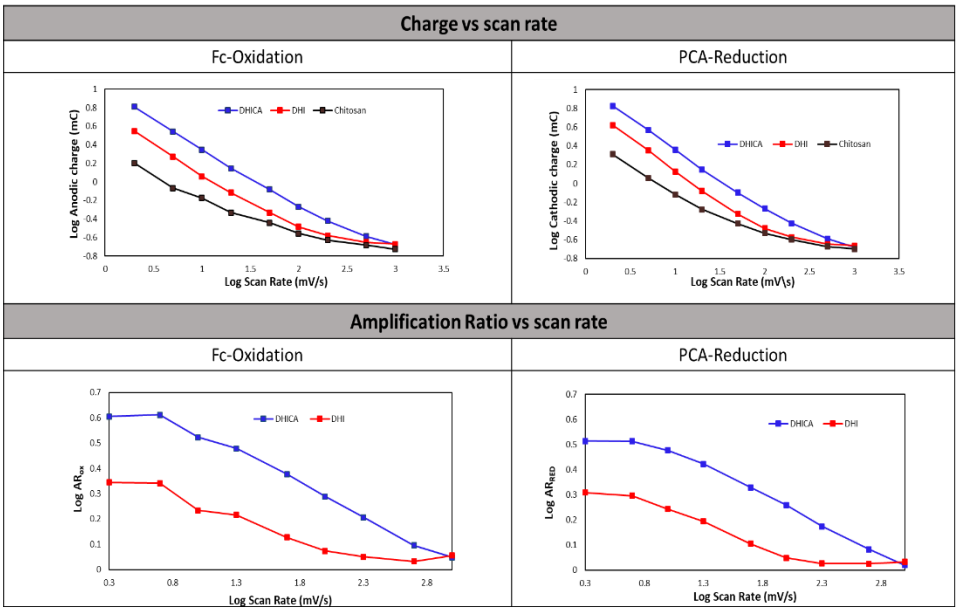

Figure 2.8. Charge transferred and amplification ratios (ARs) for Fc-oxidation and Ru^{3+}-reduction for various films probed at different scan rates.

A higher AR was observed for lower scan rate, likely due to the longer times (or slower scan rates) required for the mediators to access to the internal sites of melanin. Consistent with this expectation, at higher scan rate the ARs significantly decrease as result of the less time available for the mediators. Overall, in agreement with the previous findings, also this type of study confirmed significant higher AR values for DHICA melanin with respect to DHI melanin, though the general behaviour of DHI and DHICA melanins in terms of ARs in function of time appears to be very similar.

2.1.2 The effect of metal binding on the radical scavenging activity of DHI and DHICA melanins

On this basis in further experiments the effects of metal binding on the redox behaviour of these synthetic melanins was evaluated. The interest of this study stems from the occurrence of different metal ions in the site of biosynthesis of melanins that feature different coordination sites, the *o*-diphenol functionality and the carboxy group in the DHICA derived units. Therefore, evaluation of how the redox ability of the pigment may be altered following binding of the metal ions may bear significant biological implications and of course may be exploited to tune the redox activity of melanins.

Briefly, DHI or DHICA melanin was sonicated in the presence of a 40 mM $FeCl_3$ solution. After 90 minutes, the resulting solution was centrifuged, and the precipitated melanin was collected. Both DHI and DHICA melanin before and after treatment with $FeCl_3$ were analysed by CV in the presence of Fc and PCA as described before (see paragraph 2.1.1). As illustrated in Figure 2.9 after the treatment with Fe^{+3}, both melanin-chitosan films lost their redox activity, likely due the well-known involvement of catechol groups in the metal binding interactions. However, since Fe^{+3} can be reduced to Fe^{+2} by melanin, another metal, i.e. Zinc (+2) was selected for these experiments. In fact, this metal can only bind melanin without any side reactions. A similar result was observed also in this case, confirming the preliminary findings.

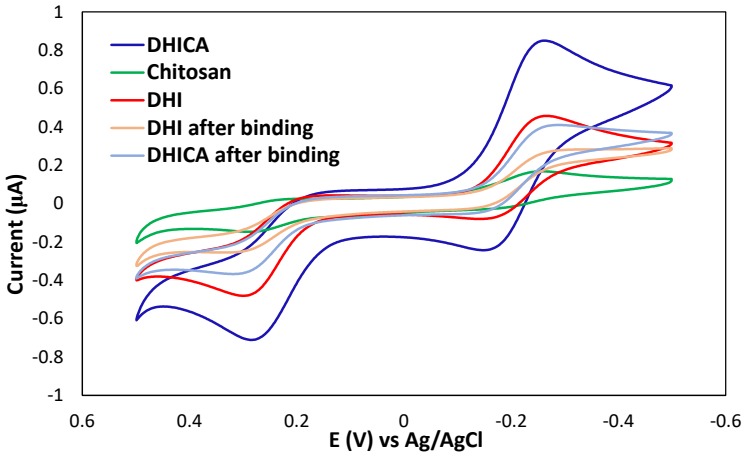

Figure 2.9. Cyclic voltammograms of films containing melanin samples before and after metal binding (scan rate of 2 mV/s) in the presence of the 2 mediators.

In another series of experiments, the electrochemical measurement of the melanin redox activity was coupled with radical-scavenging activities using Uv-Vis spectroscopy [217], with the aid of a honeycomb electrode (Figure 2.10). The usefulness of these experiments is the possibility to have simultaneously an electrochemical and optical output, by applying a voltage input. In fact, the presence of small holes on this gold electrode allows the light to pass through for optical measurements near. To get optimal results, different experimental conditions such as choice of the mediators, their concentrations and ratio were tried. Notably, some species such as ABTS (2,2'-azino-bis(3-ethylbenzothiazoline-6-sulfonic acid) are redox-state-dependent optical properties. In fact, anodic oxidation can generate the corresponding ABTS radical species ($ABTS^{+\cdot}$), characterized by an intense green color, easily monitored by Uv-Vis spectroscopy. This radical species can be then quenched in presence of antioxidant compounds, such as melanin pigments.

Compared to other methodologies, the use of melanin-chitosan films allows spectroelectrochemical measurement. In fact, for example electrodeposited DHI/DHICA melanin films would completely cover the honeycomb electrode

halls, preventing the light to pass through for optical measurements. In addition, with respect to conventional chemical assay for the evaluation of the antioxidant properties such as 2,2-diphenyl-1-picryl-hydrazyl (DPPH) and Ferric Reducing Antioxidant Power (FRAP) assay, this methodology allows to strictly and directly correlate the redox properties to the radical scavenging activities and the use of mediators makes the measurement more independent from the contact area, dimensions and supramolecular structure of melanins.

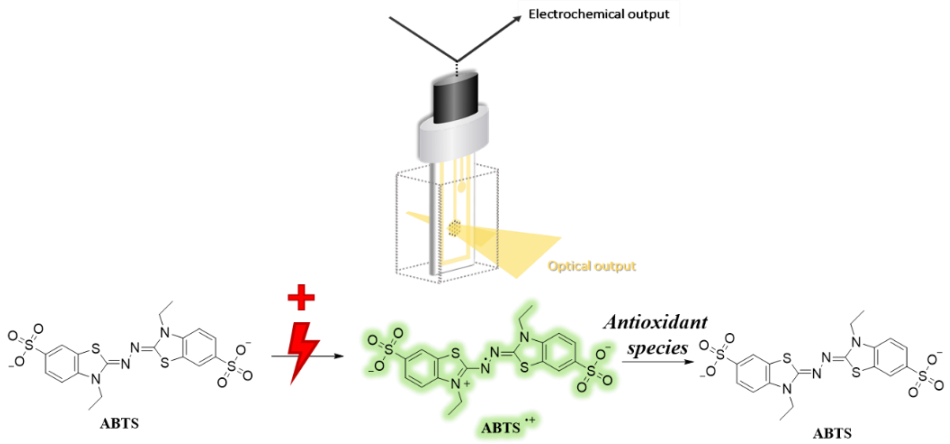

Figure 2.10. Representatives imagine of honeycomb electrode (light pass through the holes) and of ABTS redox-state-dependent optical properties.

The best results were observed when chitosan films (with or without melanin) were coated on the honeycomb electrode and then dipped into 100 µM ABTS and 100 µM PCA in PB solution at pH 7. Firstly, a steady study based on a variation of the input voltage from +0.7 V to -0.7 V at a scan rate of 5mV/s, was conducted. This allows, as already described in the previous paragraph 2.1.1, the oxidative redox-cycling of ABTS and the reductive redox-cycling of PCA. As illustrated in Figure 2.11-12, the electrochemical outputs of the current as a function of time exhibited three important features in the case of DHI and DHICA melanin: (i) both ABTS-oxidation currents and PCA reduction currents are amplified; (ii) both melanin can be repeatedly oxidized and reduced by

ABTS and PCA redox-cycling and these amplified current peaks remain nearly constant over the multiple cycles; (iii) the DHICA melanin amplification is higher respect the one observed for DHI melanin. When the applied voltage is into the oxidative range (the $ABTS^{+\bullet}$ radical is electrochemically generated), the absorbance associated with the $ABTS^{+\bullet}$ radical increases. On the other hand, when the applied voltage is into the reduction range, the $ABTS^{+\bullet}$ radical is electrochemically reduced into the ABTS species and consequently the absorbance decreases.

As expected for the control chitosan film no effect was observed, indicating no radical scavenging activity in absence of melanin. On the contrary, the optical absorbance for the melanin-containing film significantly decreases, which is consistent with the idea that the electrochemically produced $ABTS^{+\bullet}$ radical is suppressed accepting an electron from melanin. Interestingly, as evaluated by conventional chemical assay such as DPPH and FRAP assay, DHICA melanin significantly attenuated the optical absorbance, suggesting a higher radical scavenging ability respect to DHI melanin. Notably, when the same steady study was carried out on DHI and DHICA melanin coated to the honeycomb electrode after the metal binding, the radical scavenging abilities of DHI and DHICA melanin becomes comparable and lower than before metal binding. These results suggest that when melanin bind metals lose their antioxidant properties and in particular the radical scavenging abilities of DHICA melanin significantly decrease after binding with respect to DHI melanin.

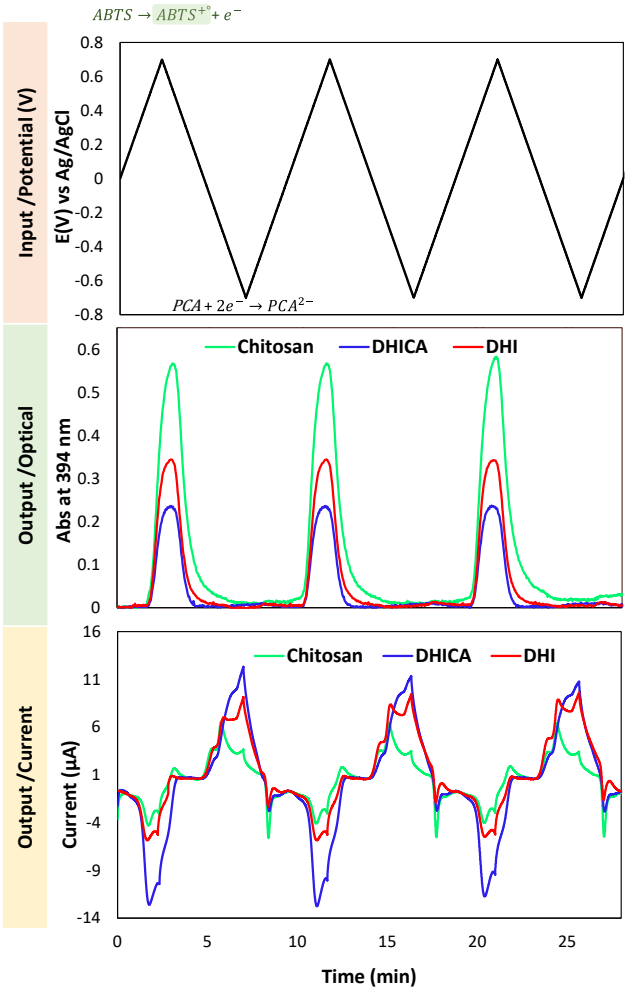

Figure 2.11. Potential input, and electrochemical and output responses of melanin-coating film, amplification of the electrochemical currents and attenuation of the optical absorbance of the $ABTS^{+\bullet}$ radical (scan rate =5 mV/s; from -0.7 to 0.7 V).

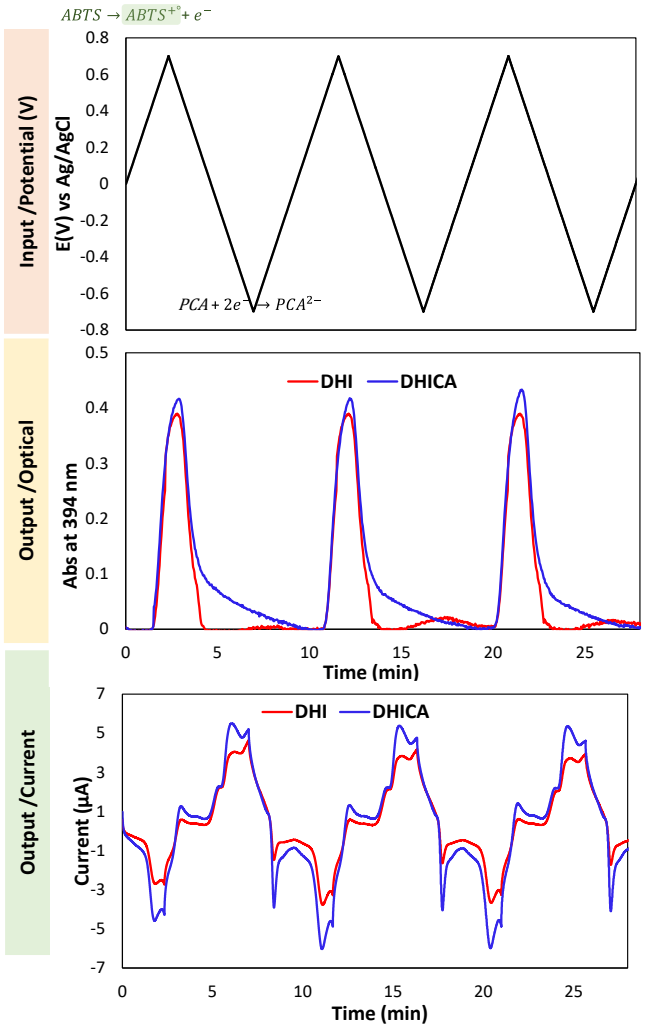

Figure 2.12. Potential input, and electrochemical and output responses of melanin-coating film after metal binding, amplification of the electrochemical currents and attenuation of the optical absorbance of the $ABTS^{+\bullet}$ radical (scan rate =5 mV/s; from -0.7 to 0.7 V).

In addition, an unsteady study case was also carried out, applying a constant potential from +0.7 V to 0 V, providing the oxidation of ABTS into its radical form and at the same time using this potential no reduction of PCA can occur. As expected under these conditions, the electrochemical output didn't show

reduction peaks for either the chitosan film or melanin-chitosan films and in agreement with the previous results, the ABTS oxidation peaks were amplified in the case of melanin-chitosan film. In this unsteady study, the optical outputs exhibited a very low initial absorbance of the $ABTS^{+\bullet}$ radical in the case of melanins, consistent with a rapid quenching. Over time, the $ABTS^{+\bullet}$ absorbance is observed to increase approaching the signal observed for the control chitosan film (i.e., the optical signal becomes less attenuated). These phenomena could be explained by the quench of the electrochemically formed $ABTS^{+\bullet}$ radical thanks to melanin, but over time as the melanin gradually loses electrons, it is no longer able to give electrons to quench the $ABTS^{+\bullet}$ radical. However also in this case DHICA melanin showed higher antioxidant ability, even over time. The same experiment was performed on melanin-chitosan film after metal binding. In agreement with the previous findings, a loss in terms of radical scavenging activity was observed for both melanins. Interestingly, an almost complete loss of radical scavenging ability was observed for DHICA melanin with respect to DHI melanin (Figure 2.13-14).

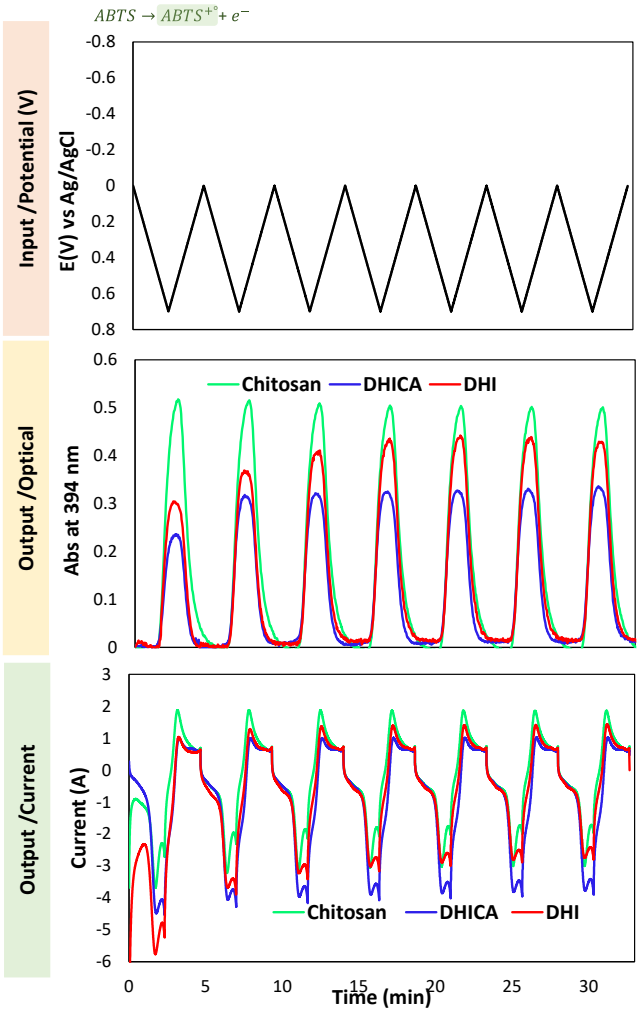

Figure 2.13. Potential input, and electrochemical and output responses of melanin-coating film, amplification of the electrochemical currents and attenuation of the optical absorbance of the $ABTS^{+\bullet}$ radical (scan rate =5 mV/s; from 0.7 to 0 V).

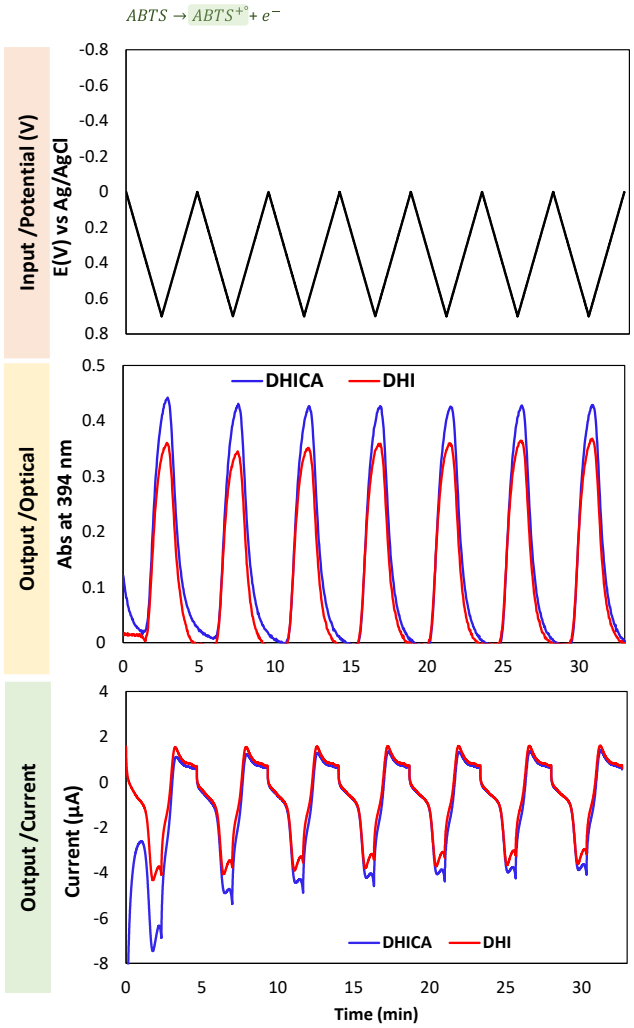

Figure 2.14. Potential input, and electrochemical and output responses of melanin-coating film after metal binding, amplification of the electrochemical currents and attenuation of the optical absorbance of the $ABTS^{+\bullet}$ radical (scan rate =5 mV/s; from 0.7 to 0 V).

Main outcomes of the study:

- A comparison between the redox properties of DHI and DHICA model synthetic pigments prepared by enzymatic oxidation was carried out using an experimental reverse engineering approach.
- Both model melanins are redox-active.
  - DHICA melanins seems to be more redox active or to have more accessible redox active sites.
- Spectroelectrochemical steady and unsteady studies allow to conclude that both melanins after metal binding significantly lose redox activity and antioxidant properties.
  - DHICA melanins loses redox activity and antioxidant properties to a more significant extent.

2.2 Non-covalent interaction in redox-active films generated from a eumelanin precursor in the presence of HMDA

2.2.1 Investigation of the key factors driving film deposition from MeDHICA/HMDA

As illustrated in the previous paragraph eumelanin are redox active catechol polymers with enhanced radical scavenging abilities. To exploit these interesting properties, the possibility to have eumelanin-based film coated on various surface was explored.

A dip coating protocol developed for DHI eumelanin film deposition promoted by HMDA was applied to other eumelanin precursors such as DHICA and MeDHICA. A 1 mM solution of the selected indole was stirred in the presence of HMDA in 0.05 M carbonate buffer at pH 9. Quartz slides were dipped into the reaction mixture and the film formation was monitored periodically by Uv–Vis analysis. Unfortunately, in the case of DHICA no detectable film was observed on the dipped quartz slide but only a dark eumelanin-type polymer (Figure 2.15). On the contrary, after 24 h in the case of MeDHICA the formation of a yellowish film on the quartz substrate was observed, together with a light-colored precipitate. The Uv-Vis analysis of the film revealed a well-defined absorption maximum around 340 nm, indicating the presence of oligomeric species. As shown in Figure 2.15 panel c, other type of surface such as metals, plastic surfaces, and glass materials were coated by dipping them in the MeDHICA/HMDA reaction mixture. A systematic investigation of the best reaction conditions in terms of HMDA molar eqs. was carried out. Based on spectrophotometric analysis of the coated quartz slide, the maximal film deposition was obtained using HMDA 1.5 M eqs. Therefore, 1 mM MeDHICA and 1.5 mM HMDA in 0.05 M carbonate buffer at pH 9.0 were selected as optimal reaction conditions.

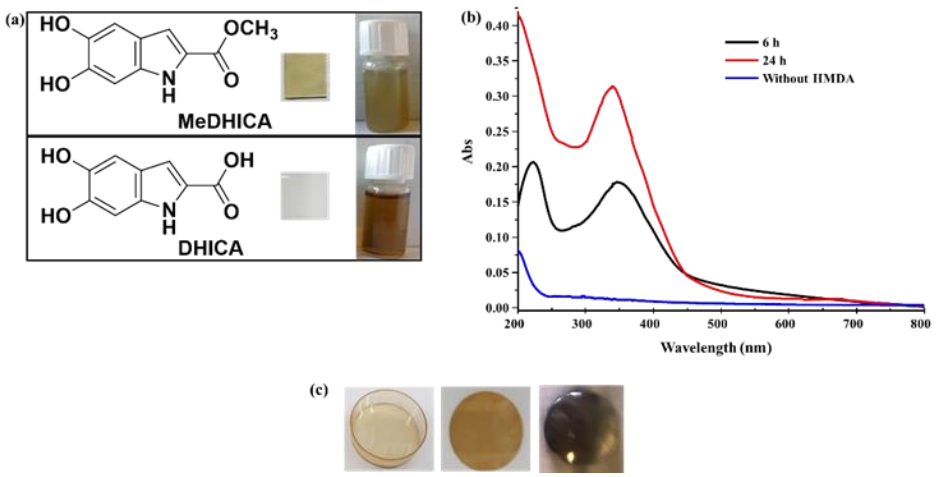

Figure 2.15. Quartz substrates dipped into reaction mixtures of MeDHICA/HMDA (top) and DHICA/HMDA (bottom) after 24 hours at pH 9.0; (b) Uv-Vis spectrum of MeDHICA reaction mixture without or with HMDA at different reaction time; and (c) MeDHICA/HMDA coatings on various materials, from left to right: polycarbonate, polystyrene, and aluminium.

Under these selected conditions, after 6 h the film showed an intense absorption maximum at 340 nm that increased over time reaching a maximum at 24 h. As expected in absence of HMDA no UV-detectable film was observed. In addition, the kinetic film deposition of MeDHICA/HMDA over 1 h was determined using Quartz Crystal Microbalance (QCM-D) methodology. The frequency and the dissipation changes over time were monitored for 1 hour, after the introduction of the MeDHICA/HMDA solution in the cell. The film thickness was estimated using the Sauerbrey equation from the QCM-D data as follows.

$$\Delta m = -C \times \frac{\Delta f}{n}$$

A film thickness of 8.7 nm was estimated after 1 h of deposition. This was based on the observation that the frequency change (f) of the oscillating quartz should

be linearly related to its mass change, provided the film is rigid and assuming a homogeneous mass density for melanin-like material (1.2 g/cm^3). Interestingly, the film deposition begins as soon as the chemicals are mixed.

To get a deeper insight into the film forming process, the effect of pH and the structural characteristics of the amine component necessary to allow film deposition were also investigated. Firstly, the reaction was carried out using different pHs. As shown in Figure 2.16, the best result was obtained in the case of pH 9, whereas a markedly lower deposition in all the other cases was observed. For pH lower than 9.0, this could be due to the slower rate of MeDHICA oxidation. On the other hand, at pH higher than 9 HMDA deprotonation and hence depletion of ammonium ions from the primary amine groups are probably the main limitations for film deposition, together with a higher oxidation rate of MeDHICA/HMDA. Secondly, different monoamines (butylamine, 6-aminohexanol), ammonium salts (tetrabutylammonium) or diamines with chains shorter or longer than 6 carbons were used, proving to be less or not effective in inducing film deposition (Figure 2.16 panel b).

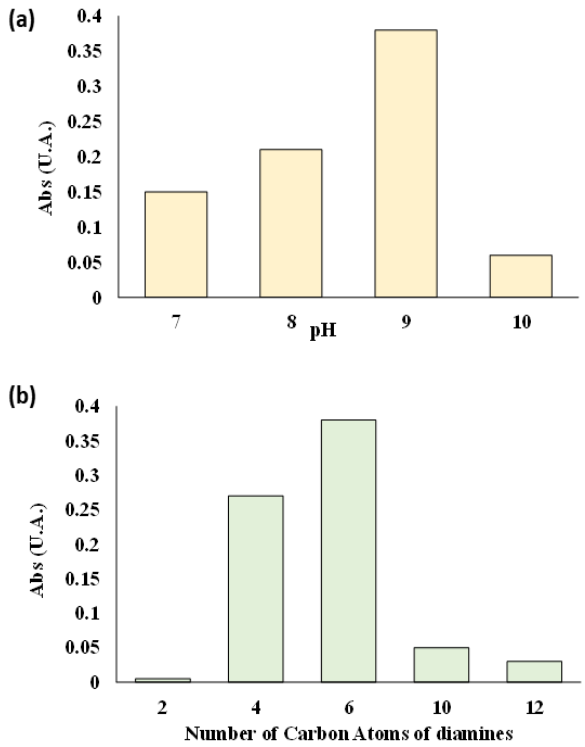

Figure 2.16. Effect on film deposition (a) of pH on film deposition and (b) of chain length of 1,n-diamines. Shown is the absorbance at 340 nm of the quartz slides immersed in the MeDHICA solution and the proper amines/diamine at the selected pH 9.0.

2.2.2 Morphological, structural, and electrochemical characterization of MeDHICA/HMDA film

To characterize the film morphology, Scanning Electron Microscopy (SEM) analysis and Atomic Force Microscopy (AFM) analysis were performed. A regular and homogeneous morphology of the film obtained under the described conditions was observed by SEM analysis. Smooth regions characterized by a fine substructure were evident together with nanoparticles around 250 nm and widespread aggregates.

In agreement with the SEM images, AFM analysis reveals smooth and homogeneous film with an estimated thickness of 37 ± 5 nm and roughness of 13.8 nm.

To get additional information, the water-contact angle (WCA) of MeDHICA/HMDA and of PDA coating, prepared as reference in the same conditions described before, were determined. Notably, a higher value around 60 ± 1 for MeDHICA/HMDA film respect to PDA coating (37.0 ± 0.3) was observed, indicating a more hydrophobic character of the main components coated on the film in the case of MeDHICA/HMDA. Additionally, after exposure to HCl vapors, the WCA value dramatically decreased to 31.2 ± 0.3, suggesting an increase in hydrophilicity, likely due to the protonation of MeDHICA-derived catechol components and the concomitant increase of ammonium ions from HMDA (Figure 2.17).

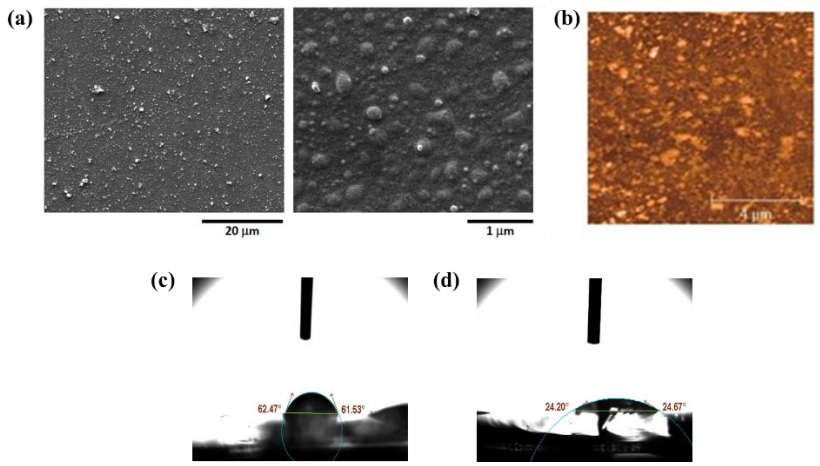

Figure 2.17. (a) SEM and (b) AFM images of coatings applied onto glass substrates from MeDHICA/HMDA reaction mixtures. WCA of the MeDHICA/HMDA coating (c) before and (d) after exposure to HCl vapors.

After exposure to aqueous sodium borohydride, the MeDHICA/HMDA film did not exhibit any clear evidence of changes in their Uv-Vis absorption spectra, which is consistent with the absence of a considerable amount of reducible

quinonoid structures. However, as illustrated in Figure 2.18, after 48 hours of exposure to ammonia vapors, the colour of the film significantly changed, becoming darker. Notably, the absorption maximum at 340 nm almost completely disappeared and a broad absorption band covering the visible spectrum was observed. These effects are consistent with the base-promoted oxidative conversion of the film components to polymeric eumelanin-type material. In agreement with the previous findings, MeDHICA/HMDA films were exposed to a UV light at 320 nm for 1 hour, and similar changes in the Uv-Vis absorption spectra were observed, indicating a possible use for the films in oxidant and UV sensing. On the other hand, when exposed to HCl vapors, the protonation of MeDHICA and similar species contained in the film resulted in a hypsochromic shift of the absorbance from 340 nm to 320 nm. An immediate and considerable drop in the absorbance at 320 nm was observed after submerging the film that had been deposited on quartz in a solution of 2:1 methanol to 0.1 M aqueous HCl.

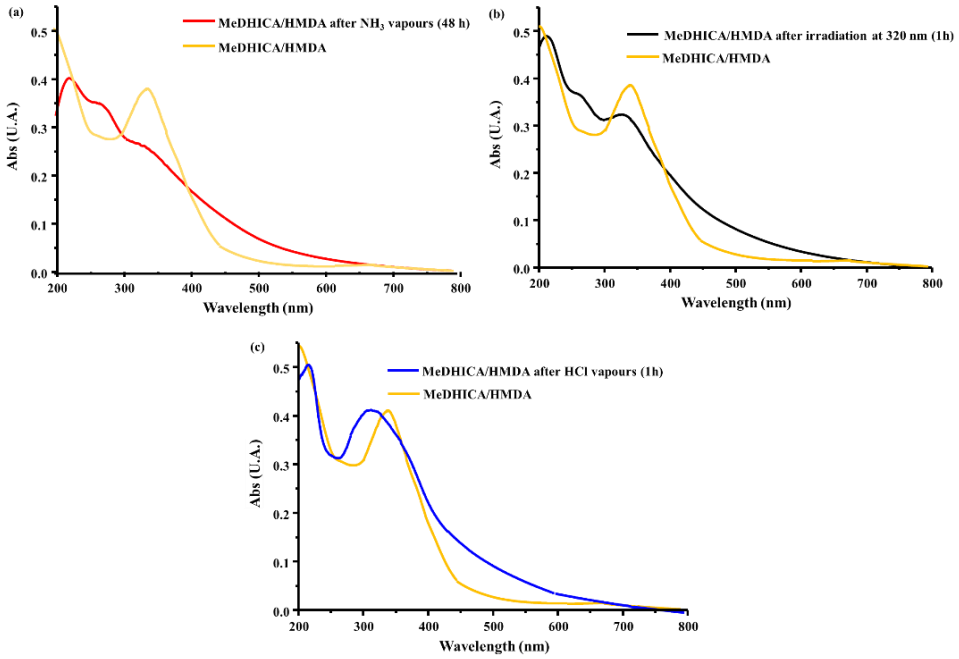

Figure 2.18. Uv-Vis spectra of MeDHICA/HMDA film before and (a) after exposure to ammonia vapors up to 48 h, (b) following irradiation with a UV lamp at 320 nm over 1 h, or (c) exposure to HCl vapors.

As illustrated in Figure 2.19, cyclic voltammetry (CV) measurements revealed an irreversible oxidation-reduction wave in the absence of the external redox probe, suggesting that the film was electroactive and in line with the observations made above that indicated a high content of reduced catechol units in the films. Additionally, in agreement with the impedance spectrum, the MeDHICA/HMDA coating on the electrode surface shown to be practically impermeable to potassium hexacyanoferrate. The linear component of the Nyquist plot showed that the film had a strong resistance to the redox probe diffusion to the electrode in the low frequency domain.

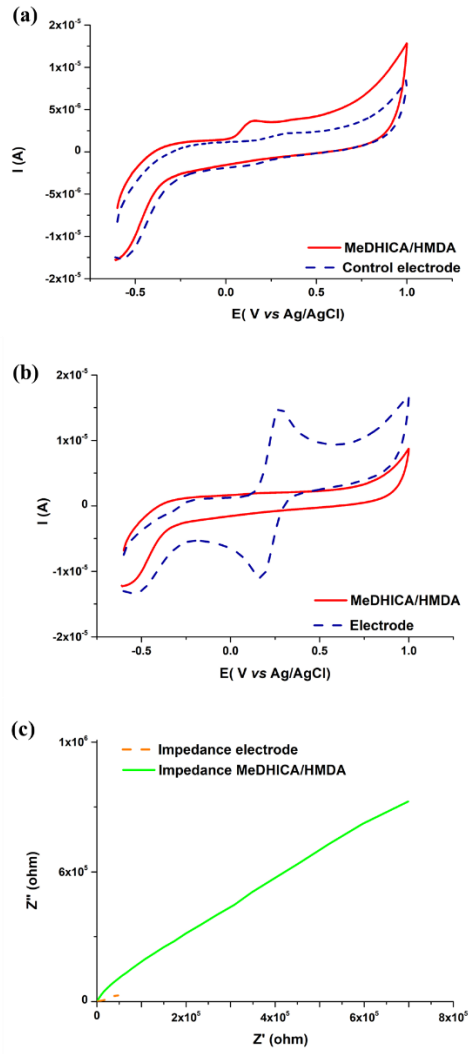

Figure 2.19. Electrochemical study of the MeDHICA/HMDA film that was deposited on the working electrodes made of amorphous carbon. (a) Film capacitive curves following a 1-hour dip of the electrode in a MeDHICA/HMDA combination in carbonate buffer at pH 9.0. (b) The CV curve of potassium hexacyanoferrate used as a redox probe on electrodes that were either pristine (dashed lines) or coated in the MeDHICA/HMDA coating. (c) Electrochemical impedance spectra with a redox probe present in the MeDHICA/HMDA film solution and a Nyquist representation.

2.2.3 Computational studies

The general properties of MeDHICA, its anion, as well as its one-electron (semiquinone) and two-electron (quinone) oxidation states in its most stable tautomeric forms, were investigated using the DFT and post Hartree-Fock levels to test the effectiveness of the postulated non-covalent interactions involved during film deposition. The results revealed that MeDHICA at the 6-OH group and semiquinone at the 5-O position exhibited pKa values of 7.5 and 6.2, respectively (average values of the two techniques), respectively.

2.2.4 Chemical characterization of the film components

To get additional information on the chemical composition of MeDHICA/HMDA films, the DMSO solution of the film was analysed by HPLC and UV analysis. Firstly, the film was dipped in DMSO solution and sonicated for 30 min. The Uv-Vis spectra of the MeDHICA/HMDA coated quartz after immersion into DMSO solution showed no detectable absorbance, indicating that all the film components were dissolved in this solvent. Then, after proper dilution 1:10, the HPLC analysis of the resulting mixture was performed. The elutographic profile reveal the presence in small amount of MeDHICA monomer (R_t=12 min) together with higher amounts of other components, such as the 4,4'-MeDHICA dimer (4,4'-biindolyl) and 4,7'-MeDHICA dimer (4,7'-biindolyl) at R_t = 16 and 18 min, respectively (Figure 2.20), identified by comparison with authentic standards.

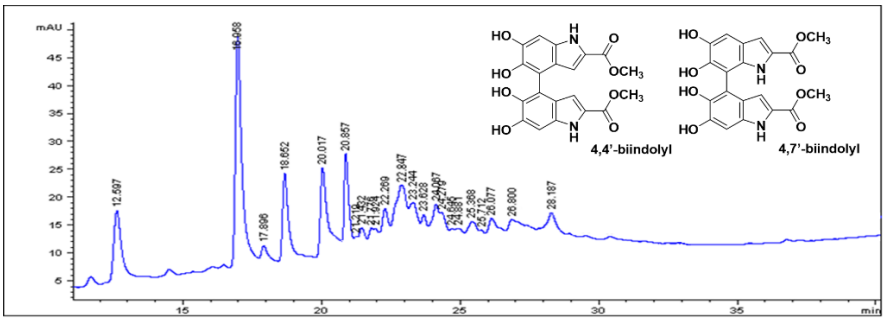

Figure 2.20. Elutographic profile of the MeDHICA/HMDA film dissolved in DMSO (Eluent: H_2O/acetonitrile 20-70% gradient, λ=300 nm).

In addition, MALDI analysis was also carried out. The film was directly coated on MALDI plate and extensively washed with water. A well detectable pseudomolecular ion peak at m/z 208 attributed to MeDHICA monomer was detected, together with its oligomers up to tetrameric species $[M+Na]^+$ at m/z 435, 640, 845. Notably, pseudomolecular ion peaks attributable to HMDA were observed as well. Furthermore, ^{1}H-NMR analysis of the DMSO soluble fraction of MeDHICA/HMDA film after acetylation was performed. Consistent with the previous findings, the presence of MeDHICA oligomers and HMDA in the mixture was also demonstrated. Signals due the acetylated HMDA at 3.2, 1.90, 1.5 and 1.3 ppm were discernible together with resonances due to methyl groups of MeDHICA oligomers in the 3.8-4.0 ppm region and the relevant aromatic protons in the sp^2 region. The peaks at 6.63 and 7.42 ppm attributable to the 4,4'-biindolyl were well discernible, while the other signals confirmed the presence of closely related oligomers (Figure 2.21).

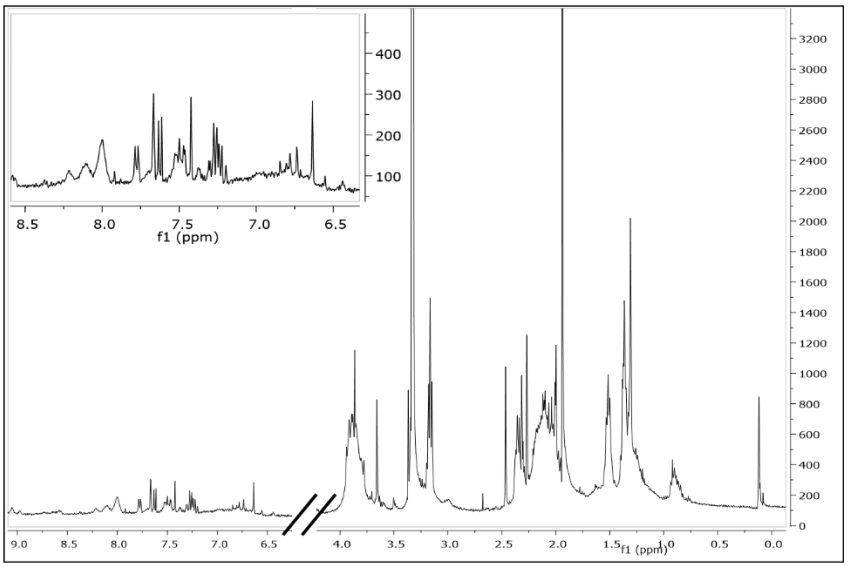

Figure 2.21. ^{1}H NMR spectrum (methanol-d_4) of the film dissolved in DMSO and subjected to acetylation treatment. Inset: aromatic resonance region.

To clarify the function of HMDA in film deposition, different attempts were devoted to looking for covalent conjugates between MeDHICA or its oligomers and the diamine. After 24 hours of oxidation, the MeDHICA/HMDA reaction mixture was extracted with ethyl acetate. In both phases no adduct was detected by HPLC analysis. Then the reaction mixture was stopped at different time, using sodium dithionite. The aliquots were then extracted with ethyl acetate, dried, and acetylated with acetic anhydride and pyridine. After that, HPLC analysis was performed. Also, in this case no adduct was observed. All the combined analysis, allowed to conclude that the presence of MeDHICA and its oligomers are the major components of the film, together with free HMDA. In addition, no species derived from a covalent coupling of MeDHICA with HMDA was apparently obtained.

2.2.5 Chemical, kinetic and morphological analysis of the MeDHICA/HMDA film

In separate experiments, the effect of HMDA on the kinetic oxidation of MeDHICA was evaluated. A marked slowing effect on the oxidation/consumption rate of MeDHICA and dimer accumulation was observed. In fact, after 3 h under stirring in absence of HMDA, the residual of MeDHICA was around 28% and almost complete after 6 h, whereas in presence of the diamine, the remaining starting material was 63%. The formation yields of 4,4'-biindolyl and 4,7'-biindolyl slightly increased in the presence of HMDA in the first 3 h (Figure 2.22), after which time their consumption becomes predominant (not shown). As result, it can be concluded that the presence of HMDA slightly delays the kinetic oxidation, probably due to a non-covalent interaction of HMDA with MeDHICA. To investigate the importance of a slow oxidation for the film formation, a fast oxidation of MeDHICA in presence of HMDA with potassium ferricyanide was performed. After 30 min no film deposition was detected on quartz by Uv-Vis spectrophotometer despite the complete oxidation of the catechol detected by HPLC analysis. This suggests that the slow oxidation rate of MeDHICA is crucial for the coexistence of larger amounts of intermediates with longer lifetimes and increased availability for non-covalent interactions, self-assembly and cross-linking.

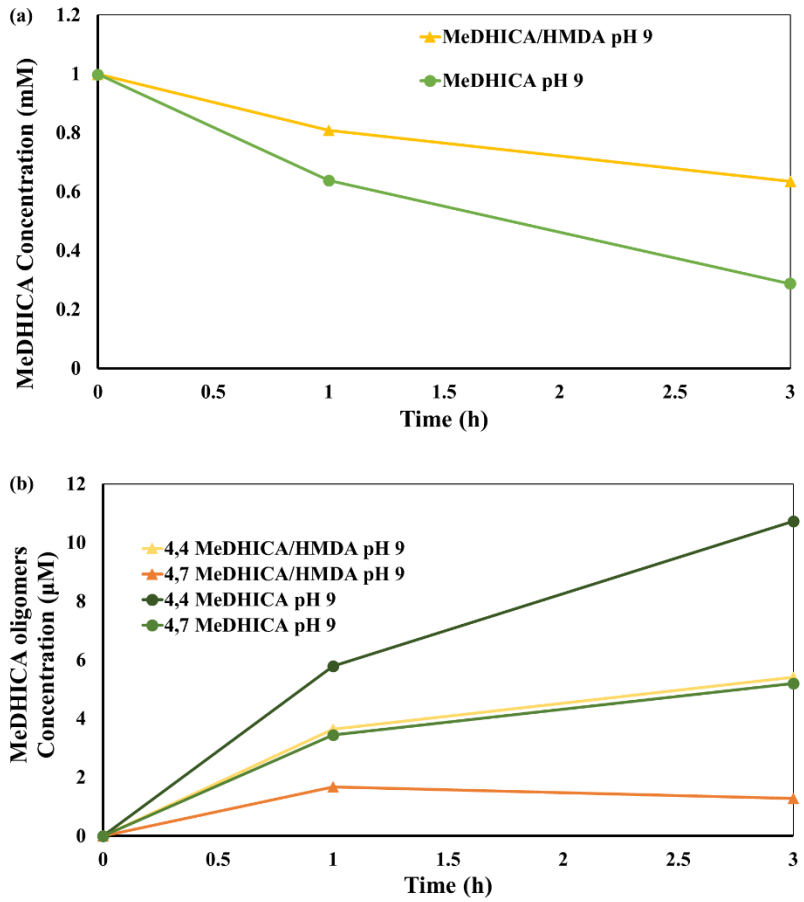

Figure 2.22. Kinetics of MeDHICA aerial oxidation at pH 9 (a) consumption of MeDHICA and (b) formation of 4,4' and 4,7' dimers in the reaction carried out with or without HMDA.

This conclusion is also supported by the absence of film deposition under the same conditions observed in the case of DHICA, characterized by a high oxidation rate. To support these observations, also Dynamic Light Scattering (DLS) was performed. Time evolution of the hydrodynamic diameter distributions of MeDHICA aerobic oxidation in the presence of HMDA exhibited a higher growth rate of particle size in solution in comparison with that observed for the oxidation mixture of MeDHICA in the absence of HMDA.

In the absence of HMDA, the particle growth was very slow and only reached the value of 450 nm after 24 h, whereas in presence of HMDA after only 90 min a maximum value of 900 nm was obtained (Figure 2.23).

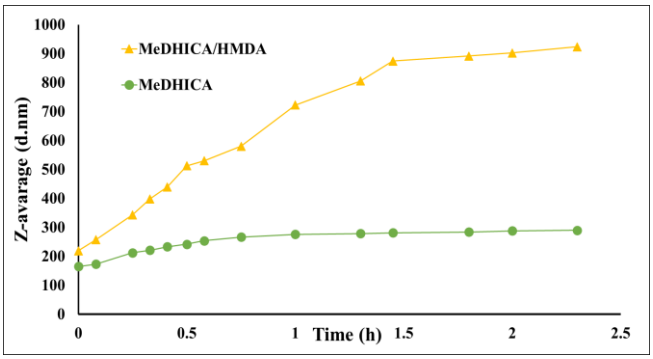

Figure 2.23. Time evolution of the hydrodynamic radius distributions of the particles produced by MeDHICA oxidation with or without HMDA.

In agreement with the previous conclusions, also these experiments support the main idea that HMDA and MeDHICA monomers or its oligomers create a network through non-covalent interactions.

Moreover, Transmission Electron Microscopy (TEM) analysis of the MeDHICA/HMDA mixture was performed. Particularly, when the TEM grid was dipped into MeDHICA/HMDA mixture, a continuous very thin film was observed together with nanoparticles of varying shapes, most of them quasi-spherical with a size ranging from 50 to 150 nm (Figure 2.24 a, left panel). Higher magnification TEM showed the film substructure, indicating the presence of uniformly dispersed domains with size below 5 nm (Figure 2.24 a, right panel). A low transparency of the film to the electron beam in absence of HMDA indicates that the MeDHICA mixture alone produced a discontinuous film with a significantly higher thickness than that formed by the MeDHICA/HDMA mixture (Figure 2.24 b, left panel). In small regions where a low thickness occurred, the TEM analysis of the film at higher magnification was allowed and then performed. TEM images revealed the substructure of the

film with the presence of embedded nanodomains with lateral size between 5 and 20 nm, thus higher than that observed at the same magnification on the film obtained from the MeDHICA/HDMA mixture (Figure 2.24 b, right panel).

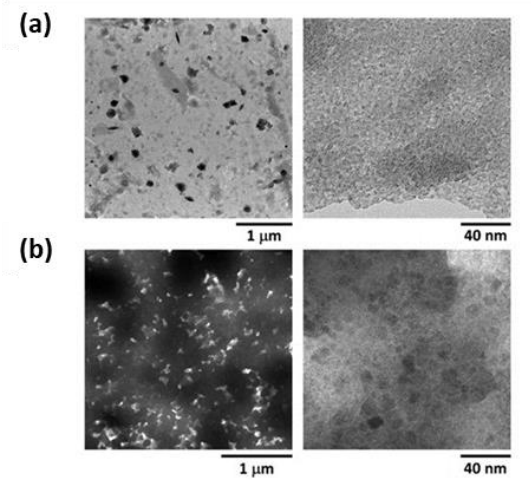

Figure 2.24. Bright field TEM images of the reaction mixtures of MeDHICA in the presence (a) without (b) or with HMDA in carbonate buffer pH 9.0 after 4 h.

2.2.6 Antioxidant properties of the MeDHICA/HMDA films and cell protection effects

Given the well-known strong antioxidant properties of MeDHICA and its polymer, the MeDHICA/HMDA film were compared to other films prepared from dopamine (DA) and DHI in the presence of HMDA under the same reaction conditions described above. At the concentration used such as 1 mM, DA alone does not result in noticeable film formation in the absence of HMDA. Subsequently, the coated substrates were dipped in a 50 μM ethanol 2,2-diphenyl-1-picryl-hydrazyl (DPPH) solution. As expected, all the films exhibited an increase of antioxidant activity within 30 minutes, whereas no effect was observed after 1 h. Interestingly, in the case of MeDHICA/HMDA film a DPPH consumption around 30% was observed, whereas in the case of DA

and DHI, lower values were determined (20% and 10%, respectively). Notably, a clear evidence of MeDHICA/HMDA antioxidant activity was the significant darkening of the exposed film area, probably due to the oxidative conversion of the MeDHICA units into melanins, as previously mentioned (Figure 2.25).

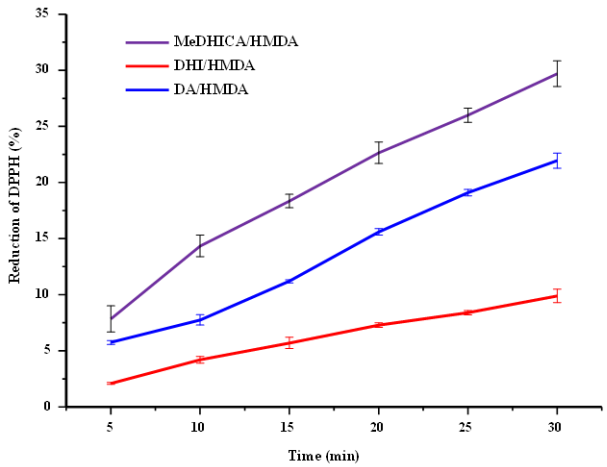

Figure 2.25. The reduction effect of glass substrates coated with MeDHICA/HMDA, DA/HMDA or DHI/HMDA films dipped into DPPH (50 μM). Shown are the results of triplicates + SD.

Based on these findings, which showed that the MeDHICA/HMDA film had greater antioxidant capacity than other coatings previously studied, two distinct electron transfer assays, i.e. the Ferric Reducing Antioxidant Power (FRAP) and the (2,2′-azino-bis(3-ethylbenzothiazoline-6-sulfonic acid) ABTS inhibition assay, were performed. For both assays the MeDHICA/HMDA film demonstrated a good antioxidant activity. In fact, a well-noticeable formation of the absorption Fe^{2+}-TPTZ complex at 593 nm for the FRAP test and a 15% decrease in ABTS over 30 minutes were observed (Figure 2.25).

Therefore, due to the promising results, in vitro study on HaCat cells were carried out. Firstly, there was no difference in cell viability between HaCaT cells grown on coated wells and those grown on unfunctionalized supports, indicating

that the MeDHICA/HMDA film was not harmful to the cells (data not shown). In additional tests, MeDHICA/HMDA films capacity to protect cell cultures from oxidative stress conditions was assessed. After being stressed by UVA on functionalized or unfunctionalized plates, the ROS levels produced by HaCaT cells were measured, using the 2',7'-dichlorofluorescin diacetate (H_2DCFDA) test. According to Figure 2.26, a small but substantial (p 0.01) decrease in ROS levels in the absence of irradiation for functionalized petri was observed. Both unfunctionalized (black bars, 1.5 fold increase, p 0.001) and functionalized (light grey bars, 1.5 fold increase, p 0.005) plates showed a substantial increase after irradiation. Notably, the functionalized plates displayed lower ROS levels than the unfunctionalized plates after 30 minutes of stress. For instance, compared to simply stressed cells, unfunctionalized plates showed a 25% drop in ROS levels (white bar, p 0.05), but functionalized plates showed a more than 50% decrease (dark grey bar, p 0.005), reaching a ROS level lower than that one observed for non-irradiated cells (20% decline, p 0.01). In a first series of studies, the recovery time, i.e., the amount of time required for the cells to recover from the irradiation stress, was optimized (not shown).

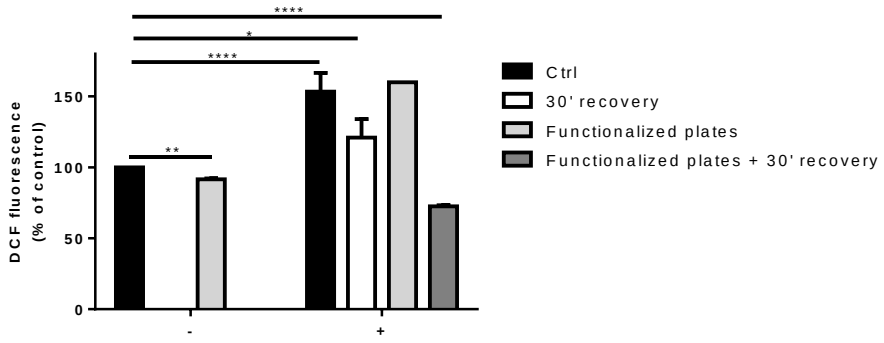

Figure 2.26. Antioxidant effects of MeDHICA/HMDA films on UVA-stressed HaCaT cells. MeDHICA/HMDA coated plates (grey bars) and unfunctionalized plates (black and white bars) were stressed by UVA radiations (100 J/cm^2) and intracellular ROS levels were measured by 2',7'-dichlorodihydrofluorescein diacetate (H_2DCFDA). Measurements were taken immediately after irradiation and after 30 min recovery * indicates $p<0.05$; ** indicates $p<0.01$; *** indicates $p<0.005$; **** indicates $p<0.001$.

According to previously published data, this result confirms the strong antioxidant activity of eumelanins from MeDHICA in cell cultures and implicates MeDHICA/HMDA films as a useful system for the development of devices that can shield cells and possibly tissues from the harm caused by oxidative stress conditions.

2.2.7 Proposed model for MeDHICA-HMDA film deposition

Based on these findings, the structural requirements and experimental factors crucial for MeDHICA-HMDA film deposition, includes: a sufficiently long and flexible aliphatic chain of the diamine group, the presence of the ester derivative of HMDA, a slightly alkaline pH, allowing the presence of HMDA in the di-protonated form (pKa_1 = 10.76, pKa_2 = 11.86) and the concomitant deprotonation of the acidic 6-OH group of MeDHICA (pKa = 7.5).

All these factors, may drive a wide spectrum of non-covalent interactions, such as:

- cation-π between the π-electron-rich system of the catechol ring of MeDHICA and the protonated primary amine groups of HMDA;
- π -type (electrostatic), including one protonated primary amine groups of HMDA aligned on the plane of the oxygen lone pairs of the o-diphenolic functionality with the MeDHICA anion at the 6-OH group;
- π -stacking, engaging MeDHICA rings;
- hydrophobic, between the long aliphatic chains of the diamine and the flat aromatic moieties.

Overall, these non-covalent interactions and the concomitant oxidation of MeDHICA in the presence of HMDA give rise to complex networks of self-assembling small-sized molecules held together by the long chain diamines.
In this view, the optimal condition for the film formation, i.e. pH 9.0, could be justified by the concomitant presence of di-protonated HMDA and the MeDHICA anion as charged aromatic building block. In addition, the positively charged ammonium ions of HMDA, due to the long aliphatic chain, can interacts with the negatively-charged phenoxide groups or π-electron rich of MeDHICA. In agreement with this hypothesis ^{1}H-NMR spectra of DMSO soluble fraction of MeDHICA/HMDA film exhibited an approx. 1:0.5 ratio of MeDHICA-derived species *versus* HMDA, despite the different initial molar ratio of the reagents (1:1.5). In this scenario, the significant decrease of the WCA after exposure to HCl vapours, could be due to protonation of phenoxide groups MeDHICA. Along the same line of interpretation, the absorbance decrease of the coated quartz slides by acid washings are likely the result of the loss of the electrostatic forces primarily responsible for film adhesion. A schematic illustration of the proposed model for film deposition from MeDHICA/HMDA is reported in Figure 2.27.

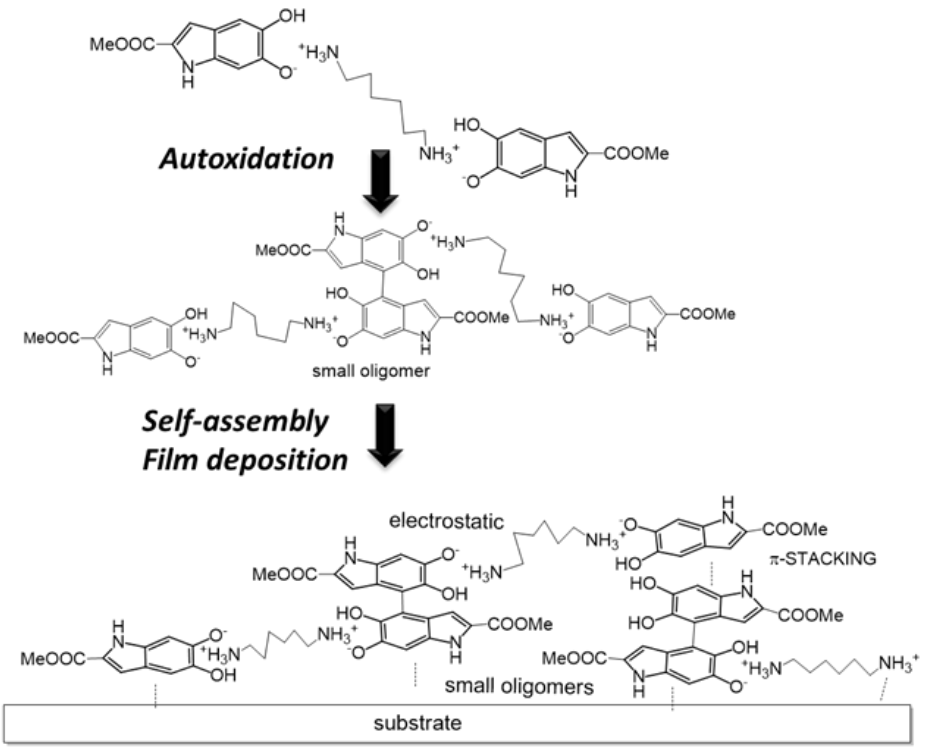

Figure 2.27. Graphic illustration of the MeDHICA/HMDA film deposition process. This diagram emphasizes the suggested interaction between the diprotonated form of HMDA and MeDHICA monomers, oligomers, and complementary non-covalent contacts.

Main outcomes of the study:

- Film forming properties were imparted to MeDHICA, a derivative of the major eumelanin precursor DHICA, by oxidation in the presence of a diamine, specifically, HMDA.
  - The films from MeDHICA/HMDA appeared light in color, were removed from the substrate on which they were deposited by washings with DMSO and retained the antioxidant properties of DHICA melanins..
  - Based on the mechanistic insights carried out deposition of MeDHICA/HMDA films represents the first example of mussel-inspired dip-coating technology based on the non-covalent self-assembly of small molecules.

2.3 Melanin pigments from 5,6-dihydroxyindole carboxamides: properties evaluation for assessment of the potential for dermocosmetic applications

The potential of other derivatives of DHICA beside esters that may allow to access to melanin related pigments with properties useful for applications in dermocosmetic field was evaluated. Amides appeared a good option because they are stable under physiological conditions and in addition the electrondonor character of the carboxyamide group was expected to favourably affect the chromophore of the final melanin pigment, leading to a melanin pigment covering the Uv- Vis region differently from that from MeDHICA. In addition, proper choice of the amino component might warrant a good solubility in organic solvents of the final melanin.

To this aim an optimized procedure for preparation of carboxamides of 5,6-dihydroxyindole-2-carboxylic acid (DHICA) was developed.

Based on a protocol previously reported [220], the main eumelanin precursor DHICA was synthetized by a one pot reaction involving the oxidation of 3,4-dihydroyphenylalanine (DOPA) using potassium ferricyanide as oxidizing agent.

In a first series of experiments, a procedure used for caffeic acid based on the use of (1-Ethyl-3-(3-dimethylaminopropyl)carbodiimide) EDC, (1-Hydroxybenzotriazole) HOBt, and triethylamine (TEA) in dry DMF, at room temperature for 18 h under controlled atmosphere was slightly adapted and carried out. Firstly, DHICA was acetylated using anhydride acetic/pyridine (Py) treatment overnight. To hydrolyse the undesired mixed anhydride generated at the carboxyl group, the resulting acetylated derivative, i.e. 5,6-diacetoxyindole-2-carboxylic acid (DAICA), was treated with 1:1 v/v methanol/water under reflux. Subsequently, the amidation reaction with 1-butanamine was carried out as indicated supra. The LC-MS analysis of the reaction mixture highlighted that

no adducts observed could be attributed to DHICA amidation products. This analysis also revealed a significant formation of the *N*-acetyl butylamine, likely arising from displacement of the acetyl group from the catechol function of DAICA by the amino group. Therefore, other synthetic strategies were investigated. After different attempts, the best results were obtained adopting a protocol reported in the literature for solid state peptide synthesis based on the use of 1-[bis(dimethylamino)methylene]-*1H*-1,2,3-triazolo[4,5-b]pyridinium-3-oxide exafluorophosphate (HATU) as coupling agent [221].

The amidation reaction was carried out adding to DAICA mixture, 1.5 eqs. of HATU and 1.5 eqs. of N, N-diisopropylethylamine DIPEA in DMF dry under controlled atmosphere. The reaction was monitored by HPLC analysis (eluent: formic acid 0.1% - methanol 40:60 at wavelength 300 nm). At 15 min reaction time, the formation of an adduct of HATU with DAICA (**A**) was observed (R_t =9.8 min), associated with the complete disappearance of the peak corresponding to DAICA (R_t = 5.5 min) and almost complete disappearance of a peak at R_t=3.9 min attributed to HATU (Figure 2.28).

Subsequently, 1 eqs. of the selected amine, i.e. 1-butanamine, was added to the reaction mixture, and, after only 10 minutes, the formation of a product eluted at 8.1 min, identified as DAICA butanamide (LC-MS evidence indicated as 1 in Figure 2.28 was observed. It seems likely that the peak with R_t at around 3.9 min is due to the N-oxide derivative of HATU, generated when the amine attacks the actived intermediate as demonstrated by its increase after addition of the selected amine. Hence, it would approximately coelute with that due to HATU. Scheme 2.1 shows all the steps of the synthetic procedure.

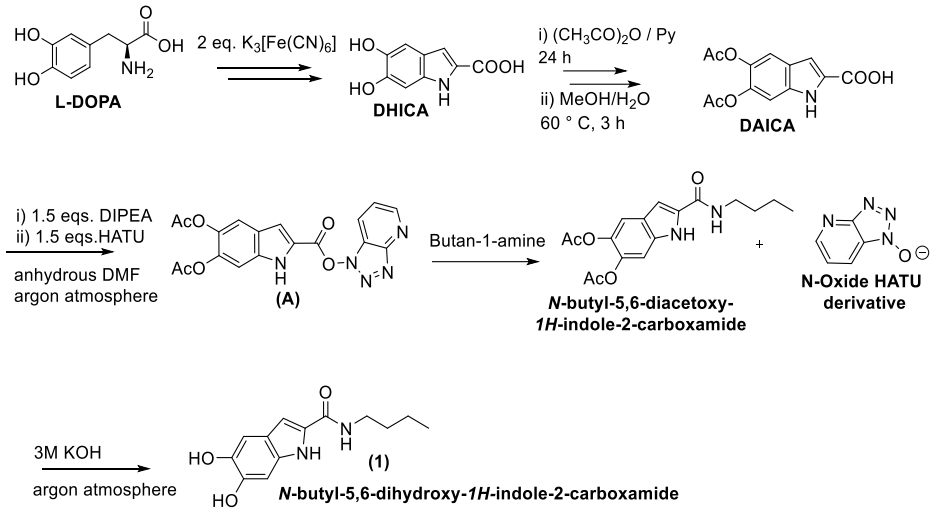

Scheme 2.1. Synthetic procedure for DHICA amides. Shown is also preparation of DHICA from DOPA.

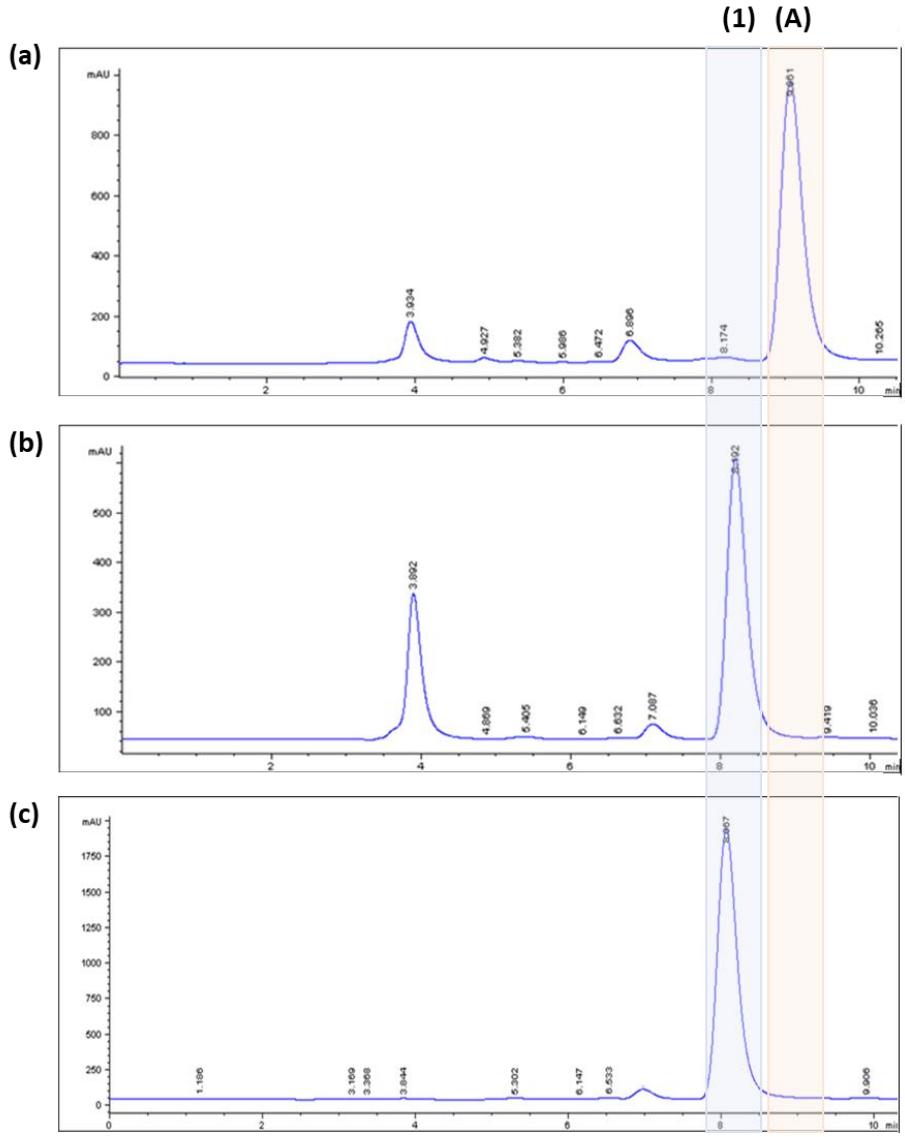

Figure 2.28. Elutographic profile of the amidation reaction of DAICA at different time: (a) at 10 min after addition of HATU; (b) at 5 minutes after addition of 1-butanamine; (c) DAICA butanamide after purification.

By simple addition of water to the reaction mixture, the formation of a precipitate was observed. This was easily recovered by filtration vacuum and

extensively washed with 0.01 M HCl and with water to remove the unreacted amine and the excess of HATU/its N-oxide, respectively. The product obtained in 85% was subjected to LC-MS and ^{1}H and ^{13}C NMR analysis (Figure 2.29).
In the aromatic area, between 7.0 and 7.5 ppm, it is possible to note the presence of 3 singlets attributable to the indole protons, whereas the NH indole singlet was detected at 11.7 ppm. Interestingly, a broad triplet at 8.5 ppm attributable to the NH amide was observed. Notably, as shown in Figure 2.29 the butyl chain can be detected in the aliphatic region, in particular the triplet at $\delta = 0.90$ ppm corresponds to the terminal CH_3, while the multiplets at 1.34, 1.52 and 3.28 ppm are due to the methylene groups at the γ, β, α position of the carbonyl of the amide, in that order. The intense singlet at $\delta = 2.26$ ppm is instead attributable to the acetyl groups.

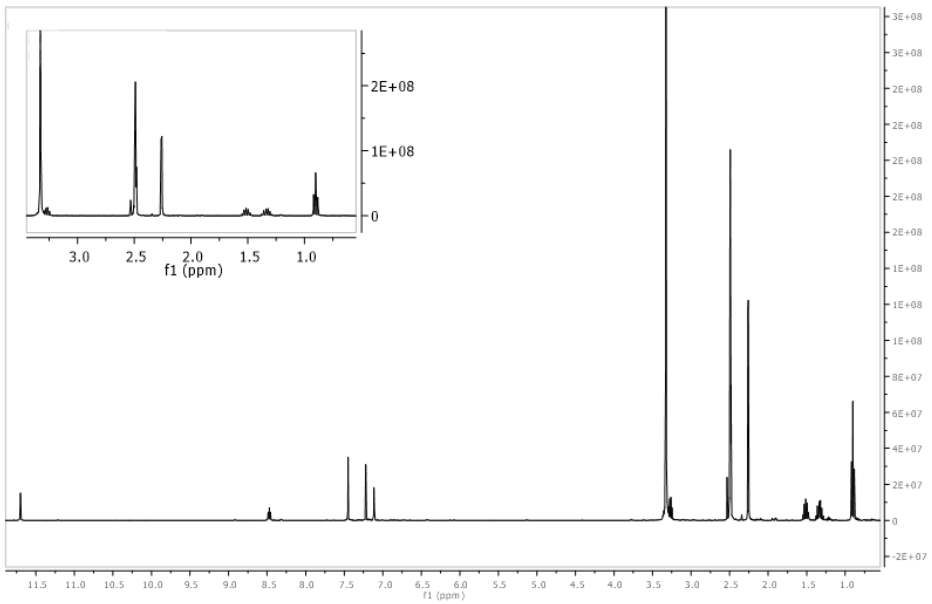

Figure 2.29. ^{1}H NMR spectrum of *N*-butane-5,6-diacetoxy-1*H*-indole-2-carboxamide (**1)** (DMSO-d_6).

The same procedure was then extended to other selected amines, including two diamines i.e. 1,4-diaminebutane and 1,6-diaminehexane and an aromatic amine,

i.e. aniline. All products were obtained in a pure form and good yields (Table 2.1). All compounds were subjected to a complete mono and bidimensional ^{1}H NMR and ^{13}C NMR analysis.

Table 2.1. Structure and yields of the synthesized DAICA carboxamides.

Amide derivatives of DAICA	Yield (%)
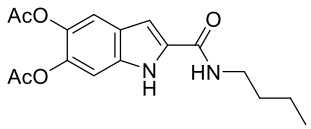 **1**	85
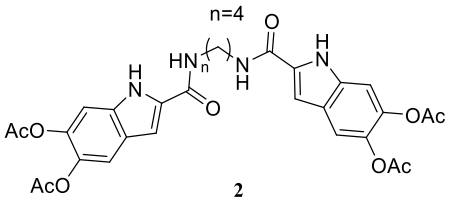 **2**	90
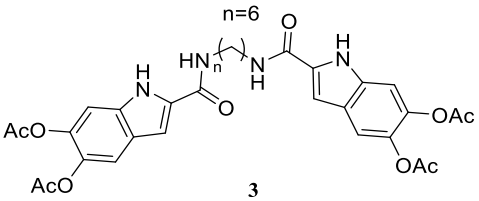 **3**	87
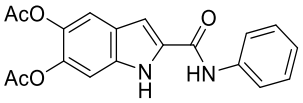 **4**	85

Removal of the acetyl group was carried out under controlled conditions, in view of the expected ease to oxidation of the deprotected compound. Briefly, the selected DAICA derivative was dissolved in dichlorometane/methanol 9:1 v/v at 8 mM concentration and taken under an inert atmosphere. Subsequently, an alcoholic 3 M KOH was added to final concentration 0.2 M. As evaluated by TLC and HPLC analysis after 5 minutes, the complete deprotection of the catechol groups occurred. Then, the mixture was acidified to pH 2 with aqueous acids. The product was recovered after work up of the mixture in almost quantitative yields. Purity of the compounds was also checked by ^{1}H-NMR analysis, showing the disappearance of the signals at 2.27 ppm attributable to the acetyl groups.

2.3.1 Oxidation of DHICA amides: pigment formation and properties characterization

The oxidative polymerization of one selected DHICA carboxamides (1 mM) was performed in air in 0.05 M carbonate buffer at pH 9.0, close to the pKa of the catechol systems. After 24 h, a significant reduction of the absorption maximum at λ 320 nm, typical of the DHICA monomer, and the concomitant increase absorption in the whole Uv-Vis range was observed (Figure 2.30 panel a), suggesting that the melanization process occurred. The reaction mixture was then acidified to pH 3, and the precipitated melanin was recovered by centrifugation and subsequent lyophilization. The pigments obtained from oxidation of DHICA amides were prepared on hundreds of milligrams scale, recovered from the reaction mixtures, extensively washed and dried.

In Figure 2.30 panel b, the absorbance over the Uv-Vis spectrum *vs* time obtained at 24 h for all the amides normalized against the absorbance at 300 nm was plotted. All of them exhibited a similar profile respect that one observed for DHICA, suggesting that the synthetic pigments prepared from DHICA amides

derivative could be considered similar to the natural melanins. All the samples, except DHICA and particularly evident for compound **4,** exhibit a higher absorption in the UVA region (350-450 nm) compared to the monotonic profile of an ideal melanin pigment.

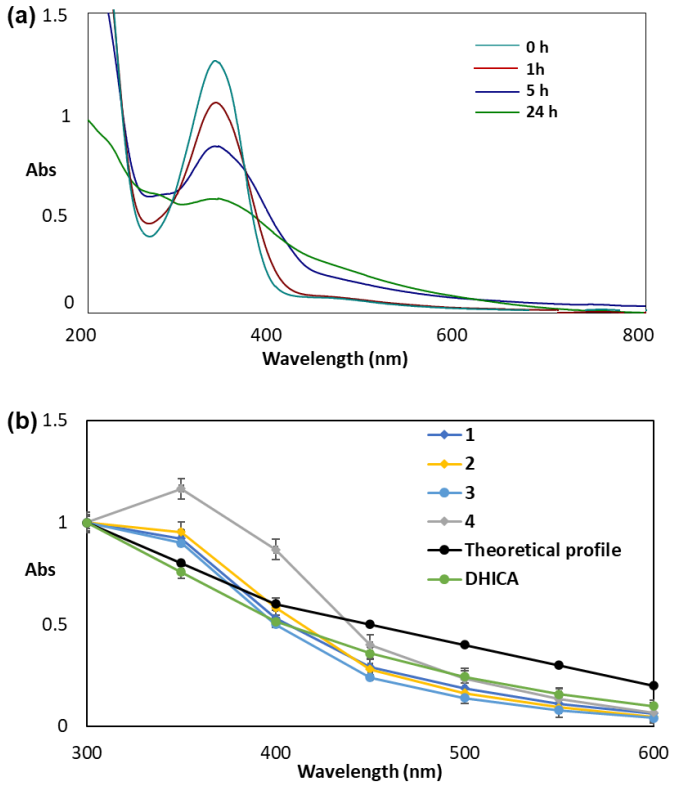

Figure 2.30. a) UV-Vis spectrum of the course of the aerial oxidation of **1** over time; b) Relative absorbance of the oxidation mixtures of all the synthesized amides and DHICA at 24 h reaction time against the theoretical monotonic profile. (Values normalized against the absorbance at 300 nm for each mixture)**.**

2.3.2 *N*-butane-5,6-dihydroxy-1*H*-indole-2-carboxamide and its melanin for dermocosmetic application

As representative example and most interesting for dermoscometic application, *N*-butane-5,6-dihydroxy-1*H*-indole-2-carboxamide (DHICA butanamide) was selected in order to fully characterized and analysed the corresponding melanin properties.

To clarify if the introduction of a long aliphatic chain *via* amide bond affects the polymerization pattern in comparison with DHICA, in a first series of experiments the oxidative chemistry of DHICA butanamide was preliminarily investigated. A protocol described in literature for the synthesis of the 4,4' dimer of DHICA, was slightly adapted and carried out, involving the indole oxidation at 3 mM concentration in the presence of equimolar copper acetate in HEPES buffer at pH 7.5 [222]. The resulting mixture was taken under stirring for 10 min. The reaction mixture was analysed by HPLC (eluent: formic acid 0.1% - methanol 40:60 at wavelength 300 nm). In order to improve the HPLC resolution, the preliminary acetylation of the mixture was performed. A main dimeric compound (LC-MS evidence) eluted at ca. 14 min was observed, together with a minor product eluted at 17 min. Subsequently, the main product was isolated in good yield (76% yield) by preparative HPLC and identified by a complete ^{1}H and ^{13}C NMR analysis as the DHICA butanamide 4,4'-dimer (Figure 2.31) and by comparison with data previously reported for DHICA dimers. As result, it can be concluded that the introduction of a long aliphatic chain *via* amide bond did not impact on the polymerization pattern in comparison with DHICA.

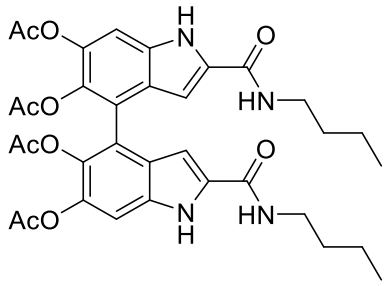

Figure 2.31. Structure of acetylated 4,4 dimer of DHICA butanamide.

2.3.2.1 Preparation and structural characterization of DHICA amide melanins

In subsequent experiments synthetic melanins, obtained from DHICA butanamide monomer and for comparison DHICA, were prepared as described before (see paragraph 2.3.1). EPR analysis of DHICA butanamide and DHICA melanins was carried out. This analysis revealed that DHICA butanamide melanin showed the broad singlet typical of eumelanins, with a g-factor value indicating the prevalence of carbon centred radicals. As shown in Table 2.2, the EPR features of DHICA butanamide and DHICA melanins were very comparable, though some peculiarities of the DHICA butanamide pigment could be emphasized. As an example, its spin density was lower than that measured for DHICA melanin but still in line with the values reported for natural and synthetic melanins [223]. The low gaussian fraction in DHICA butanamide melanin pointed to the presence of resonant radicals all presenting a similar chemical nature. The ΔB value observed for DHICA butanamide is slightly larger than that observed DHICA melanin, which is in substantial agreement with the values previously reported for DHICA melanin prepared under different oxidation conditions [60], suggesting increased dipolar interaction of unpaired magnetic moments of free radicals located at short distance. The lower number of spins, located on the average at shorter distance, points to a slightly less

homogeneous distribution of the radical centres within DHICA butanamide with respect to DHICA melanin. This is confirmed by the power saturation profiles, which are very similar, but still allow to appreciate that DHICA butanamide pigment show a slightly less homogeneous relaxation behaviour.

Table 2.2. EPR data for DHICA and DHICA butanamide melanin.

Samples	Spin/g Concentration	ΔB (± 0.2)	Gauss fraction	g-factor (± 0.0003)
DHICA melanin	1.9E+18	3.9 ± 0.2	0.47	2.0029± 0.0003
DHICA butanamide melanin	4.8E+17	4.7 ± 0.2	0.28	2.0030± 0.0003

To fully characterized DHICA butanamide melanin, ATR-FTIR spectra, Uv-Vis analysis and HPLC were performed and compared to DHICA melanin. In the case of ATR, both melanins exhibited a broad band (*Band 1*) at 3500-3000 cm^{-1}, attributed to OH stretching. A *Band 2* at 1685 cm^{-1}, typically associated to the COOH carbonyl stretching, was observed for DHICA melanin, whereas in the case of DHICA butanamide melanin a *Band 3* at 1650 cm^{-1} related to the CONH carbonyl bond stretching was detected. Moreover, the presence of a *Band 4* at 1260 cm^{-1} and 1445 cm^{-1} attributed to CH_3 and CH_2 bending of the aliphatic chain of DHICA butanamide melanin, respectively were observed (Figure 2.32).

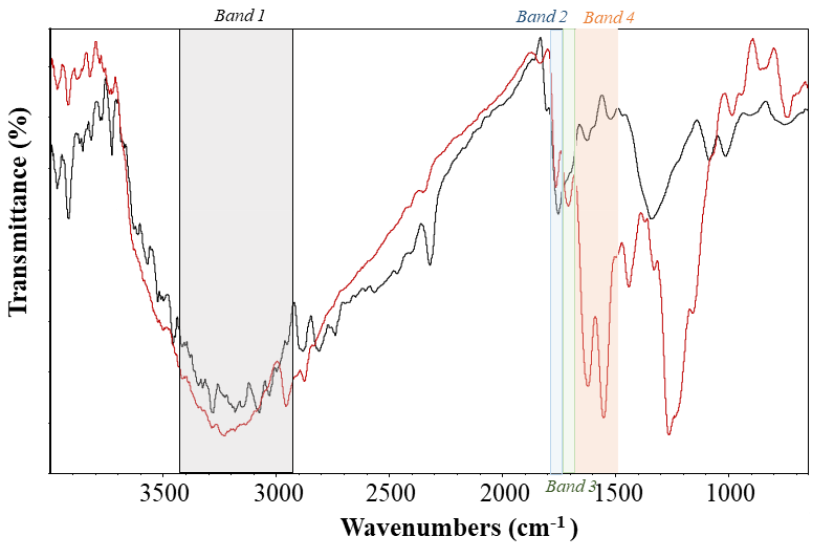

Figure 2.32. FTIR-ATR spectra of DHICA butanamide (red line) and DHICA (black line) melanin.

Secondly, Uv-vis analysis of DHICA butanamide and DHICA melanin at 0.01 mg/mL in methanol were carried out, exhibiting similar absorbance in all visible range and even higher in the case of DHICA butanamide melanin in the UV range, region of great interest for dermo-cosmetic application (Figure 2.33).

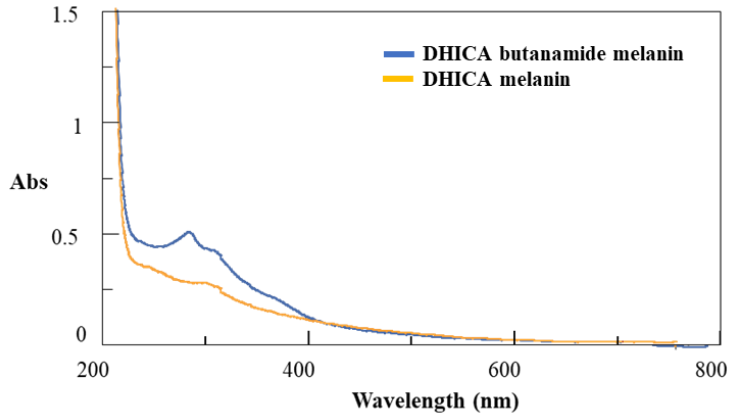

Figure 2.33. Uv-Vis spectrum of DHICA butanamide and DHICA melanins 0.01 mg/mL in methanol.

Finally, the HPLC analysis of the solution after acetylation (C_f 1 mg/mL) revealed the presence of DHICA butanamide oligomeric species, attributable to dimers (R_t 13 and 17 min), trimers and tetramers (probably R_t ranging from 28 to 31 min) of the mixture. MALDI analysis confirmed the presence of these products up to tetrameric specie (Figure 2.34).

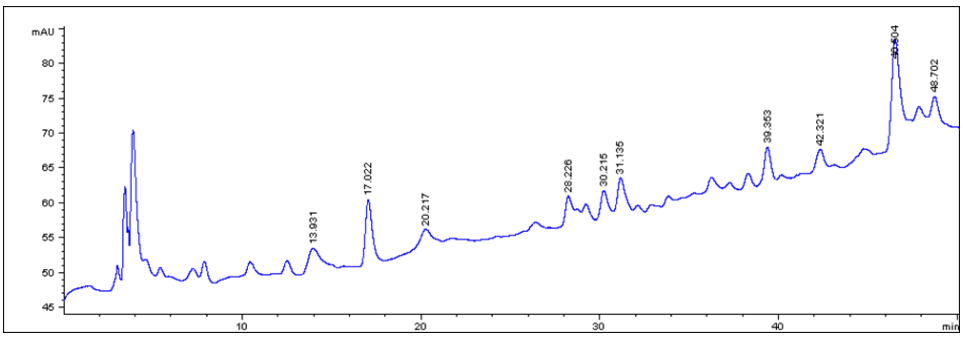

Figure 2.34. Chromatogram of the DHICA butanamide melanin at 1 mg/mL.

2.3.2.2 Solubility properties of DHICA amide melanins in solvents of dermocosmetic interest

Initial experiments showed remarkable solubility properties of DHICA butanamide melanin compared to DHICA melanin. On these bases, the solubility profile of DHICA butanamide melanin in different solvents was investigated. Among all the solvent used, some are of relevance for dermocosmetic applications. With this perspective, DHICA butanamide melanin were dissolved at different concentration (0.25 - 5 mg/mL) in DMSO, methanol, ethanol, propylene glycol, propylene glycol/glycerol 1:1 v/v and stirred for 15 minutes. After centrifugation, the Uv-Vis spectra of supernatants were recorded following appropriate dilution (1:100). The maximum solubility of each solvent was calculated by plotting the absorbance versus concentration curve. Notably, DMSO showed greater solubility up to 5 mg/mL (Table 2.3). For all plots the

range of concentrations in which a linearity of the absorbance was obtained is shown, at higher doses the linearity was lost (Figure 2.35).

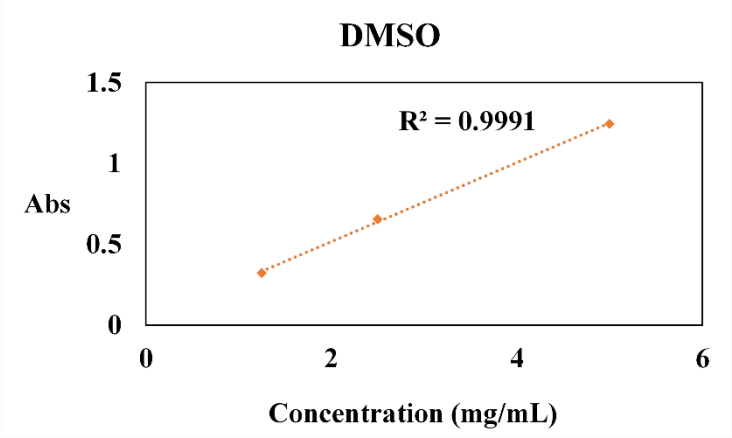

Figure 2.35. Absorbance versus concentration plots for DHICA butanamide melanin in DMSO as solvent.

Table 2.3. Solubility properties of DHICA butanamide melanin.

Solvent	Maximum solubility (mg/mL)
DMSO	5
Ethanol	1.5
Methanol	1
Propylene glycol	0.33
Propylene glycol/glycerol	0.25

2.3.3.3 Antioxidant properties of DHICA butanamide melanin

The last part of this project was aimed at the evaluation of the antioxidant properties of DHICA butanamide melanin in comparison with DHICA melanin, using two common chemical assays such as DPPH assay, measuring the hydrogen- and/or electron -donor ability of a given species, and the FRAP test, measuring the iron (III) reducing power. A DMSO stock solution (0.5 mg/mL) of each melanin and for comparison, the starting monomers were also tested. In

the DPPH assay, DHICA butanamide melanin showed an EC_{50} value 5 times lower respect to DHICA melanin. On the contrary, in the FRAP assay, the two melanins exhibited comparable Trolox eqs.

These results could be explained by the different solubility of DHICA and DHICA butanamide melanins in the assay media. In the case of the DPPH assay the use of ethanol as the solvent is expected to favour DHICA butanamide melanin. Although the different solubilities of the two samples in ethanol (medium used for the DPPH experiment), this cannot account for the 5-fold better antioxidant capabilities of DHICA butanamide melanins compared to DHICA melanins. In fact, in the concentration range used to establish the EC_{50} value (that is 0.005-0.286 mg/mL) also DHICA melanin previously dissolved in DMSO shows an acceptable solubility in ethanol. This suggest that the amide group considerably enhances the pigments antioxidant capabilities (Table 2.4). On the other hand, both melanin performed comparably in the FRAP assay indicating that DHICA butanamide exhibited a comparable Fe (+3) reduction ability with respect to DHICA melanin. Based on these findings, it is reasonable to conclude that the introduction of the amide group affects the electronic delocalization of the aromatic ring and consequently, the redox properties of the resulting melanins.

Table 2.4. Results of the (a) DPPH and (b) FRAP assay for DHICA and DHICA butanamide related melanins. Reported are the mean ± SD values of at least three experiments.

Samples	**EC_{50} (mg/mL)**	**Trolox eqs. (mg/mL)**
DHICA melanin	0.242 ± 0.004	0.33 ± 0.01
DHICA butanamide melanin	0.0374 ± 0.0004	0.246 ± 0.004

In another series of experiments, the ability of DHICA butanamide and for comparison DHICA melanin to prevent the peroxidation of critical biological targets was evaluated. The effect on the peroxidation of linoleic acid as a model system of lipid components of cellular membranes was tested in comparison

with DHICA melanin. Therefore, the peroxidation of linoleic acid using 2,2′-azobis(-amidinopropane) dihydrochloride (AAPH) as a radical initiator in aqueous solution at pH 7.4, in the presence or absence of melanin (0.02 - 0.04 mg/mL) was performed. During the peroxidation process, the formation of conjugated diene hydroperoxide generally occurred, allowing to observe the formation of an absorbance maximum at 234 nm. In this case, DHICA butanamide melanin exhibited an EC_{50} value lower than the value determined for DHICA melanin. In another series of experiments, the peroxidation of linoleic acid was induced using sunlight, in the presence of riboflavin as a photosensitizer. In agreement with the previous results, DHICA butanamide melanin had a much higher EC_{50} of 0.062±0.001 mg/mL in comparison to DHICA melanin, which displayed no detectable activity at the same dose (Table 2.5). The stronger peroxidation inhibition capacity and synergistic effects of physical screening are probably the main driving factors for the lower EC_{50} values shown in the case of DHICA butanamide.

Table 2.5. Chemical and photo induced lipid peroxidation assay in the presence of DHICA and DHICA butanamide melanin.

	DHICA melanin	**DHICA butanamide melanin**
EC_{50} (chemical lipid peroxidation)	0.0598 ± 0.0008	0.037 ± 0.004
EC_{50} (photoinduced lipid peroxidation)	Not detectable	0.062 ± 0.001

Main Outcomes of The Study.

- A procedure for preparation of carboxamides of the melanin precursor DHICA in satisfactory yields (> 85%) was developed with the aim of gaining access to pigments with more favourable properties, including solubility in organic solvents.
- The melanin deriving from the oxidative polymerization of the carboxybutanamide of DHICA showed marked antioxidant and inhibition of lipid peroxidation properties together with good solubility in solvents of dermocosmetic relevance.

2.4 Experimental section

Materials and Methods. 3,4-dihydroxy-L-phenylalanine (L-DOPA), potassium ferricyanide, sodium bicarbonate, sodium dithionite, hexamethylenediamine (HMDA), 1,2-ethylenediamine, 1,4-butanediamine, 1,12-dodecanediamine, 1,10-decanediamine, aniline, 1-butanamine, lysine, pyridine, 6-amino-1-hexanol, tetrabutylammonium hydrogen sulfate, *N*,*N*-diisopropylethylamine (DIPEA), anhydrous dimethylformamide (DMF), 1-[bis(dimethylamino)methylene]-1*H*-1,2,3-triazolo[4,5-b]pyridinium-3-oxide hexafluorophosphate (HATU), copper acetate, 4-(2 -hydroxyethyl)-1 -piperazineethanesulfonic acid (HEPES), linoleic acid,, 2,2′-azobis(-amidinopropane) dihydrochloride (AAPH), sodium dodecyl sulfate (SDS), 2,4,6 -tris(2 -pyridyl) -s-triazine, 6-hydroxy-2,5,7,8-tetramethylchroman-2-carboxylic acid (Trolox) were acquired by Fulkra. 2,2-diphenyl-1-picrylhydrazyl (DPPH), iron chloride (III) hexahydrate, 2,4,6-tri(2-pyridyl)-s-triazine (TPTZ), 2,2′-azino-bis(3-ethylbenzothiazoline-6-sulfonic acid) (ABTS), potassium persulfate, and 2′,7′-dichlorofluorescein diacetate (H_2DCFDA) were purchased by Sigma-Aldrich. Chitosan, Phenazine-1-carboxylic acid (PCA), 1,1'-ferrocenedimethanol (Fc) was purchased from Acros organics.

The water (>18 ML) used in this study was obtained from a Super Q water system (Millipore). All solvents were HPLC grade.

Human immortalized keratinocytes (HaCaT) were from Innoprot (Derio, Spain).

Uv-Vis spectra were run on a V-730 Jasco instrument.

^{1}H and ^{13}C NMR spectra were recorded at 400 MHz and 100 MHz, respectively, on a 400 Bruker spectrometer, in methanol-d_4 - DMSO-d_6. In the case of DHICA amide derivatives, proton and carbon resonance assignments were based on 2D NMR analysis (^{1}H, ^{1}H COSY, ^{1}H,^{13}C HSQC, ^{1}H,^{13}C HMBC, not shown).

Water contact angle analyses were performed using a contact angle goniometer (Digidrop-gbx, France) equipped with video capture. 1 μL of distilled water was

dropped on the air side surface of the substrate. Quartz Crystal Microbalance measurement were performed with a quartz crystal microbalance-dissipation (QCM-D) system from Q-Sense (Göteborg, Sweden).

ATR-FTIR spectra were recorded on a Nicolet 5700 Thermo Fisher Scientific instrument. Spectra were recorded as an average of 128 scans in the range 4000−450 cm^{-1} (resolution of 4 cm^{-1}).

HPLC analyses were performed on an Agilent 1100 binary pump instrument equipped with a Shimadzu SPD-10AV VP UV-visible detector using an octadecylsilane-coated column, 250 mm × 4.6 mm, 5 μm particle size (Phenomenex Sphereclone ODS). Detection wavelength was set at 300 nm. 0.1% formic acid - methanol 40:60 v/v as the eluant at a flow rate of 0.7 mL / min was used; a 0.1% formic acid (solvent A)/methanol (solvent B) gradient elution was performed as follows: 50% B, 0 – 5 min; from 50 to 70% B, 5 – 45 min. Preparative HPLC was performed coupled with a UV spectrophometer set at 300 nm; an Econosil C18 column (10 μm, 22 x 250 mm) was used at a flow rate at 25 ml/min; Eluent system: 0.1% formic acid (solvent A)/methanol (solvent B) in ratio 40:60 respectively.

LC-MS analyses were performed in positive ion mode using an Agilent 1260/6230DA ESI-TOF instrument under the following conditions: 35 psig nebulizer pressure; drying gas (nitrogen) flushed at 5 L/min at a temperature of 325 ° C; capillary voltage 3500 V; fragmentor voltage 175 V. An Eclipse Plus C18 column (150 × 4.6 mm, 5 μm) and 0.1% formic acid - methanol 40:60 v/v as the eluant at a flow rate of 0.4 mL / min was used.

DLS measurements were performed using a home-made instrument, composed of a Photocor compact goniometer, an SMD 6000 Laser Quantum 50 mW light source (Quantum Laser, Heaton Mersey, UK) operating at 532.5 nm, a photomultiplier (PMT-120-OP/B), and a correlator (Flex02-01D) from Correlator.com.

AFM analysis were conducted with the integrated apparatus Alpha300 RS (WITec, Germany). The samples topographies were studied by AFM in AC mode.

Bright Field Transmission Electron Microscopy (TEM) analysis was performed by a FEI TECNAI G12 Spirit-Twin (120 kV, LaB6) microscope equipped with a FEI Eagle 4k CCD camera (Eindhoven, The Netherlands). The specimens were collected by gently dipping holey carbon copper grids into the MeDHICA-HDMA-mixture (1:1.5 molar ratio) and into the MeDHICA mixture at 30 min and 4 h reaction time. Prior to observations, the collected specimens were air dried. Morphological analysis was performed on MeDHICA/HDMA films applied onto glass substrates after 6 h and 24 h reaction in carbonate buffer. The films were observed by a FEI Quanta 200 FEG scanning.

Scan electron microscope (SEM) with a secondary electron detector at 10 kV accelerating voltage in high vacuum mode. Before the analysis the samples were sputter coated with a thin Au/Pd layer. SEM micrographs were analysed by means of the public domain software ImageJ (release 1.43u).

The electrochemical characterization of the MeDHICA/HMDA film was carried out by cyclic voltammetry and electrochemical impedance spectroscopy using a three-electrode set-up (ChI 604B, CH Instruments, Houston, Texas). Electron paramagnetic resonance (EPR) measurements were performed using a Bruker Elexys E-500 spectrometer equipped with a superhigh sensitivity probe head. The samples were transferred to flame-sealed glass capillaries, which in turn were coaxially inserted in a standard 4 mm quartz sample tube. Measurements were performed at room temperature. The instrumental settings were as follows: sweep width, 100 G; resolution, 1024 points; modulation amplitude, 1.0 G; scansion time 20.97 s. The amplitude of the field modulation was preventively checked to be low enough to avoid detectable signal overmodulation. The number of scans and microwave power were optimized to avoid microwave saturation of resonance absorption curve. For power saturation experiments, the

microwave power was gradually incremented from 0.02 to 164 mW. The *g* value and the spin density were evaluated by means of an internal standard, Mn^{2+}-doped MgO, prepared by a synthesis protocol reported in the literature [224]. Since sample hydration was not controlled during the measurements, spin density values have to be considered as order of magnitude estimates [225].

Preparation of film-coated electrode. Chitosan flakes were dissolved into HCl solution to achieve a final pH of 5-6. To prepare the melanin film entrapped into chitosan film, DHI and DHICA melanins (5 mg/mL) were suspended in the chitosan solution prepared as described above. 20 μL of this suspension were dropped on a standard gold electrode (radius 1 mm) and dried in a vacuum oven for 20 minutes. Subsequently, the coated melanin-chitosan film was dipped into 0.1 M phosphate buffer solution at pH 7 for 20 min. Electrochemical measurements (cyclic voltammetry) were performed using a three-electrode system with Ag/AgCl as a reference electrode, Pt wire as a counter electrode (CHI Instruments 600C electrochemical analyzer) and gold electrode as working electrode. N_2 was purged into mediator solutions (50 μM of Fc and PCA), prepared in phosphate buffer (0.1 M; pH 7.0). For spectroelectrochemical experiment, 20 μL of the melanin-chitosan solution was dropped on the honeycomb electrode (Pine research instrumentation, NC) and dried in a vacuum oven and dipped in phosphate buffer (0.1 M, pH 7.0; 10 min). The honeycomb electrode contains two gold electrodes, one used as a working electrode and the other used as the counter electrode. The film-coated honeycomb electrode and Ag/AgCl reference electrode were placed into a spectroelectrochemical cuvette. N_2 was purged into mediator solutions (100 μM of ABTS and PCA), prepared in phosphate buffer (0.1 M; pH 7.0) during all the experiment. The optical absorbance was monitored over time at a fixed wavelength (394 nm). Simultaneously, the optical (absorbance) and electrochemical (current) output responses were individually recoded over time.

Oxidation of MeDHICA in the presence of amines/additives. MeDHICA, DHI and DHICA were prepared as reported [213,226] . 4,4'-MeDHICA and 4,7' MeDHICA dimers were obtained by oxidation of MeDHICA in the presence of copper sulfate and purified by preparative HPLC [213].

MeDHICA monomer at C_f of 1 mM was added to a 0.05 M carbonate buffer solution at pH 9.0 containing the appropriate amine, diamine or other additives, at an indole/additive molar ratio of 1:1.5 and taken under vigorous stirring. Different molar ratios were investigated for HMDA from 0.5:1 up to 1:5.

A piranha solution containing 96% H_2SO_4/30% H_2O_2 5:1 v/v was prepared. Before use, quartz substrates were cleaned by soaking in a piranha solution overnight, rinsed with distilled water and dried under vacuum. Quartz substrates, glass substrates, plastics or aluminium slides were immersed into the reaction mixture for various time, and extensively washed with distilled water with the aid of ultrasound treatment. Only in the case of the quartz, the substrate was then analysed by Uv-Vis spectrophotometry. In control experiments the reaction was carried out in the absence of amines. To a final concentration of 1 mM, at an indole/additive molar ratio of 1:1.5, and the mixture was taken under vigorous stirring.

Antioxidant property assays. The glass substrates, coated with MeDHICA, DHI or DA and HMDA, were dipped into 20 mL of a 50 μM solution (2,2-diphenyl-1-picrylhydrazyl) DPPH in methanol [227]. The antioxidant power was evaluated by Uv-Vis spectroscopy measuring the absorbance at 515 nm every 5 min over 1 h. The same procedure was applied to a solution containing $FeCl_3$ (20 mM) and 2,4,6-tris (2-pyridyl)-s-triazine (10 mM) in 0.3 M acetate buffer (pH 3.6) in the ratio 10:1:1 v/v/v, monitoring the absorbance at 593 nm periodically over 1 h [228]. In addition, also the 2,2′-Azino-bis(3-ethylbenzthiazoline-6-sulfonic acid) (ABTS) assay was carried out. The 2,2′-Azino-bis (3-ethylbenzothiazoline-6-sulfonic acid) radical cation ($ABTS^{+\cdot}$) by reacting with potassium persulfate, showing a final Abs of 0.5 at 745 nm. The

glass substrates were dipped in this solution and the absorbance at 745 nm was measured periodically over 1 h. All above-described experiments were performed in triplicate [229].

UVA irradiation of HaCat cells and ROS levels determination. 35 mm eukaryotic cell plates were washed extensively with a 1:1 water/ isopropanol mixture. Subsequently, the Petri dishes were dipped into a solution of MeDHICA and HMDA at 1:1.5 molar ratio as described above. After 24 h, the plates were rinsed with distilled water in an ultrasonic bath. Then the coated Petri dishes were sterilized with the aid of a UV lamp for 15 min. Cells were plated onto dishes coated with MeDHICA/HMDA films and uncoated dishes at a density of 3.5x104 cells/cm^2 and irradiated by UVA light for 10 min (100 J/cm^2) [214]. After a recovery time of 30 min, ROS levels were determined by H_2DCFDA assay.

Synthesis of DHICA and DAICA. Based on a procedure reported in literature, DHICA was synthesized by ferricyanide oxidation of DOPA [230]. To obtain the corresponding acetylated derivative (DAICA), DHICA (700 mg) was added to a solution containing acetic anhydride (7 mL) and pyridine (350 µL). After 24 h the resulting mixture was dried using a rotatory evaporator. The hydrolysis of the mixed anhydride with a 1:1 v/v water-methanol mixture at 90° C for 2 h was performed. After removal of the volatile components with the aid of a rotary evaporator, a powder lightly yellow in colour was obtained (98% yield). Purity of the compound was checked by ^{1}H NMR, LC-MS and UV Vis analysis.

Synthesis of DAICA carboxamides: general procedure. To a mixture of DAICA (281 mg) in anhydrous DMF (5.62 mL), 1.5 eqs of HATU and 2 eqs of DIPEA were added and stirred under an argon atmosphere for 15 min. Subsequently, 1.5 eqs of the selected amine, i.e. 1-butanamine, 1,4-diamminobutane, 1,6-diamminohexane or aniline were added, and the mixture was taken under stirring. After 30 minutes, to the reaction mixture was added water, and the resulting precipitate was filtered and washed 3 times with water,

followed by 0.01 M HCl. The product thus obtained (yields reported in Table 2.1) was analysed for purity by LC-MS and ^{1}H NMR.

N-butane-5,6-diacetoxy-1*H*-indole-2-carboxamide (1)

ES-MS: *m*/*z* 333 $(M+H)^{+}$

^{1}H-NMR (DMSO-d_6): δ (ppm): 0.90 (3H, t, J= 7.2 Hz), 1.33 (2H, sext, J=7.2 Hz), 1.51 (2H, quint, J=7.6 Hz), 2.25 (3H, s), 2.26 (3H, s), 3.21 (2H,m), 7.14 (1H, dd, J=2.0, 0.8 Hz), 7.21 (1H, d, J=0.8 Hz), 7.45 (1H, bs) 8.47 (1H, t, J=5.8 Hz), 11.74 (1H, bs)

^{13}C-NMR (DMSO-d_6): δ (ppm): 14.3 (CH_3), 20.1 (CH_2), 20.8 (CH_3), 20.9 (CH_3), 31.8 (CH_2), 39.3 (CH_2), 102.8 (CH), 106.7 (CH), 115.2 (CH), 124.9 (C), 133.9 (C) 134.0 (C), 136.9 (C), 139.5 (C), 161.0 (CONH), 169.2 (COOCH$_3$), 169.3 (COOCH$_3$).

N,*N*'-(Butane-1,4-diyl)bis(5,6-diacetoxy-1*H*-indole-2-carboxamide) (2)

ES-MS: *m*/*z* 607 $(M+H)^{+}$

^{1}H-NMR (DMSO-d_6): δ (ppm): 1.58 (4H, t, J= 8.0 Hz), 2.25 (3Hx2, s), 2.26 (3Hx2, s), 3.32 (4H, m), 7.12 (1Hx2, dd, J=2.4, 0.8 Hz), 7.22 (1Hx2, dd, J=0.8 Hz), 7.45 (1Hx2, bs) 8.51 (2H, t, J= 6 Hz), 11.75 (1Hx2, bs)

^{13}C-NMR (DMSO-d_6): δ (ppm): 20.8 (CH_3), 20.9 (CH_3), 27.2 (CH_2), 39.8 (CH_2), 102.8 (CH), 106.7 (CH), 115.2 (CH), 124.9 (C), 133.9 (C) 134.0 (C), 136.9 (C), 139.5 (C), 161.0 (CONH), 169.2 (COOCH$_3$), 169.4 (COOCH$_3$).

N,*N*'-(Hexane-1,6-diyl)bis(5,6-diacetoxy-1*H*-indole-2-carboxamide) (3)

ES-MS: *m*/*z* 635 $(M+H)^{+}$

^{1}H-NMR (DMSO-d_6): δ (ppm): 1.37 (4H, m), 1.56 (4H, m), 2.25 (3Hx2, s), 2.26 (3Hx2, s), 3.32 (4H, m), 7.12 (1Hx2, bs), 7.22 (1Hx2, bs), 7.45 (1Hx2, s) 8.51(2H, t, J= 6 Hz), 11.72(1Hx2, bs)

^{13}C-NMR (DMSO-d_6): δ (ppm): 20.8 (CH_3), 20.9 (CH_3), 26.7 (CH_2), 29.6 (CH_2), 39.3 (CH_2), 102.8 (CH), 106.5 (CH), 115.2 (CH), 124.9 (C), 133.9 (C), 134.0 (C), 136.8 (C), 139.3 (C), 161.0 (CONH), 169.2 (COOCH$_3$) 169.4 (COOCH$_3$).

5,6-diacetoxy-*N*-phenyl-1*H*-indole-2-carboxamide (4)

ES-MS: *m*/*z* 353 $(M+H)^+$

^{1}H-NMR (DMSO-d_6): δ (ppm): 2.27 (3H, s), 2.28 (3H, s), 7.10 (1H, t, J=8 Hz), 7.27 (1H, t, J=0.8), 7.37 (2H, t, J=8.0 Hz), 7.44 (1H, dd, J=2.4, 0.8), 7.55 (1H, bs), 7.88 (2H, d, J=2.0 Hz), 10.24 (s, 1H), 11.92 (s, 1H)

^{13}C-NMR (DMSO-d_6): δ (ppm): 20.8 (CH_3), 20.9 (CH_3), 104.4 (CH), 106.8 (CH), 115.4 (CH), 120.6 (2xCH), 124.5 (C), 124.1 (1xCH) 129.2 (2xCH), 133.4 (C), 134.5 (C), 137.1 (C), 139.3 (C), 140.0 (C), 159.9 (CONH), 169.2 (COOCH$_3$), 169.4 (COOCH$_3$)

Synthesis of DHICA carboxamides. DHICA carboxybutanamide (final concentration 3.6 mM) were dissolved into dichlorometane/methanol 9:1 v/v under an argon atmosphere and a 0.2 M KOH solution in methanol that has been previously purged with argon was added for 15 minutes. Subsequently, the reaction mixture was acidified to pH 3 and dried using a rotatory evaporator the precipitate was dissolved in an acid water solution (pH 3) and extracted three times with ethyl acetate. The organic layers were collected and dried. The desire product without further purification was obtained in yield of 75% and in a pure form as confirmed by HPLC and ^{1}H-NMR analysis. The same hydrolytic procedure was applied to the other carboxamides synthesized.

^{1}H-NMR of deacetylated 1 (DMSO-d_6): δ (ppm): 0.89 (3H, t, J= 7.2 Hz), 1.32 (2H, sext,J= 7.2 Hz), 1.48 (2H, quint, J= 7.2 Hz), 3.28 (2H, m), 6.77 (1H, bs), 6.81 (1H, bs), 6.84 (1H, bs), 8.22 (1H, t, J=6 Hz,), 10.95 (1H, bs)

Synthesis of 4,4, DHICA butanamide dimer. Oxidation of DHICA butanamide was run following a procedure previously reported with slight modifications[222] DHICA butanamide (245 mg, 3 mM) and 1 molar eq of copper acetate (197 mg) were dissolved in 0.1 M HEPES buffer (329 mL, pH 7.5) and the mixture was stirred for 10 minutes. The reaction was stopped by addition of 40 mg of sodium dithi-onite and acidification to pH 3 with 6 M HCl. The mixture was extracted with ethyl acetate (4 × 200 mL) and the combined organic phases were filtered on anhydrous so-dium sulphate and taken to dryness at a rotary evaporator. The residue (169 mg) was treated with 2 mL of acetic anhydride and 100 μL of pyridine overnight. After removal of the solvents the acetylated mixture was dissolved in DMSO and purified by preparative HPLC to give the 4,4'-dimer of DHICA butanamide in its acetylated form (150 mg, 75% yield)

ES-MS: *m/z:* 663 $(M+H)^+$, 685 $(M+Na)^+$, 701 $(M+K)^+$

^{1}H-NMR (DMSO-d_6): δ (ppm): 0.85 (3H x 2, t, J=6.0 Hz), 1.25 (2H x 2, m), 1.43 (m, 2H x 2, quint., J=6.0 Hz), 1.95 (3H x 2, s), 2.28 (3H x 2, s), 3.18 (2H x 2, m), 6.60 (1H x 2, bs), 7.35 (1H x 2, bs), 8.39 (1H x 2, t, J=4.8 Hz), 11.83 (1H x 2, bs).

^{13}C-NMR (DMSO-d_6): δ (ppm): 14.08 (CH_3), 20.01 (CH_2), 20.32 (CH_3), 20.97 (CH_3), 31.56 (CH_2), 38.81 (CH_2), 102.80 (CH), 106.83 (CH), 125. 04 (C), 133.68 (C), 134.76 (C), 139.87 (C), 160.77 (C), 168.53 (C), 169.14 (C)

Preparation of DHICA and DHICA butanamide melanin. DHICA or deacetylated DHICA carboxyamides (C 1mM) were taken under stirring at pH 9 in 0.05 M carbonate buffer. After 24 h, the resulting mixture was acidified and bought to pH 3. The precipitate was centrifuged (7000 rpm, 10 min, 4°C). The sample was washed three times with 15 mL of 0.01 M HCl and lyophilized.

Melanins from DHICA carboxyamides and DHICA were obtained in good yields (average 95 and 85 w/w %, respectively).

Chapter 3

Natural and synthetic derivatives of phenolic compounds as tyrosinase inhibitor for the treatment of pigmentary disorders

Hyperpigmentary disorders associated with melanin overproduction or accumulation are among the most common skin disorders [231]. Melasma and lentigo are two main examples of such disorders but many other skin dyschromia phenomena caused by inflammatory reactions, or abnormal melanocyte activity are known [232]. Although these disorders usually do not represent a hazard for human health, they are often disfiguring and burdensome, with devastating effects on patient psychological health.

The aesthetically impact on the patient life of such conditions have urged the search for compounds possibly of natural origin and with a low toxicity profile that could act as skin lighteners by modulation of pigmentation [233]. One of the most common pursued approaches revolves on the inhibition of the activity of the enzymes involved in melanogenesis primarily tyrosinase, the key enzyme of the biosynthetic pathway [234]. Tyrosinase (EC 1.14.18.1) is a copper enzyme whose structure is extraordinarily conserved across various species, and promotes two different reactions (Scheme 3.1) [235]:

- hydroxylation of monophenol to *o*-diphenol (cresolasic activity)
- dehydrogenation of catechol to *o*-quinone (catecholasic activity)

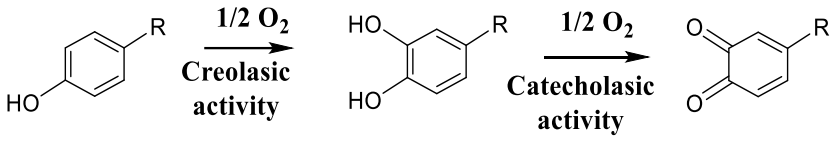

Scheme 3.1. Reactions catalysed by tyrosinase.

Tyrosinase catalyses the hydroxylation of the monophenol L-tyrosine to the *o*-diphenol L-3,4-dihydroxyphenylalanine (DOPA) and the oxidation of DOPA to the *o*-quinone DOPAquinone. L-tyrosine and L-DOPA have the same binding site, and the process involves an electron exchange with copper atoms coordinated by histidine residues inside the active site of the enzyme [236,237].

Traditionally, compounds of synthetic origin have been developed and largely used as depigmenting agents thanks to their efficacy typically hydroquinone and related compounds. Yet, the side effects associated to their applications, e.g. induced vitiligo condition, have directed the research toward other safer tyrosinase inhibitors able to reduce skin hyperpigmentation for dermocosmetic applications. Unfortunately, since a number of requirements should be met by these compounds including low or null cytotoxicity, solubility, cutaneous absorption, and stability, only a few numbers of tyrosinase inhibitors have proved actually useful.

Many tyrosinase inhibitors, that have been investigated and shown to possess some efficacy, are of natural origin and have been extracted from various natural sources. Examples include phenols, hydroquinones, flavonoids, stilbenes, or coumarins. In addition, chemical modification of naturally occurring phenolic systems have also been explored to ameliorate some unfavourable features. In this latter regard, a remarkable example is represented by caffeic acid derivatives regarded as promising lead compounds as tyrosinase inhibitors for the topical treatment of skin hyperpigmentation. Conjugates of caffeic acid (CA) and caffeic acid methyl ester (CAME) with dihydrolipoic acid (DHLA), namely the 2-*S*-lipoyl caffeic acid (LCA) and 2-*S*-lipoyl caffeic acid methyl ester

(LCAME) [238], have been shown to be effective inhibitors of tyrosine hydroxylase and dopa oxidase activities of mushroom tyrosinase and tyrosinase from human melanoma cells.

Within this context the research activity developed has pursued two goals:

- development of a green protocol based on eco-friendly solvent for the extraction of phenolic compounds from agri-food by-products after proper mechanical pre-treatment.
- Optimization of a synthetic protocol for preparation of an amide derivative of caffeic acid conjugated with dihydrolipoic acid.

Results and Discussion

3.1 Preparation of extracts from selected agri-food by-products

The agri-food by-products were selected based on the content of phenolic compounds with potential inhibitor activity against tyrosinase (Table 3.1). In addition, sludges or residues from pomegranate wine or fruit spirits production following fermentation of the fruits (made available from small enterprises) were considered.

Table 3.1. Selected natural sources and corresponding phenolic compounds with potential inhibitory activity against tyrosinase.

By-products	**Compounds with potential enzymatic inhibition activity**
Chestnut shells	Gallic acid and ellagic acid ester derivatives
Pecan nut shells	Condensed tannins
Hazelnut shells	Condensed tannins
Peanut shells	Flavonoids and luteolin, eriodictyol and 5,7-dihydroxychromone
Tomatoes and onions	Quercetin and kaempferol
Morus Alba leaves	Resveratrol, moracin, flavonoids
Morus Alba branches	Resveratrol, moracin, flavonoids
Sludges from apples spirit production	Flavonoids and phenolic acids
Sludges from strawberry spirit production	Flavonoids and phenolic acids
Sludges from Ficus spirit production	Flavonoids and phenolic acids
Sludges from peaches spirit production	Flavonoids and gallic, ferulic, chlorogenic acids
Residues from fermented pomegranate by-products	Ellagitannins, ellagic acid

The first part of the work was aimed at optimizing the extraction process from different agri-food by-products. Briefly, all the selected wastes were roughly

grinded using a blender and then homogeneously pulverized with the aid of a ball mill (15 min, 50 oscillations/s). Indeed, a ball mill is a type of grinder which works on the principle of impact and attrition. Pulverization of the samples was found to be crucial in order to decrease the particles size, increasing the surface extension and thus making the extraction process more efficient and reproducible. In addition, in the case of the onions, tomatoes, *Morus alba* branches, a preliminary step of lyophilization was essential. All the samples were then extracted in non-toxic and eco-friendly solvents such as water, ethanol, water/ethanol 4:6 v/v or DMSO (100 mg/mL solid/liquid ratio). The mixtures were taken under stirring for 90 min at room temperature, then centrifuged for 10 min and the residual solid lyophilized.

Table 3.2 reports the extraction yields, calculated with respect to the dry weight of the starting materials. As shown in Table 3.2 (**in orange values ≥ 45 %**), the highest yields were obtained in the case of the residues from fermented pomegranate by-products and sludges from different wastes spirit production. Notably, DMSO extract of the sludges from peaches spirit production showed a value up to 74%. On the contrary, the lowest values were obtained in the case of nutshells.

Table 3.2. Yields of extracts obtained from the selected agri-food by-products in each solvent, referred to the dry weight of the starting material. Reported are the mean of two experiments.

By-products	**Extraction yields (w/w %)**			
	EtOH	**H_2O**	**H_2O/EtOH**	**DMSO**
Chestnut shells	34%	4%	42%	**46%**
Pecan nut shells	**45%**	18%	40%	28%
Hazelnut shells	23%	11%	14%	22%
Peanut shells	20%	16%	12%	3%
Morus alba leaves	26%	40%	26%	21%
Morus Alba branches	14%	40%	25%	13%
Tomatoes	12%	14%	**47%**	5%
Onions	**48%**	**68%**	**66%**	**61%**
Sludges from Ficus spirit production	35%	**54%**	**55%**	**51%**
Sludges from peaches spirit production	38%	**58%**	**51%**	**74%**
Sludges from apples spirit production	59%	**53%**	**51%**	34%
Sludges from strawberry spirit production	26%	27%	29%	36%
Residues from fermented pomegranate by-products	**48%**	43%	**54%**	**56%**

3.1.1 Inhibition of mushroom tyrosinase activity by natural phenolic compounds extracts from agri-food by-products

The tyrosinase inhibitory activity of all prepared extracts was preliminary investigated using commercially available mushroom tyrosinase that is commonly used as a model of human tyrosinase.

Each extract was incubated in 50 mM phosphate buffer (pH 6.8) in the presence of mushroom tyrosinase (20 U/mL) at room temperature for 10 minutes. Following incubation, L-DOPA was added (1 mM final concentration) and the

concentration of dopachrome in the reaction mixture was determined spectrophotometrically at 475 nm after 10 minutes (Figure 3.1).

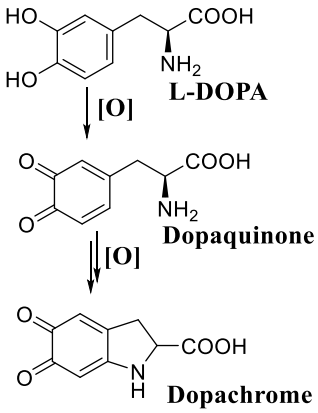

Figure 3.1. Simplified scheme of enzymatic reaction in the mushroom tyrosinase assay.

The inhibitory capacity was expressed as IC_{50}, *i.e.* the concentration of inhibitor at which 50% inhibition of enzyme activity occurs. As reported in Table 3.3, the best result was observed in the case of the hydroalcoholic extract of chestnut shells, showing an IC_{50} value of one order of magnitude lower than that determined for kojic acid, the compound used as reference inhibitor of the enzyme. In addition, in the case of ethanol extracts from chestnut shells and DMSO extract from tomatoes, IC_{50} values comparable to that obtained for kojic acid were determined. Furthermore, among the other nut shells only the hydroalcoholic and water extracts from pecan nut shells exhibited remarkable inhibition properties. Moreover, ethanol extracts of *Morus alba* branches, *Morus alba* leaves and tomatoes showed good inhibitor activity, similarly to DMSO and water/ethanol extract of *Morus alba* leaves (**bold values in Table 3.3**). On the other hand, data obtained from the other extracts were less encouraging. In some cases, it was not even possible to determine IC_{50} values.

Table 3.3. IC_{50} values (mg/mL) determined in the mushroom tyrosinase inhibition assay using L-DOPA as a substrate.* Reported are the mean + SD values of at least three separate experiments.

By-products	**IC_{50} value (mg/mL)**			
	EtOH	**H_2O**	**H_2O/EtOH**	**DMSO**
Chestnut shells	**0.0060 ±0.0005**	/	**0.0006 ±0.0004**	/
Pecan nut shells	/	**0.068 ±0.002**	**0.054 ±0.002**	/
Hazelnut shells	1.404 ±0.006	2.28 ±0.03	1.69 ±0.03	1.404 ±0.006
Peanut shells	0.53 ±0.03	/	0.306 ±0.005	/
Morus alba leaves	**0.045 ±0.003**	/	**0.0328 ±0.0002**	**0.0206 ±0.0007**
Morus Alba branches	**0.0090 ±0.0003**	/	/	/
Tomatoes	**0.013 ±0.002**	/	2.08 ±0.07	**0.0082 ±0.0003**
Onions	0.351 ±0.002	/	0.261 ±0.008	0.44 ±0.01
Sludges from Ficus spirit production	/	/	1.404 ±0.006	/
Sludges from peaches spirit production	1.09 ±0.01	/	1.07 ±0.03	/
Sludges from apples spirit production	0.557 ±0.005	/	0.937 ±0.001	2.56 ±0.05
Sludges from strawberry spirit production	0.711 ±0.007	/	0.4800 ±0.0005	/
Residues from fermented pomegranate by-products	0.475 ±0.003	0.620 ±0.002	0.511 ±0.002	0.5410 ±0.0006

*IC_{50} for kojic acid = 0.0050 $\pm$ 0.0004 mg/mL

In a second series of experiments, for the most promising extracts in terms of extraction yields and IC_{50} values, the inhibitory capacity against mushroom tyrosinase was also evaluated, using L-tyrosine as a substrate. The IC_{50} values thus determined are reported in Table 3.4 using kojic acid as a reference compound.

The highest inhibitory activity was observed for the ethanol extracts from chestnut shells, followed by its hydroalcoholic extracts, together with the ethanol extract of *Morus Alba* branches and all solvents of *Morus Alba* leaves. Also, the hydroalcoholic extract from pecan nut shells is comparable to these values **(bold values in Table 3.4**.). Overall, all the other samples were significantly less active than kojic acid.

Table 3.4. IC_{50} values (mg/mL) determined in the mushroom tyrosinase inhibition assay using L-tyrosine as a substrate*. Reported are the mean + SD values of at least three separate experiments.

By-products	**IC_{50} value (mg/mL)**			
	EtOH	**H_2O**	**H_2O/EtOH**	**DMSO**
Chestnut shells	**0.0070 ±0.0005**	/	**0.012 ±0.001**	/
Pecan nut shells	/	0.36 ±0.03	**0.028 ±0.009**	/
Morus alba leaves	**0.0304 ±0.0005**	/	**0.0273 ±0.001**	**0.01982 ±0.0006**
Morus Alba branches	**0.0110 ±0.0001**	/	/	/
Sludges from peaches spirit production	1.77 ±0.05	/	/	/
Sludges from apples spirit production	1.21 ±0.03	/	1.14 ±0.05	/
Sludges from strawberry spirit production	0.591 ±0.003	/	0.351 ±0.004	/
Residues from fermented pomegranate by-products	1.34 ±0.06	1.5±0.3	0.838 ±0.004	1.22±0.08

* IC_{50} for kojic acid = 0.0004 $\pm$ 0.0002 mg/mL

3.1.2 Inhibition of enzymatic browning in fruit smoothies by natural phenolic compounds extracts from agri-food by-products

A final series of experiments was aimed at evaluating the ability of these extracts to inhibit or at least delay enzymatic browning processes. As is well known this process is caused by the action of cytosolic tyrosinase on polyphenols that are confined in organelles inside fruit tissues but that are liberated following injuries or cuttings. The possibility to delay the process is of great commercial interest as it allows for industrial processing of fruit and for

prolonging the shelf life of the products thereof. Typically apple smoothies in which such browning process is well apparent are used as model system.

In particular, apples of the "Red Delicious" variety were peeled, rapidly cut into small pieces and finely ground with the aid of a blender in the presence or absence of the selected agri-food by-products extracts, previously prepared in the chosen solvent, at 0.1% w/w in water. Ascorbic acid and kojic acid were used as positive controls. Kojic acid acts as an inhibitor of polyphenol oxidase activity through the chelation of copper ions present in the active site of the enzyme. Ascorbic acid, which is typically used in the food industry to delay the enzymatic browning processes, instead acts both as an acid, causing a lowering of the pH of the food matrix (polyphenol oxidases exert their action at a pH value between 6 and 7), and as a reducing agent towards the quinone species generated by the oxidation of the phenolic compounds in the food matrix.

For these last series of experiments the extracts that appeared most promising, based on inhibition of mushroom tyrosinase and extraction yields, were selected. Most of the samples did not show any inhibitory effect, whereas the extract from pomegranate waste in DMSO (Figure 3.2), from chestnut shells in H_2O/EtOH (4:6 v/v) (Figure 3.3) and sludges from strawberry spirit production in H_2O/EtOH (Figure 3.4) showed a delay effect on the browning process, more evident in the first minutes.

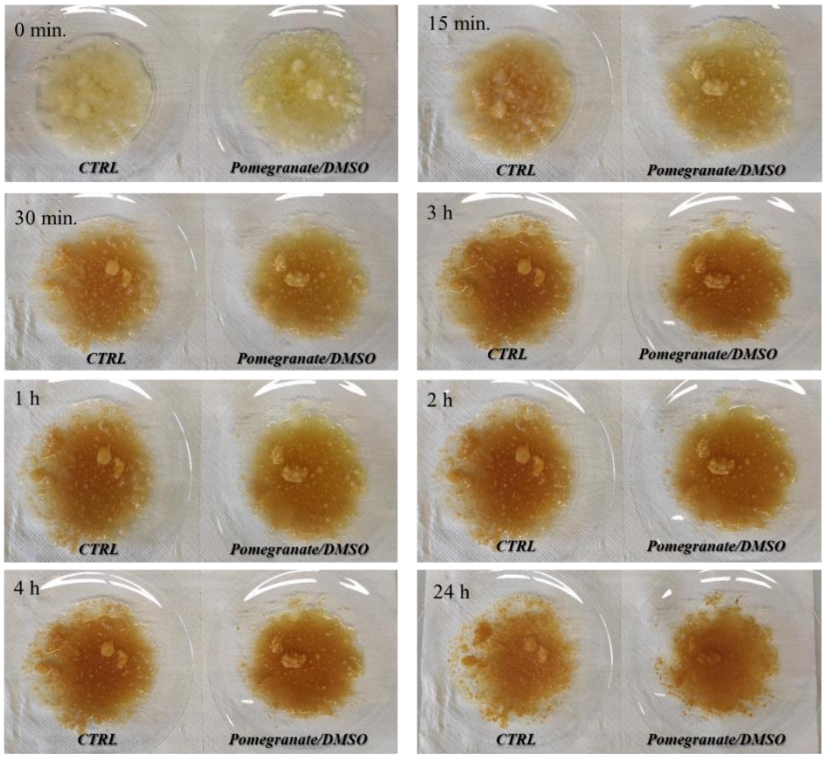

Figure 3.2. Effect of Pomegranate/DMSO extract on the apples fruit browning process at different time.

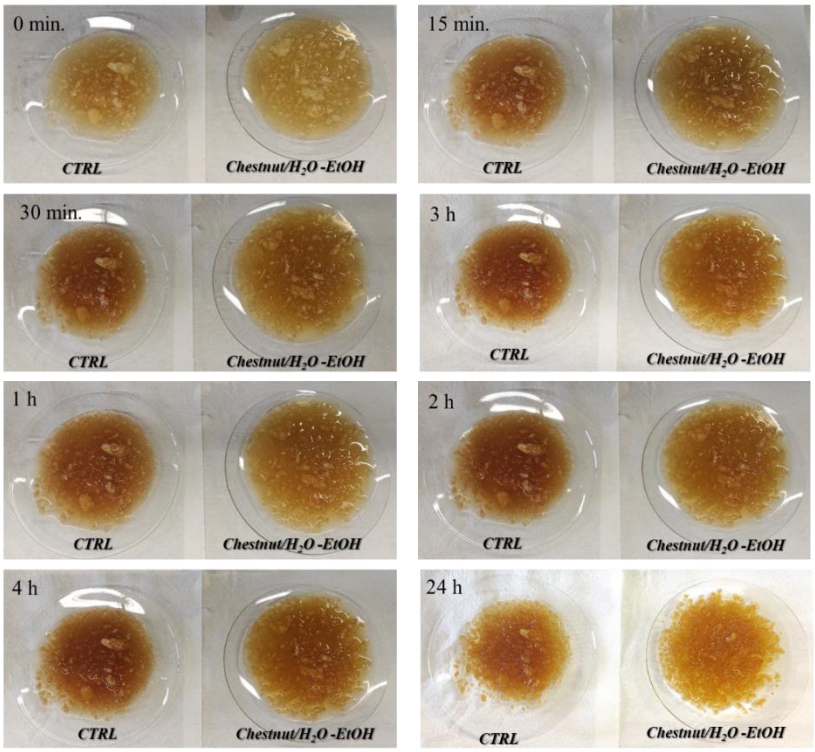

Figure 3.3. Effect of Chestnut/H_2O-EtOH extract on the apples fruit browning process at different time.

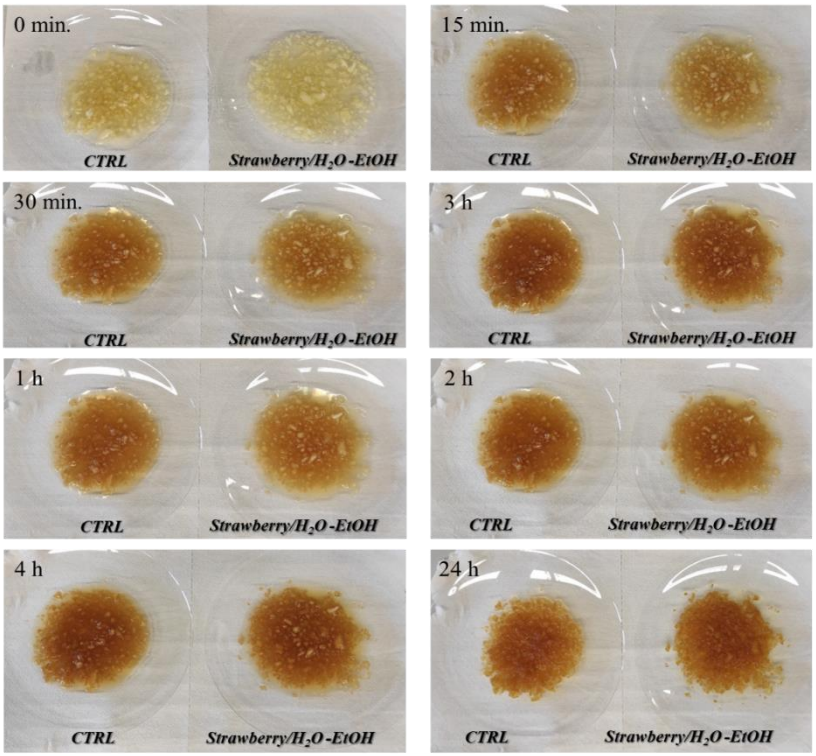

Figure 3.4. Effect of Strawberry/H_2O-EtOH extract on the apples fruit browning process at different time.

In the case of these extracts, a colorimetric analysis was also performed (Table 3.5). The colorimeter is a tool that quantify colours according to international standards. The L*a*b* colour space (CIELAB) is currently one of the most popular colour spaces, measuring the colour of an object. In this colour space, L* indicates brightness while a* and b* are chromaticity coordinates: +a* is red direction, -a* is green direction, +b* is yellow direction, and -b * is the direction of blue. For the evaluation of the colour changes of apple smoothies over time, the browning index (BI) was calculated, considering all three factors of the CIELAB space (L*a*b*):

$$Browning\ Index\ (B.I) = \frac{[100(x - 0.31)]}{0.17}$$

$$X = \frac{(a^* + 1.75\ L^*)}{(5.645\ L^* + a^* - 3.012 b^*)}$$

In particular, the colorimetric analysis up to 3 hours was carried out every 30 minutes. This analysis confirmed the retarding effect on the enzymatic browning process of the selected extracts. In the case of the strawberry extract in the first 30 minutes the results were comparable to that observed for kojic acid or ascorbic acid and so particularly encouraging, though this effect immediately disappeared in the following times. In contrast, extracts from pomegranate and especially chestnut shells showed a significant effect up to 60 min with respect to the control experiment.

Table 3.5. BI values calculated for apple smoothies treated or not with selected extracts, kojic acid or ascorbic acid. Mean values + SD (≤ 10) from at least three separate experiments are reported.

Samples	t_{0min}	t_{30min}	t_{60min}	t_{90min}	t_{120min}	t_{150min}	t_{180min}
CTRL (w/o additive)	7.08	14.86	12.54	12.67	9.44	9.4	9.41
Residues from fermented pomegranate by-products DMSO	3.15	12.34	7.08	10.67	8.77	12.93	12.51
Chestnut shells H_2O/EtOH	3.12	9.47	6.4	7.11	9.61	5.86	10.07
Sludges from strawberry spirit production in H_2O/EtOH	3.25	1.94	10.61	13.96	17.12	14.35	14.73
Kojic acid	0.78	3.33	1.38	3.31	1.71	1.36	1.91
Ascorbic acid	0.77	1.54	1.24	1.86	1.62	1.46	1.79

Main Outcomes Of The Study:

- Extracts containing phenol compounds prepared by a green procedure from agri-food by-products showed remarkable inhibition activities in model enzymatic inhibition assays.
  - Chestnut shells, *Morus alba* and pecan nutshells extracts, showed IC_{50} values against tyrosinase higher or comparable with respect to the value determined for the reference compound kojic acid.
  - Strawberry, pomegranate and especially chestnut shells extracts were able to retard significantly the enzymatic browning process of apples smoothies.

3.2 Preparation of 2-S-lipoylcaffeic acid butanamide

3.2.1 Synthesis of the amide derivative of coumaric acid

Following a previously described protocol for caffeic acid and its corresponding methyl ester, the synthesis of the conjugate of caffeic amide derivative with dihydrolipoic acid (DHLA) was carried out (Figure 3.5).

A strategy based on the generation of the *o*-quinone of caffeic acid from *p*-coumaric acid, followed by in situ addition of DHLA was adopted.

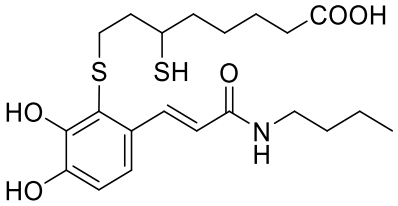

Figure 3.5. 2-S-lipoylcaffeic acid butanamide.

Firstly, the synthesis of *p*-coumaric acid butanamide was performed. Based on a procedure previously described (paragraph 2.3), the amidation reaction of *p*-coumaric acid using HATU as coupling agent was carried out. In addition, also in this case the preliminary protection of the OH functionality with an acetyl group turned out to be crucial. The total synthesis is represented in Figure 3.6.

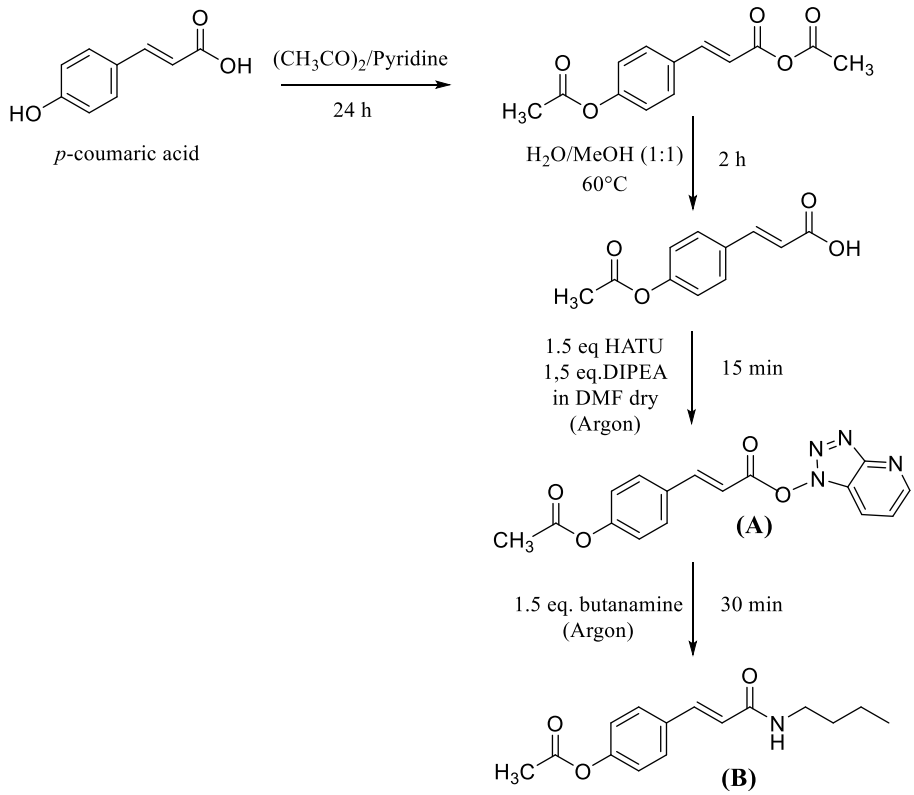

Figure 3.6. Synthetic route to the butanamide derivative of acetylated coumaric acid.

The reaction was monitored by HPLC analysis. After 15 minutes, (panel a Figure 3.7), a peak at 12.8 minutes attributable to the adduct (**A**) was observed, together with the concomitant disappearance of the peak of acetylated coumaric acid (R_t = 6.3 min) and of HATU (R_t = 4.5 min). Subsequently, to the reaction mixture, 1.5 eqs. of butanamine were added. After 30 min, the decrease in intensity of the adduct (**A**) was observed and two peaks at 3.8 and 10.5 minutes, presumably due to the N-oxide of HATU and butanamide of acetylated *p*-coumaric acid **(B)** respectively, were detected. Then, after addition of water to the reaction mixture, separation of a white precipitate was obtained. The precipitate was recovered by filtration under vacuum and the compound

appeared as a single peak eluting at 10.4 minutes on HPLC analysis (panel c of Figure 3.7).

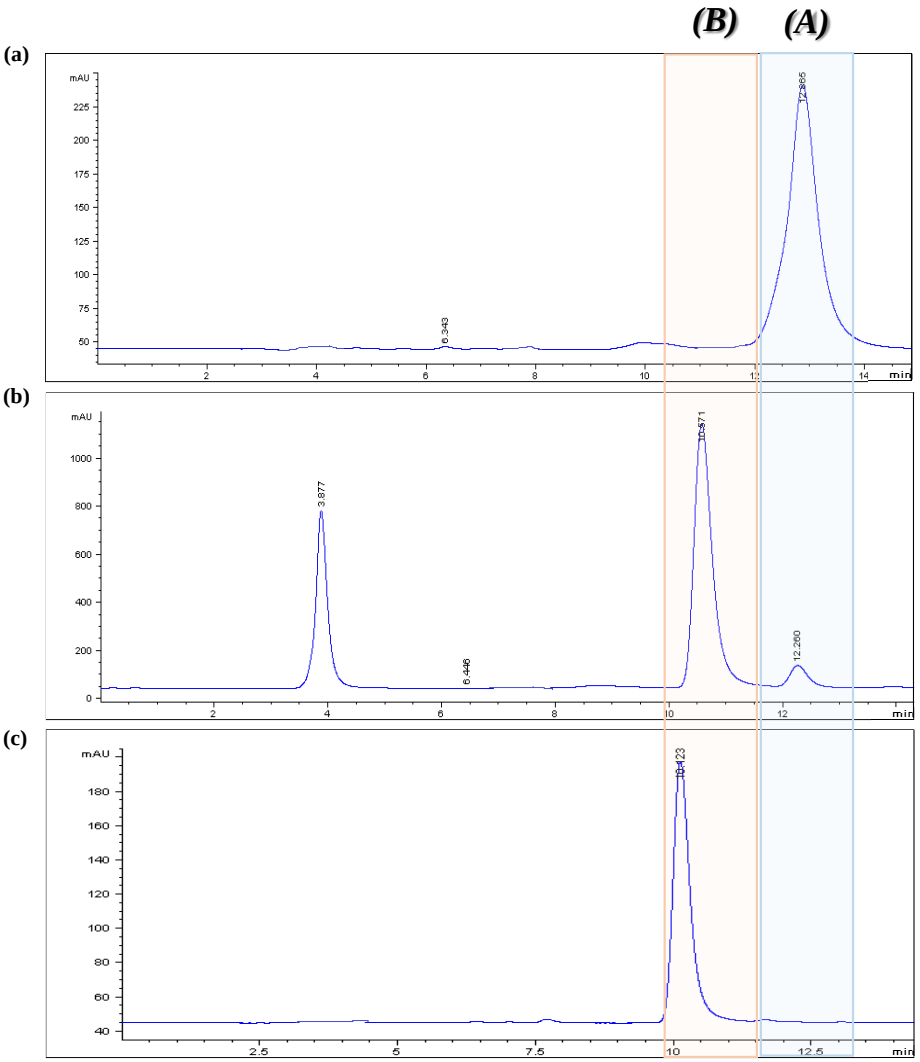

Figure 3.7. Elutographic profile of the amidation reaction of O-acetyl *p*-coumaric acid (a) 15 minutes after the addition of HATU; (b) 30 minutes after the addition of butanamine; (c) acetylated butanamide of *p*-coumaric acid after filtration.

The identity of the product was confirmed by ^{1}H-NMR analysis (Figure 3.8). The spectrum showed the signal at 8.07 ppm attributable to the amide NH and those of the aliphatic chain of the amide CH_2 at 3.16, 1.42, 1.30 and the CH_3 at 0.88 ppm.

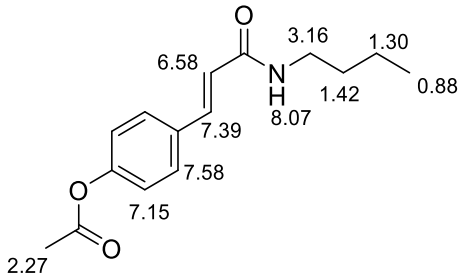

Figure 3.8. ^{1}H-NMR assignment of acetylated butanamide of *p*-coumaric acid (DMSO-d_6).

Removal of the acetyl group of the butanamide was carried out under vigorous flow of argon using methanol as solvent with the product at 3.6 mM in the presence of 8 eq. of sodium tert-butoxide for 15 minutes at room temperature. The reaction mixture was acidified using HCl 3M and extracted with ethyl acetate. To confirm the deacetylation of the phenol group, ^{1}H-NMR analysis was performed. The disappearance of the signal at 2.27 ppm attributed to the acetyl groups was observed, indicating a complete deprotection (Figure 3.9).

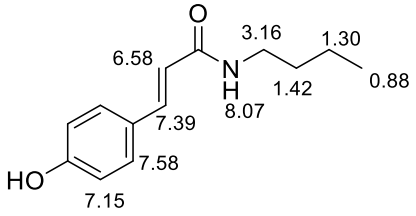

Figure 3.9. ^{1}H-NMR assignment of butanamide of *p*-coumaric acid (DMSO-d_6).

3.2.2 Synthesis of the 2-S-lipoylcaffeic acid butanamide

The *o*-quinone of caffeic acid was obtained by the regioselective hydroxylation of coumaric acid with 2-iodoxybenzoic acid (IBX) [239]. Based on the proposed mechanism of reaction of this reagent [240], the process involves the initial formation of an intermediate **C** arising by interaction of coumaric acid with IBX, with the elimination of water. Then this latter rearranges to **D** *via* oxygenation of the ortho-position of the phenolic group and concomitant reduction of the iodine from I(V) to I(III). Tautomerization of **D** produces the intermediate **E**, which decomposes into *o*-quinone and 2-iodobenzoic acid, whilst iodine (III) is reduced to iodine (I) (Figure 3.10).

IBX was synthesized by oxidizing 2-iodobenzoic acid with Oxone® in water at 70° C, as described before.

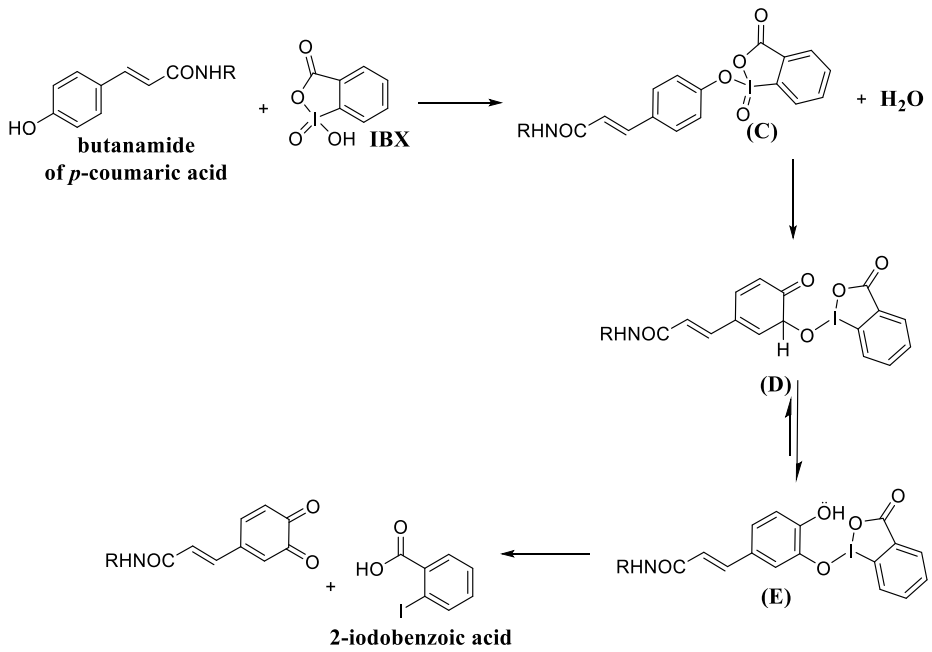

Figure 3.10. Proposed mechanism for the generation of *o*-quinone of caffeic acid.

According to a previously published procedure, DHLA was synthesized by reducing lipoic acid (LA) with sodium borohydride [241].

To an aqueous solution of a racemic LA (0.25 M) in 0.25 M $NaHCO_3$ and $NaBH_4$ (1.0 M) was added and taken under stirring for 2 hours at 0°C. Subsequently, the mixture was acidified to pH 1 and extracted with toluene (89%).

To a methanolic solution of *p*-coumaric acid (70 mM), solid IBX (1.5 eq.) was added at room temperature. After 4 minutes, 4 eq. of this latter were added drop by drop to promote nucleophilic addition and the formation of the desire product minimizing the side reaction of redox exchange between the *o*-quinone and DHLA yielding caffeic acid as a by-product (Figure 3.11) [242,243]. No traces of a possible adduct derived from addition onto the side chain were detected.

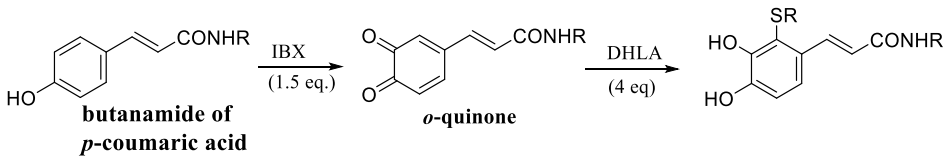

Figure 3.11. Reaction mechanism of butanamide of coumaric acid with IBX and DHLA.

To isolate the conjugate, the mixture was diluted with water, acidified to pH 1, then extracted with solvents of increasing polarity. A hexane/toluene (8:2, v/v) combination was used to remove 2-iodobenzoic acid, LA, and DHLA, while chloroform was used to extract the lipoylcaffeic adduct, which was isolated in 20% yield. Ethyl acetate extraction can be used to recover the more polar caffeic acid that has remained in solution (Figure 3.12).

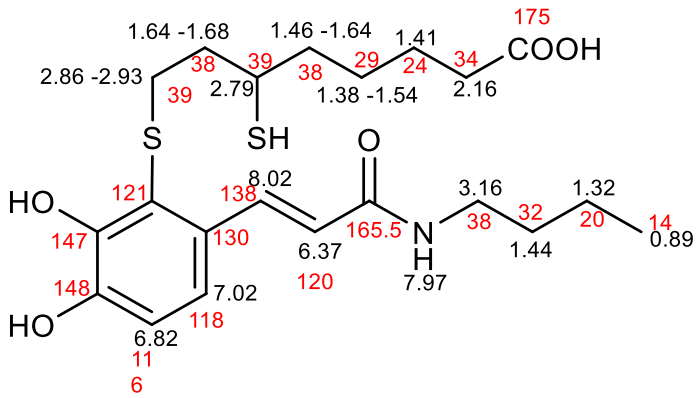

Figure 3.12. ^{1}H-NMR and ^{13}C-NMR assignment of 2-S-lipoylcaffeic acid butanamide (DMSO-d_6).

3.2.3 Inhibition of mushroom tyrosinase activity by 2-S-lipoylcaffeic acid butanamide

The tyrosinase inhibitory activity of 2-S-lipoylcaffeic acid butanamide was investigated using mushroom tyrosinase as described in the paragraph 3.1.1. The IC_{50} value obtained around 30.01 ± 0.08 μM was comparable or even lower respect to the other calculated for the lipoyl conjugate of the methyl ester of caffeic acid (8.6 ± 0.2 μM) or caffeic acid (53.7 ± 0.3 μM).

Main Outcomes Of The Study:

- ☐ The synthesis of a new derivative of caffeic acid, i.e. 2-S-lipoylcaffeic acid butanamide was developed.
  - Preliminary results show a good ability to inhibit tyrosinase, with IC IC_{50} values comparable to those reported in literature for similar compounds.

3.3 Experimental section

Materials and Methods. The distilled by-products were provided from the agrifood company Berolà (Portico di Caserta, Caserta, Italy), fermented pomegranate was obtained from Cuatrociénegas, Coahuila, México. Chestnut shells were provided from the agrifood industry Malerba (Montella, Avellino, Italy). All the other agri-food wastes were purchased at a local supermarket. *Morus Alba* was obtained from a local garden.

Mushroom tyrosinase (EC 1.14.18.1), L-3,4-dihydroxyphenylalanine (L-DOPA), L-tyrosine, kojic acid, ascorbic acid, 2-iodobenzoic acid, oxone®, lipoic acid (LA), sodium borohydride, sodium dithionite were purchased from Sigma-Aldrich. Coumaric acid (CA) was purchased by Fluka. All solvents were HPLC grade. Bidistilled deionized water was used throughout the study.

All solvents and reagents were obtained from commercial sources and used without further purification.

Uv-Vis spectra were recorded on V-730 UV-visible spectrophotometer.

^{1}H and ^{13}C NMR spectra were recorded at 400 MHz and 100 MHz, respectively, on a 400 Bruker spectrometer.

HPLC analyses were performed on a Agilent 1100 binary pump instrument equipped UV-visible detector using an octadecylsilane-coated column, 250 mm x 4.6 mm, 5 μm particle size (Phenomenex Sphereclone ODS) at 0.7 mL/min, Eluent system: 0.1% formic acid (solvent A)/methanol (solvent B) in ratio 40:60 respectively. Detection wavelength was set at 300 nm.

Preparation of extracts from the selected agri-food by- products. Firstly, all the agri-food by-products were roughly ground using a common blender. Subsequently, they were pulverized with the aid of a ball mill (50 oscillations/min for 15 minutes). In the case of leaves and branches of Morus Alba, onions, tomatoes a preliminary step of lyophilization was necessary.

300 mg of each agri-food by-products were added to 2 mL of one of the selected solvents (water, ethanol, water/ethanol 4:6 v/v or DMSO). The mixture was then

stirred at room temperature for 90 minutes, and centrifuged (5000 rpm for 10 min) at 20°C. The supernatants were then recovered, while the residual solids were lyophilized. The residual solid obtained with DMSO was washed two times with water.

Synthesis of 2-iodoxybenzoic acid (IBX). 37.2 g of Oxone® were dissolved in 200 mL of bidistilled water. To this solution, 5.0 g of 2-iodobenzoic acid were added and the resulting mixture was taken under stirring at 70°C for 1 h. Subsequently, the solution was cooled at 4°C for 30 min, filtered and washed with cold water (6 x 300 mL) and acetone (2x30 mL), recovering a white solid in yield around 55%.

Preparation of DHLA (6,8-dimercaptoottanoic acid). 1.0 g of lipoic acid was dissolved in 20.0 mL of an aqueous solution of $NaHCO_3$ (0.25 M). To this solution, 740.0 mg of $NaBH_4$ (in two portions) were added and the mixture was taken under stirring at 0 °C for 2 h. Then, the reaction mixture was acidified until pH 1 with HCl 6 M and extracted with toluene (5x20 mL) (89% yield).

Synthesis of butanamide of acetylated *p*-coumaric acid. 3.5 mL of acetic anhydride and 175 µL pyridine were added to 300 mg of *p*-coumaric acid. After 24h, the compound was dried using a rotary evaporator and stirred under reflux in a water/methanol 1:1 v/v solution at 60°C for 2 hours. The product thus obtained was dried and a white powder was obtained with yields of (98%). A mixture of acetylated *p*-coumaric acid (281 mg), HATU (1.5 eq., 759 mg) and DIPEA (2 eq, 474.5 µL) in anhydrous DMF (5.62 mL) was stirred under inert atmosphere for 15 min. To the resulting mixture, 1.5 eqs. of butanamine (202 µL) were added and stirred for 30 min at 25°C. The mixture thus obtained was treated with distilled water. The obtained precipitate was filtered through a buckner and washed with distilled water. The solid was then obtained in 45% yields.

^{1}H-NMR (DMSO-d_6): δ (ppm): 0.89 (t, 3H), 1.30 (m, 2H), 1.42 (m, 2H), 3.16 (m, 2H), 8.07 (t, 1H), 6.58 (d, J = 16 Hz ,1H), 7.39 (d, 1H), 7.58 (d, J = 8 Hz, 2H), 7.15 (d, 2H), 2.27 (s, 3H).

Synthesis of deacetylated butanamide of *p*-coumaric acid. The deprotection of *p*-coumaric acid butanamide was carried out, dissolving 314 mg (1.2 mmol) of this compound in methanol (3.6 mM). Subsequently, to the resulting mixture 864 mg (8 eq. in moles) of sodium tert-butoxide under an inert atmosphere were added and stirred for 15 minutes. The solution was bought to pH 3 slowly adding HCl 3M and dried using a rotatory evaporator. Then extracted with water at pH 3 and ethyl acetate (100 mL) 3 times. A yellow oil was obtained in a good yield (85%).

^{1}H-NMR (DMSO-d_6): δ (ppm): 0.89 (t, 3H), 1.31 (m, 2H), 1.52 (m, 2H), 3.18 (m, 2H), 8.21 (t, 1H), 6.46 (d, J = 16 Hz ,1H), 7.37 (d, 1H), 7.25 (d, J = 8 Hz, 2H), 6.65 (d, 2H).

Synthesis of 2-S-lipoylcaffeic acid butanamide. To 90 mg of *p*-coumaric acid butanamide (0.9 mmol), dissolved in 5.4 mL of methanol, 176 mg of IBX (1.38 mmol) were added. The solution was kept under magnetic stirring at room temperature for 7 minutes, then added dropwise to a solution of DHLA (342 mg, 3.6 mmol) in 5.4 mL of methanol and stirred for further 15 minutes. To the resulting mixture, acid water (pH 1) was added, then extracted with hexane-toluene 8:2 v/v (5×50 mL), and subsequently with chloroform $CHCl_3$ (3×50 mL). The combined organic extracts were dried using a rotatory evaporator (yield of 20%).

^{1}H-NMR (DMSO-d_6): δ (ppm): 2.16 (t, 2H), 1.41 (m, 2H), 1.38 (m, 1H), 1.54 (m, 1H), 1.46 (m, 1H), 1.64 (m, 1H), 2.79 (m, 1H), 1.64 (m, 1H), 1.68 (m, 1H), 2.86 (t, 1H), 2.93 (t, 1H), 0.89 (t, 3H), 1.32 (m, 2H), 1.44 (m, 2H), 3.16 (m, 2H),

7.97 (t, 1H), 6.37 (d, J = 16 Hz, 1H), 8.02 (d, 1H), 7.02 (d, J = 8 Hz, 1H), 6.82 (d, 1H).

^{13}C-NMR (DMSO-d_6): δ (ppm): 175 (C), 34 (CH_2), 24 (CH_2), 29 (CH_2), 38 (CH_2), 38 (CH_2), 39 (CH_2), 39 (CH), 118 (CH), 116 (CH), 120 (CH), 121 (C), 130 (C), 138 (CH), 148 (C), 147 (C), 165.5 (C), 38 (CH_2), 32 (CH_2), 20 (CH_2), 14 (CH_3).

Tyrosinase inhibition assay. The following solutions were used for the assay:

- mushroom tyrosinase (20 U/mL); the stock solution was prepared by dissolving 1 mg in 1 mL of 50 mM phosphate buffer (pH 6.8);
- 100 mM solution of L-DOPA dissolved in 0.6 M HCl (1 mM);
- 100 mM solution of L-TYROSINE dissolved in 0.6 M HCl (1 mM).

Stock solutions of the various samples incubated with mushroom tyrosinase (20 U/mL) in 2 mL of 50 mM phosphate buffer at room temperature (pH 6.8). After 10 minutes, 20 μL of a 100 mM solution of L-DOPA in 0.6 M HCl (final concentration 1 mM) were added, and the reaction was monitored by measuring the absorbance at 475 nm every 10 minutes. The reaction was carried out in the absence of the sample or in the presence of kojic acid as a positive control in control studies. The extracts were added 10 minutes after the tyrosinase, followed immediately by the L-DOPA. The same procedure was performed for the experiment with L-TYROSINE.

Apple smoothie browning inhibition assay. Red Delicious apples were rapidly cut in small pieces after removing the peel, and ca. 50 g were finely blended with a domestic mixer in the presence of a 0.1% w/w (extract solution/bidistilled water) and transferred on a watch glass. Blank smoothie samples were prepared in the absence of extracts. Chroma Meter CR-400/410 (Konica Minolta) colorimeter was used to analyze changes in color. The browning index (BI) (three different measurements were taken during the same experiments and three different experiments were performed) was calculated as follows:

$$Browning\ index\ (BI) = \frac{100(\mathrm{x} - 0.31)}{0.17}$$

$$x = \frac{\alpha * +1.75\mathrm{L} *}{5.645L * + \alpha * -3.012b *}$$

Kojic acid and ascorbic acid were used as reference compounds.

Chapter 4

Mussel inspired bioadhesives from waste proteins and plant derived phenolic compounds for biomedical applications

The search of bioadhesives for soft tissue healing is now an active issue in the scientific committee. Many kind of materials, primarily hydrogels, have been explored in literature [244]. Among the many requirements that these materials must satisfy, a top position is occupied by biocompatibility, which can be combined with antibacterial activity to boost their potential in wound healing applications. Furthermore, tissue adhesives should have great mechanical characteristics under physiologically relevant conditions and among this underwater resistance still represents a major problem in the design of these materials. In this regard, the adhesion mechanism of some marine organisms is a great source of inspiration [245]. The exceptional wet adhesion capabilities of mussel byssus foot proteins originate from interaction of the catechol system of the abundant 3,4-dihydoxyphenylalanine (DOPA) residues with lysine amino groups, giving rise to cross-linked networks endowed with excellent underwater resistance. On this basis synthetic mussel-inspired materials with water-resistant adhesion and cohesion properties have been developed by modifying polymer systems with DOPA or using its analogue dopamine that combines the catechol and amino functionality [57,246,247].

Examples in the literature are countless so as the combinations of dopamine with different biopolymers and natural macromolecules. Cross-linking Al^{3+}-coordinated alginate-dopamine chains with acrylamide-acrylic acid polymers produced hydrogels with high mechanical characteristics and strong fibroblast

cell adhesion [248]. Dopamine catechol moieties conjugated to natural anionic poly(-glutamic acid) and cross-linked through horseradish peroxidase/hydrogen peroxide oxidation, with an additional physical cross-linking with a synthetic bioactive nanosilica, demonstrated strong adhesiveness to various tissue layers and excellent hemostatic properties [249].

Concerns of potential neurological effects entailed by the use of dopamine in the mussel-inspired strategy was overcome by use of alternative phenolic compounds. Tannic acid oxidative coupling with nucleophilic residues of animal gelatin resulted in low-cost and easily scalable water-resistant plant-inspired bioadhesives [250]. Similarly, a plant catechol-based glue was created by starting radical polymerization of acrylic acid and relying on the redox properties of lignin nanoparticles to form a pectin-polyacrylic acid hydrogel network [251,252].

In addition to polysaccharides and synthetic polymers, proteins from readily available sources have been investigated [253]. Soy proteins isolates (SPI) the main industrial waste in soybean processing, appears to be an ideal candidate for the implementation of environmentally friendly bioadhesives because they are cost-effective, easy to handle, and have been considered as alternative aldehyde-free materials also in the wood industry [254,255]. Furthermore, these proteins are high in amino groups, with lysine concentration reaching up to 6% [256]. Despite this, SPI-based hydrogels have few uses due to their low water resistance, time-consuming gelation process, and poor mechanical characteristics. Chemical cross-linking modification is the most effective way to improve the performance of soy proteins, and it can be done with either synthetic or natural compounds that have been covalently linked to the protein scaffold. [257–262]. Cross-linking based on polyphenol oxidation chemistry has also been used to create high performance materials employing tannic acid [263], modified tannins [264], lignins [265], or other phenolic polymers [263].

However, the use of SPI as a starting material for the creation of hydrogels with acceptable characteristics for tissue healing has thus far received little attention. Based on these findings, the research activity was directed to the preparation of hydrogels from SPI and plant derived polyphenols using mild conditions. Another type of proteins such as whey proteins able to give hydrogels in the presence of natural extracts from agri-food wastes was also evaluated.

Results and Discussion

4.1 Bio adhesives from soy proteins and plant derived polyphenols

4.1.1 Preparation of SPI/polyphenols hydrogels

Firstly, our attention was devoted to the optimization of the procedure for the preparation of hydrogels based on SPI/polyphenols. In previous research the use of SPI for adhesive preparation in presence of a denaturing agent such as urea and guanidine was shown to significantly increase the mechanical characteristics of the final materials [266]. In the current investigation, preliminary results evidenced that protein denaturation represents a key step for the adhesive preparation. In fact, to interact with additives or cross linkers, the exposure of aminoacidic residues, notably lysine amino groups, to the medium is essential. The interaction of aminoacidic residues with polyphenols and their oxidation products could significantly affect the characteristics of SPI. To minimize oxidative breakdown of the polyphenols and their oxidation products, as well as to make the hydrogel production conditions compatible with their usage in tissue healing, harsh alkaline conditions were avoided. A systematic investigation of thermal denaturation conditions and the choice of appropriate SPI pre-treatment for the fabrication of SPI/polyphenols hydrogels was developed. Due to their availability and broad distribution in plant sources, caffeic acid (CA), chlorogenic acid (CGA), and gallic acid (GA), were selected as polyphenols to investigate. Briefly, SPI were dissolved in water (at 10% w/w) and incubated for 1 hour at 85 °C, the denaturation temperature of SPI. The polyphenol component was then added, and the final solution was stirred for 2 hours at 50°C and pH 9. Under these conditions the polyphenol component is expected to smoothly oxidize. Different polyphenols concentrations (range 10-30mM) were tried, indicating as the best option a concentration of 28 mM. During this

process, a hydrogel is produced, exhibiting a higher consistency than of SPI treated according to the same protocol but in absence of the polyphenols.

In the case of CGA, the formation of a brilliant green chromophore in the hydrogel provided a clear proof of SPI interactions with the polyphenol. Formation of benzacridine pigments featuring a green chromophore have previously been described from the oxidative coupling of caffeic acid esters including CGA in the presence of amines and/or amino groups of proteins [267] (Figure 4.1). On the other hand, aerial oxidation of CGA under the same conditions, produced a brown solution, indicating that the lysine residues of the protein were involved in the production of the green pigment. The optimized protocol was extended to the other polyphenols selected. In all cases the hydrogel was recovered by centrifugation of the final mixture to remove the supernatant. These latter were subjected to spectrophotometric analysis to assess the consumption of the starting polyphenol, which was found to be almost complete for all polyphenols.

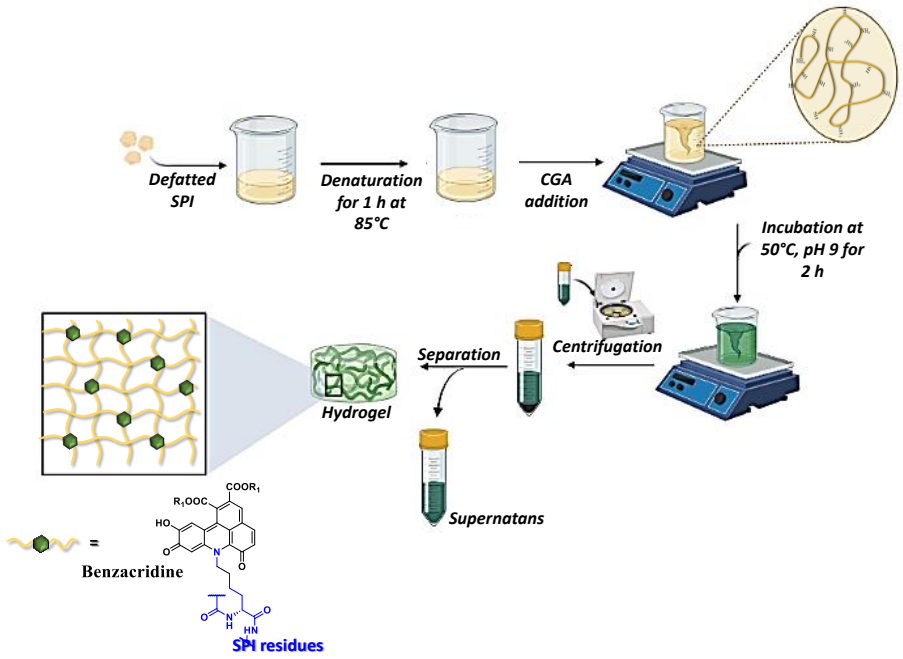

Figure 4.1. Schematic protocol for the preparation of SPI/polyphenols hydrogels exemplified for CGA.

4.1.2 Mechanical properties of SPI/polyphenols hydrogels

The application of the SPI/polyphenols hydrogels on wood specimens, pressed together with a clamp for 24 hours and dipped in water, allowed us to have a preliminary evaluation of the adhesive features of the produced hydrogels and their underwater resistance. They were periodically checked until the wood specimens detached.

The resistance of the glue from SPI/CGA was 22 days, a value significantly higher than the one of SPI but without additives (24 h). As shown in Table 4.1, SPI/CA and SPI/GA glues showed lesser resistance, with values of 9 and 5 days, respectively. Using an Instron testing equipment, the failure stress of the adhesive was evaluated by measuring the lap shear strength, which corresponds to the failing load divided by the bond area (4.0 cm^2). In Table 4.2, the results of

lap shear testing are reported. For comparison, SPI /Urea glue, known for its excellent performance, were also tested [266]. The stress values for the soy protein-based adhesive samples ranged from 2.1 (SPI/urea) to 3.2 (SPI/CA). The noticeable performance of SPI/CA is most likely due to the sample's considerably more compact structure, which revealed a homogenous and dense structure as shown by SEM studies (Figure 4.7 panel 3). A commercial vinyl-based glue was used as a control experiment under the same experimental conditions, showing a value of 4.0 Mpa, confirming the good adhesive performance of the SPI samples reported herein. In subsequent tests, the underwater resistance of the SPI/polyphenols glues was evaluated using chicken skin, defatted and washed repeatedly as previously described [23]. Unfortunately, the underwater resistance was found to be relatively weak in all samples tested, with values not reaching 30 minutes. On this basis, alternative experimental settings, more relevant to the possible use of the hydrogels as surgical glues were investigated. Slices of chicken breast muscle were bonded together with SPI/polyphenols hydrogels before being submerged in PBS. Table 4.2 shows the adhesive properties of SPI/polyphenols hydrogels. The best result was observed in the case of GA, although CGA also provided good resistance. The differences in the natural compositions of the adherends obviously accounts for the wet resistance test results, notably the performance of the SPI/polyphenols hydrogels was higher to SPI alone in all circumstances.

Table 4.1. Underwater resistance of wood specimens and chicken muscle slices glued with SPI or SPI/polyphenols. Shown are the mean of experiments in triplicate. SD±1

	Underwater resistance (days)			
Adherend	*SPI*	*SPI/CA*	*SPI/CGA*	*SPI/GA*
Wood specimens	1	9	22	5
Chicken muscle slices	1	2	7	15

Table 4.2. Lap shear strengths of single lap wood joints glued with SPI-polyphenols adhesive, and a reference *vinyl adhesive* and SPI/*urea*.

Sample	Lap shear strength (Mpa)
SPI/urea	2.07±0.70
SPI/CGA	2.16±0.41
Vinyl adhesive	4.02±0.83
SPI /CA	3.21±0.19
SPI/ GA	2.40±0.37

4.1.3 Characterization of SPI/polyphenols hydrogels

To get insight into the type of interaction of SPI with polyphenols, various characterisation approaches were executed. The percentage of SH and NH_2 groups in SPI after the reaction with polyphenols, were evaluated by traditional chemical assays based on the Ellman's reagent and the *o*-phtalaldehyde reaction, followed by spectrophotometric measurement. Figure 4.2 panel (a) reveals that SH groups play a key role in the SPI/polyphenols hydrogels, compared to SPI alone after denaturation. Based on a calibration curve with glutathione as reference thiol, the denatured SPI showed an SH content of 1.8% w/w. In terms of reacted amino groups, SPI/GA exhibited a higher involvement compared to SPI/CA and its ester SPI/CGA. The NH_2 group content of denatured SPI was

determined to be 3% w/w based on a calibration curve constructed with alpha *N*-BOC lysine as amino reference. For both tests, the contribution of the samples to the detection wavelength was appropriately considered. These findings indicate an involvement of SPI's amino and sulfhydryl groups in the interaction with polyphenols. MALDI MS analysis previously demonstrated the covalent binding of tannins including polyphenol moieties with amino groups of SPI [268]. ATR FT IR investigations on the glues as lyophilized powders suggested additional information about the interaction mode of the polyphenols with SPI. Due to the poor amount in the final hydrogels of polyphenols with respect to SPI, differential FTIR spectra were generated by subtracting the SPI spectrum from the SPI/polyphenols spectrum (panel b of Figure 4.2). Significant modifications were observed in the 3500-3000 cm^{-1} range (Band 2), especially above 3300 cm^{-1} (Band 1), indicating the involvement of SPI's amino groups in the interaction with polyphenols and their oxidation products [269].

Furthermore, a difference in the ratio of the bands at 1625 cm^{-1} (Band 3) and 1545 cm^{-1} (Band 4) compared to those observed for SPI alone, presumably indicates that bands due to C=O stretching of the carboxyl groups and the C=C stretching of the aromatic ring of the polyphenol components overlap and contribute to some extent to the dominating amide I and II band of the protein in the SPI/polyphenols materials. This finding is consistent with earlier studies revealing minor alterations in the SPI major bands as a result of physical/chemical crosslinking with caffeic acid [261].

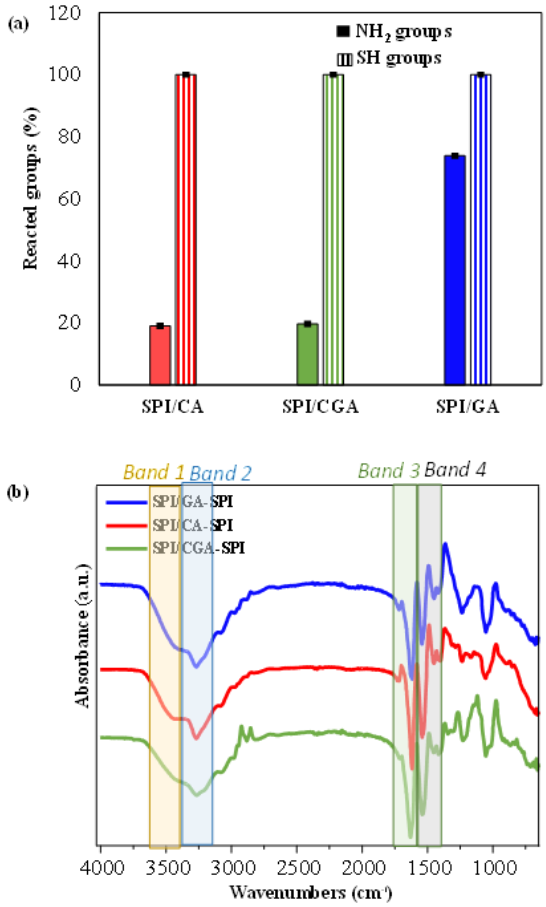

Figure 4.2. (a) Percentage of reacted SH and NH_2 groups of SPI/polyphenols with respect to SPI. Shown are means of at least triplicates ± SD; (b) Differential spectra obtained by subtracting SPI spectrum from those of the SPI/polyphenols samples.

EPR analysis was also performed on the SPI/polyphenols hydrogels. This is the ideal approach for identifying structural alterations in polymeric phenolic systems, as evidenced by the different types and amounts of radicals produced by quinone/catechol disproportionation [270]. An asymmetrical free-radical signal was discovered during preliminary investigation of denatured SPI (Figure 4.3 panel a). Similar findings have been reported in the literature and attributed to carbon-centered radicals produced in the dry protein during storage and

trapped in the solid matrix [271,272]. Figure 4.3 compares spectra obtained from SPI/polyphenols reactions (full lines) to those obtained from oxidative polymerization of polyphenols alone under same circumstances (in air, pH 9, 50°C, dotted lines). All spectra have a similar lineshape, i.e. a singlet at a slightly higher g-factor value than that observed for the denatured soy proteins (Table 4.3), suggesting the contribution of heteroatoms to the molecular orbitals in which the free electrons are delocalized. The lineshapes are in the middle of the lorentzian and gaussian derivatives. A lorentzian lineshape is produced by the presence of a single population of equal radicals, whereas a gaussian lineshape is produced by signal distribution convolution; thus, our results suggest that an ensemble of similar, but not completely equal, radical species contribute to the observed signal.

Table 4.3. EPR spectral parameters of SPI and SPI/polyphenols. Data for the materials obtained by oxidation of polyphenols at pH 9 in air in the absence of SPI (polyphenol polymers) are shown for comparison.

Samples	Spin density/g^{-1}	ΔB/G (± 0.2)	Gaussian contribution	g-factor (± 0.0003)
SPI/CGA	2.1×10^{17}	5.4	0.74	2.0040
CGA	2.7×10^{17}	3.9	0.72	2.0040
SPI/GA	9.8×10^{15}	6.7	0.35	2.0046
GA	1.9×10^{15}	3.0	0.49	2.0045
SPI/CA	3.1×10^{16}	6.2	0.72	2.0039
CA	1.0×10^{18}	6.1	0.64	2.0049
SPI	3.4×10^{15}	5.5	-	2.0027

In the case of CA, both in the presence and absence of soy proteins, a nearly symmetric, wide signal is detected. The spin density of both samples is greater than that of soy proteins. The drop in spin density reported for the SPI/CA sample when compared to the CA polymer generally reflects the quantity of CA-derived components present in the final material, which is around 1%. The predominant gaussian line form indicates that the radical centers are polydisperse as well as not affected by the presence of the protein.

The polymer derived from GA has a narrow symmetric line with a lorentzian lineshape that suggests a relatively limited dispersity of resonant radical origin. The GA polymer has a limited ability to stabilize radicals (note the low spin density). The asymmetric line observed in the SPI/GA clearly illustrates the superposition of signals from the protein and the GA polymer, which also explains the enhanced signal broadness, as measured by the peak-to-peak distance in G. The spin density is of the same order of magnitude as that measured for the protein in both samples.

In the case of CGA, both the CGA polymer and the SPI/CGA exhibit almost symmetric signals. The spin density of the CGA polymer is comparable to that of other polyphenol polymers [270] and, significantly, stays unchanged in the SPI/CGA hydrogel despite the final material containing around 1% w/w CGA generated species. The considerable rise in broadness (B from 3.9 to 5.4 G going from the CGA polymer to the SPI/CGA) in this example cannot be attributed to the weak protein signal superposition. As a result, our findings suggest that the interaction of CGA oxidation products with protein results in species with a strong radical character. The predominant gaussian line form in both samples suggests a polydispersity of the radical center type.

Overall, the presence of SPI alters the EPR spectroscopic parameters of all polyphenols, revealing some interactions between the proteins and the oxidative polymerization products. The different effects observed depending on the considered polyphenol suggest that different interactions can take place.

The microstructure of the SPI/polyphenols hydrogels was investigated by SEM analysis. In order to perform the SEM images, the hydrogels were air-dried. It should be considered that slight modifications of the structure can occur after the drying process.

The pristine SPI gel (Figure 4.3 panel 1) has a loose structure with large and irregular macroporosity and pore sizes ranging from 20 to 150 micron, indicating poor protein-molecule connection in the gel. The gels formed from SPI with CGA or GA (Figure 4.3 panel 2,3) retain the substantial presence of macropores with diameters equivalent to those reported in pure SPI, but a more irregular and corrugated morphology is evident, with many creases on the sample surface walls. The SPI/CA gel, on the other hand, has a distinct microstructure (Figure 4.3 panel 4). SPI/CA had a more compact morphology than other samples, with just a few macropores on the sample surface, showing that CA can promote the production of a more uniform and dense protein gel structure. This property might explain why the SPI/CA hydrogel performed effectively as glue in the adhesive experiments mentioned in Section 4.1.2.

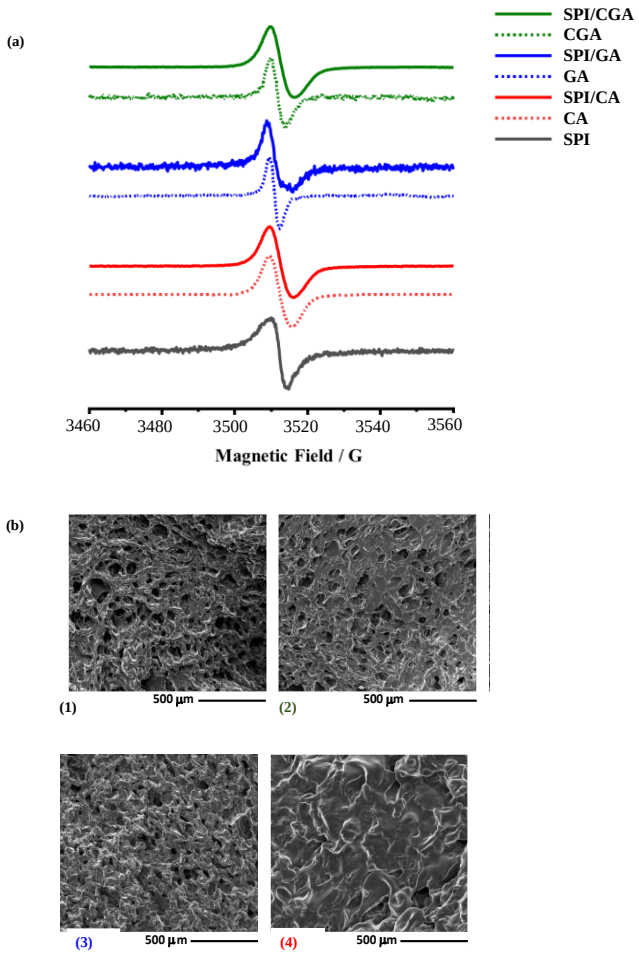

Figure 4.3 (a) EPR spectra of SPI and SPI/polyphenols. Data for the materials obtained by oxidation of polyphenols at pH 9 in air in the absence of SPI (polyphenol polymers) are shown for comparison; (b) SEM images of SPI (panel 1), SPI/CGA (panel 2), SPI/GA (panel 3), SPI/CA (panel 4).

4.1.4 SPI/agarose/polyphenols hydrogels

Encouraged by the features of the SPI/polyphenols hydrogels, the possible applications of these materials in wound treatment were evaluated. To achieve this goal, several additives and reaction conditions for imparting resilience,

stretchability, and toughness to the materials were studied. Finally, an improved procedure with agarose as extra component was developed.

At 70 °C, an agarose/SPI gel was prepared using an agarose solution in water and thermally denatured SPI. The resultant hydrogel was dipped in a 10 mM water solution of the relevant polyphenol at pH 9 after cooling in a Petri dish. In the case of CGA, after 2 hours the resulting gel becomes green, suggesting that CGA may penetrate the hydrogel and interact with SPI, thus generating the benzacridine systems. The same procedure was then extended to the other polyphenols selected. Before evaluating their mechanical characteristics, all the hydrogels were air-dried and then rehydrated.

Under these conditions, the hydrogels have great toughness and stretchability. When compressed, the hydrogel reverted to its original cylindrical form. The mechanical characteristics of the hydrogel were apparently also quite good based on simple qualitative tests. Because of its high stretchability and compressive performance, the hydrogel could be applied to human joints with varying degrees of bending without causing any discomfort to those who volunteered for these studies. Figure 4.4 depicts these features for a typical SPI/agarose/CGA hydrogel.

The hydrogels demonstrated long-term and reproducible adhesion to a variety of hydrophilic and hydrophobic surfaces, including glass, steel, polypropylene, and polycarbonate (Figure 4.4). Furthermore, remarkable adhesive properties on the skin were discovered. Remarkably, the hydrogel adhering to the skin did not cause anaphylactic responses. Furthermore, the hydrogel can be removed without leaving any residues. Even after 25 peeling/adhering cycles, the hydrogel retained strong adherence. The adhesiveness to glass, as well as to chicken and human skin, even under unfavorable conditions such as underwater was maintained.

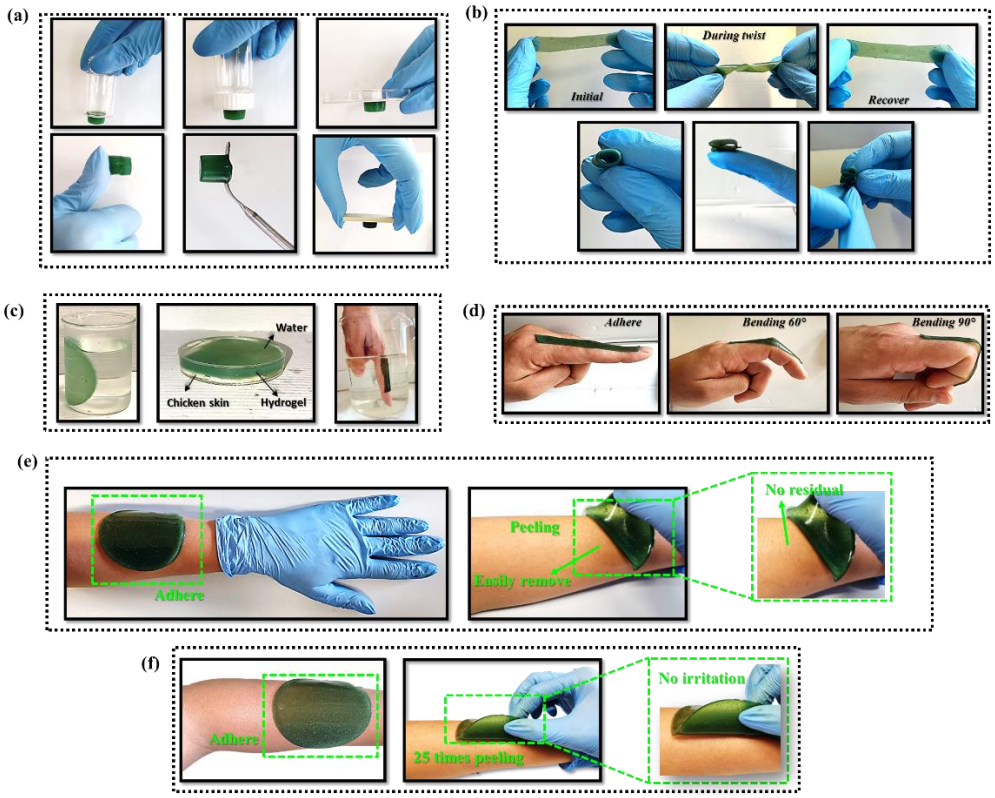

Figure 4.4. Macroscopic demonstration of the physical properties and repeated adhesion properties of the SPI/agarose/CGA hydrogel: (a) Adhesion of the hydrogel to various materials (b) Mechanical performance of the hydrogel: bending and crossover stretching. The hydrogel quickly returned to its original shape after removing the twisting force; (c) Underwater resistance of SPI/agarose/CGA hydrogels to glass, chicken skin, human finger. (d) The hydrogel tightly adhered to a human finger and accommodated its movements; (e) The hydrogel exhibited no residue after being peeled from arm skin and (f) The hydrogel was repeatedly adhered to human skin showing no irritation.

The water vapor permeability (WVP) of the air-dried SPI/agarose/polyphenol hydrogels was investigated, considering their prospective application as wound dressing devices.

In general, including an additive into a polymer hydrogel can change its characteristics by diminishing intermolecular contacts between the polymer chains or causing structural defects that raise the WVP of the hydrogels. According to the findings in Table 4.4, the inclusion of all polyphenols in the hydrogel formulations resulted in a one-order-of-magnitude improvement in water vapor permeability compared to SPI/agarose. This was most likely due to polyphenol molecules aggregating in the polymer matrix, resulting in a discontinuous structure of the hydrogels. WVP values achieved were almost two orders of magnitude higher than those reported for films manufactured from commodity polyolefins such as LDPE and HDPE.

Table 4.4. WVP results of the hydrogels.

Sample	WVP (g/m Pa s)
SPI/agarose	$5.13\pm0.27 \times 10^{-12}$
SPI/CA	$4.64\pm0.22 \times 10^{-11}$
SPI/GA	$3.88\pm0.18 \times 10^{-11}$
SPI/CGA	$4.99\pm0.22 \times 10^{-11}$

4.1.5 Cytocompatibility and wound healing properties

We investigated the cytotoxic effects of SPI/agarose/polyphenols hydrogels on human keratinocytes (HaCaT cells) and human dermal fibroblasts (HDF cells) to determine their therapeutic potential (Figure 4.5 a). Different concentrations of the SPI/agarose/polyphenols were tested. For all the samples, a slight toxicity was observed, although it appeared not statistically significant. In the case of SPI/CGA the low but appreciable toxicity cannot be attributed to the presence of benzacridines. In fact, as demonstrated on various cellular systems, these latter are not toxic [273] and they even proved able to support efficiently stem cell growth [274].

In another series of experiments, the ability of these hydrogels to promote the wound re-epithelialization by human keratinocytes (HaCaT cell line) was also investigated. To this aim, an in vitro wound healing test to assess the impact of hydrogels on cell migration was performed. HaCaT cell monolayers were wounded using a pipette tip. Cells were then rinsed with PBS and treated with various mixtures of SPI/polyphenol hydrogel components.

In Figure 4.5, images of a wound healing experiment performed on control cells and cells treated with SPI/polyphenol at t_0 and t_{24} hours of incubation are reported. As the most representative example CGA was chosen.

For the cells treated with each SPI/polyphenols system, the percentage of closure was calculated as the ratio of the defect area at the final time to the starting time, measured by Zen Lite 2.3 software. The values in Table 4.5 are the average of three experiments. According to Figure 4.5 and Table 4.5, SPI/CGA hydrogels significantly reduce the closure rate of the scratched region in human keratinocytes compared to untreated cells. On the contrary, no significant changes in wound healing rate were revealed in the case of the other SPI/ polyphenols hydrogels.

Table 4.5. The percentage of closure was expressed as the ratio of the areas at t_0 and t_{24} h evaluated using Zen Lite 2.3 software. *P < 0.05 was obtained for control versus treated samples.

Sample	Reduction of Area (fold)
CTRL	0.97 ± 0.03
SPI/CGA	1.35 ± 0.01*
SPI/CA	1.01 ± 0.03
SPI/GA	0.96 ± 0.04
SPI	0.77 ± 0.49

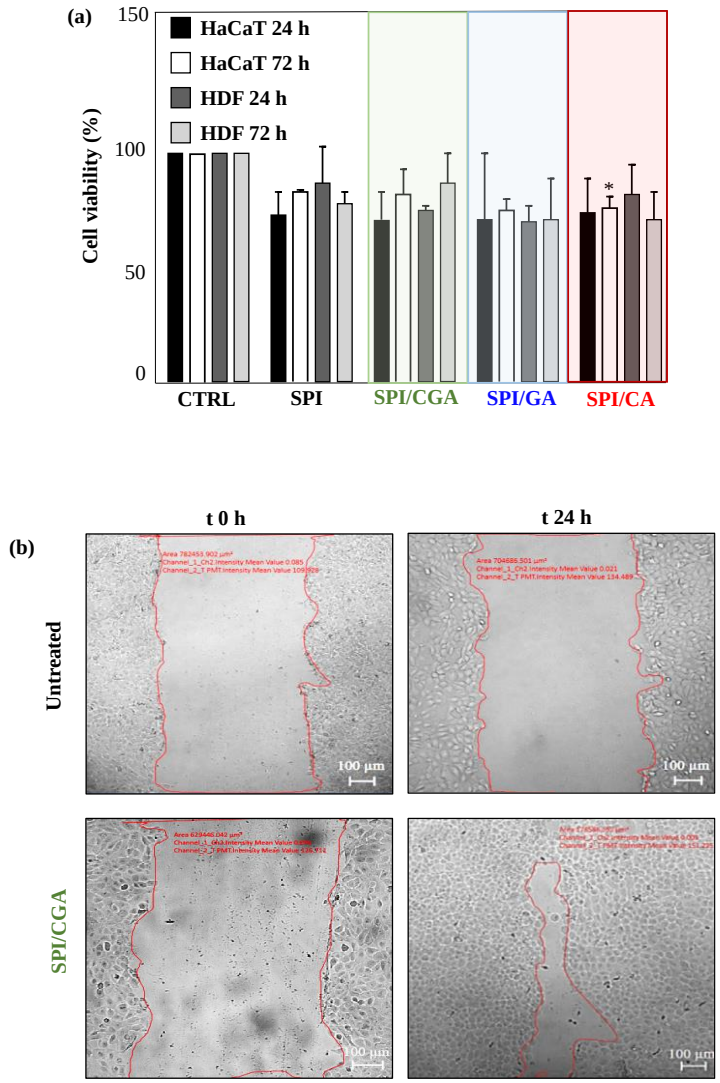

Figure 4.5. (a) Biocompatibility of SPI based hydrogels on HaCaT and HDF cells after 24 and 72 h of incubation. Cell viability was assessed by MTT assay and expressed as the percentage of viable cells with respect to controls (untreated cells). Error bars indicate standard deviations obtained from at least three independent experiments, each one carried out with triplicate determinations. (b) Wound healing activity of SPI-hydrogels on HaCaT cells monolayer. Cells were wounded prior to treatment with each compound for 24 h. Images were acquired at t_0 and t_{24} h of incubations.

4.1.6 Hemocompatibility

To assess blood behaviour in contact with the hydrogels, hemocompatibility experiments were carried out. TEG analysis includes four parameters: the reaction time, which is the time between the start of the test and the start of the coagulation process (physiologically values 3.8-9.8 min); the coagulation time (K), which measures the length of the coagulation process (physiologically values 0.7-3.4 min); the alpha angle, which represents the coagulation velocity (physiologically values 47.8-77.7 degrees); the maximum amplitude which describes the clot strength (physiologically values 49.7-72.7 mm). All hydrogels examined showed no effect on the physiological behaviour of the blood. In fact, all the parameters determined are within the normal range. Furthermore, there are no significant differences between the three hydrogels, indicating that the polyphenols don’t affect SPI's hemocompatibility. The blood clot formation test was used to confirm the results of the TEG study. The results obtained are in line with the previous one, showing no significant changes between SPI and SPI/polyphenols hydrogel. Blood coagulation on the various hydrogels also demonstrates that there are no major variations between the polyphenols (Figure 4.6).

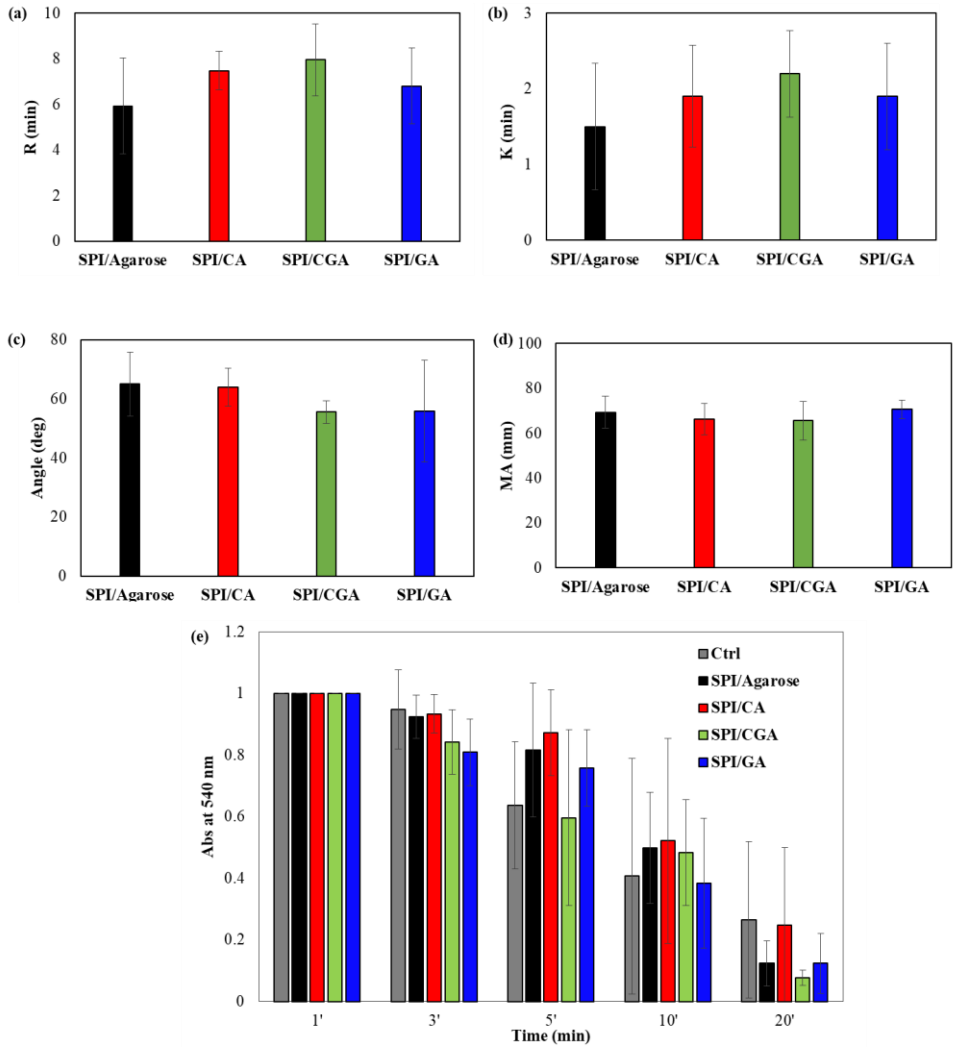

Figure 4.6. Coagulation Parameters: (a) Reaction time (R) (b) Coagulation time (K) (c) Coagulation velocity (alpha angle) (d) Clot strength (MA) (e) Clotting time of SPI with and without polyphenols.

SEM examination revealed inactive platelets, as well as white and red blood cells, in all samples. These results suggest that none of the hydrogels induce blood coagulation, confirming prior findings concerning the hydrogels' effect on

blood behaviour. Overall, for all samples, with or without polyphenols, optimum hemocompatibility was observed (Figure 4.7).

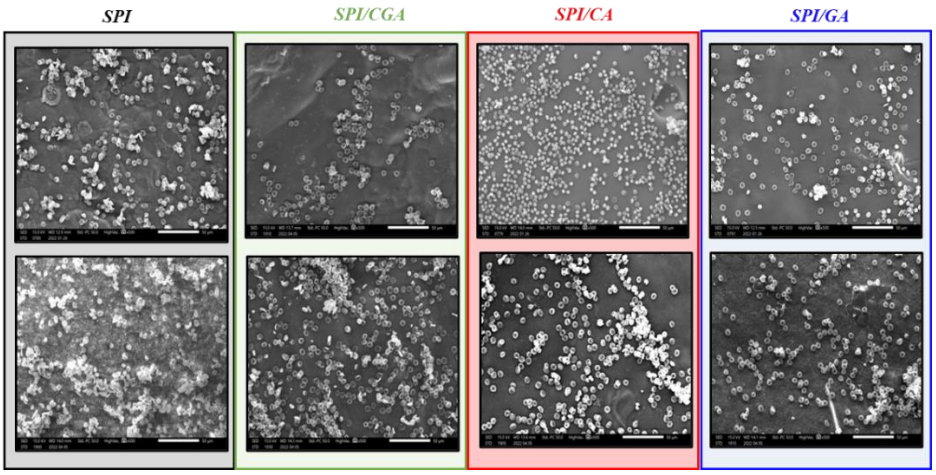

Figure 4.7. SEM of SPI with and without polyphenols in the hemocompatibility test.

4.1.7 Antibacterial evaluation

The antibacterial activity of air-dried SPI/agarose/polyphenols hydrogels against a panel of common pathogenic bacteria, including *Staphylococcus*, *Acinetobacter,* and *Pseudomonas* species, was investigated. The inhibitory halo on inoculated plates was used to test the efficacy of the SPI/Agarose-based hydrogels to suppress bacterial growth. As shown in Figure 4.8, all the hydrogels were capable of causing Gram-positive *Staphylococcus* species death, either on *S. aureus ATCC 12600*, *S. epidermidis ATCC 35984*, or clinically isolated *MRSA WKZ-2 strain*. Only the SPI/agarose/CA combination, on the other hand, was effective against the *Gram-negative A. baumannii ATCC 9606 strain*. To further study the antibacterial action, the percentage of bacterial growth in liquid medium in the presence or absence of the hydrogels was determined. In the presence of SPI/CA and SPI/GA hydrogels, bacterial growth was nearly completely suppressed in the case of *Staphylococcus* and

Acinetobacter baumannii strains (max. value 0.002048), and *S. epidermidis cells* were completely killed. Interestingly, all the hydrogels were able to considerably lower the survival of *Pseudomonas aeruginosa cells*, with the SPI/agarose/GA and SPI/agarose/CGA hydrogels reducing survival by more than 50%.

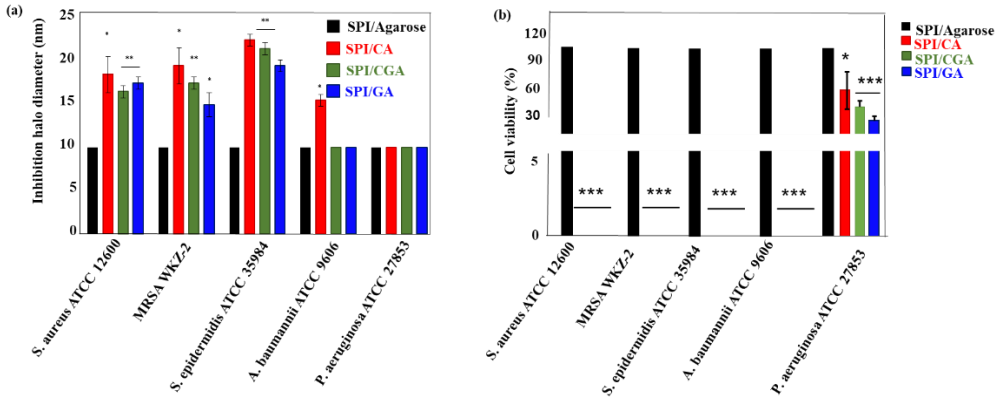

Figure 4.8. Antimicrobial activity of SPI/agarose-based hydrogels. Agar diffusion assays were performed and the diameter of zones of inhibition were calculated and reported for each sample (a). Experiments were also performed by determining the ability of samples to inhibit bacterial growth in liquid medium (c). Each graph refers to at least a biological duplicate and statistical analyses were performed by using Student's t-test. Significant differences were indicated as *P < 0.05, **P <0.01 or ***P < 0.001.

Main Outcomes Of The Study:

- Hydrogels were implemented by use of natural, easily accessible components, namely soy proteins, and plant-derived polyphenols,.
  - The hydrogels demonstrated remarkable adhesiveness and underwater resistance.
- The incorporation of agarose in the SPI/polyphenols hydrogel formulation allowed access to hydrogels with good toughness and long-lasting adhesiveness, bio/hemo-compatibility, marked contact-active antibacterial activities and, in some cases, wound healing activity.
- An insight into the nature of the interaction of the polyphenols with the protein is represented in the following Scheme 4.1.

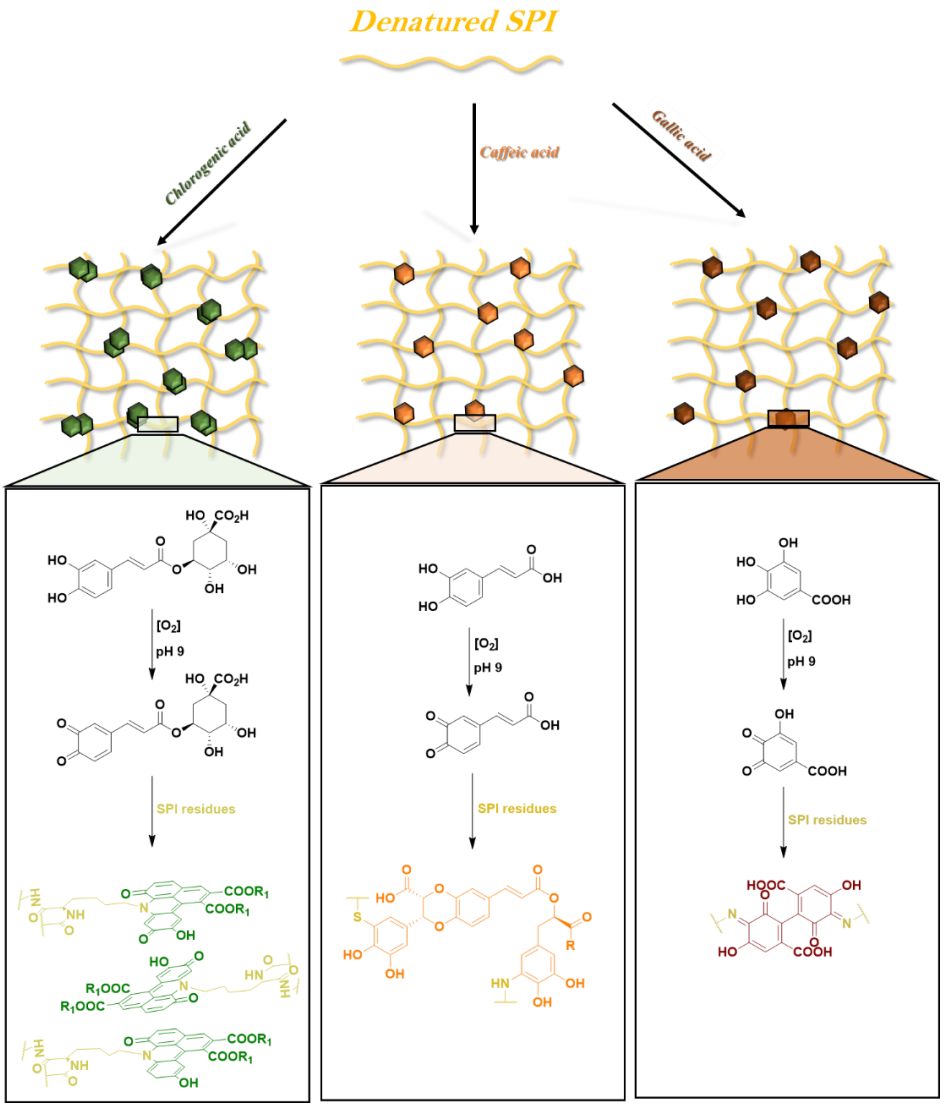

Scheme 4.1. Proposed mode of interaction of the polyphenols investigated with SPI in the hydrogel formation.

4.2 Bioadhesives from whey proteins and extracts from agri-food by-products

4.2.1 Preparation of WPI/polyphenols hydrogels

Due the interesting characteristics of SPI/polyphenols hydrogels, the adhesive properties of another type of protein, i.e. Whey Proteins Isolate (WPI), easily accessible as by-product of the dairy industry, were investigated. Previous studies have shown that a non-covalent modification of the WPI with polyphenols (gallic acid, chlorogenic acid and epigallocatechin gallate), is able to impart a series of advantages, such as greater solubility and emulsifying capacity [236].

On these bases, the possibility to open new perspectives and to increase the potential applications of WPI as surgical glues, combining these proteins with phenolic rich extracts from selected agri-food by-products was evaluated. The use of coupling agents or chemical additives was discarded since they are harmful to the environment and generally expensive, limiting their application on an industrial scale. Therefore, a green procedure, based on the use of biocompatible solvent and alkaline conditions, was followed.

Initially, our attention was devoted to the optimization of WPI denaturation. Several denaturing conditions such as pH and/or temperature were explored. The best conditions in terms of underwater resistance on wood specimens as described in paragraph 4.1.2 were then selected. Briefly, WPI were dissolved in water (at 10% w/w) and incubated for 30 min at pH 12, the WPI denaturation pH. Subsequently, the effect of the addition of green extracts from agri-food by-products to denatured WPI was evaluated. For this purpose, extracts of grape pomace, apple, orange and pomegranate peel and seeds, and *Ficus* leaves were selected based on the content of phenolic compounds presumably able to interact with denatured WPI (Table 4.6).

Table 4.6. Selected natural sources and corresponding phenolic compounds.

Natural Sources	**Phenolic compounds**
Grape Pomace	Gallic acid, ellagic acid, catechin
Orange	Hydroxycinnamic acids
Apple	Chlorogenic acid, caffeic acid
Pomegranate	Anthocyanins, flavonoids
Ficus leaves	Quercetin, luteolin

Subsequently, the extraction process from selected agri-food wastes was optimized. Firstly, the various by-products were roughly grinded using a blender, lyophilized and then homogeneously pulverized with the aid of a ball mill (15 min, 50 oscillations/s), ensuring a more efficient and reproducible extraction process. All the samples were then extracted in water (100 mg in 1 mL solid/liquid ratio), used as extraction solvent that can be directly added to denatured WPI. The mixtures were taken under stirring for 90 min at room temperature, then centrifuged for 10 min. The recovered supernatant of each extract (1mL) was directly added to the previously denatured proteins (500 mg in 5mL of H_2O), stirred for 24 h and centrifuged for 10 min. The precipitate thus obtained represents the WPI/polyphenols hydrogel.

4.2.2 Properties of WPI/polyphenols hydrogels

To have a preliminary evaluation of the adhesive properties of the prepared hydrogels and on their underwater resistance, the application of the WPI/polyphenols hydrogels on chicken breast muscle, pressed together with a clamp for 24 hours and dipped in PBS as described in paragraph 4.1.2, was evaluated. Table 4.7 shows the adhesive properties of WPI hydrogels in the presence or in absence of polyphenols. Surprisingly, WPI showed optimum underwater resistance up to 35 days. The results obtained from WPI in the presence of apple, grape pomace and *Ficus* leaves extracts are comparable to

WPI alone. On the contrary, in the case of pomegranate and orange extracts a slight and a significant decrease, respectively, was observed. The differences in the polyphenols compositions obviously accounts for the different results of the wet resistance test.

Table 4.7. Underwater resistance of chicken muscle slices glued with WPI or WPI/polyphenols in PBS. Shown are the mean of experiments in triplicate SD±1.

Samples	**Underwater resistance (days)**
WPI	≥35
WPI/apple extract	≥35
WPI/pomegranate extract	33
WPI/grape pomace extract	≥35
WPI/*Ficus* leaves	≥35
WPI/orange extract	**24**

Based on these results, the orange extract was discarded for further analysis. As shown in Table 4.8 although the addition of polyphenols does not affect the already excellent underwater resistance of WPI, they could confer additional characteristics to WPI hydrogels such and antioxidant properties.

Therefore, a further step of this work was devoted to the evaluation of the antioxidant properties using conventional chemical assays such as DPPH and FRAP. Firstly, the WPI/polyphenols hydrogels were lyophilized to warrant more reproducible results. In the case of DPPH assay it was not possible to evaluate the antioxidant activity due to the poor solubility of WPI/polyphenols in the ethanol medium, whereas in the case of FRAP assays interesting results were observed.

Table 4.8. Trolox eqs. of lyophilized WPI/polyphenols hydrogels. Reported are the mean ± SD values from at least three experiments.

Samples	mg Trolox /mg samples
WPI	0.002203 ± 0.000001
WPI/apple extract	0.0026 ± 0.0002
WPI/pomegranate extract	0.019 ± 0.002
WPI/grape pomace extract	0.037 ± 0.007
WPI/*Ficus* leaves	0.024 ± 0.003

As shown in Table 4.8, WPI/grape pomace, *Ficus* leaves and pomegranate extracts exhibited higher antioxidant properties respect to WPI alone, whereas in the case of WPI/apple no difference in terms of Trolox eqs. was observed. Overall, the presence of polyphenols confers antioxidant properties to WPI. No significant information was gained by a direct comparison of the WPI/extracts antioxidant properties with the corresponding extracts alone. In fact, in order to prepare the WPI/extract a preliminary pre-treatment at pH 12 was carried out. This can cause the oxidation of the phenolic compounds, diminishing their antioxidant properties. In addition, some covalent interactions between the quinone groups of the phenolic compounds with the protein residues such as Schiff base can reduce the amount of total free OH groups, causing a loss of antioxidant activity.

Moreover, to get an insight of these antioxidant properties, the extraction yields of each extract were determined. In Table 4.9 the extraction yields, calculated with respect to the dry weight of the starting materials are reported. The highest yields were determined in the case of grape pomace and apples. On the contrary, the lowest value was obtained in the case of *Ficus* leaves.

Therefore, based on these extraction yields, the highest antioxidant activity observed in the case of grape pomace could be due to the highest concentration of polyphenols added to denatured WPI. In fact, after the extraction (100 mg in 1mL) and subsequent centrifugation, the resulting supernatants are directly

added to denatured WPI water solution. On the contrary, Ficus leaves showed the lowest extraction yields respect all the other extracts, consequently the lowest concentration inside WPI/polyphenols hydrogels. Notwithstanding this, the antioxidant activity is significantly higher than WPI alone. The apple extract showed high extraction yields and no antioxidant activity, indicating that a low content of phenolic compounds was extracted.

Table 4.9. Reported the extraction yields, calculating with respect to the dry weight of the starting materials. Shown are the mean of experiments in triplicate SD±1.

By-products	**Extraction yields (% w/w)**
Grape pomace	55%
Apple	48%
Pomegranate	44%
Ficus leaves	29%

Main Outcomes Of The Study:

- Whey proteins WPI, representing the major by-product of dairy industries, were used for bioadhesive preparation in combination with water extracts of selected agri-food by-products were added to denatured.
  - Good antioxidant properties and adhesive properties of these hydrogels were demonstrated.

4.3 Experimental section

Materials and Methods. Whey protein isolate (WPI) and soy protein isolate (SPI) (99%) was purchased from a commercial source (MyProtein). Caffeic acid (CA), chlorogenic acid (CGA), gallic acid (GA), agarose (analytical nucleic acid electrophoresis grade), and all other chemicals listed below were acquired from Sigma-Aldrich. Pomegranates, apples were provided at a local supermarket. *Ficus* leaves at a local garden. Grape pomace was kindly provided by Prof. Daniele Naviglio (Department of Chemical Sciences, University of Naples "Federico II", Naples, Italy. All experiments were conducted using deionized water. A carpentry shop provided the pine wood specimens. Fresh chicken tissues (skin and muscle) were acquired from a local butcher and kept at 4 °C until usage, which was usually within 1-2 days.

Uv-Vis spectra were recorded using a Jasco V-730.

A ball mill (Pulverisette 23-Fritsch) was used to pulverized the agrifood by-products.

Preparation of the SPI/polyphenols hydrogels. To promote denaturation, SPI (1 g) was dissolved in water (10 mL) and taken under stirring at 85 °C. After 1 hour, the appropriate polyphenol was added (C_f 28mM). The resulting solution was brought to pH 9 with 0.1 M NaOH and stirred for 2 h in air at 50 °C. The material thus obtained was centrifuged at 7000 rpm for 10 minutes at 4 °C. When reqiored, the hydrogels were lyophilized.

Preparation of the SPI/agarose/polyphenols hydrogels. Denatured SPI (10% w/w) produced as stated above was added to a 2% w/w solution of agarose in water at a ratio of 2:1 v/v and heated at 70 °C for 15 minutes before pouring into a Petri dish and cooling at room temperature for 1 hour. The resultant hydrogel was dipped in a 10 mM polyphenol solution in 0.05 M phosphate buffer at pH 9. The hydrogel was rinsed with water after 2 hours (3x10 mL). The hydrogels were air dried before being rehydrated in a Petri plate with water.

Preparation of the WPI/polyphenols extracts. Firstly, 500 mg of WPI were added to 5 mL of a water solution, bought to pH 12 adding 6M NaOH and stirred for 30 minutes at room temperature. All the agri-food by-products were roughly ground, lyophilized and subsequently pulverized using a ball mill (50 oscillations/min for 15 minutes). 100 mg of each agri-food wastes were added to 1 mL of water. Subsequently, the mixture was stirred at room temperature for 90 minutes, and centrifuged (5000 rpm for 10 min) at 20°C. The supernatants were then recovered, while the residual solids were lyophilized. The recovered supernatant of each extract (1 mL) was directly added to the previously denatured proteins (500 mg in 5mL of H_2O), stirred for 24 h and centrifuged for 10 min. The precipitate thus obtained represents the WPI/polyphenols hydrogel.

2,2-diphenyl-1-picryl-hydrazyl (DPPH) assay. To a 0.2 mM ethanolic solution of DPPH (3-5 mL), the lyophilized WPI/polyphenols hydrogels were added (60−400 mg), and after 10 min under stirring at room temperature the absorbance of the solution at 515 nm was measured. Experiments were run in triplicate [227,275].

Ferric Reducing/Antioxidant Power (FRAP) Assay. To 0.3 M acetate buffer (pH 3.6) containing 1.7 mM $FeCl_3$ and 0.83 mM TPTZ, the lyophilized WPI/polyphenols hydrogels were added (2-10 mg) and after 10 min under stirring at room temperature the absorbance of the solution at 593 nm was measured. Results were expressed as Trolox equivalents (eqs). Experiments were run in triplicate [228].

Determination of the NH_2 and SH content in SPI/polyphenols hydrogels.

Sulfhydryl groups. As previously described, the sulfhydryl content was measured using Ellman's reagent [276]. Ellman's reagent was made by dissolving DTNB (4 mg) in 1 mL of Tris-glycine buffer (0.086 M Tris, 0.09 M glycine, and 4 mM ethylenediaminetetraacetic acid (EDTA), pH 8.0). SPI/polyphenols hydrogel powder was dissolved in Tris-glycine buffer to a concentration of 3 mg/mL and combined with 50 L of Ellman's reagent. The

combined solution was stirred at room temperature for 1 hour. As reference of SH group, only SPI sample were used. The absorbance at 412 nm was measured by Uv-Vis spectrophotometer and the result was adjusted for the contribution of each SPI/polyphenol material at the concentration employed (determined in the absence of Ellman's reagent). The data were represented as a percentage of reacted SH groups in SPI/polyphenols compared to pure SPI. A calibration curve was constructed using a glutathione solution at values ranging from 0.002-0.01 mg/mL to assess the quantities of free SH groups in the denatured SPI.

Amino groups. The free amino group content of the sample was measured using a slightly modified version of the o-phthalaldehyde (OPA) technique for soy proteins [276]. OPA (40 mg) was dissolved in methanol (1 mL), a 20% (w/v) sodium dodecyl sulfate (SDS) solution (2.5 mL), a 0.1 M borax solution (25 mL), and 100 L of -mercaptoethanol. Finally, the OPA reagent was made by adding distilled water to the solution in a volumetric flask until the total volume reached 50 mL. The samples were mixed with the OPA reagent until a final concentration of 0.18 mg/mL was reached.

ATR FT IR measurements. The FTIR spectra of the lyophilized powder samples were obtained using a Perkin Elmer Spectrum 100 spectrophotometer (USA) fitted with a Universal ATR diamond crystal sampling attachment. Spectra were collected using an average of 16 scans at a resolution of 4 cm^{-1}.

EPR measurements. EPR measurements were performed using a X-band spectrometer (Bruker, Rheinstetten, Germany). Flame-sealed glass capillaries containing the samples were coaxially inserted in a standard 4 mm quartz sample tube. Spectra were acquired at room temperature. The instrumental settings were as follows: sweep width: 100 G; time constant: 10.24 ms; conversion time: 20.48 ms; modulation frequency: 100.00 kHz; modulation amplitude: 1.0 G; receiver gain: 60 dB. Power saturation experiments were preliminarily performed, with the microwave power gradually increasing from 0.001 to 128 mW. Single spectra were then acquired at a microwave power

optimized for each sample to avoid microwave saturation of resonance absorption curve. Several scans, typically 128, were accumulated to improve the signal-to-noise ratio. The g value and the spin density were evaluated by means of an internal standard, Mn^{2+}-doped MgO. The broadness of each spectrum was evaluated as distance, in G, between the maximum and the minimum of the observed signal (DB).

SPI/polyphenols hydrogels morphological properties. The hydrogels were dried at room temperature for 24 h. Morphological analysis was performed by scanning electron microscopy (SEM) using a FEI Quanta 200 FEG SEM in high vacuum mode. Before SEM observations, samples were mounted onto SEM stubs by means of carbon adhesive disks and sputter coated with a 5-10 nm thick Au-Pd layer. All the samples were observed at 10 kV acceleration voltage using a secondary electron detector.

SPI/polyphenols hydrogels mechanical properties.

Adhesive strength. Soft wood (pine) specimens (30 x 20 x 50 mm thickness, breadth, and length) were utilized [266]. Weighted SPI or SPI/polyphenol slurry was produced as indicated before and brushed on a 2 × 2 cm area of each support (approximate protein concentration 1.80 mg/cm^2). The pieces were clamped together for 24 hours. Wood specimens shear strength was evaluated using an Instron testing equipment (model 4505) with a crosshead speed of 25 mm/min. The amount of force (N) needed to shatter the glued wood specimen was measured. All adhesive strength measurements shown are the results of six replications. The specimens were equilibrated for 48 hours before to measurement at 25 °C and 50% relative humidity (RH). For the water resistance test, the wood specimen was soaked in deionized water at room temperature and monitored on a regular basis.

Adhesion tests of SPI/polyphenols hydrogels on animal tissues and underwater resistance. For tests on chicken skin a protocol previously described was adopted [277]. In brief, the fat layer below the skin was removed

using a scalpel and the tissue was cut into pieces of approx. 15 x 20 mm, washed gently with hand soap once, rinsed with tap water, immersed in ethanol for 2 min and again rinsed with water. Skin samples prepared this way were kept immersed into 10 mM HEPES buffer at pH 7.5 for 30 min before their use for the adhesion tests. The SPI or SPI/polyphenols slurry was deposited on the skin on a 2 x 2 cm area.

For the chicken breast muscle studies, slices of approximately 5 x 3 mm were cut with a knife and then submerged in HEPES buffer as described above, rinsed with deionized water, and gently wiped onto a tissue paper to blot the excess liquid. SPI or SPI/polyphenols slurry was added to the slices before they were squeezed together for 10 hours.

Skin samples were soaked in PBS at room temperature and tested on a regular basis for water resistance.

Water vapor permeability (WVP) tests.WVP measurements were performed according to ASTM E96 standard method. Air dried SPI/agarose/polyphenols hydrogels with exposed area of 2.83 cm^2 were sealed over a circular opening of aluminum permeation cells filled with distilled water. The cells were kept in an environmental chamber at 25 °C under 50% RH. After the system reached steady state conditions, the weight change of the cell was measured every 24 h. Air dried SPI/agarose/polyphenols hydrogels were tested three times to confirm repeatability of measurements.

The weight loss of hydrogels was plotted with respect to time, and the linear least-square method was used for the calculation of the parameters given by Equation:

$$WVP = L \times WVTR/\Delta P$$

where WVTR is the water vapor transmission rate of air-dried SPI/agarose/polyphenols hydrogels with (g s/m^2), L is average thickness of the hydrogels (m), ΔP is the difference in water vapor pressure between the two exposed sides of the hydrogels (Pa).

Cytocompatibility. Immortalized human keratinocytes (HaCaT) and human dermal fibroblasts (HDF) were cultivated at 37 °C in a humidified environment containing 5% CO_2 in high-glucose Dulbecco's modified Eagle's medium (DMEM) supplemented with 10% fetal bovine serum (FBS), 1% antibiotics (Pen/strep), and 1% l-glutamine. Cells were seeded on 96-well plates at a density of 3 103 cells/well 24 hours before treatment, then incubated for 24 and 72 hours in the presence of the chemicals (agarose (0.625 mg/mL) or agarose as above/0.875 mg/ml SPI or agarose/SPI as above/0.0875 mg/ml CGA/0.005 mg/ml CA or GA). MTT tests were done after treatments by replacing the cell culture supernatants with 0.5 mg/mL MTT reagent diluted in DMEM medium without red phenol (100 L/well). After 4 hours of incubation at 37 °C, the resultant insoluble formazan salts were solubilized in 0.01 M HCl in anhydrous isopropanol and measured using an automated plate reader spectrophotometer (BioTek Instruments, Inc., Winooski, VT) by measuring absorbance at 570 nm. Cell vitality was represented as a percentage value relative to untreated control cells.

Hemocompatibility tests. Blood clot formation test, tromboelastogram, and scanning electron microscopy (SEM) analyses were used to assess sample hemocompatibility. All investigations were carried out using blood samples from four healthy human donors, graciously given by the Ospedale Maggiore della Carità's transfusional center in Novara. For statistical significance, the tests were performed in triplicate.

Samples were put on 48-well plates and 50 L of human blood was poured over them for the blood clot formation test. After 1, 3, 5, 10, and 20 minutes, 0.5 mL of ultrapure water was added, and 100 L of the mixture was analyzed spectrophotometrically at 450 nm. Blood coagulation was inversely proportional to absorbance values.

Tromboelastograms were generated by pouring 1 mL of human whole blood onto air dried SPI/agarose/polyphenols hydrogels for 30 minutes at 37°C. The

blood was then collected and mixed with Kaolin to speed up the coagulation process. 0.34 mL of the mixture was placed in a cuvette containing 20 L of a 0.2 M $CaCl_2$ solution. Tromboelastograph (TEG 5000, Haemonetics, USA) analysis was performed on the mixture, yielding four parameters: clot starting time, coagulation time, coagulation speed, and clot strength.

SEM analysis was performed on the samples utilized in the tromboelastograph test. Samples were washed twice with 0.2 M cacodylate buffer (pH 7.4) before being fixed for 30 minutes using Karnovsky buffer (8% formalin, 2.5% glutaraldehyde in 0.2 M cacodylate buffer, pH 7.4). After that, samples were washed with cacodylate buffer and dehydrated with ethanol concentrations ranging from 50% to 100%. Finally, samples were soaked for 16 hours in hexamethyildisilazane. Finally, samples were examined using a JSM-IT500 InTouchScopeTM Scanning Electron Microscope (JEOL, Tokyo, Japan).

Scratch test. As previously mentioned [278], the wound healing efficacy of SPI/polyphenols hydrogels was investigated in vitro. Human HaCaT keratinocytes were seeded at a density of 300 000 cells/well in 0.3 mL media per well in an 8-well chamber (NuncTM Lab-TekTM Chambered Coverglass). After a 24-hour incubation at 37 °C, cell monolayers were injured using a pipette tip to remove cells from a specified location of the monolayer. After removing the culture medium, the cells were washed twice with PBS. The cells were subsequently treated in new culture media using agarose (0.625 mg/mL) or agarose as described above/0.875 mg/mL SPI or agarose/SPI as described above/0.0875 mg/mL CGA/0.005 mg/mL CA. At t_0 and t_{24} h of incubation, wound closure was assessed using an inverted microscope (Zeiss LMS 700, Carl Zeiss, Germany) by measuring the regions. The ratio of the areas at t0 and t24 h for each sample is used to calculate wound closure. To account for repeatability, the data from three different experiments were averaged, and the standard error of the mean was computed.

Antibacterial activity.

Bacterial strains and growth conditions. Bacterial strains Staphylococcus aureus ATCC 12600, Methicillin Resistant Staphylococcus aureus (MRSA) WKZ-2, Staphylococcus epidermidis ATCC 35984, Acinetobacter baumannii ATCC 9606, and Pseudomonas aeruginosa ATCC 27853 were cultured in Muller Hinton Broth (MHB, Becton Dickinson. Bacterial cells were injected and cultured overnight in MHB at 37 °C in all studies to examine the antibacterial activity of air dried SPI/agarose/polyphenols hydrogels. The bacteria were transferred to a new MHB tube the next day and grew to the mid-logarithmic phase.

Inhibition halo and percentage of bacterial growth. Bacterial cells were diluted into 0.5x nutritional broth (NB) to roughly 2 x 108 CFU/mL and injected onto LB plates to test the inhibitory halo of air dried SPI/agarose/polyphenols hydrogels. The hydrogels were then put in a square of 1 cm2 on the inoculation plate and pushed to achieve complete contact with the agar surface. Plates were then incubated at 37 °C overnight to assess bacterial growth surrounding the hydrogels. Bacterial cells were diluted in 0.5x NB to roughly 2 x 106 CFU/mL to determine the percentage of cell viability. 500 L of bacterial culture was deposited on a 1 cm^2 square of each hydrogel examined and incubated overnight at 37 °C. The next day, each culture sample was diluted in 0.5xNB media and colony counted on LB agar.

Statistical analysis. Statistical analysis was performed by using a Student's *t*-Test. Significant differences were indicated as *($P < 0.05$), **($P < 0.01$) or ***($P< 0.001$).

Chapter 5

Green methodologies for the recovery of low and high molecular weight phenolic compounds from agri-food by-products

As mentioned in the Introduction, agri-food industry is responsible for the generation of high volumes of organic wastes, consisting mainly of fruit and vegetable by-products. On the other hand, these materials may be considered as an easily accessible, low-cost source of value-added active compounds. Of particular interest are phenolic compounds due to their unique and varied properties [36,279,280]. Therefore, the wide distribution of phenolic compounds in agri-food by-products has focused intense research work on the development and optimization of extraction methodologies. Typically, solid-liquid extraction techniques are used, which involve long extraction times, high costs, and use of organic solvents with inherent drawbacks such as low boiling points, flammability, toxicity, and non-biodegradability. To overcome these limitations efforts have devoted to the development of recovery methods using low environmental impact solvents, with strong extraction qualities and at the same time low cost and minimal environmental impact.

Recently, Deep Eutectic Solvents (DES) have become increasingly popular as eco-friendly as well as biocompatible solvents for the recovery of phenolic compounds from agri-food by-products [281–285]. In fact, DES are easily prepared and are typically less expensive, biodegradable, and biocompatible when compared to standard organic solvents [154,155]. Lately, to achieve a more efficient recovery and a more reproducible extraction procedure, the use of mechanical treatments, including a ball or a planetary mill, has been evaluated.

Yet, despite the considerable interest, rational approaches for a complete valorisation of the phenolic compounds have not been deeply explored.

On these bases in this Chapter, a green procedure based on DES combined with proper mechanical pre-treatment for the recovery of lignin from agri-food by-products was evaluated.

Secondly, a sequential conventional/DES based extraction method for the recovery of low and high molecular weight phenolic compounds from agri-food by-products, including defatted spent coffee ground (dSCG) and pomegranate peels and seeds, was assessed.

Results and Discussion

5.1 Lignin extraction from nut shells

Based on a previous developed protocol [286], a procedure involving choline chloride and lactic acid as DES for the extraction of lignin from selected nut shells was adopted. Firstly, all the shells were finely minced with the aid of a ball mill. This preliminary step is crucial to improve the extraction yields by increasing surface area and cleaving glycosidic linkages and β-O-4 bonds of lignin components [287–290]. As result, the release of phenolic hydroxyl groups and therefore an improvement of the antioxidant properties could be obtained. Extraction was performed at 120°C for 24 h. Therefore, lignin was recovered in the form of brown/black powders by simple precipitation, centrifugation, and lyophilization.

In Table 5.1 the extraction and recovery yields obtained from various nut shells, calculated with respect to the amount of starting or DES-dissolved material, are reported. The highest values were observed in hazelnut and pistachio shells. Particularly, the hazelnut shell lignin yields were higher than those reported in literature using other extraction processes [291,292], whereas no data for pistachio and pecan nut shells lignin have been reported yet. A 36% w/w yield of peanut shell lignin was recently reported utilizing 6:4 v/v ethanol/water as the solvent at 180 °C for 100 minutes [293]. In this last case, our developed extraction protocol allows comparable yields respect to the other one already reported in literature, and at the same time a low cost and ecologically friendly procedure. Finally, chestnut shell exhibited the lowest extraction/recovery yields, although comparable to those reported in literature using different solvents [294].

Table 5.1. Lignin extraction and recovery yields from selected nut shells. [1] w_s: weight of starting material; w_d: weight of the DES-dissolved material.

Shell	Extraction Yield (% w/w_s)[1]	Recovery Yield (% w/w_d)[1]
Peanut	***19***	***34***
Chestnut	***19***	***27***
Hazelnut	***25***	***36***
Pecan nut	***19***	***34***
Pistachio	***27***	***38***

5.1.1 Structural Characterization of Nut shell Lignin

5.1.1.1 Spectroscopic analysis

EPR spectroscopy is widely used as a powerful, sensitive and specific technique for the identification of phenolic polymers, due to the presence of intrinsic free radical centers [279,286,295–297]. Therefore, the recovered lignins were structurally characterized by EPR. In all samples, EPR spectra showed a singlet (Figure 5.1 panel a) at g values compatible with the existence of carbon-centered radicals (Table 5.2) [269,286]. Notably, while the starting nut shells had apparently asymmetric spectra (Figure 5.2), likely due to the superposition of signals from distinct radical species, all the recovered lignins had a symmetric signal (Figure 5.1) with an intermediate line shape between Gaussian and Lorentzian derivatives functions, except for chestnut and hazelnut lignin (Table 5.2)

Furthermore, recovered lignin exhibited higher spin density and lower signal amplitude (ΔB) values than the starting material (Table 5.2), indicating that the DES-based extraction is efficient and provide samples enriched in the lignin component, characterized by a more homogeneous free radical population and a relatively higher degree of pi-electron delocalization. In addition, the normalized power saturation curves (Figure 5.1 b) for chestnut, hazelnut, and pecan nut shell lignin showed a well-pronounced intensity decrease at high microwave

power, indicating a strong homogeneous relaxation behavior, thus confirming a low degree of variety of the free-radical population in the DES-recovered samples [286].

Table 5.2. EPR data for nut shell and related lignins. [1]For the spectra of the starting material, showing the superposition of signals, the Gaussian fraction was not determined.

Sample		**spin/g concentration**	**ΔB (± 0.2)**	**Gauss fraction (± 0.05)[1]**	**g-factor (± 0.0003)**
Peanut shell	Starting	2.6E+16	5.6	-	2.0038
	Lignin	***2.2E+17***	***5.1***	***0.42***	***2.0030***
Chestnut shell	Starting	1.6E+16	5.9	-	2.0031
	Lignin	***3.5E+17***	***4.2***	***0.70***	***2.0031***
Hazelnut shell	Starting	2.1E+16	7.0	-	2.0031
	Lignin	***6.6E+16***	***5.3***	***0.21***	***2.0036***
Pecan nut shell	Starting	1.4E+16	4.8	-	2.0026
	Lignin	***4.6E+17***	***4.5***	***0.48***	***2.0030***
Pistachio shell	Starting	5.9E+15	6.8	-	2.0037
	Lignin	***2.5E+17***	***4.7***	***0.43***	***2.0027***

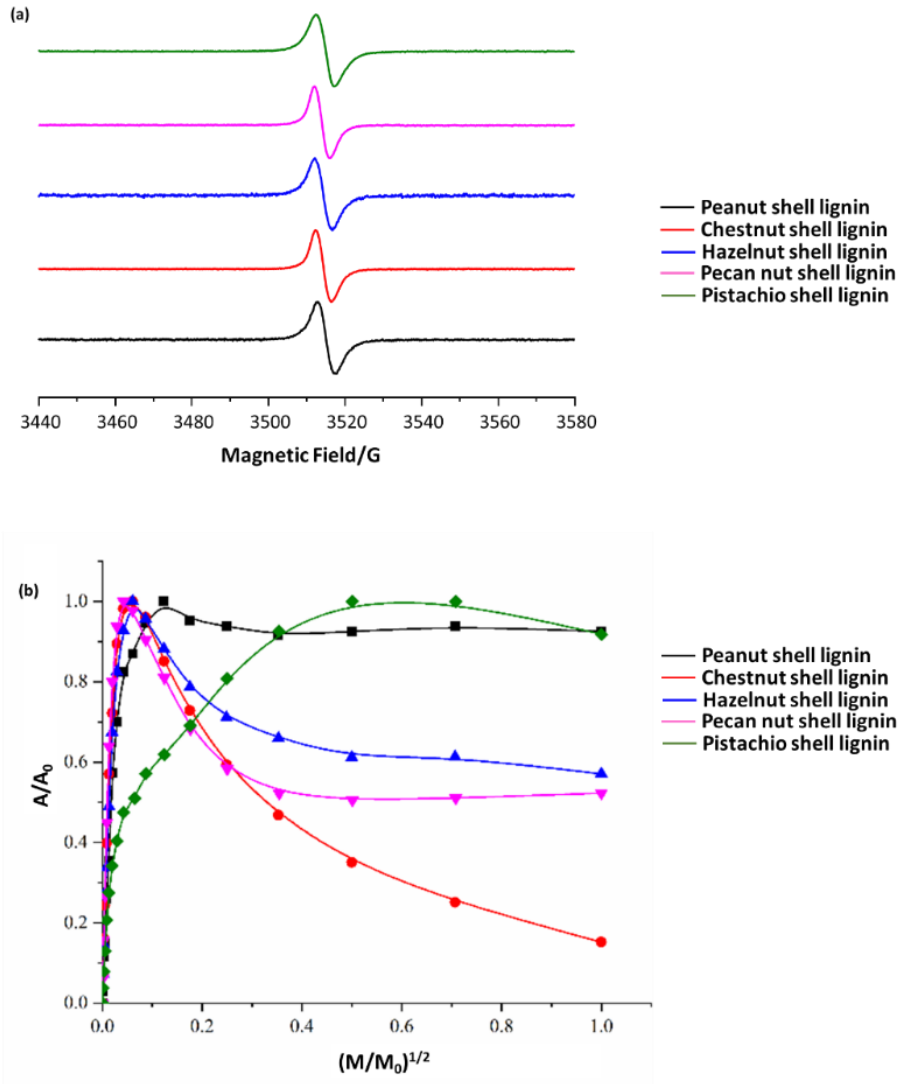

Figure 5.1. (a) Solid state EPR spectra and (b) power saturation profiles of lignins recovered from the different nut shells.

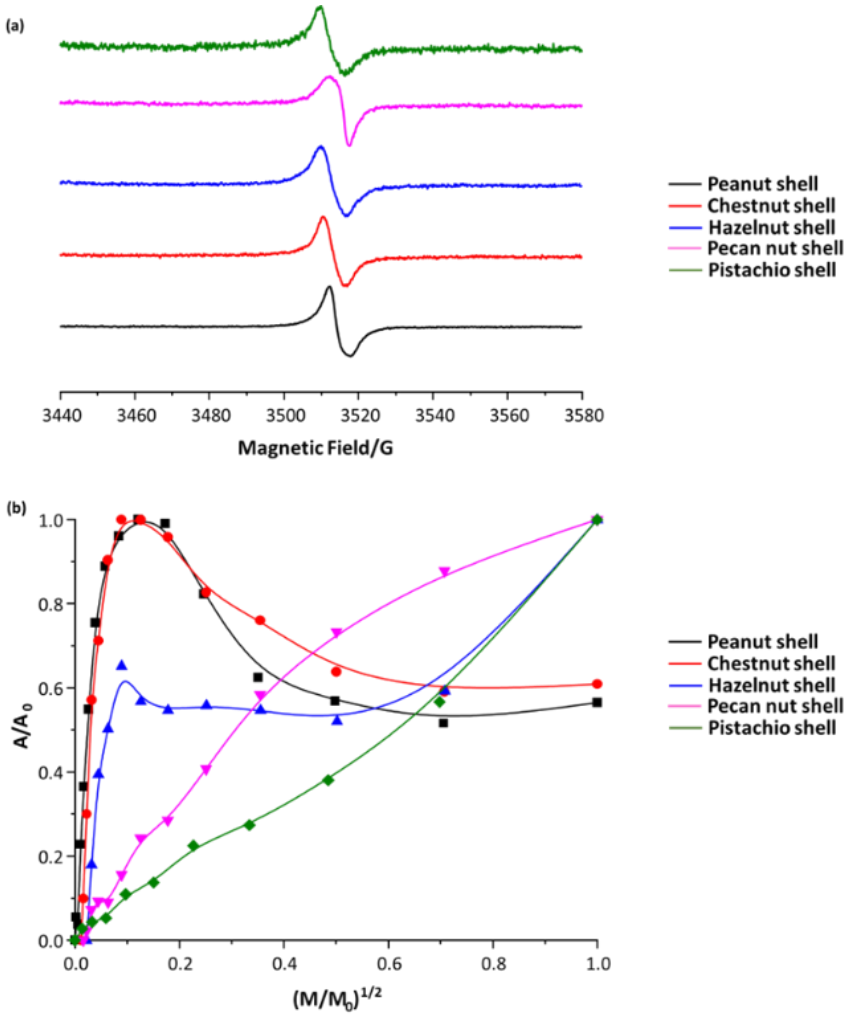

Figure 5.2. (a) Solid state EPR spectra and (b) power saturation profiles of starting nut shells.

To gain more information on the recovered lignins, in subsequent experiments an ATR-FTIR analysis was carried out. As an example, the ATR-FTIR spectra of extracted lignin and pistachio shells is reported. The spectra revealed the existence of two prominent peaks in the 2950-2850 cm^{-1} region (*Band 1*), which are likely attributable to the CH bond stretching vibration of lignins (Figure 5.3) [117,279]. A significant decrease in the signal at around 1000 cm^{-1} (*Band 2*),

associated with C-O-C skeletal vibration of polysaccharides, was observed in the lignin sample, most likely due to the removal of this component from the starting material following DES-based treatment.

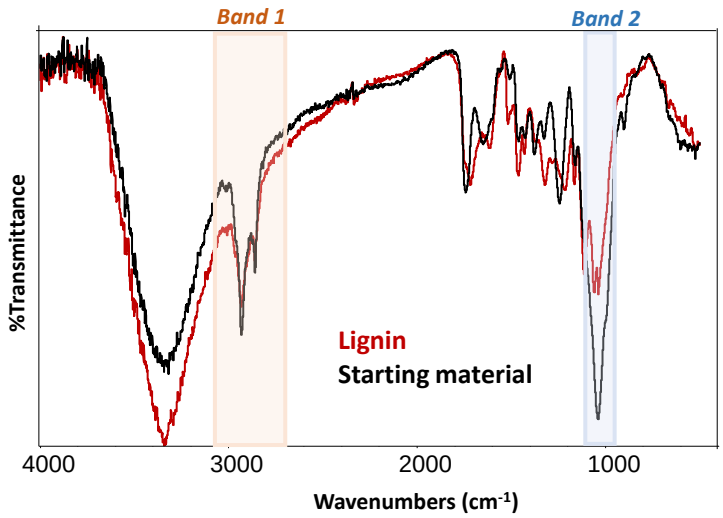

Figure 5.3. ATR-FTIR spectra of pistachio lignins (red line) and nut shells (black line). Highlighted are the bands associated to the aromatic C−H bond stretching vibration of lignins and C-O-C skeletal vibration of polysaccharides.

The Uv-Vis spectra of the DMSO-soluble portion of the recovered lignins were also recorded (Figure 5.4). This solvent is commonly known for its ability to dissolve a wide spectrum of phenolic compounds. All the samples displayed broadband absorption in the 240-640 nm range, with a maximum at 280 and 310 nm characteristic of lignin moieties [298,299], marked in the samples derived from peanut, hazelnut, and pistachio shells.

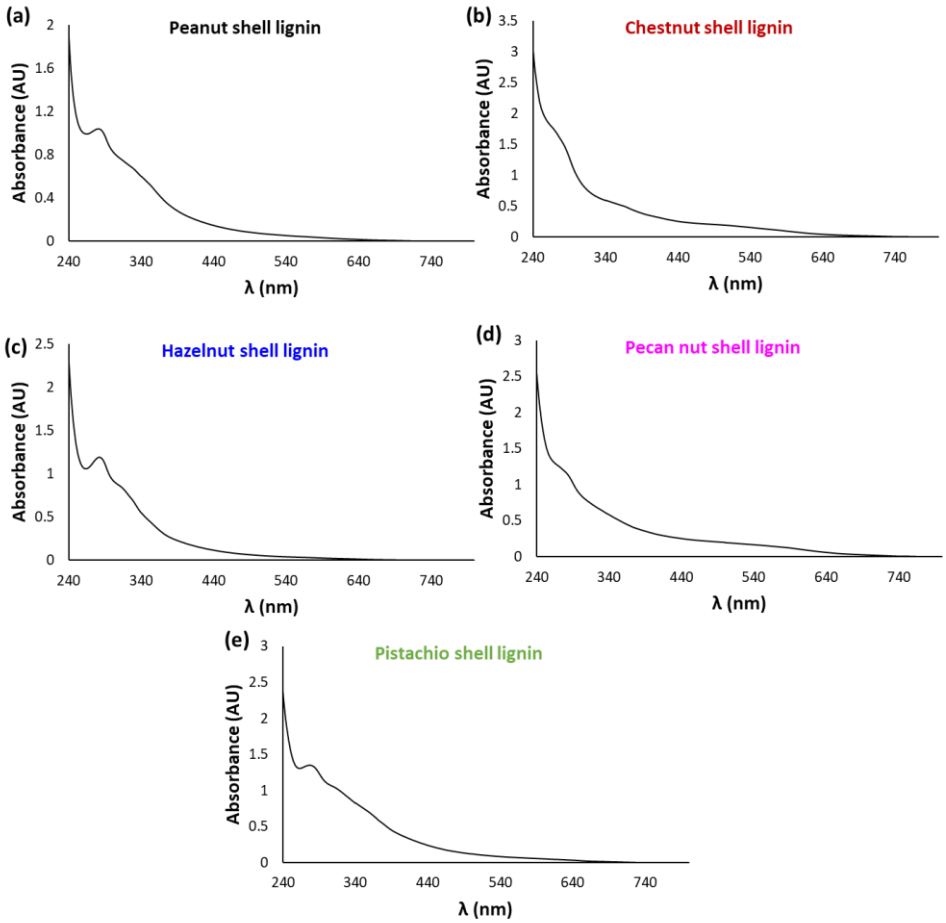

Figure 5.4. Uv-Vis spectra of the DMSO-soluble fraction of (a) peanut, (b) chestnut, (c) hazelnut, (d) pecan nut, and (e) pistachio shell lignins.

Finally, ^{1}H NMR analysis of the recovered lignins using DMSO-d_6 as solvent was performed. A very broad complex signal at 6.0-7.4 ppm was detected for all samples, indicating the presence of a heterogeneous phenolic polymer such as lignin [286,300]. Notably, in the case of chestnut shell lignin, a singlet at 7.48 ppm was also observed, most likely due to the presence of a minor quantity of ellagic acid [301], consistent with prior findings for DES-based chestnut shell extractions [302,303]. Chestnut shell lignin and, to a lower extent, pecan nut

shell lignin were the only samples with a discernible wide signal in the 8.5-9.5 ppm range, most likely due to the presence of a considerable amount of phenolic OH. As representative and most interesting example, the ^{1}H-NMR spectra of chestnut shell is reported in Figure 5.5.

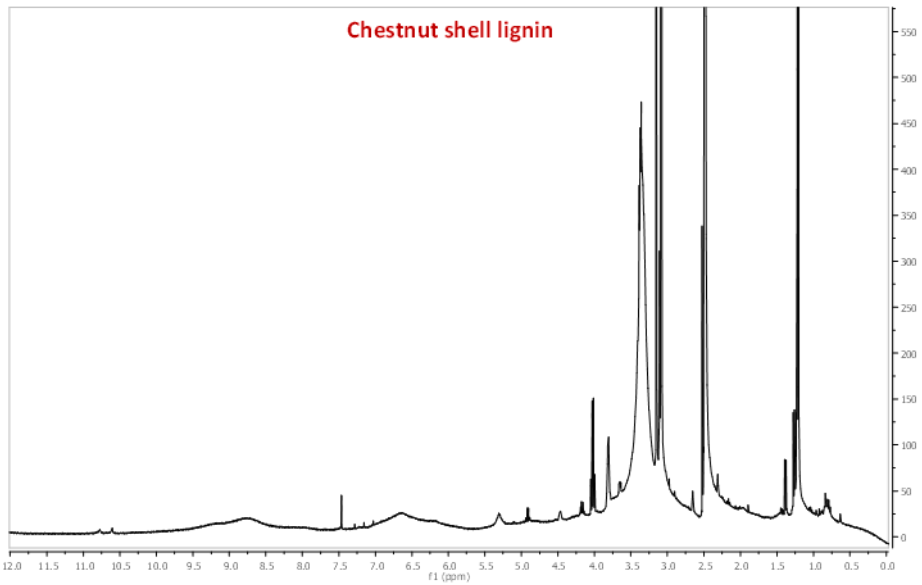

Figure 5.5. ^{1}H NMR spectra (DMSO-d_6) of chestnut shell lignins.

5.1.1.2 Chromatographic Analysis

To obtain additional data on the composition of the DES-recovered lignins from the various nut shells, the DMSO-soluble fractions were analyzed by HPLC after proper dilution in methanol. Elutographic profiles for all samples revealed no appreciable peaks, demonstrating the lack of low molecular weight phenolic substances. The only exception was the chestnut shell-derived sample, which showed a peak around 36 min (Figure 5.6), attributed to ellagic acid by LC-MS analysis and by comparison of chromatographic profile with an authentic standard. This compound was found in approximately 0.9w/w % concentration in the chestnut shell DES-extracted sample. Overall, these results confirmed the data already obtained by ^{1}H-NMR analysis.

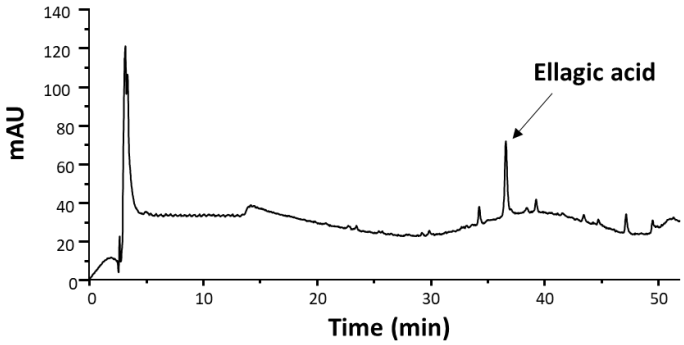

Figure 5.6. HPLC profile of the DMSO-soluble fraction of chestnut shell lignin.

Chemical degradation treatments commonly used for the qualitative and quantitative analysis of phenolic polymers were used, in order to obtain additional information on the non-chromatographable components of the different samples. Thiolysis, acid degradation, and alkaline hydrogen peroxide degradation were all carried out. The first method is frequently used to analyze condensed tannins [304], whereas acid degradation is used to detect extractable and non-extractable ellagitannins [305]. Alkaline hydrogen peroxide degradation allows for the analysis of insoluble and structurally complex phenolic polymers such as melanin pigments and lignins, and is based on the identification of chromatographable, low-molecular weight markers derived from the polymer oxidative breakdown [306,307]. No amounts of hydrolysable tannins and condensed tannins in all lignins were detected by the spectrophotometric acid degradation and vanillin-HCl assay, respectively [304] .

On the contrary, the HPLC profiles of the alkaline hydrogen peroxide degradation mixtures exhibited, among others, two main peaks eluted at 25.0 and 26.7 min identified as vanillic and syringic acid, respectively, based on LC-MS analysis and on the comparison of the chromatographic properties with those of authentic standards.

Both compounds, indicating the presence of guaiacyl and syringyl units in the lignin samples, were found in the elutographic profiles of hazelnut, peanut, and pistachio shell lignin degradation mixtures. On the other hand, chestnut shell lignin contained only low amounts of syringic acid, whereas pecan shell lignin only vanillic acid. As an example, the hazelnut lignin is represented in Figure 5.7.

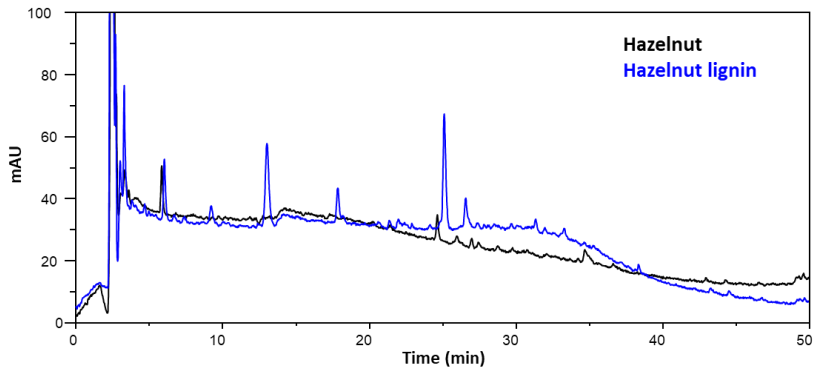

Figure 5.7. HPLC elutographic profiles alkaline hydrogen peroxide degradation mixture of hazelnut by-product and lignin thereof.

According to the spectroscopic and chromatographic results, the ball milling/DES-based extraction method allow the recovery of structurally diverse lignin-rich samples of high purity from all of the selected nut shells.

5.1.2 Antioxidant Properties of the Nut Shell-Derived Lignin

Another series of experiments were devoted to the evaluation of the recovered lignins for their TPC and antioxidant properties using standard spectrophotometric assays.

Chestnut shell lignin was the most active substance in the DPPH experiment, with an EC_{50} value lower than that found for the reference antioxidant substance Trolox. Pecan nut shell lignin also exhibited good DPPH-reducing activities, demonstrating the great efficacy of this agrifood by-product as a source of

antioxidant phenolic compounds. On the other hand, compared to chestnut and pecan nut shell lignins, the EC_{50} values of peanut, hazelnut, and pistachio nut shell lignins were significant higher.

In agreement with the DPPH assay, also chestnut shell lignin exhibited the highest reducing properties in the FRAP assay, whereas all the other samples were characterized by comparable Trolox equivalent values (Figure 5.8 panel b). The presence of a large amount of phenolic OH groups of chestnut shell lignin found by ^{1}H NMR analysis would be consistent with the better antioxidant abilities in both the DPPH and FRAP assays. The EA, present in the chestnut shell lignin, accounts for only 5-12% of the DPPH and Fe^{3+} reducing properties, demonstrating the real antioxidant activity of chestnut lignin.

The highest TPC levels, determined by the Folin-Ciocalteu assay, were found in pecan nut shell and chestnut lignins, which are consistent with the findings of the antioxidant assays.

The differences in the results of the three assays may be accounted for in terms of the different properties evaluated by each of them. In fact, DPPH assay measures the electron transfer and hydrogen atom transfer ability of a given compound, whereas the FRAP assay reflects the ability to transfer electrons to iron III. On the other hand, Folin-Ciocalteu assay requires relatively high pH and may cause the phenolic content and, thus, the antioxidant capabilities, to be overestimated. Of course, the relative solubility in the test media may also impact the antioxidant properties of all the tested samples.

Notably, a very good direct linear correlation between the EC_{50} values from the DPPH assay and the ΔB values of the EPR spectra was obtained (R^2= 0.94). This is consistent with previous findings for bio-inspired phenolic polymers and would emphasize the significance of p-electron spin delocalization, one of the primary factors of EPR signal narrowing, as a structural determinant of the antioxidant properties of phenolic polymers, including lignin. (Figure 5.9).

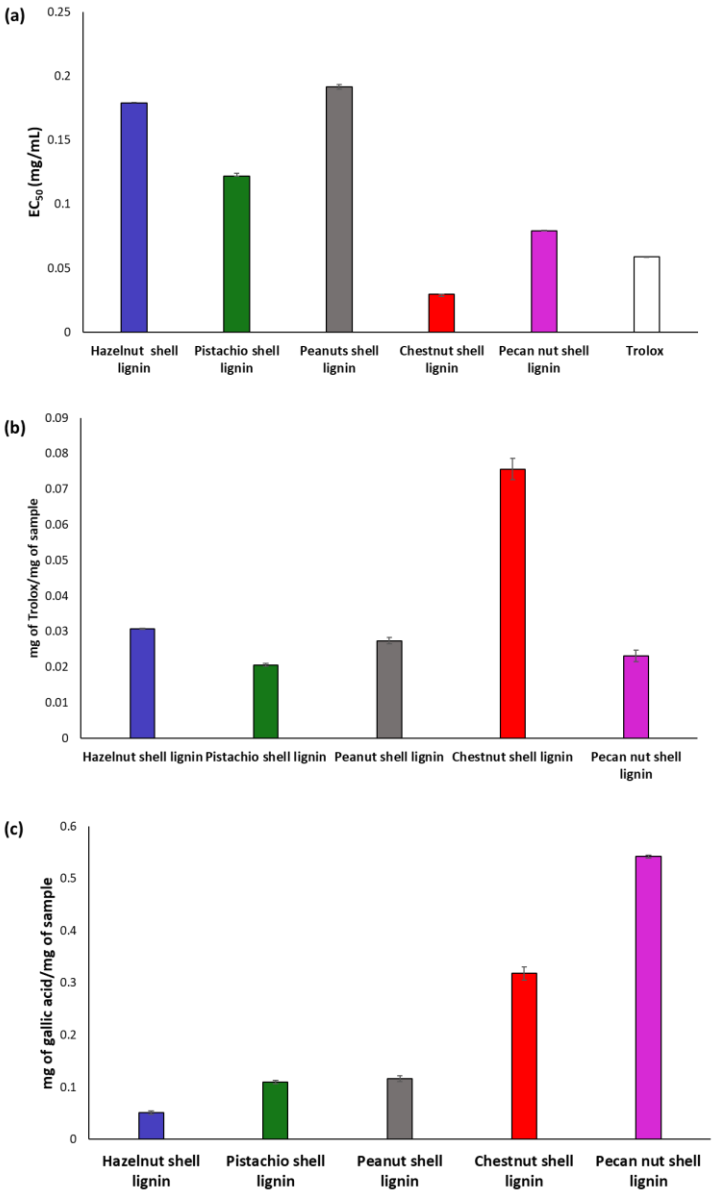

Figure 5.8. Antioxidant properties and TPC of nut shell-derived lignins. (a) DPPH assay; (b) FRAP assay; (c) Folin-Ciocalteu assay.

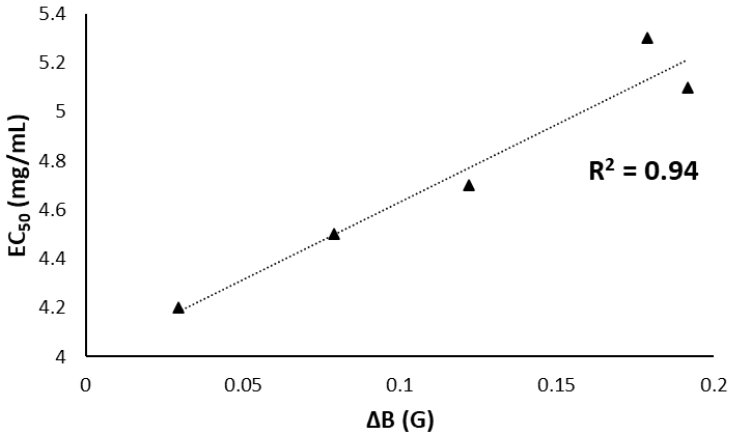

Figure 5.9. Correlation between antioxidant properties (expressed as EC_{50} values determined in the DPPH assay) and ΔB values (determined by EPR spectroscopy) of nut shell lignin (EC_{50} = (-0.58 ± 0.10) + (1.15 ± 0.02) ΔB, R^2 = 0.94).

Given the promising results obtained a complete evaluation of costs of the procedure, including those derived from electric power usage and equipment operation will be addressed in further studies.

Main Outcomes Of The Study:

- ☐ A straightforward, low-cost, and green method based on DES/ball mill extraction for the recovery of high molecular weight phenolic compounds such as lignin from the edible nuts shells was developed.
    - All the samples exhibited marked antioxidant activity comparable or even higher than those of the reference antioxidant Trolox, as evaluated by DPPH and FRAP assays and a high phenolic content as demonstrated by TPC assay.

5.2 Extraction of low and high molecular weight phenolic compounds from defatted Spent Coffee Ground (dSCG)

Based on the results reported in the previous paragraphs, the possibility to use the developed protocol for the recovery of lignin from other agri-food by-products, such as defatted spent ground coffee (dSCG), was assessed.

In particular, a sequential two-step extraction protocol was developed, selectively affording phenolic compounds extracts and a lignin-enriched sample. To exploit at best possible defatted SCG, made available from some collaborators after the recovery of triglycerides, an extraction procedure involving two sequential treatments was carried out: the first one was aimed at the extraction of low molecular weight phenolic compounds from dSCG, whereas the second at the recovery of lignin from the solid residue obtained after this first treatment. A representative scheme of the sequential extraction procedure is shown in Figure 5.10. The final solid residue obtained after the recovery of lignin was used as a source of sugars through enzymatic hydrolysis.

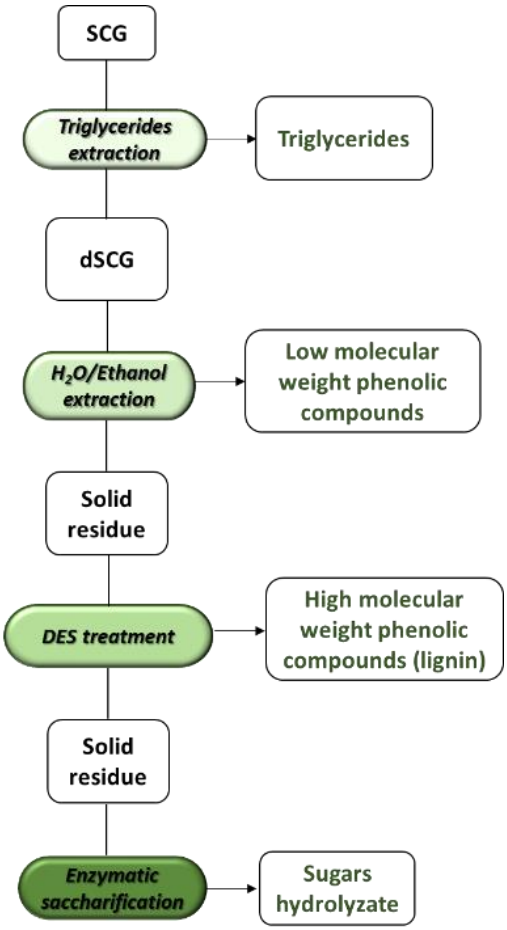

Figure 5.10. Representative scheme of the sequential extraction procedure.

5.2.1 Extraction of low molecular weight phenolic compounds from dSCG

Firstly, the procedure for the extraction of low molecular weight phenolic compounds was implemented. Briefly, dSCG was extracted using water, ethanol or ethanol/water 6:4 v/v at a 100 mg/mL s/l ratio. The mixtures were kept under magnetic stirring for 90 min at 50°C and then centrifuged for 10 minutes.

The three extracts were preliminarily analyzed by Uv-Vis spectroscopy and HPLC. All the Uv-Vis spectra exhibited two absorption maxima at 280 and 320

nm (Figure 5.11 a), presumably attributed to the presence of hydroxycinnamic acids. In addition, the aqueous and hydroalcoholic extracts showed an absorption about 2-fold higher than that observed for the ethanolic extract. For all samples, HPLC analysis showed quite similar elutographic profiles in qualitative and quantitative terms. In particular, a slightly lower intensity of peaks eluted around 12 and 18-19 min, in agreement with Uv-Vis analysis was observed.

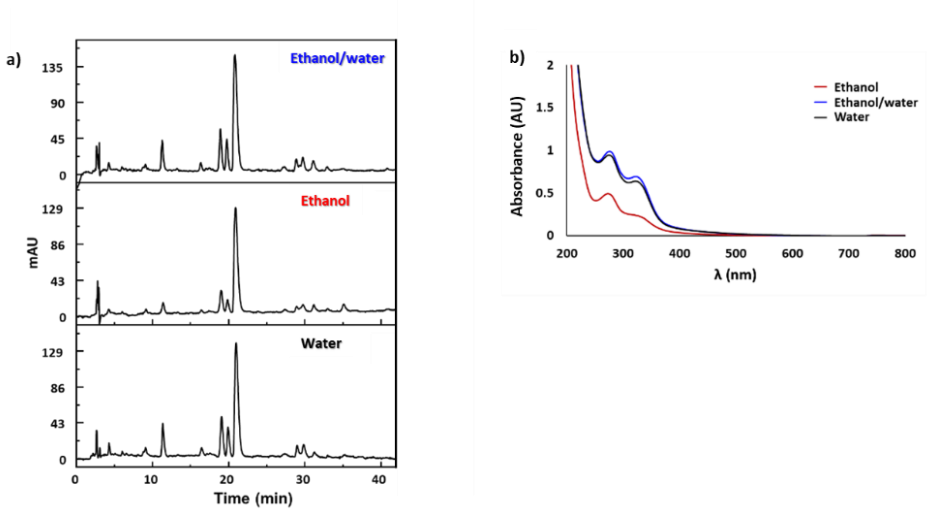

Figure 5.11. a) HPLC profiles and b) Uv-Vis spectra of dSCG aqueous, ethanolic and hydroalcoholic extracts.

Among the selected solvents, best results were observed using ethanol/water as extraction solvent of low molecular weight phenolic compounds. Therefore, all the other experiments were focused on the hydroalcoholic extract. The extract was again analyzed by HPLC using a Uv-Vis detector, at different wavelength such as 254 nm (a universal detection wavelength for aromatic compounds), 280 nm (specific for dihydrocalcones and flavanols), 320 nm (specific for hydroxycinnamic acids), and 400 nm (specific for flavonols).

In Figure 5.12 the elutographic profiles at 254 nm of the hydroalcoholic extract is reported. Several products eluted at 12, 18-22 and around 30 min were

observed, whereas the elutographic profiles at 320 nm, showed the presence of three main peaks at 12, 18 and 19 min, attributed to hydroxycinnamic acids. The compounds eluted at 19 and 22 min were identified as chlorogenic acid and caffein, as demonstrated by LC-MS analysis and using an authentic standard as reference. The other compounds, detected at 320 nm, could likely be isomers of chlorogenic acid, commonly found in coffee. The content of chlorogenic acid and caffein was estimated as much as 2 and 21% w/w, respectively. Finally, the HPLC profile recorded at 400 nm proved the absence of flavonols in the dSCG extract.

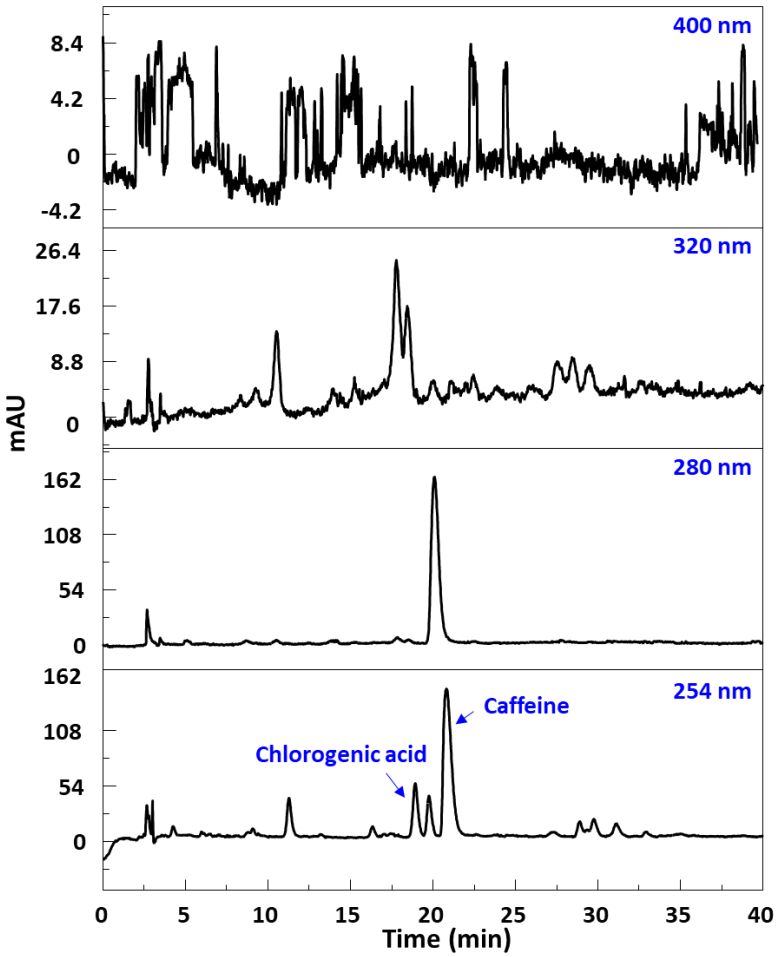

Figure 5.12. Elutographic profiles of dSCG hydroalcoholic extract detected at λ 254 nm, 280 nm, 320 nm and 400 nm.

Subsequently, the hydroalcoholic extract was partially dried using a rotatory evaporator to remove ethanol, lyophilized and an extraction yield of about 6% calculated with respect to the starting dSCG was determined. In order to increase this value, the extraction process was repeated three times, providing an almost 2-fold higher extraction yield (11 w/w %). In addition, in the perspective of a large-scale treatment, the extraction from a 15-fold larger amount of starting material was performed and proved to be repeatable.

5.2.2 Green extraction of lignin of solid residue from dSCG hydroalcoholic treatment

In addition to low molecular weight phenolic compounds, SCG contains also high molecular weight phenolic compounds, in particular lignin. A green protocol based on the use DESs was adopted and slightly changed for the recovery of lignin from the solid residue deriving from dSCG after the treatment with conventional organic solvents. Therefore, four different DESs were prepared, including ChCl and lactic acid (at 1:2 or 1:9 mol/mol ratio), ChCl and glycerol (at 1:2 mol/mol ratio), ChCl and 1,2- propanediol (at 1:2 mol/mol ratio). In addition, for all the DESs, a 20 w/w % of water was added. The solid residue resulting from hydroalcoholic extraction was extracted at 120°C (100 g/kg s/l ratio) for 24 h. After that, the resulting mixture was precipitated, centrifuged, and lyophilized, allowing the recovery of lignin as black-brown powder in yields ranging from 2 to 8 w/w % with respect to the starting material. On the contrary, in the case of ChCl:glycerol, the extraction yield was very low (<1%) and therefore was excluded for further analysis.

The three lignin samples were then dissolved in DMSO, and their antioxidant properties were initially assessed using the DPPH assay. In Figure 5.13, the EC_{50} values are reported, revealing excellent results for all the lignins extracted.

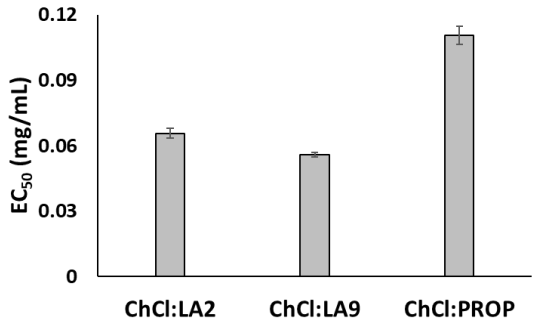

Figure 5.13. DPPH assay results for lignins obtained with selected DESs. Reported are the mean ± SD values of at least three experiments.

Although no substantial difference was observed, considering previous literature work demonstrating the excellent ability of DES ChCl/LA2 to recover phenolic compounds from other by-products, the lignin sample obtained using this solvent was selected for further analysis.

To get additional information on the ChCl:LA2-recovered lignin, the sample was dissolved in DMSO and then analyzed by Uv-Vis spectroscopy after proper dilution in methanol. The Uv-Vis spectra of lignin showed a broadband absorption in the range 250-700 nm, typical of lignin moieties and at the same time the disappearance of the absorption maxima at around 280 and 310 nm, typical of hydroxycinnamic acid, suggesting the absence of low molecular weight phenolic compounds (Figure 5.14 panel a). In agreement with these results, the HPLC analysis with a Uv-Vis detector at 254 nm showed no significant peaks.

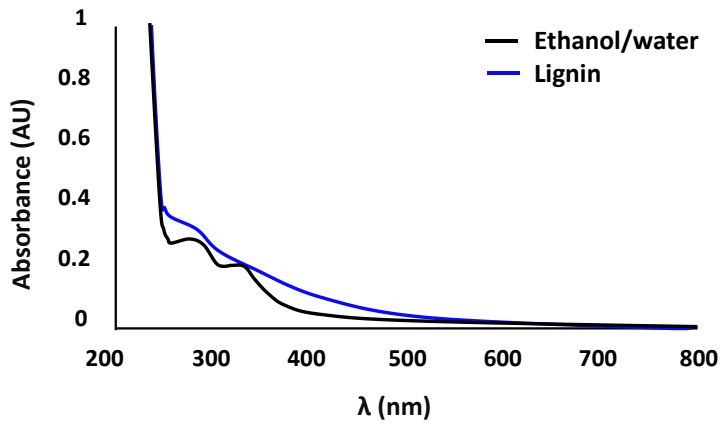

Figure 5.14. Uv-Vis spectrum of lignin solubilized in DMSO, after proper dilution in methanol.

In addition, chemical degradation treatments, such as alkaline hydrogen peroxide degradation and acid degradation, commonly used for the qualitative and quantitative analysis of lignin markers and hydrolazable tannins, respectively were carried out. In the case of acid degradation mixture, no

products were detected by HPLC analysis, indicating the absence of significant amounts of hydrolyzable tannins in the lignin sample. On the other hand, the HPLC profile of the alkaline hydrogen peroxide degradation mixture showed, among others, a peak eluted at around 24.5 min (Figure 5.15), identified as vanillic, by comparison with an authentic standard, indicative of the presence of guaiacyl units in the lignin sample.

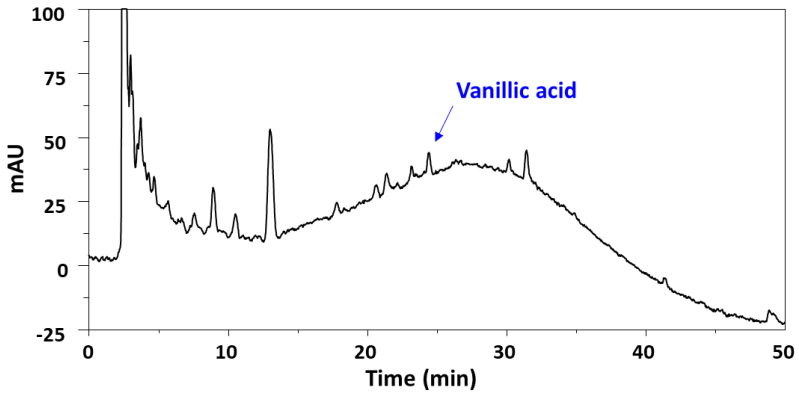

Figure 5.15. Elutographic profile of the alkaline hydrogen peroxide degradation mixture of lignin.

5.2.3 Antioxidant properties of dSCG extracts

The sequential treatment of dSCG with ethanol/water and then with ChCl:LA2, allowed the recovery of a low molecular weight phenolic compounds and a lignin enriched sample, respectively. In addition, the antioxidant activity of the two fractions was evaluated by DPPH and FRAP assays, whereas the total phenol content (TPC) was determined by Folin-Ciocalteu assay.

As shown in Table 5.3, in the case of DPPH comparable EC_{50} values between lignin and hydroalcoholic extract was determined, whereas in the FRAP assay lignin was found to be about 2.5-fold less active. Despite this, both samples exhibited marked reducing properties and even higher with respect starting spent coffee ground reported in literature [117]. On the contrary, the total phenol

content was higher in the case of lignin of about 2-fold than that observed for the hydroalcoholic extract. As already proposed in paragraph 5.1.2, the observed differences could be due to the different mechanisms by which the compounds exert the antioxidant activity and the different solubility of the compounds in the media of the assays.

Table 5.3. Antioxidant properties and total phenolic content of the two fractions recovered from the sequential extraction of dSCG. Reported are the mean ± SD values of at least three experiments.

	DPPH EC_{50} (mg/mL)	**FRAP (mg of Trolox/mg of samples)**	**TPC (mg of gallic acid/mg of samples)**
Hydroalcoholic extract	0.054 ±0.002	0.635 ±0.002	0.098 ±0.008
Lignin	0.061 ±0.001	0.257 ±0.021	0.171 ±0.004

Finally, the presence of condensed tannins and of flavonoids was determined by the vanillin-HCl and the total flavonoids content (TFC) assay, respectively. In all samples and for both assays, no appreciable values were obtained.

5.3 Recovery of low and high molecular weight phenolic compounds from other agri-food by-products by a sequential two-steps protocol

5.3.1 Evaluation of the antioxidant properties of low molecular weight phenolic compounds recovered from different agri-food by-products

Based on the results reported in the previous paragraph, the possibility to extend the sequential two-step protocol to the recovery of low and high molecular weight phenolic compounds from other agrifood by-products was evaluated.

In this perspective, the first part of this work was aimed at the preparation and evaluation of the antioxidant properties of different agrifood wastes. Pomegranate peel and seeds, grape pomace, spent coffee ground, nuts shells,

pineapple peel and stem, tomato and apples peel and seeds, orange peels were selected as fruit and vegetable by-products.

In the initial extraction procedure, each waste was lyophilized and roughly minced using a common blender. On the other hand, chestnut, pistachio, hazelnut and peanut shells were also finely minced with the aid of a ball mill. The resulting materials were extracted using water at a 100 mg/mL s/l ratio. The mixtures were kept under magnetic stirring for 60 min at room temperature and then centrifuged for 10 minutes. The solid residue was lyophilized, and the supernatants collected. Among all, the highest extraction yields ($\geq$ 50 w/w %) were observed in the case of grape pomace and pomegranate, whereas the other wastes exhibited values lower than 10 w/w %

Furthermore, the antioxidant properties of all the selected by-products were investigated by DPPH and FRAP assays (Table 5.4). Among all by-products investigated, pomegranate and grape pomace extracts showed the most promising results. In particular, pomegranate extract exhibited EC_{50} value and Trolox eqs. 10-fold higher than grape pomace extract. On these samples, the Folin-Ciocalteu assay was also carried out. In agreement with the antioxidant properties, pomegranate extract revealed the highest content of phenolic compounds (up to 10- fold with respect to the others).

Table 5.4. Antioxidant properties and total phenolic content of the selected by-products extracts. Reported are the mean ± SD values of at least three experiments.

Samples	DPPH EC_{50} (mg/mL)	FRAP (mg of Trolox/mg of samples)	TPC (mg of gallic acid/mg of samples)
Pomegranate	*0.0222 ± 0.0002*	*0.35 ± 0.01*	*0.1575 ± 0.0003*
Pineapple	3.4 ± 0.1	0.0046 ± 0.0002	0.0034 ± 0.0002
Tomato	5.3 ± 0.1	0.0029 ± 0.0001	0.0019 ± 0.0001
Spent coffee ground	0.507 ± 0.001	0.139 ± 0.007	0.063 ± 0.002
Grape Pomace	*0.4 ± 0.01*	*0.037 ± 0.001*	*0.0201 ± 0.0001*
Peanuts	1.3 ± 0.2	0.0174 ± 0.0003	0.0106 ± 0.0001

The optimal waste product for the sequential two-step protocol was selected based on the antioxidant properties of low molecular weight phenolic compounds recovered from different agri-food by-products. Actually, in the perspective of incorporating these compounds into biopolymers for food packaging applications, it is of the outmost importance to have very active low molecular phenolic compounds in terms of antioxidant properties. In fact, these compounds are generally soluble in common solvents and can better interact with foods. Based on these findings, pomegranate extract, that exhibited the highest antioxidant activity and recovery yields with respect to all the other by-products examined, was used in further analysis.

5.3.2 Extraction and characterization of low molecular weight phenolic compounds from pomegranate peel and seeds by-products

Firstly, the pomegranate extraction process of low molecular weight phenolic compounds was optimized. Other two solvents such as water and water/ethanol 4:6 v/v were selected, and the extraction process described in the previous

paragraph 5.3.1 was performed. The supernatants were recovered by centrifugation and the extraction yields calculated. As shown in Table 5.5, the aqueous and hydroalcoholic extracts were obtained in quite similar and high yields, whereas in the case of ethanolic extract a very low value was observed.

Table 5.5. Yields of aqueous and hydroalcoholic extracts obtained from pomegranate, referred to the dry weight of the starting material. Reported are the mean of two experiments.

	Extraction yields (w/w %)
H_2O	48.7
EtOH	13.6
EtOH/H_2O	43.5

In addition, the antioxidant properties, and the total content of phenols (TPC) of the three extracts were evaluated by DPPH, FRAP and Folin-Ciocalteau assay, respectively. As shown in Table 5.6, the water and hydroalcoholic extracts showed similar antioxidant activity and content of phenols and 2-fold higher than that observed in the case of ethanol as extraction solvent.

Table 5.6. Antioxidant properties and total phenolic content of the water, alcoholic and hydroalcoholic extracts. Reported are the mean ± SD values of at least three experiments.

Solvent	**EC_{50} (mg/mL) DPPH**	**mg of Trolox/mg of sample FRAP**	**mg of gallic acid/ mg of sample TPC**
water	0.0222 ± 0.0002	0.35 ± 0.01	0.1575 ± 0.0003
Ethanol	0.049 ± 0.001	0.26 ± 0.02	0.087 ± 0.02
Ethanol/water	0.020 ± 0.001	0.33 ± 0.02	0.24 ± 0.04

To get information on the phenolic composition, all the three extracts were then analyzed by Uv-Vis spectroscopy and HPLC. As representative example, in Figure 5.16 the elutographic profile of the hydroalcoholic extract is reported. In all cases, the presence of two peaks eluted at ca. 21 and 36 min and identified as

punicalagin and ellagic acid, by LC-MS analysis and comparison of chromatographic profile with an authentic standard, were observed.

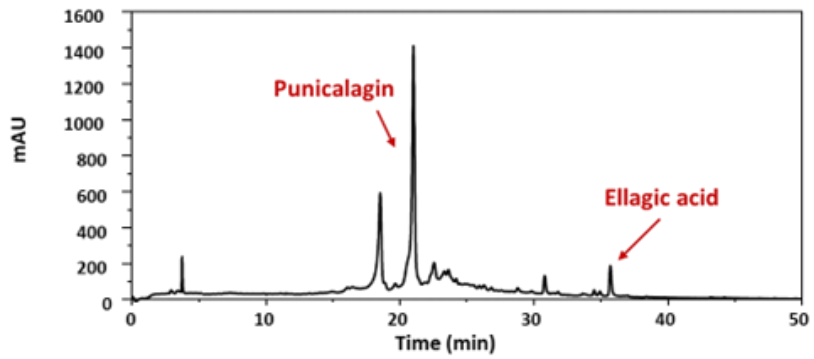

Figure 5.16. HPLC profile of pomegranate extracts (0.085 mg/mL).

In addition, for each extracts the amount of ellagic acid was determined and compared to extract obtained using DMSO as extraction solvent, commonly known for its ability to dissolve a wide spectrum of phenolic compounds. As shown in Table 5.7, the extraction yields for all the selected solvent are very similar and only 25-45% lower than that observed in the case of DMSO.

Table 5.7. EA extraction and recovery yields from water, ethanolic, hydroalcoholic pomegranate extracts.

Pomegranate	**Extraction Yield (% w/w_s)[1]**
Water	0.20
Ethanol	0.23
Hydroalcoholic	0.27
DMSO	0.36

[1] w_s: weight of starting material; w_d: weight of dissolved material.

In addition, the Uv-Vis spectra exhibited two absorption maxima at about 260 nm and 375 nm, typical of ellagic acid and punicalagin. In agreement with the higher antioxidant activity, the Uv-Vis spectra of the aqueous and

hydroalcoholic extracts showed a slightly more intense absorbance with respect to that observed for the ethanolic extract (Figure 5.17).

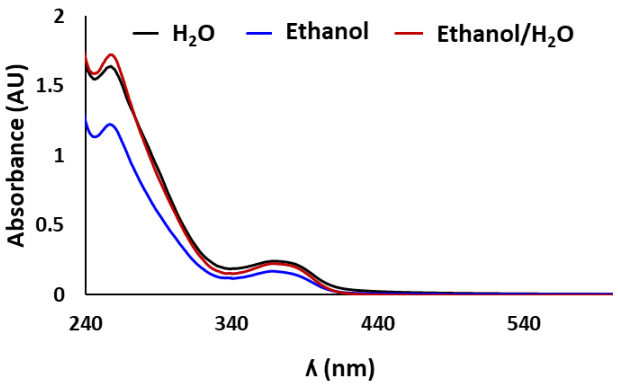

Figure 5.17. Uv-Vis spectra of hydroalcoholic pomegranate extracts (0.085 mg/mL).

Despite the lower antioxidant activity, preliminary antimicrobial studies showed best results in the case of ethanolic extracts, indicating the presence of non-chromatographable species with antimicrobial properties (Table 5.8). In fact, for all the other extracts no activity was observed.

Table 5.8. Antibacterial activity ethanol extract of pomegranate. All the experiments were run in triplicate.

Bacterial Strain		
Salmonella typhimurium ATCC® 14028	*Salmonella enteriditis* RIVM 706	*Enterococcus faecalis* ATCC® 29212
> 0.5 mg/mL	**> 0.5 mg/mL**	**> 0.5 mg/mL**
E. coli ATCC® 25922	*S. aureus methicillin resistant* (MRSA)	*S. aureus* ATCC® 12600
> 0.5 mg/mL	**0.5 mg/mL (MCB)**	**0.5 mg/mL (MCB)**

Therefore, the ethanolic extract was selected as the most promising low molecular weight functional additive for active packaging. With a view to fully exploit the phenolic compounds present in pomegranate waste, in subsequent experiments the possibility to recover high molecular weight phenolic compounds from the solid residue deriving from the ethanol extraction using green solvents was evaluated.

5.3.3 Extraction and characterization of high molecular weight phenolic compounds from ethanol solid residue of pomegranate by-products

Based on the protocol reported in paragraph 5.2.2, the recovery of high molecular weight phenolic compounds from the solid residue deriving from the treatment of pomegranate by-products with ethanol using DESs, such as ChCl:LA2 and ChCl:LA9, was performed. The solid residue resulting from ethanolic extraction was treated under the experimental conditions previously reported (100 g/kg s/l ratio, 120 °C, 20w/w % of water), for 24 h. Subsequently,

the recovered lignin was precipitated using KCl 1% w/v solution. After centrifugation and lyophilization, the yields of recovered high molecular weight phenolic compounds was determined, calculated with respect to the starting material (5 and 12 w/w %) and dissolved DES material (5.4 and 14.3 w/w %), in the case of ChCl:LA2 and ChCl:LA9, respectively. Based on the higher yields observed in the case of ChCl:LA9, this latter was selected as the best DESs. In subsequent experiments, to further improve the extraction procedure, the water content in the DES was varied from 0% to 40 w/w %. As shown in Table 5.9 no significant differences were observed.

Table 5.9. Extraction yields of high molecular weight phenolic compounds from the solid residue obtained after ethanol extraction of pomegranate waste following treatment with ChCl:LA9 (100 g/Kg, 120°C, 24h), in the presence of different water contents.

	Extraction yields (%)	
Water content	**(% w/w_s)[1]**	**(% w/w_d)[1]**
0%	12	15
20%	12	14
40%	9	11

[1] w_s: weight of starting material; w_d: weight of dissolved material.

In addition, the DMSO- soluble fraction (5 mg/mL) of the recovered high molecular weight phenolic compounds, was characterized in term of antioxidant properties and TPC. The high molecular weight phenolic compounds exhibited higher antioxidant properties than those obtained for the ethanolic extract (see Table 5.10), likely due to the cleavage and consequential release, after DES treatment, of more active antioxidant compounds.

Table 5.10. Antioxidant properties and TPC of sample recovered by treatment with ChCl:LA9. Reported are the mean ± SD values from at least three experiments.

	DPPH EC_{50} (mg/mL)	FRAP (mg Trolox/mg of sample)	TPC (mg gallic acid/mg of sample)
ChCl: LA9	0.017 ± 0.001	0.75 ± 0.01	0.38 ± 0.01

To gain further information on the main components of the DES-recovered high molecular weight phenolic fraction, this was analyzed by HPLC and Uv-Vis spectroscopy. The elutographic profiles show the presence of two detectable species at 31 and 36 min (Figure 5.18 panel a), identified as gallagic acid dilactone and ellagic acid, respectively. This latter likely derives from the hydrolysis of hydrolysable tannins, induced by DESs treatment [305]. A percentage of EA around 6% was quantified. The total extraction yield of ellagic acid, given by the sum of the quantity of this compound extracted by the two-step treatment, turns out to be higher with respect to that obtained with DMSO, a solvent in which ellagic acid is completely soluble. As result, the main reasonable conclusion is that the treatment with eutectic solvents allows effective degradation of hydrolyzable tannins, in particular punicalagin, with the concomitant release of the powerful antioxidant ellagic acid. In agreement with the high content of EA, the Uv-Vis spectrum showed an absorption maximum at 360 nm, typical of this compound.

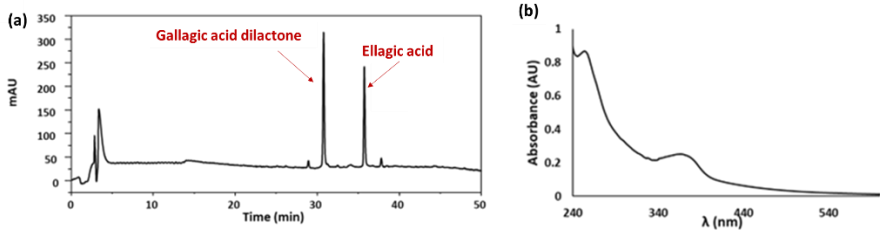

Figure 5.18. (a) HPLC profile (1 mg/mL) and (b) Uv-Vis spectrum (0.0125 mg/mL) of ellagic acid-rich fraction recovered by treatment with ChCl:LA9.

In order to obtain more information on the non-cromatographable components of the ellagic acid-rich fraction, chemical degradation treatments commonly used for the qualitative and quantitative analysis of phenolic polymers were performed. In the case of alkaline hydrogen peroxide degradation mixture, as well as for the supernatant of the acid degradation, no products were detected for the sample. On the other hand, the HPLC profile of the precipitate of the acid degradation and the alkaline fusion mixture showed elutographic profiles (Figure 5.19) very similar to that of the starting high molecular weight fraction dissolved in DMSO (Figure 5.19 panel a). In particular, the elutographic profile of the alkaline fusion mixture highlighted the presence, among others, of two peaks eluted between 24 and 26 min, characterized by an extremely low intensity and associated with vanillic acid and syringic acid, respectively, two markers of high molecular weight phenolic polymers, such as lignin.

Furthermore, a quantitative analysis of the acid degradation mixture showed an ellagic acid content of 11 w/w %, about twice that determined for the ellagic acid-rich fraction obtained by the treatment with ChCl:LA9, probably due to further degradation of residual hydrolysable tannins, not degraded during DES treatment (Figure 5.19).

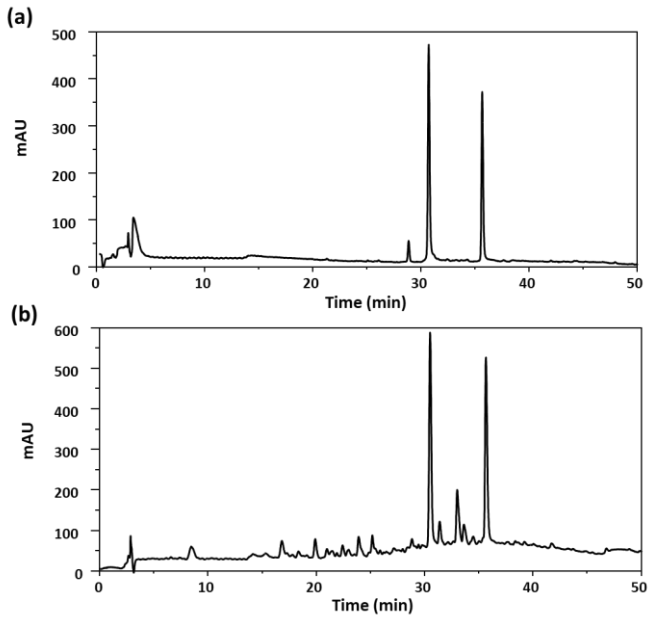

Figure 5.19. HPLC profiles of the chemical degradation mixtures of ellagic-acid-rich fraction obtained from the DES treatment. (a) Precipitate from the acid degradation mixture. (b) Alkali fusion mixture.

***Main Outcomes of The Study*:**

- A sequential two-steps conventional/deep eutectic solvent (DES)-based treatment as an efficient strategy for the recovery of antioxidant low and high molecular weight phenolic compounds from defatted SCG (dSCG) and pomegranate peel and seeds was developed.
  - All the recovered high and low molecular weight phenolic compound samples exhibited very marked antioxidant properties as evaluated by DPPH and FRAP assays and a high phenolic content as demonstrated by TPC assay.

5.4 Experimental Section

Materials and Methods. Pomegranates, apples, pistachios, chestnuts, peanuts, hazelnuts and pecan nuts were purchased at a local supermarket and shells were recovered by hand peeling. Spent coffee grounds were collected from a local coffee shop. Grape pomace was kindly provided by Dott. Daniele Naviglio (Department of Chemical Sciences, University of Naples "Federico II", Naples, Italy). 30 w/v % hydrogen peroxide, 2,2-diphenyl-1-picrylhydrazyl (DPPH), iron (III) chloride, 2,4,6-tris(2-pirydyl)-s-triazine (TPTZ), Folin-Ciocalteu reagent, (±)-6-hydroxy-2,5,7,8-tetramethylchromane-2-carboxylic acid (Trolox), gallic acid, ellagic acid, vanillin, benzyl mercaptan, vanillic acid, and syringic acid were obtained from Sigma-Aldrich.

Uv-Vis spectra were recorded using a Jasco V-730 spectrophotometer.

ATR-FTIR spectra were recorded on a Nicolet 5700 Thermo Fisher Scientific instrument. Spectra were recorded as an average of 132 scans in the range 4000−450 cm^{-1} (resolution of 4 cm^{-1}).

^1H NMR spectra were recorded in DMSO-d_6 at 400 MHz on a Bruker instrument.

HPLC analysis were performed on an instrument equipped with an Agilent G1314A Uv-Vis detector, using a Phenomenex Sphereclone ODS column (250 × 4.60 mm, 5 µm) at a flow rate of 1.0 mL/min; the gradient elution was as follows:

Eluant I: 0.1% formic acid (solvent A)/methanol (solvent B), 5% B, 0-10 min; from 5 to 80% B, 10-47.5 min; the detection wavelength was set at 254 nm.

Eluant II: 0.1% formic acid (solvent A)/acetonitrile (solvent B), from 5 to 20% B, 0-47.5 min; the detection wavelengths were set at 254, 380, 320 and 400 nm.

LC-MS analysis were run on an Agilent LC-MS ESI-TOF 1260/6230DA instrument operating in positive ionization mode in the following conditions: nebulizer pressure 35 psig; drying gas (nitrogen) 5 L/min, 325 ◦C; capillary voltage 3500 V; fragmentor voltage 175 V. A Eclipse Plus C18 column (150 ×

4.6 mm, 5 µm) at a flow rate of 0.4 mL/min was used, using the same eluant as above.

Electron paramagnetic resonance (EPR) measurements were performed using a Bruker Elexys E-500 spectrometer equipped with a superhigh sensitivity probe head. The weighed amounts of the samples were transferred to flame-sealed glass capillaries, which in turn were coaxially inserted in a standard 4 mm quartz sample tube. Measurements were performed at room temperature. The instrumental settings were as follows: sweep width 140 G; resolution 1024 points; scan time 20.97 s. The amplitude of the field modulation (1.0 G) was preventively checked to be low enough to avoid detectable signal overmodulation. The microwave power was optimized to avoid microwave saturation of resonance absorption curve. 16 scans were accumulated to improve the signal-to-noise ratio. For power saturation experiments, the microwave power was gradually incremented from 0.02 to 164 mW. The g value and the spin density were evaluated by means of an internal standard, Mn^{2+}-doped MgO, prepared by a synthesis protocol reported in the literature [224]. Since sample hydration was not controlled during the measurements, spin density values have to be considered as order of magnitude estimates [225].

Preparation of agri-food by-products extracts. Each agri-food by-products was roughly minced using a common blender. In the case of dSCG, the agrifood by-products was extracted with water, ethanol or ethanol/water 6:4 v/v for 90 min at 90°C (100 mg/mL s/l ratio). In the case of all the other agrifood by-products, each waste was extracted with 10 mL of water, ethanol or ethanol/water 6:4 v/v for 60 min at room temperature. The mixtures were then centrifuged (7000 rpm) for 10 min and the supernatants were recovered. Subsequently, the solid residues were treated with fresh solvent under the same conditions described above for two times. The combined supernatants were collected, and when ethanol was used as extraction solvent, it was removed by

use of a rotatory evaporator. The resulting solids were subjected to freeze-drying and to remove traces of residual solvent, kept under vacuum for 24 h.

Deep eutectic solvents (DES) extraction procedure. A procedure previously reported was followed with slight modifications [286]. In the case of nutshells, these by-products were roughly minced using a common blender and then pulverized by treatment in a Fritsch Pulverisette 23 ball mill for 15 min at 50 osc/s. Briefly, choline chloride and lactic acid were mixed at 1:2 mol/mol ratio and heated at 50 °C under stirring until a homogeneous liquid was formed. The DES thus obtained, indicated as ChCl:LA2, was stored in the dark at ambient temperature. No crystal precipitation was observed over the period of use. Subsequently, each shell were added to of ChCl:LA2 containing 20 w/w % water in ratio 1:10 w/w respectively. The resulting mixture was stirred in a pyrex glass bottle at 120 °C. After 24 h, the mixture was cooled at room temperature and centrifuged (7000 rpm, 4 °C, 10 min). The solid residue and supernatant were separated. Subsequently, the solid residue was washed three times with 50 mL of ethanol (7000 rpm, 4 °C, 10 min), collected and dried using a rotary evaporator. The obtained residue was added to the supernatant collected from the initial centrifugation, which was then poured into 1 L of 0.01 M HCl (for 10 g of nutshells) and kept at 4 °C over night. After that the formation of a brown precipitate was observed. The precipitate was then recovered by centrifugation (7000 rpm, 10 min, 4 °C), washed twice with 0.01 M HCl and once with distilled water, and lyophilized.

In the case of dSCG, in addition to the previous reported DES, other type of DESs were prepared:

1. Choline chloride/lactic acid at 1:9 mol/mol ratio (ChCl:LA9)
2. Choline chloride/glycerol at 1:2 mol/mol ratio (ChCl:GLY)
3. Choline chloride/1,2- propanediol at 1:2 mol/mol ratio (ChCl:PROP)

In the case of pomegranate only ChCl:LA2 and ChCl:LA9 were performed. To this latter, different percentage of water (0-20-40 w/w %) were added. To

recover HMW phenolic compounds fraction, the supernatants collected from the initial centrifugation were poured into 200 mL of 1% KCl and kept at 4 °C until the precipitation of a light brown solid was observed.

DPPH Assay. Samples were added to 200 μM ethanolic solution of DPPH and stirred for 10 min. After this time, the absorbance of the solution at 515 nm was measured. Trolox was used as a reference antioxidant. Experiments were run in triplicate [227,275].

The final doses of each material tested are:

- 0.02-0.4 mg/mL (lignin nutshells)
- 0.025-0.075 mg/mL (hydroalcoholic extract of dSCG)
- 0.025-0.4 mg/mL (lignin of dSCG)
- 0.01-6.3 mg/mL (LMW pomegranate extract)
- 0.006-0.025 mg/mL (HMW pomegranate extract)

Ferric Reducing/Antioxidant Power (FRAP) Assay. Samples were added to 0.3 M acetate buffer (pH 3.6) containing 1.7 mM $FeCl_3$ and 0.83 mM TPTZ and stirred for 10 min. After this time, the absorbance of the solution at 593 nm was measured. Results were expressed as Trolox equivalents (eqs). Experiments were run in triplicate [228].

The final doses of each material tested are:

- 0.025-0.2 mg/mL (lignin nutshells)
- 0.00312-0.0125 mg/mL (hydroalcoholic extract of dSCG)
- 0.0025-0.01 mg/mL (lignin of dSCG)
- 0.0003-0.787 mg/mL (LMW pomegranate extract)
- 0.0015-0.01 mg/mL (HMW pomegranate extract)

Total Phenolic Content (TPC) Assay. Samples were added at a final dose of 0.0125−0.4 mg/mL to a solution consisting of Folin-Ciocalteu reagent, 75 g/L Na_2CO_3, and water in a 1:3:14 v/v/v ratio. After 30 min incubation at 40 °C, the absorbance at 765 nm was measured. Gallic acid was used as reference compound. Experiments were run in triplicate [308].

The final doses of each material tested are:

- 0.0125-0.4 mg/mL (lignin nutshells)
- 0.025-0.05 mg/mL (hydroalcoholic extract of dSCG)
- 0.025-0.04 mg/mL (lignin of dSCG)
- 0.005-3.15 mg/mL (LMW pomegranate extract)
- 0.0037-0.015 mg/mL (HMW pomegranate extract)

Vanillin-HCl Assay. Samples were added to 1 mL of 1 w/v % vanillin solution in methanol. Subsequently, 1 mL of 9 M HCl was added. The resulting mixture was incubated at 30 °C for 10 min. Finally, the absorbance at 500 nm was measured. Catechin was used as reference compound. Experiments were run in triplicate [309].

The final doses of each material tested are:

- 0.0625–2 mg/mL (lignin nutshells)
- 20 µL of a DMSO solution (2 mg/mL) of the lignin

Alkaline Hydrogen Peroxide Degradation. To 1 M NaOH (1 mL), 10 mg of each sample and 50 µL of 30% hydrogen peroxide were added in this order. The mixture was stirred and after 24 h treated with 5 w/v % $Na_2S_2O_5$, taken to pH 3 with 6 M HCl, filtered on a 0.45 µm PVDF filter, and analyzed by HPLC [306].

Alkali Fusion. Finely grinded KOH (100 mg), NaOH (100 mg) and $Na_2S_2O_4$ (2 mg) were mixed in a Pyrex tube. Subsequently, they were kept at 240 ◦C until fusion of the reagents occurs. Then, to this mixture, 20 mg of the HMW phenolic compounds (ChCl:LA9 with 0 w/w % of water) was added and kept at 240 ◦C. After 10 minutes, 10 mL of a 1% sodium dithionite ($Na_2S_2O_4$) and of 6 M HCl solution were added. The resulting mixture were extracted with ethyl acetate (3 × 15 mL) and the combined organic layers were dried over sodium sulfate and evaporated to dryness. The solid residue was reconstituted in 2 mL of methanol, filtered on a 0.45 µm polyvinylidene fluoride (PVDF) filter, and analyzed by HPLC [310].

Acid Degradation. 50 mg of each sample were placed in a pyrex tube with 5 mL of 4 M HCl. The mixture was vortexed for 1 min and incubated in an oven at 90 ◦C. After 24 h, they were cooled, and the pH was adjusted to 2.5 with 6 M NaOH and centrifuged for 10 min at 7000 rpm. The supernatants were recovered, taken to 10 mL by addition of water. After filtration on a 0.45 μm PVDF filter, all the obtained solution were analysed by HPLC, whereas the solid residues were dissolved in 10 mL of DMSO/methanol 1:1 v/v before being analysed (*Eluant I*: 0.1% formic acid (solvent A)/methanol (solvent B), 5% B, 0-10 min; from 5 to 80% B, 10-47.5 min; detection wavelength: 254 nm) [305]**.**

Thiolysis. To 2 mL of methanol, 20 μL of 37% w/w HCl and 50 μL of benzyl mercaptan 8 mg of each sample were added and stirred at 40 °C. After 1 h, the mixture was diluted in 5 mL of methanol/water 1:1 v/v and directly analyzed by HPLC.

Total Flavonoid Content (TFC) assay. 20 μL of a DMSO solution (2 mg/mL) of the lignin obtained from the extraction with ChCl:LA2, were added to water up to a total volume of 600 μL and then mixed with 600 μL of a 2% w/w aluminum chloride solution in water. After mixing, the solution was incubated for 60 min at room temperature. The absorbance of the reaction mixtures was measured at 420 nm. Quercetin was used as standard. Experiments were run in triplicate.

Chapter 6

The Yin (organic) and Yang (inorganic) hybrid systems for biomedical and electronic applications

Over the past two decades, significant research efforts have been devoted to development of hybrid systems, combining the great versatility of organic materials with the interesting property profiles often associated with inorganic materials. These intrinsic characteristics make hybrids promising compounds for a variety of applications in electronic and biomedical fields [311].

Of great interest for biomedical applications are biopolymer-based hybrids, representing a solid bridge between scientific and technological world as a result of their excellent adaptive nature and various properties. A most representative example is represented by silver nanoparticles (AgNP) for which a wide range of applications in photonics, electronics and catalysis [312], as well as in medicine as bactericidal, antifungal and antitumor agents has been described [313]. Yet, preparation of AgNPs may prove critical, due to the environmental toxic stabilizing agents sometimes used. Therefore, green and alternative strategies have been developed in the last decades. In fact, the use of agri-food by-product-derived phenolic compounds as functional additives have become increasingly attractive, since, beside acting as reducing agents capable of generating silver nanoparticles, they may provide antioxidant properties, antimicrobial activity, and mechanical properties. In addition, the incorporation of natural bioactive compounds represents a green alternative to minimize the use of chemical additives [314].

On the other hand, for electronic applications, the undisputed star is represented by graphene-based materials. As already mentioned in the Introduction, one of

the reasons for the fast progress of graphene research is the treasure of the unique properties of this material. However, what makes it special, is that all these properties are combined in a single material. Transparency–conductivity–elasticity can find use in flexible electronics, while transparency–impermeability–conductivity can be exploited for transparent protective coatings. The list of such combinations is ever growing and the combination of these materials with phenols and polyphenols can give rise to unexpected, so far unexplored properties opening new applications perspectives [315].

On these bases, this chapter will be focused on:

- exploitation of Pecan Nut Shells (PNS) as reducing agent for *in situ* synthesis of silver nanoparticles using a mechanochemical or wet-chemical synthesis route and the evaluation of the photocatalytic, antimicrobial and antioxidant properties;
- the use of the lignin recovered from chestnut shells as reducing agents for the *in situ* mechanochemical synthesis of antibacterial silver nanoparticles and their encapsulation as active compounds into D,L-polylactic acid as biopolymer in the form of electrospun fibers containing cellulose nanocrystals or chitosan;
- the electrofabrication of catechol-graphene-chitosan composite hydrogels, possessing the graphene metallic conductivity and catechol redox-activity, evaluated using an array of electrochemical top-down methods.

Result and Discussion

6.1 Pecan Nut Shell-mediated synthesis of silver nanoparticles *via* mechanochemistry: a green approach to a multifunctional material with photocatalytic, antibacterial and antioxidant properties

6.1.1 Silver ion reduction by Pecan Nut Shell: wet-chemical *versus* mechanochemical approach

Pecan Nut Shells (PNS) particles were finely minced with the aid of a vibratory sieve shaker, to obtain a homogenous powder with size distribution ranging from 75 to 125 μm. The final material was then employed for the preparation of AgNPs, following a previously developed procedure for a wet-chemical approach with slight modifications [197]. Briefly, PNS (1% w/v) powder was taken under vigorous stirring in a 10 mM $AgNO_3$ aqueous solution for 24 h, after that the solid material was recovered by centrifugation in 75% w/w yield.

In addition to the conventional wet methodology, a mechanochemical approach, based on the use of a vibrational ball mill, was developed. A 85:15 w/w PNS/$AgNO_3$ ratio was used and the resulting solid mixture was placed into a ball mill for 90 min operating at 60 Hz. To get information on the Ag(0) content, XRD analysis was then performed. As shown in Figure 6.1 panel a, in all samples a strong diffraction peak at 38.3° 2θ was observed, suggesting the presence of Ag(0) with a face-centred cubic structure. In particular, a percentage of Ag(0) about 4 ± 2% w/w and 8 ± 4% w/w for the wet-chemical sample and for the ball-milled sample, respectively, was determined.

These findings highlighted the higher efficacy of the mechanochemical approach for the reduction process of Ag^+ ions. On this basis, further experiments were devoted to the optimization of the experimental conditions for

the mechanochemical preparation of AgNPs. To develop a large-scale process, a planetary ball-mill was employed, allowing to work on 10 grams of material. Initially, several experiments were devoted to the optimization of milling times and PNS/$AgNO_3$ ratios. As evident from XRD analysis (Figure 6.1 panel b), prolonging the milling time up to 180 min not only increased the amount of Ag (0) in the sample, but also resulted in lowering of the width of the peak at 38.3° 2θ indicating the presence of AgNP of increased size. As illustrated in Figure 6.1 panel c the full width at half maximum (FWHM) of the peaks decreases almost linearly with the increase of the time.

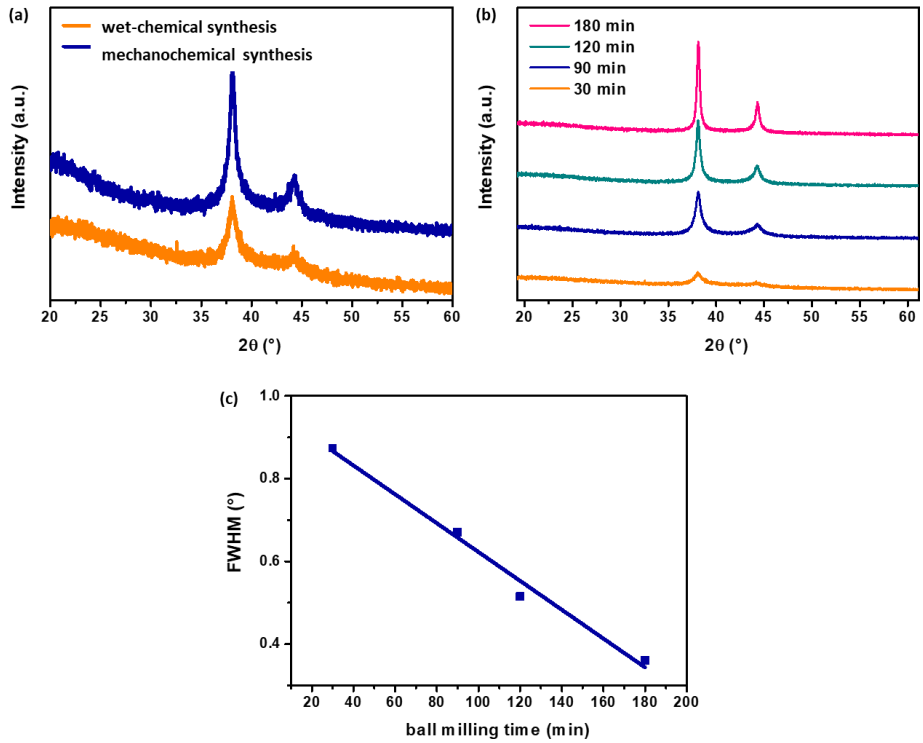

Figure 6.1. (a) XRD patterns of 85:15 w/w PNS/$AgNO_3$ samples obtained by mechanochemical and wet-chemical synthesis; (b) XRD spectra of 85:15 w/w PNS/$AgNO_3$ subjected to varying ball-milling times (increasing from bottom to top); (c) dependence of the FWHM of the main peak on the milling treatment time 85:15 w/w PNS/$AgNO_3$;

In addition, in Figure 6.2 the 55:45 w/w PNS/$AgNO_3$ ratio exhibited a higher percentage content of Ag(0) with respect to 85:15 w/w. In fact, under these conditions and in agreement with the expected theoretical value (about 30%) a 36 ± 7% w/w Ag(0) amount was estimated.

Based on these findings, for further experiments the 55:45 w/w PNS/$AgNO_3$ mixture treated in the planetary ball mill for 180 min was selected. The efficacy of the proposed methodology in providing a quantitative reduction of Ag^+ ions is remarkable and is probably the result of the extremely potent reducing properties of PNS in combination with the successful solvent-free mechanochemical approach. In fact, no characteristic diffraction patterns of the AgCl crystalline phase at 27.8, 32.2, 46.2, 54.8, and 57.5 °2θ were detected [197].

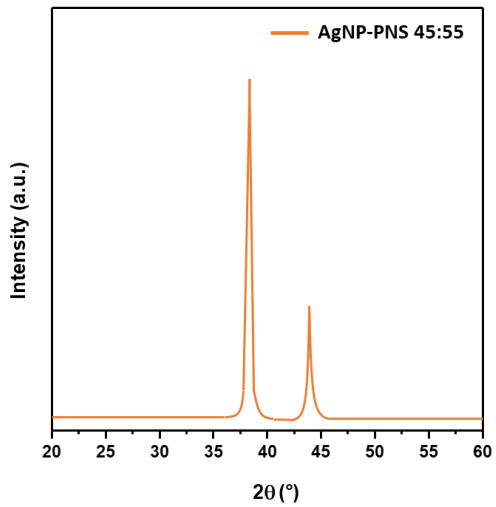

Figure 6.2. XRD pattern of AgNP-PNS 45:55 w/w.

Notably, not many studies reporting a direct comparison between one-step solid state mechanochemical synthesis and traditional wet-chemical methods for AgNPs production are available in the literature.

In addition, the proposed protocol satisfies most of the 12 principles of Green Chemistry: 1) Prevention (no waste is created); 2) Atom Economy (all materials exploited in the process are incorporated into the final product, and PNS act as a stabilizing and reducing agent); 3) Less Hazardous Chemical Synthesis (PNS is a natural substance); 5) Safer Solvents and Auxiliaries (solvent free); 6) Design for Energy Efficiency (the synthesis is performed at room temperature and pressure); 7) Renewable Feedstocks (PNS is a largely available agri-food by-product); 8) Reduce Derivatives (no nanoparticle stabilizers are needed); 12) Inherently Safer Chemistry for Accident Prevention (non-flammable and non-toxic reagents are used).

6.1.2 Morphological and structural characterization of AgNP-PNS

To get addition information on AgNP-PNS, ATR-FTIR analysis was also performed. With regards to ATR analysis, as shown in Figure 6.3 (panel a) a significant decrease compared to PNS of the band at 3300 cm^{-1} associated to OH bond stretching vibration together with CH stretching of methylene (2923 cm^{-1}) and of the band at 1615 cm^{-1} ascribed to the aromatic C═C bonds were observed. This can be explained by the expected involvement of the reducing phenolic OH groups of the B ring of the prodelphinidin type tannins in PNS. The structural modifications induced in the tannins is likely due to the Ag^{+}-induced oxidative dimerization giving rise to purpurogallin-like moieties (Figure 6.3 panel b).

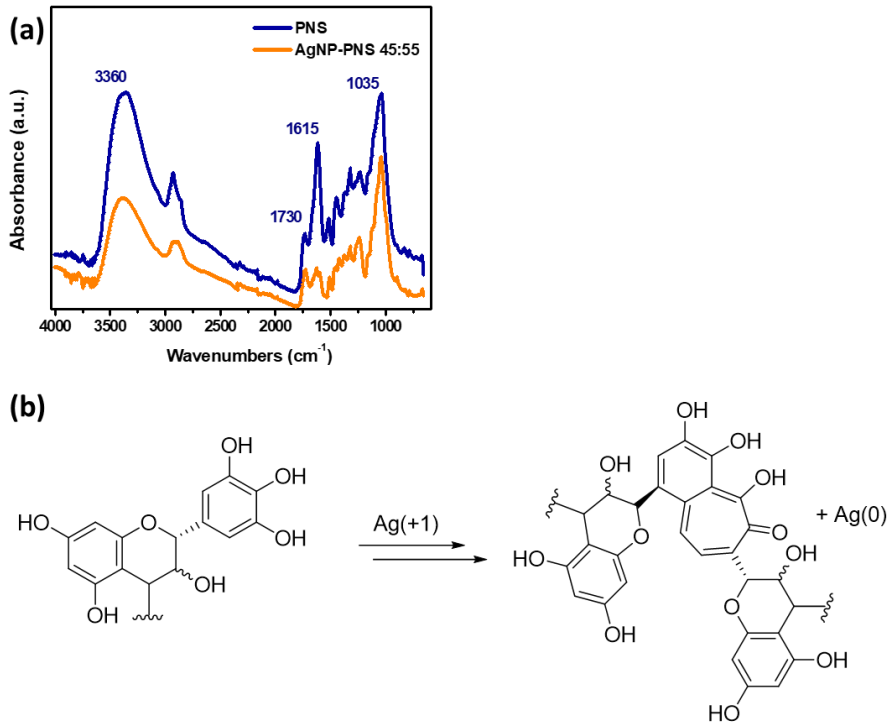

Figure 6.3. (a) ATR-FTIR spectrum of AgNP-PNS (compared with parent PNS); (b) proposed mechanism for Ag^{+} ions reduction by prodelphinidin-type PNS tannins.

In addition, the size and the possible agglomeration of the AgNP-PNS dispersion was measured using DLS analysis. In Figure 6.4 the intensity and the number of particle distributions are reported as a function of the particle size. DLS analysis revealed two distinct peaks at 20 nm and 150 nm, indicating the presence of a moderate number of aggregates within the samples.

Consistent with this result, the examination of the number-based distribution exhibited a very low concentration of aggregates. In fact, most of the sample contained particles of 20 nm, with aggregates percentage lower than 1%.

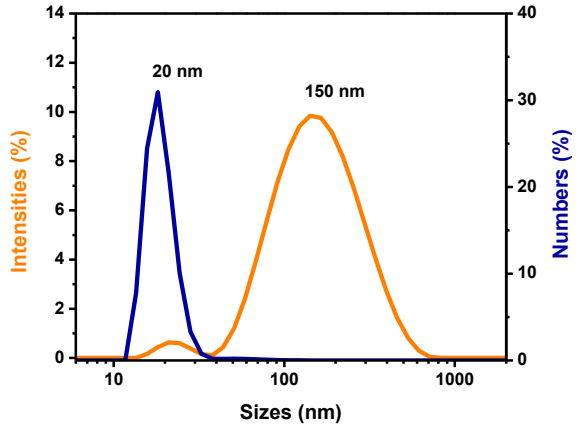

Figure 6.4. Particle size distributions of AgNP-PNS measured by DLS.

SEM and TEM analysis (Figure 6.5 panel a and panel b, respectively) revealed the presence of small particles embedded within the organic biomass matrix. Higher magnification images showed that the observed structures were composed of largely aggregated, complex architecture clusters with dimensions ranging from 100 to 250 nm, and reasonably spherical particles of around 50 nm diameter. These silver nanoparticles exhibited the same order of magnitude of other AgNPs prepared following a wet procedure using a different agri-food by-products [197]. Further investigation will be devoted at assessing whether the small phenolic polymers are coated or linked on silver nanoparticles.

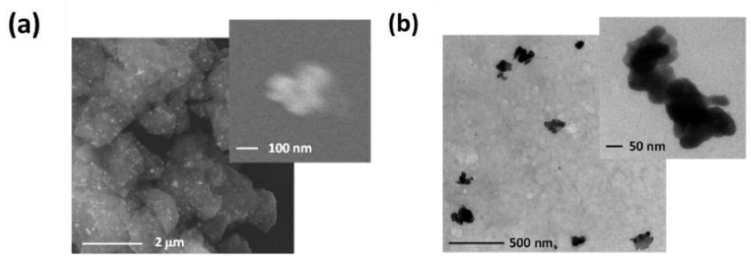

Figure 6.5. Structural and morphological analysis of AgNP-PNS. measured by DLS; (a) SEM and (b) TEM images.

6.1.3 Antioxidant properties of AgNP-PNS

Due to the well-known antioxidant properties of PNS, the antioxidant properties of AgNP-PNS were evaluated as well by two widely used assays, i.e. the DPPH and the FRAP assay, following the "QUENCHER" method. In the case of DPPH assay, AgNP-PNS exhibited a significant decrease of the antioxidant properties in comparison to starting PNS (Table 6.1), due to the lower content of PNS in the AgNP-PNS sample (55% w/w) and to the efficient reduction of Ag^{+} ions by the phenolic units. In spite of the such lowering of the antioxidant activity of AgNP-PNS, it must be noted that the value obtained is still comparable to those of the other phenol-rich waste materials from the agri-food sector reported in literature. On the other hand, in the case of FRAP assay, both PNS and AgNP-PNS exhibited a very low reducing properties toward Fe^{3+} ions. Notably, the obtained results are consistent with the ATR IR spectroscopy, showing a lower relative content of phenolic OH groups in AgNP-PNS compared to PNS. Indeed, the FRAP assay measures the electron transfer capacity of an antioxidant compound, whereas the DPPH assay is a mixed-mode assay measuring both electron transfer and a hydrogen atom transfer mechanism. Therefore, due to the involvement of the phenolic OH groups in AgNP production (Figure 6.3 panel b), a decrease of the hydrogen atom transfer capacity of PNS was expected and can be taken as the main reason for the differences observed between PNS and AgNP-PNS in the two assays.

Table 6.1. Antioxidant properties of AgNP-PNS and PNS. Reported are the mean ± SD values of three experiments.

Sample	EC_{50} (mg/mL)	Trolox eqs (µg/mg of sample)
AgNP-PNS	5.8 ± 0.5	37 ± 4
PNS	0.036 ± 0.002	51.7 ± 0.9

6.1.4 Photocatalytic properties of AgNP-PNS

Diverse Ag(0)-doped materials have been reported in literature for their ability to accelerate the photodegradation of organic dyes such as Methylene Blue (MB). Based on this, several MB photodegradation experiments were performed in order to examine the photocatalytic properties of AgNP-PNS. To a 30 mg/mL MB solution, 0.4 mg/mL solution of AgNP-PNS were added and irradiated for 120 min under visible-light using a solar simulator. The decrease of MB was periodically monitored by Uv-Vis spectroscopy and the percentage of the MB residual amount was calculated. As control experiment, MB degradation was also carried out in absence of AgNP-PNS under visible-light irradiation. As shown in Figure 6.6, an almost complete consumption of MB was obtained within 120 min under visible-light irradiation in the presence of AgNP-PNS, whereas only 23 % dye degradation was detected in the absence of the sample. Notably, a MB consumption around 58% was also detected in the presence of AgNP-PNS without irradiation, suggesting a persistent pro-oxidant activity of the sample. The reactive oxygen species generated through the well-known ability of AgNP to induce oxygen reduction may be responsible for the decay of MB observed under these conditions.

Of course, it is not possible to rule out the possibility that the observed effects are due to adsorption of MB on the AgNP-PNS surface. Yet, this process has been shown to achieve a plateau after 30 minutes, as was actually observed when PNS was utilized in place of AgNP-PNS. Using PNS alone, there were no appreciable changes in the dye degradation with and without irradiation, indicating that AgNPs specifically played a part in the AgNP-PNS sample photocatalytic abilities.

In another series of experiments, the recycling and stability properties of AgNP-PNS as a photocatalyst were examined. AgNP-PNS continued to operate at a

high efficiency in the MB photodegradation studies after three cycles (Figure 6.6 panel b).

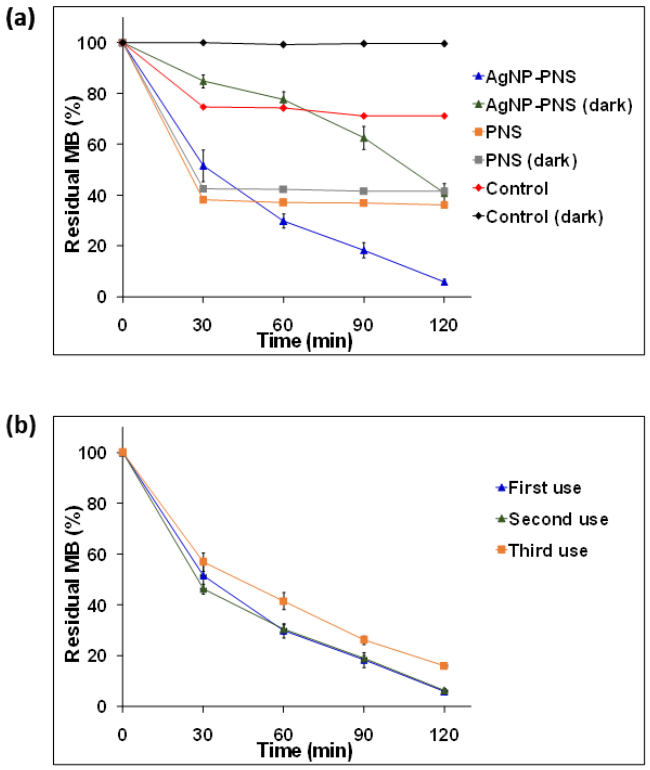

Figure 6.6. MB degradation: (a) photocatalytic properties of AgNP-PNS and controls as evaluated in MB photodegradation experiments; (b) recycling properties of AgNP-PNS as a photocatalyst. Reported are the mean ± SD values of three experiments.

The XRD patterns of AgNP-PNS before and after three-cycle of operation showed that the intensity ratio between the two diffraction peaks didn't change, indicating no changes in the crystal structure and demonstrating its stability (Figure 6.7).

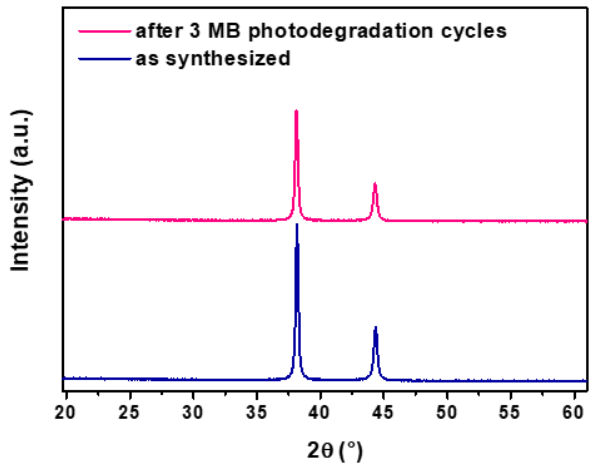

Figure 6.7. XRD pattern of AgNP-PNS as synthesized (blu line) and after three cycles of MB photodegradation (pink line).

6.1.5 Antibacterial and antibiofilm activity of AgNP-PNS

As already reported in literature, AgNPs are well known for their ability to inhibit

bacterial growth. On these bases, firstly the ability of AgNP-PNS to inhibit bacterial growth of two pathogenic bacterial strains, namely *P. aeruginosa* PAO1 and *S. mutans* was evaluated. The first bacterial strains are generally responsible for bloodstream, soft tissue, urinary tract, surgical sites, and wound infections, whereas the second one for dental caries.

As shown in Figure 6.8, the AgNP-PNS at concentrations ranging from 250 to 1000 μg/mL ($p < 0.01$) significantly inhibit bacterial growth after 12 h of incubation. A 54% of growth inhibition against *P. aeruginosa* PAO1 with respect to the control ($p<0.001$) at 24 h was observed.

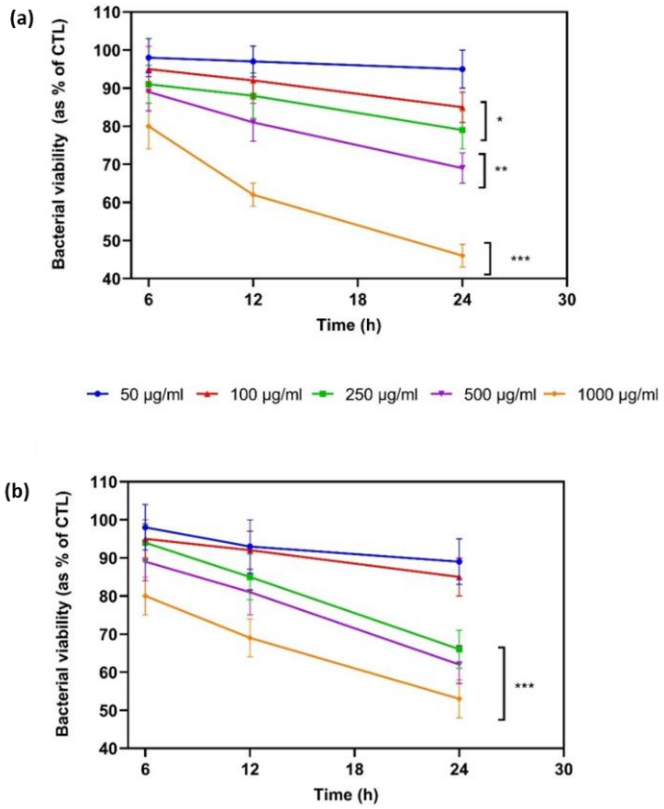

Figure 6.8. AgNP-PNS antibacterial activity against (a) *P. aeruginosa* (PAO1) and (b) *S. mutans* in liquid medium. Bacterial cultures in absence of AgNP-PNS were used as positive controls (CTL). Data were reported as a percentage in comparison with CTRL. For each sample, three different experiments were run, and the results were expressed as the mean ± SD of the values obtained. Statistically significant variations: ** $p<0.01$ and *** $p<0.001$ versus 50 µg/mL and 100 µg/mL.

When AgNP-PNS was tested on agarose beds, a similar antibacterial activity against the two bacterial strains was obtained (Figure 6.9). Notably, when the culture plates were incubated under light irradiation, a significant higher zone of inhibition was observed for AgNP-PNS at all tested doses. At every AgNP-PNS dose, the variations in the mean zone of inhibition were substantially different from controls ($p < 0.05$). It is important to note that PNS alone also exhibited

antibacterial activity, although its effect was significantly less than that of AgNP-PNS.

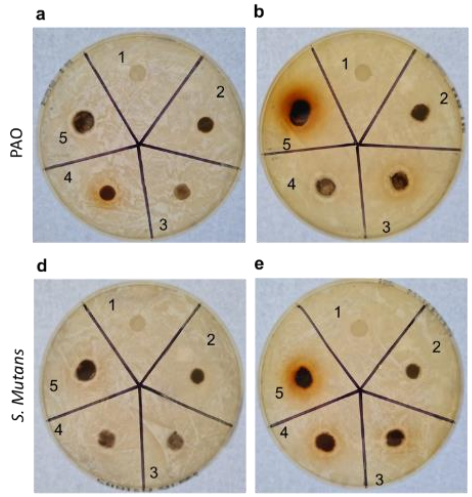

c

Group	Sample	Concentration (µg/ml)	Zone of inhibition (mm) (Mean ± SD)	
			No IR	IR
1	CTL	--	--	--
2	PNS	1000	0.91 ± 0.06	1.80 ± 0.09
3	AgNP-PNS	250	1.05 ± 0.10	2.93 ± 0.15
4	AgNP-PNS	500	1.90 ± 0.12	3.85 ± 0.22
5	AgNP-PNS	1000	2.81 ± 0.19	5.77 ± 0.27

f

Group	Sample	Concentration (µg/ml)	Zone of inhibition (mm) (Mean ± SD)	
			No IR	IR
1	CTL	--	--	--
2	PNS	1000	0.80 ± 0.05	1.31 ± 0.08
3	AgNP-PNS	250	0.91 ± 0.06	2.28 ± 0.10
4	AgNP-PNS	500	0.86 ± 0.07	3.12 ± 0.15
5	AgNP-PNS	1000	1.33 ± 0.07	4.82 ± 0.12

Figure 6.9. Antibacterial activity of AgNP-PNS by agar diffusion test against *P. aeruginosa* PAO1 (a) not irradiated (IR), (b) irradiated), and *S. mutans* ((d) not irradiated, (e) irradiated). Tables (c) and (f) report the values of antibacterial mean zone of inhibition for PAO1 and *S. mutans*, respectively. Bacterial cultures in absence of AgNP-PNS or PNS were used as positive controls (CTL). For each sample, three different experiments were conducted, and the results expressed as the mean of the values obtained (mean ± SD).

As reported in literature, both PAO1 and *S. mutans* have the capacity to form biofilm, which can be considered as one of the most critical determinants of the antibiotic resistance. Therefore, in other experiments, the antibiofilm activity of AgNP-PNS was examined at selected times and at concentrations ranging from 250 to 1000 g/mL. Regardless of the bacterial strain employed, Figure 6.10 illustrates a substantial decrease ($p<0.001$) in biofilm development in the presence of 1000 g/mL AgNP-PNS. Furthermore, a decrease in PAO1 and *S. mutans* biofilm of around 54±4% and 47±2%, respectively, was found after just 6 hours of incubation in the presence of the sample.

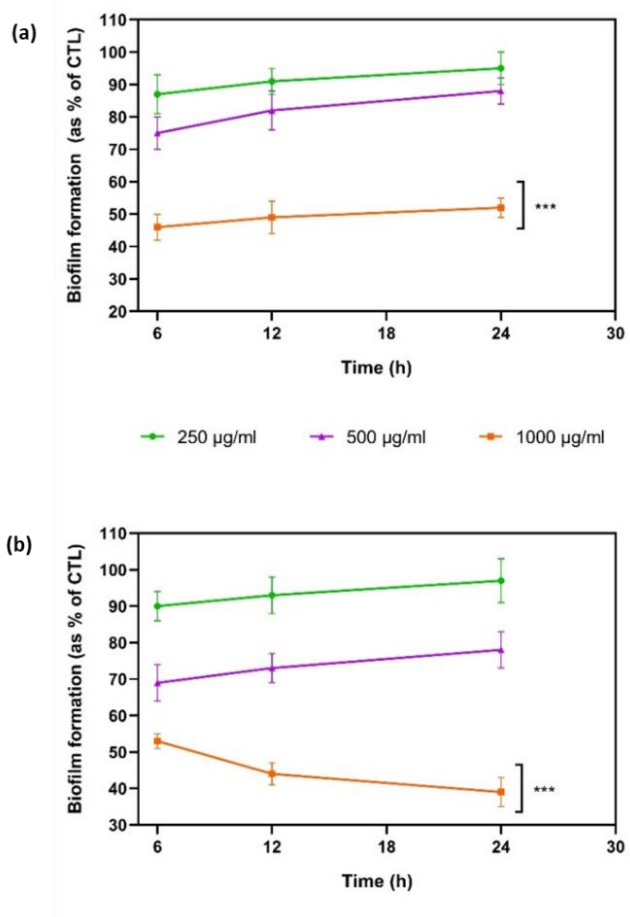

Figure 6.10. Antibiofilm activity of AgNP-PNS. Biofilm formation was evaluated by CV assay, after 6, 12 and 24 h of incubation at 37°C in presence of (a) *P. aeruginosa* PAO1, and (b) *S. mutans*. Biofilm formation was reported as a percentage in comparison with the maximum amount of biofilm produced by PAO1 and *S. mutans* growth (CTL). For each sample, three different experiments were run and the results expressed as the mean of the values obtained (mean ± SD). Statistically significant variations: ### versus 250 µg/mL, and 500 µg/mL.

Although the precise antibiofilm as well as bactericidal mechanisms of AgNPs remain still uncertain, it is reasonable to attribute the ability of AgNPs to modify the structure and characteristics of the biofilm by stopping bacterial metabolic pathways involved in, for example, motility, oxidative stress defense,

respiration, and quorum sensing systems. Further experiments will be devoted at investigating other issues related to the observed effects e.g. the possible release of silver nanoparticles in different solvents using ICPMS analysis or to assess the antibacterial activity of AgNPs-PNS possibly released in the medium of cell cultures.

***Main Outcomes Of The Study*:**

- Pecan Nut Shells a low-cost agri-food by-product were exploited as a rich source of phenolic compounds for the *in situ* synthesis of AgNP-PNS.
  - The resulting AgNP-PNS exhibited remarkable antibacterial and good antioxidant activity together with an appreciable ability to accelerate the photodegradation of organic dyes such as Methylene Blue (MB).

6.2 Lignin from chestnut shells as a potent reducing agent for the preparation of silver nanoparticles and implementation of high antioxidant and antibacterial poly (lactic acid) electrospun fibers

6.2.1 Synthesis of AgNP-CLN following a green procedure

The lignin recovered from chestnut shells (CLN) as described in the Chapter 5 was selected for further studies and investigations. Based on the promising results described in the previous paragraph, the recovered lignin was used as reducing agent for the *in situ* synthesis of silver nanoparticles, following a mechanochemical approach based on the use of a ball mill.

In particular, as already demonstrated before, this lignin exhibited the highest antioxidant activity compared to all the other selected nut shells (pecan, pistachio, hazelnut, peanuts) and corresponding lignins. Therefore, presumably CLN should be a stronger reducing agent compared to the others.

Initially, several experiments were devoted to the optimization of the experimental conditions, in terms of CLN/$AgNO_3$ ratio, time of all process and frequency. The highest content of Ag(0), revealed by X-ray diffraction (XRD) analysis, was observed using a 85:15 w/w CLN/$AgNO_3$ ratio for 180 minutes at 50 Hz. In fact, under these reaction conditions a 8 $\pm$ 1 % Ag(0) amount was calculated.

6.2.2 Incorporation of AgNP-CLN into poly(lactic acid) electrospun fibers containing cellulose nanocrystals or chitosan films and evaluation of their antioxidant and antibacterial properties

The AgNP-CLN prepared as described in the previous paragraph or CLN alone were incorporated at 0.7 and 2.1 wt % into D,L-polylactic acid electrospun fibers containing various amount of chitosan or cellulose nanocrystals. In Table 6.2 the main components of each prepared film are reported.

Table 6.2. Composition of prepared scaffolds (the ctrl samples are reported in red).

Scaffold name	PDLLA (% m/v)	Chestnut lignin (wt %)	AgNP-CLN (wt %)	Cellulose nanocrystals CNC (wt %)	Chitosan (wt %)
A	14	0.7			
B	14	2.1			
C	14		0.7		
D	14		2.1		
E	**14**				
F	13	0.7		3	
G	13	2.1		3	
H	13		0.7	3	
I	13		2.1	3	
J	**13**			**3**	
K	12	0.7			1
L	12	2.1			1
M	12		0.7		1
N	12		2.1		1
O	**12**				**1**

The average diameter of the prepared fibers was measured. As reported in Table 6.3, a general increase in terms of diameter sizes was observed for scaffolds prepared using PDLLA/Chitosan or PDLLA/ CNC in the presence of AgNP-CLN (e.g. I vs J and N vs O), whereas in the case of scaffold made of PDLLA alone the diameters did not change significantly or slightly decreased (D vs E).

Table 6.3. Average fiber diameters of the electrospun scaffolds (the ctrl samples are reported in red). [a] Mean value ± standard deviation (n>100 from three different images).

Scaffold name	Average fiber diameter [a] (nm)
A	768 ±262
B	1196 ±353
C	1037± 356
D	1244± 407
E	**1286 ±563**
F	1013 ±328
G	1090 ±332
H	665 ±246
I	1063 ± 343
J	**884 ±363**
K	1342 ±440
L	775 ± 246
M	700 ±154
N	706 ± 299
O	**612 ± 242**

Moreover, SEM images for all prepared scaffolds was performed. As representative example, the images of the electrospun fibers containing PDLLA/CNC with lignin (0.7 and 2.1%) or AgNPs (0.7 or 2.1 %) are reported in Figure 6.11. With respect to the control (**J**), it is possible to note the presence of small agglomerates, likely due to lignins or silver nanoparticles.

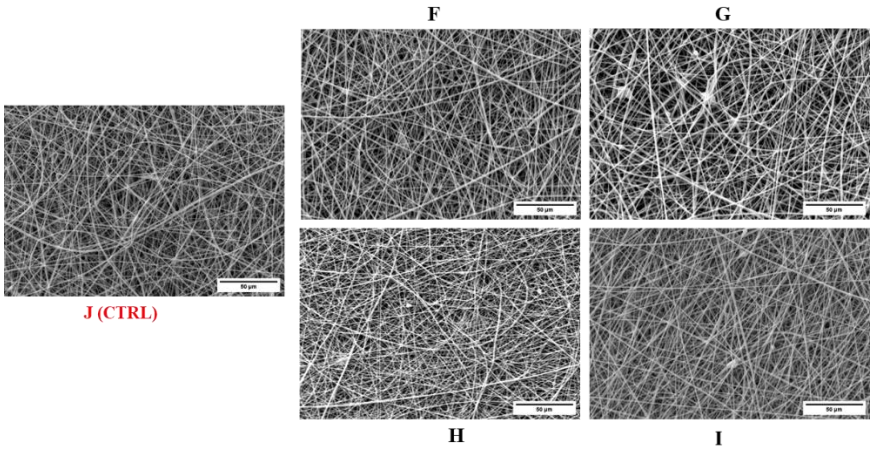

Figure 6.11. SEM images of the prepared electrospun fibers containing PDLLA/CNC with/without lignin (0.7 and 2.1%) or AgNPs (0.7 or 2.1 %).

To assess the therapeutic potential of the thus prepared electrospun fibers, the cytotoxic effects towards human mesenchymal stem cells was analyzed. For all prepared scaffolds an optimal cytocompatibility on mesenchymal stem cells over 120 hours was observed. As representative examples, the SEM imagines of the O sample as control and K, L, M, N samples are reported in Figure 6.12. As apparent a layer of cells completely covers the electrospun fibers, this is especially true for sample N, containing the highest percentage of AgNPs. The evidence that even at the highest concentrations of silver nanoparticles the prepared fibers exhibited good cytocompatibility is extremely valuable, as it is well known that at high level these nanoparticles can become toxic.

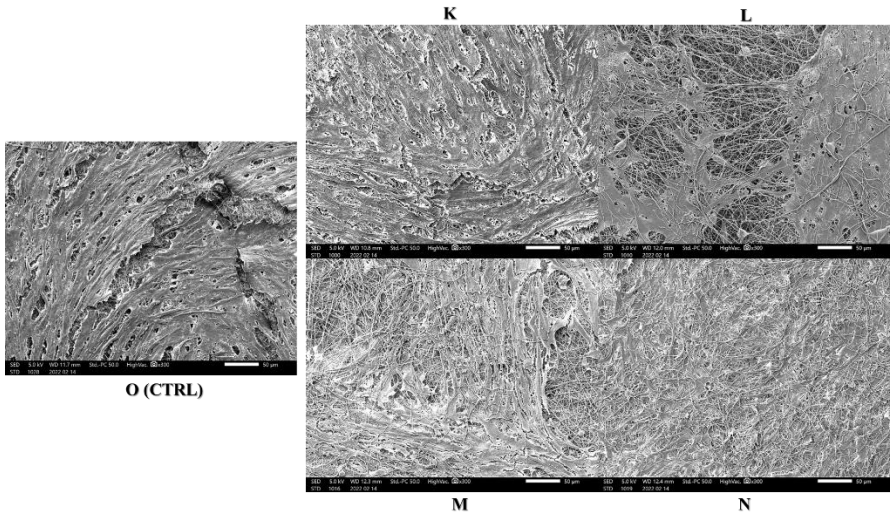

Figure 6.12. SEM images of mesenchymal stem cells growth on electrospun fibers.

In addition, the antimicrobial activity on *E.coli* and *S.epidermidis* of samples C, D, H, I, M and N, those one containing AgNPs, was tested. As illustrated in Figure 6.13, the best results were observed for all the samples with the highest amount of silver nanoparticles.

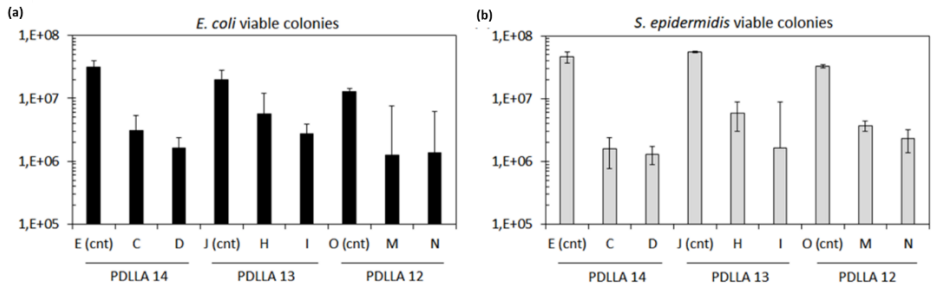

Figure 6.13. Antimicrobial activity of electrospun fibers containing AgNPs on (a) *E. coli* and (b) *S. epidermidis.* The data were reported as a number of viable colonies produced by *E.coli* and *S. mutans* growth respect to controls (cnt). For each sample, three different experiments were performed and the results expressed as the mean of the values obtained (mean ± SD).

In addition, to assess if the incorporation of CLN into electrospun fiber and/or the use of lignin as reducing agent for the synthesis of silver nanoparticles affects its excellent antioxidant properties, DPPH and FRAP assay were performed.

In particular, the antioxidant properties of the prepared fibers incorporating the highest content of CLN or silver nanoparticles were selected for further experiments. Hence, their antioxidant activity was evaluated by DPPH and FRAP assay. In the first case, each film was cut into pieces of 1 cm^2 total surface area and placed in 2, 4, 6 mL of 200 μM DPPH ethanolic solution. The DPPH consumption was monitored by Uv-Vis analysis, following the decrease of absorbance at 515 nm at selected time over 120 minutes. As expected, the highest DPPH consumption was observed using only 2 mL of ethanolic solution. As representative example, in Figure 6.14 the DPPH consumption of the sample B, containing the 2.1 wt % of CLN, at different volumes is reported.

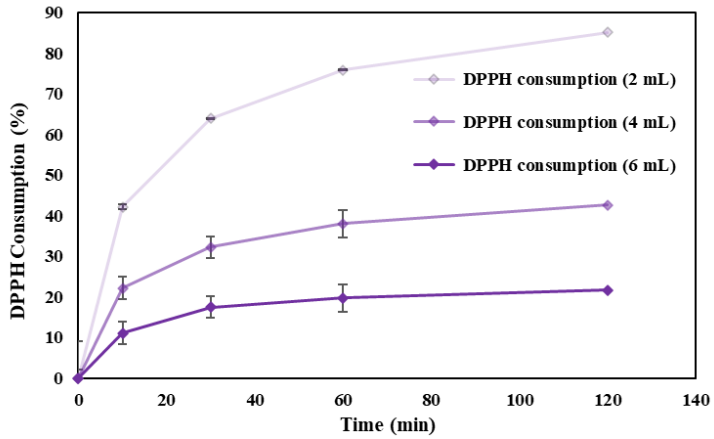

Figure 6.14. Antioxidant properties of the sample B, determined by dipping a cutting of 1 cm^2 total surface area in 2, 4, 6 mL of 200 μM DPPH ethanolic solution. Reported are the mean ± SD values of at least three experiments**.**

In Table 6.4 the DPPH consumption of each film using 2 mL of DPPH solution is reported. Notably, for all samples containing CLN an almost complete

consumption of DPPH within 120 minutes was observed, indicating an effective and preserved antioxidant activity of this high molecular weight phenolic compounds even after incorporation. On the other hand, in the presence of AgNP-CLN an approximate 50% of consumption was observed. This can be explained by the lower content of CNL in the AgNP-CNL sample compared to CNL alone and to the efficient reduction of Ag^{+} ions by the phenolic units. As reported in Table 6.3, the control fibers such as samples E, I and O exhibited a poor but still existing DPPH consumption, probably due to the absorption of DPPH. Although this, the consumption observed for controls is significant lower respect to the functionalized films, suggesting that almost all the antioxidant ability can be related to the presence of CLN or AgNP-CLN. Interestingly, no significant difference was observed for the prepared materials containing different percentage of chitosan or nanocellulose crystals.

Table 6.4. DPPH consumption of 2, 4, 6 mL solution (the ctrl samples are reported in red).

Scaffold	2 mL-DPPH Consumption (%)	4 mL-DPPH consumption (%)	6 mL-DPPH consumption (%)
B (14% PDLLA-2.1% chestnut lignin)	85.2±0.2	62.1±0.7	25.0±3.9
D (14% PDLLA-2.1% AgNPs)	48.3±2.9	38.0±5.5	46.3±0.1
E (14% PDLLA)	17.7±4.3	17.5±1.5	4.7±2.3
G (14% PDLLA- 3% CNC-2.1% chestnut lignin)	89.5±1.2	61.7±1.8	35.0±2.3
I (14% PDLLA- 3% CNC-2.1% AgNPs)	35.0±1.3	7.4±3.9	8.7±3.8
J (14% PDLLA- 3% CNC)	57.3±5.5	30.7±1.5	20.4±7.4
L (14% PDLLA- 1% chitosan- 2.1% chestnut lignin)	90.7±1.4	42.7±3.8	27.9±1.4
N (14% PDLLA- 1% chitosan- 2.1% AgNPs)	62.6±9.8	22.0±1.7	13.7±0.24
O (14% PDLLA- 1% chitosan)	31.5±1.7	14.8±7.6	13.3±1.7

The same procedure described before was then extended to FRAP assay. In this case, the increase of the absorbance at 593 nm was monitored by Uv-Vis spectroscopy. As shown in Table 6.5, a good antioxidant activity compared to the control film was observed for all samples and in particular for samples L and N, likely due to the lower hydrophilicity of PDLLA and CNC in the assay medium. The same trend was observed using 4 mL of FRAP solution, whereas no absorbance was detected using 6 mL.

Table 6.5. FRAP absorbance of 2 mL solution (the ctrl samples are reported in red).

Scaffold	2 mL-FRAP Absorbance (U.A)	4 mL-FRAP Absorbance (U.A)
B (14% PDLLA-2.1% chestnut lignin)	0.22±0.04	0.34±0.04
D (14% PDLLA-2.1% AgNPs)	0.206±0.007	0.151±0.001
E (14% PDLLA)	0.14±0.01	0.12±0.02
G (14% PDLLA- 3% CNC- 2.1% chestnut lignin)	0.22±0.02	0.26±0.01
I (14% PDLLA- 3% CNC- 2.1% AgNPs)	0.25±0.01	0.24±0.04
J (14% PDLLA- 3% CNC)	0.20±0.02	0.26±0.07
L (14% PDLLA- 1% chitosan- 2.1% chestnut lignin)	0.26±0.06	0.27±0.09
N (14% PDLLA- 1% chitosan- 2.1% AgNPs)	0.4±0.2	0.190±0.007
O (14% PDLLA- 1% chitosan)	0.17±0.02	0.118±0.009

For both assays, control experiments in only the medium were performed, showing a negligible release amount of materials.

***Main Outcomes Of The Study*:**

- ☐ The lignin recovered from chestnut shells (CLN) with the aid of DES and ball mill (Chapter 5), were employed as efficient reducing agent for the *in situ* synthesis of AgNPs.
  - The AgNP-CLN or CLN only were incorporated into electrospun fibers, giving rise to valuable materials with interesting antioxidant, antibacterial and cytocompatibility compounds.

6.3 Electron flow characterization of catechol-graphene composite hydrogels for charge storage application

6.3.1 Structural characterization of catechol-graphene hydrogel

Recently, the possibility to control the electron flow in aqueous media is emerging as one of the main features required for electronic material. As already mentioned in the Introduction section, to confer conducting properties, graphene is widely incorporate into materials.

In this scenario, an hydrogel film containing catechol (Cat), graphene (Gr) and chitosan (Chit) was assembled on an electrode surface by two electrofabrication steps. This part of the thesis work was performed during a training period, carried out at Institute for Bioscience and Biotechnology Research and Fischell Department of Bioengineering of University of Maryland (U.S.A.) under the supervision of Prof. G. Payne and Dr. E. Kim.

Based on consideration of the pH-responsive film-forming ability of chitosan, a graphene-chitosan (Gr-Chit) hydrogel was electrodeposited in the presence of a slightly acid suspension of graphene. In fact, chitosan is frequently employed to co-deposit nanoparticles; in particular when a negative potential is applied on the electrode, a locally high pH is generated, allowing chitosan to self-assemble into a hydrogel coating due to a decrease of its solubility with entrapping of particles suspended, in this specific case graphene. During the second electrodeposition step, the Gr-Chit-coated electrode was dipped into a catechol solution and a positive potential (relative to catechol E^0) was applied, thus generating the reactive quinone that could chemically interact with chitosan. This mechanism is based on the oxidation and concomitant grafting of catechol systems to the Gr-Chit-coated electrode.

Interestingly, these two step electrofabrication methods allow to prepare hydrogel with controlled compositions of the main components. In fact, in the first step changes in the deposition time (t) allow to control the graphene

content, in the second step the concentration of catechol and the oxidation charge qFab allow to control the catechol content. In particular, qFab is the number of electrons transferred during this anodic oxidation and serves as a measure of the extent of catechol modification.

Like the related melanin and polydopamine compounds, the complexity of the catechol chemistry precludes a complete structural characterisation of the Cat-Gr-Chit composite hydrogel. Therefore, the chemical structures for the oxidatively grafted catechol systems to chitosan can be only proposed (Figure 6.15) based on the known chemistry of related systems.

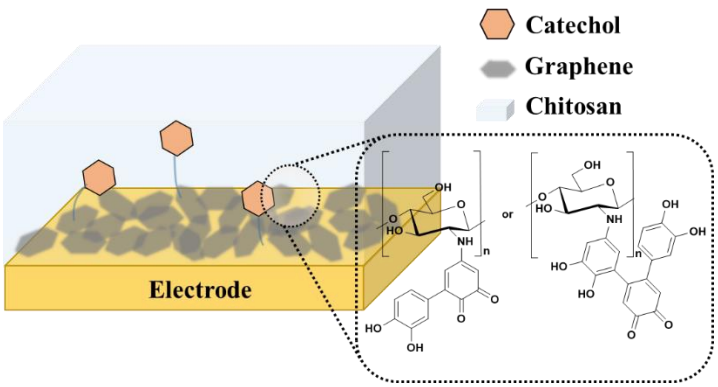

Figure 6.15. Representative illustration of the electrochemical grafting of catechols into chitosan.

To characterize the microstructure of the composite hydrogels and to confirm the proposed chemical reactivity, scanning electron microscopy (SEM) was used. As control experiments, a Chit-or Gr-Chit-hydrogel on an electrode surface were electrodeposited using a constant current density of 0.6 mA cm^{-2} for 3 min. On the other hand, to create the catechol-modified hydrogels (Cat-Chit or Cat-Gr-Chit), catechol was oxidatively grafted to chitosan by dipping coated Chit-or Gr-Chit-hydrogel electrode into 10 mM catechol solution and qFab=0.32 C cm^{-2} was achieved. Subsequently, to remove the adsorbed

catechol, the electrofabricated catechol-grafted hydrogels were extensively washed with water. As expected, the Chit- and Cat-Chit hydrogels SEM images are featureless, while the Gr-Chit and Cat-Gr-Chit hydrogels exhibited homogenously dispersed graphene flakes. In addition, for Cat-Gr-Chit hydrogel no significant difference was observed compared with Gr-Chit hydrogel. These results suggest that the main microstructure of graphene is retained during the electrodeposition process (Figure 6.16 panel a). Moreover, Uv-Vis analysis was performed. To allow the optical analysis a lower graphene content was necessary. To this aim, the electrodeposition of a chitosan solution (1 % w/v) containing only 0.2 % w/v graphene using a transparent gold electrode and applying a constant current density (0.6 mA cm^{-2}) for 90 minutes was performed. As expected, in the case of Chit-hydrogel coated electrode a very low absorbance was observed, whereas Gr-Chit hydrogel showed a monotonic broadband absorbance in the all visible region, likely due to π–π^* transition of sp^2 C=C bonds of graphene. Notably, Cat-Gr-chit hydrogel exhibited the highest absorbance as a result of the combined Uv-Vis spectra of Gr-Chit and Cat-Chit-hydrogel, prepared as controls (Figure 6.16 panel b).

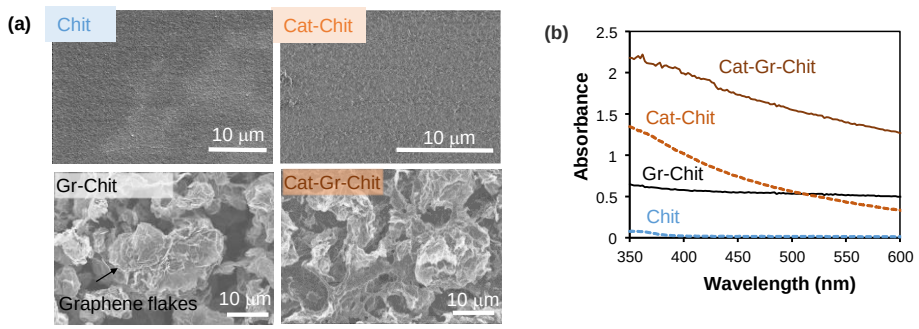

Figure 6.16. Characterization of Cat-Gr-Chit composite hydrogel: (a) SEM images of electrofabricated hydrogels on the gold electrode; (b) Uv-Vis spectra and images of electrofabricated hydrogels on the transparent gold electrode.

To chemical characterize the final material, also Raman and FT-IR spectroscopy were carried out, preparing the Gr-Chit and Cat-Gr-Chit hydrogel coated on the electrodes as described before for SEM experiment. As illustrated in Figure 6.17, the characteristic D-band (≈1334 cm^{-1}) and G-band (1576 cm^{-1}) of graphene, attributed to structural defects in the hexagonal sp^2 carbon lattice and to edge defects respectively, were detected. Notwithstanding that, a slight increase of the I_D/I_G ratio in Cat-Gr-Chit (1.11) compared to the Gr-Chit (1.07) was observed, indicating that the second electron deposition process may induce local defects in the graphene structure (Figure 6.17 panel a).

For FT-IR spectroscopy each hydrogel was peeled from the electrode surface and suspended in water. For the Chit-hydrogel, the characteristic broad peak at 3000 cm^{-1} ascribable to OH and NH stretching vibrations (Band 1) were observed. In the case of the Cat-Chit hydrogel two bands between 1700 and 1200 cm^{-1} (Band 2), likely due to the C=C stretching vibration were detected together with a concomitant decrease of the peak at 1050 cm^{-1} (Band 3: C-O stretching vibration). In the case of Gr-Chit-hydrogel few characteristic broad peaks were observed, while the spectrum of Cat-Gr-Chit hydrogel shows the increases of peaks between 1680 and 1200 cm^{-1} (Band 2), in agreement with the Cat-Chit-hydrogel. Additionally, the Band 2/Band 3 ratio is higher in the Cat-Gr-Chit hydrogel (than the Cat-Chit hydrogel), which may be due to π-π interactions between the species produced from catechol and graphene (Figure 6.17 panel b).

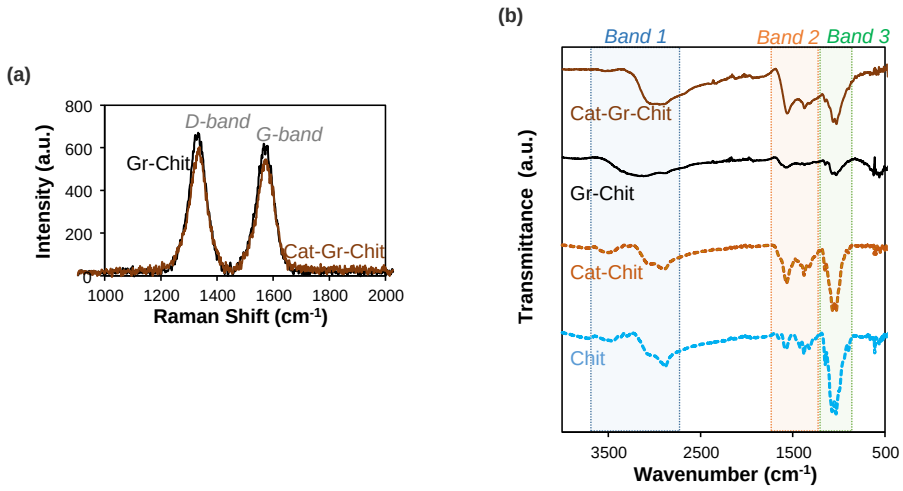

Figure 6.17. Characterization of Cat-Gr-Chit composite hydrogel: (a) Raman spectra of Gr-Chit and Cat-Gr-Chit hydrogel electrofabricated on a gold electrode; (b) FT-IR spectra of electrofabricated hydrogels.

To characterize the electrical properties of the composite hydrogel, electrochemical impedance spectroscopy (EIS) was also performed. Although EIS measurements are frequently very sensitive, it can be difficult to relate the electrical properties observed (such as capacitance and resistance) to the underlying molecular-level phenomena (such as reaction and diffusion). As a result, various methods were employed for data interpretation. With a perturbation amplitude of 5 mV from the open circuit potential, an EIS studies using a frequency range of 0.05 Hz to 10 kHz were carried out.

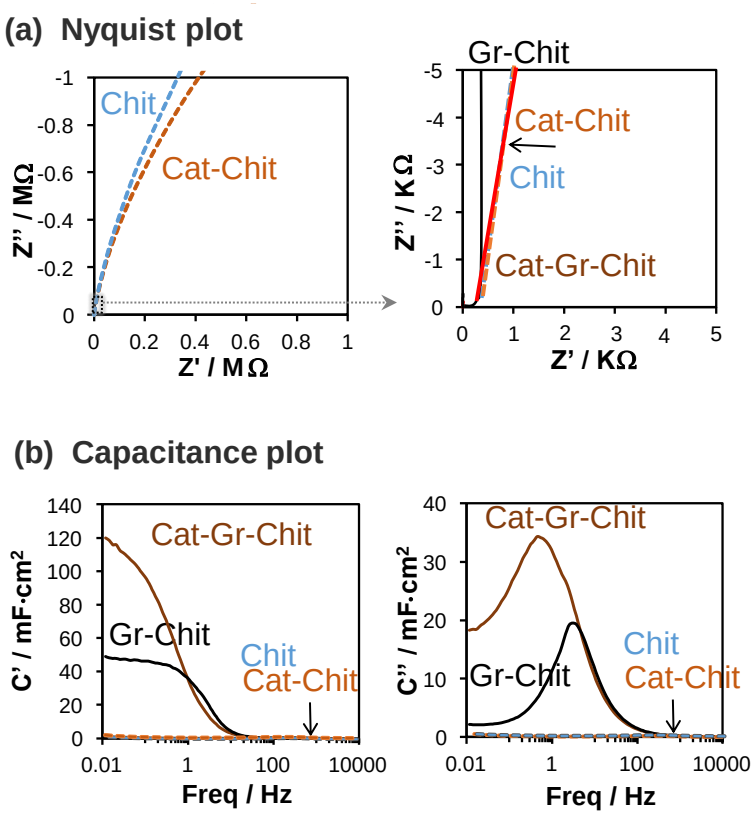

Figure 6.18. Characterization of Cat-Gr-Chit composite hydrogel: (a) nyquist plots from electrochemical impedance spectroscopy (EIS); (b) real (C′) and imaginary (C″) capacitance plots from EIS analysis.

As shown in Figure 6.18, the Nyquist plots offer one method for comparing the behaviour of the various hydrogels. The real component (Z′) and imaginary portion (Z″) of impedance for hydrogels without Gr (i.e., Chit and Cat-Chit) are about 500 times bigger than hydrogels including Gr, as shown by the left plot of Figure 6.18 (i.e., Gr-Chit and Cat-Gr-Chit). The right plot in Figure 6.18 is a focus on the low Z′ and Z″ area and demonstrates that the responses of the two hydrogels without Gr are different from those of the hydrogels that include Gr. The charge transfer resistance that occurs in the Cat-Gr-Chit hydrogel may be

the cause of a little variation between the Gr-Chit and Cat-Gr-Chit hydrogels. These results overall suggest that as expected Gr confers conductivity to the film. Figure 6.18 panel b shows the frequency-dependent capacitance plot. In particular, the real capacitance (C′) approaches the maximum capacitance for each film at the lowest frequency (50 mHz) (in the left plot of Figure 6.18 panel a). In comparison to hydrogels without Gr, those containing Gr exhibit 300 times greater C′ capacitance. Additionally, the capacitance of Cat-Gr-Chit is 4.3 times greater than that of Gr-Chit, likely due to the catechols additional contribution to the Gr-Chit. The sharp peak of imaginary capacitance (C″) at frequency (f_0) are reported in Figure 6.18. The relaxation time (τ_0) for discharging was determined from f_0 by using the formula $\tau_0 = 1/f_0$. The electron transfer to catechols may be the cause of the delayed response in Cat-Gr-Chit (τ_0= 1.5 s) compared to Gr-Chit (τ_0= 0.2 s).

Overall, these results confirmed the main conclusion that the electrofabricated Cat-Gr-Chit composite hydrogel exhibited both catechol and graphene main features.

6.3.2 Mechanisms for charge-storage and electron-transfer without mediators

6.3.2.1 Electrochemical characterization of conducting catechol

To further characterize how the conductivity (conferred by graphene) and redox activity (conferred by catechol) affect the composite hydrogel properties, the electrochemical behaviour of hydrogels films prepared with different compositions were measured.

Briefly, a thick hydrogel of 25 μm was coated on the electrode by electrodeposition of a graphene (0.5%)-chitosan (1%) solution using a constant current of 0.6 mA cm^{-2} for 3 min. Then the resulting coated electrode was dipped into a 10 mm catechol solution and to achieve the oxidative charge (qFab) of 0.6 C cm^{-2} a constant potential (+0.6 V versus Ag/AgCl) was applied.

The CVs of this Cat-Gr-Chit hydrogel-coated electrode are reported in Figure 6.19 panel a and compared with CVs of control hydrogels. All measurement were carried out in 0.1 M phosphate buffer at pH 7.0. Briefly, in the CVs of the Chit- and Cat-Chit controls an horizontal flat was detected, indicating a non-conductive nature of the hydrogel. On the contrary for the Gr-Chit control hydrogel a rectangular shape was observed, suggesting a capacitive hydrogel with a significant electrical double layer (EDL) as result of the increase of conducting surface area due to the presence of graphene. Notably, the Cat-Gr-Chit hydrogel exhibited unique features such as 3 reduction peaks and the corresponding 3 oxidation peaks, whereas Cat-Chit hydrogel shows no such peaks in the absence of Gr. These interesting results indicated that some catechols are bound to the conducting surface, i.e. to graphene and electrons can be directly transferred through graphene from/to the conducting catechols. As evident from the CV of Cat-Chit hydrogel, where an horizontal flat lines was observed, there was not direct electron transfer between catechol and the gold electrode. In addition, the very particular shape of the redox peaks could be due to the different redox states of catechols or their forms (e.g., monomer or oligomers), probably generated during the electro-fabrication process. In Figure 6.19 panel b, the CV data were expressed as function of time and the charge was calculated by integrating the current over time.

For the Cat-Gr-Chit hydrogel, the total charge Q_{Total}^{Ox} can be expressed as the sum of the double layer $Q_{Con.DL}^{Ox}$ and redox oxidative charge $Q_{Con.Redox}^{Ox}$

$$Q_{Total}^{Ox} = Q_{Con.DL}^{Ox} + Q_{Con.Redox}^{Ox}$$

As illustrated in Figure 6.19 panel b the difference in oxidative charge between the Cat-Gr-Chit and the Gr-Chit hydrogels represents the redox oxidative charge (orange area), whereas the Gr-Chit represent the oxidative charge (grey area).

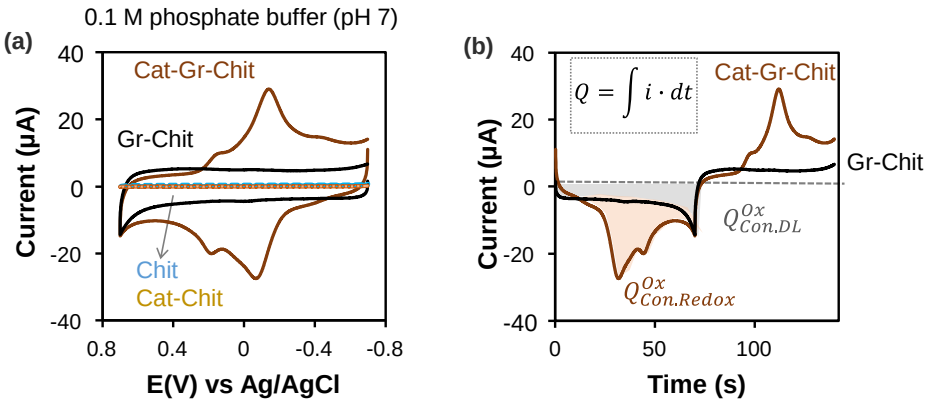

Figure 6.19. Electrochemical characterization without mediators: (a) cyclic voltammograms (CV) of all the 4 composite hydrogel-coated electrodes in phosphate buffer (scan rate of 10 mV s^{-1}); (b) current–time plots for Gr-Chit and Cat-Gr-Chit composite hydrogel.

In another series of experiments, the effect on the charge of the graphene and catechol content was evaluated. Firstly, Gr-Chit hydrogels with different graphene content were electrofabricated by dipping the electrode into chitosan (1%) solutions in the presence of different graphene concentration (0, 0.1%, 0.5%, 1%) and then a constant current of 0.6 mA cm^{-2} for 3 min was applied.
As expected, the $Q^{Ox}_{Con.DL}$ increase with graphene content as result of the increase in corresponding double layer capacitance and in conductive surface area.

After these experiments, the same hydrogel-coated electrodes were dipped into a catechol (10 mm) solution and a constant potential of +0.6 V was imposed to achieve an oxidative charge qFab of 0.32 C cm^{-2}. The calculation of the total oxidative charge Q^{Ox}_{Total} was obtained by CV measurement of the Cat-

$$Q^{Ox}_{Con.Redox} = Q^{Ox}_{Total} - Q^{Ox}_{Con.DL}$$

Gr-Chit hydrogels and by subtraction from this latter $Q^{Ox}_{Con.DL}$, the conductive

oxidative charge $Q_{Con.Redox}^{Ox}$, attributed to catechol was estimated (following equation).

As illustrated in Figure 6.20, in absence of graphene (Gr = 0%) no double layer and no redox charge was observed. In the presence of Gr, hydrogels with the same catechol content showed a rise of $Q_{Con.Redox}^{Ox}$ due to an increasing of only the graphene content. These findings suggest that although catechols cannot directly exchange electrons with the electrode in absence of graphene, these redox active molecules confer a redox conductivity to the film in presence of graphene. In addition, focusing the attention on the effect of grafted catechol content 5 identical Gr-Chit hydrogel coated electrodes were prepared by electrodeposition of chitosan (1%) solution with only 0.5% graphene using a cathodic current density of 0.6 mA cm^{-2} for 3 min. CVs of the 5 Gr-Chit-hydrogel coated electrodes allowed to calculate the $Q_{Con.DL}^{Ox}$ for the prepared 5 coated electrodes.

Using the same 5 Gr-Chit hydrogel coated electrodes, the electrodeposition of catechol was carried out, dipping the Gr-Chit coated electrodes into a 10 mm catechol solution and imposing a positive voltage of +0.6 V (versus Ag/AgCl) for selected times. This allowed to obtain oxidative charge (qFab) values from 0.06 to ≈0.96 C cm^{-2}. Subsequently, the $Q_{Con.Redox}^{Ox}$ was calculated as described before for these other electrodes.

As shown in Figure 6.20 panel b the conductive redox charge increased with the increase of qFab. After a while a plateau from 0.6 to 0.96 C cm^{-2} was achieved. This can be related to a limitation in the available graphene surface area. On the whole, these results highlighted the importance of graphene for the double layer charging and also for the conductive redox charging given by the catechol molecules.

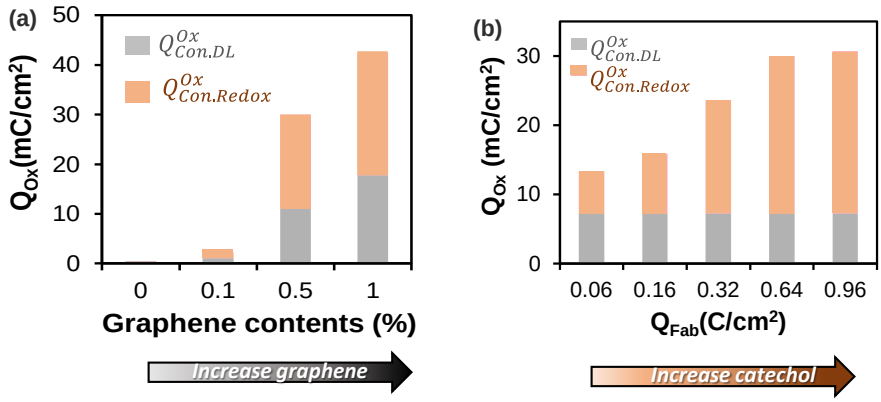

Figure 6.20. Electrochemical characterization without mediators: (a) the effect of graphene; (b) the effect of catechol (qFab) on the oxidative charge-transfer mechanisms.

These results support the main idea of the existence of conducting catechol that can directly transfer electrons through an interconnected graphene network.

6.3.2.2 Molecular switching of conducting catechol

Spectroelectrochemical studies were carried out to evaluate the conductive redox electron flow through the Cat-Gr-Chit composite hydrogel and to identify redox-state switching of the conducting catechol. In this case, the use of a transparent gold electrode and slightly modified electrodeposition condition to create a partially-transparent Gr-Chit hydrogel film were necessary. In particular, a chitosan solution (1%) with a lower level of graphene (0.2%) was electrodeposited and a cathodic current (0.6 mA cm^{-2}) for 90 minutes was applied. In fact, under these circumstances the measurement of the absorbance was allowed, creating a thin Gr-Chit hydrogel coated electrode. This latter, to generate the Cat-Gr-Chit hydrogel, was then dipped into a 10 mm catechol solution and a positive potential (+0.6 V versus Ag/AgCl) was applied, reaching a qFab of 0.3 C cm^{-2}. For spectroelectrochemical measurements, the resulting thin hydrogel coated electrode was dipped into a specific cuvette containing 0.1 M phosphate buffer at pH 7. Subsequently, an oscillating potential input was

applied to the electrode and the two outputs, such as optical absorbance and electrical current were simultaneously measured.

The electrical and optical outputs for the Cat-Gr-Chit *versus* the control Gr-Chit hydrogel lacking catechol are reported in Figure 6.21. As evident, the electrical current observed in the case of Cat-Gr-Chit composite hydrogel was higher than the Gr-Chit hydrogel, in agreement with the higher charge $\Delta Q_{Cat.Gr.Chit} = 2.8 \pm 0.06$ mC estimated by integrating the current output over time ($Q=\int i \times dt$) respect its control Gr-Chit film ($\Delta Q_{Gr.Chit} = 1.0 \pm 0.01$ mC). This can be easily explained by the additional redox-based electron transfer mechanism of catechol systems. The third output in Figure 6.21 is the optical absorbance at 480 nm, generally attributed to the redox state of the grafted catechol moieties (note: the absorbance is normalized by subtracting the initial absorbance to emphasize its change). An oscillating absorbance output was observed only in the case of the Cat-Gr-Chit hydrogel, while the control Gr-Chit hydrogel shows no oscillations in the absorbance output ($\Delta A_{Gr.Chit} \approx 0$). This can be taken as a direct evidence of the redox state of some catechol moieties, that can be repeatedly switched between in their reduced (catechol) and oxidized (quinone) states by electron transfer through the graphene network. In fact, in absence of graphene, i.e. in the case of Cat-Chit-hydrogel, a ΔA value ≈ 0 was observed.

Notably, when the maximum (i.e., reductive) charge (Q_{max}) occurred, the minimum absorbance (A_{min}, associated with the reduced catechol state) was observed, and when the minimum (i.e., oxidative) charge (Q_{min}) occurred, the maximum absorbance (A_{max}, associated with the oxidized quinone state) was detected.

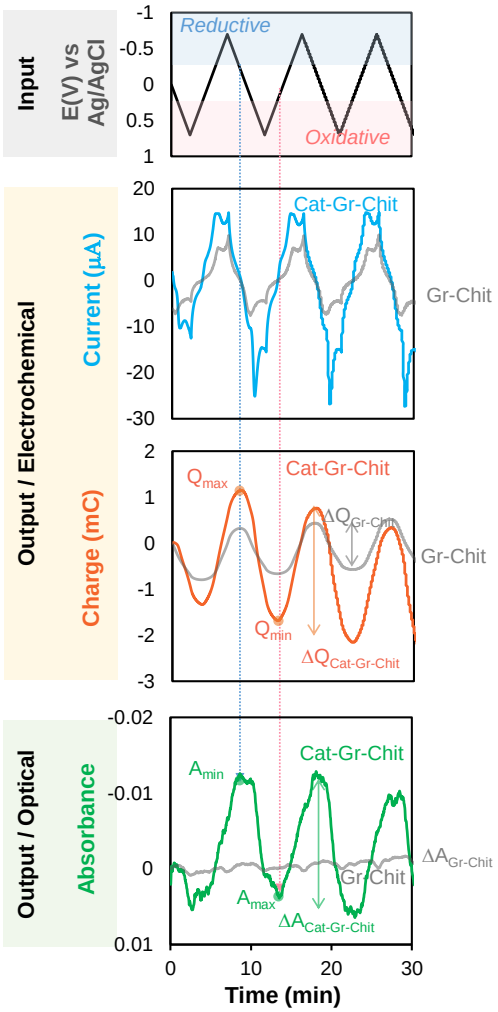

Figure 6.21. Molecular switching without mediators (detect the conducting catechols). Time series output curves of the response to cyclically-oscillating input potential in buffered solutions without mediators.

Overall these results provide another evidence of the presence of a conducting catechols population that can directly exchange electrons with graphene, able to transfer electrons with the electrodes (Figure 6.22).

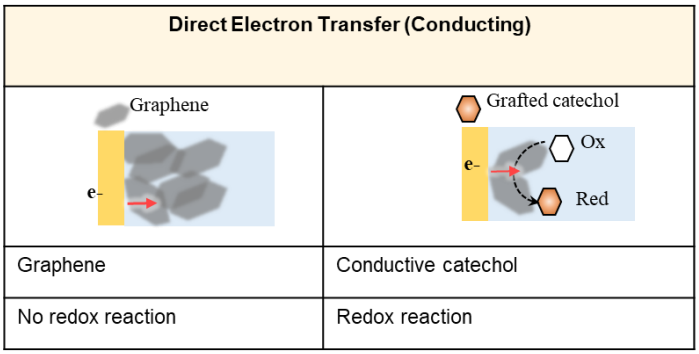

Figure 6.22. Representative scheme for conductive catechol and graphene.

6.3.3 Mechanisms for charge-storage and electron-transfer with mediators

6.3.3.1 Molecular switching of non-conducting catechol

While the above results provide evidence for a population of conducting catechols that can directly exchange electrons with Gr, to evaluate if there are a second functional population of catechols that remains redox-active but cannot directly exchange electrons with Gr without mediators, another series of experiments were carried out. In particular, a series of spectroelectrochemical measurements using hydrogel coated electrodes as described in the previous paragraph in presence of two mediators (i.e., diffusible electron shuttles) were performed.

As already described in Chapter 1, the use of mediators allows to transfer electron from/to the electrodes to/from non-conducting catechols in redox-cycling reactions. It must be kept in mind that in the oxidative region, the ferrocene dimethanol (Fc) mediator undergoes oxidative redox-cycling, switching the non-conducting catechols to their oxidized (e.g., quinone) state. On the contrary, in the reductive region, the $Ru(NH_3)_6Cl_3$ (Ru^{3+}) mediator

undergoes reductive redox-cycling, switching the non-conducting catechols to their reduced (e.g., catechol) state. In Figure 6.23. the measurements for the Cat-Gr-Chit hydrogel in presence of the Fc and Ru^{3+} mediators (0.1 mM each) and the same film without mediators are reported.

The first set of output curves in Figure 6.23 shows the electrical current. When the Cat-Gr-Chit composite hydrogel was probed in the presence of both mediators, a larger current compared to the same hydrogel in absence of mediators was observed. This amplification can be taken as an evidence of the existence of a second non-conducting catechol population, requiring the presence of mediators to induce their redox-switching. Consistent with these results, also the oscillating $Q_{Cat\text{-}Gr\text{-}Chit}$ composite hydrogel was higher in presence of mediator respect with the same hydrogel in absence of mediators or Gr-Chit hydrogel with mediators.

The third set of output curves is the optical absorbance associated with the catechol moieties redox state. A semi-quantitative indicator of the catechol moieties redox-state switching is the amplitude of the oscillating optical absorbance output (A). As expected, no absorbance was observed in the case of the Gr-Chit film, due to absence of the catechols. On the other hand, the Cat-Gr-Chit film in presence of mediators exhibited a significant higher absorbance 0.05±0.003 compared to the same film probed without mediators 0.015±0.002. These values maybe suggest that this Cat-Gr-Chit hydrogel is composed by 1/3 of the redox-active conducting catechols and 2/3 of non-conducting catechols approximately.

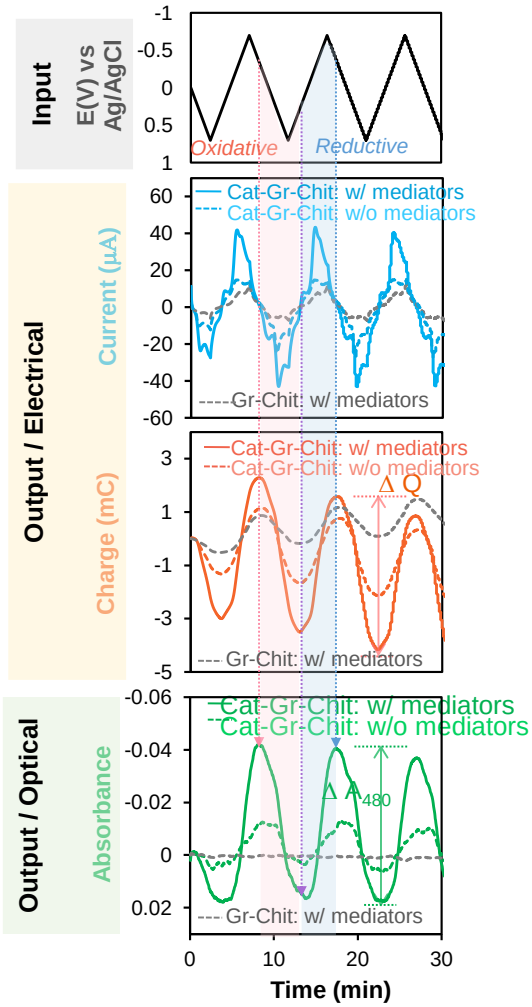

Figure 6.23. Molecular switching with mediators (detect the non-conducting catechols). Time series output curves of the response to cyclically oscillating input potential in buffered solutions (PB) without or with mediators (0.1 mM ferrocene dimethanol [Fc] and 0.1 mM ruthenium hexamine chloride [Ru^{3+}]).

To further examine the responses of the conducting and non-conducting catechols, dynamic analysis of the Cat-Gr-Chit hydrogel in the presence and absence of mediators using various scan rates were carried out.

As shown in Figure 6.24, an increase of the scan rates is associated to a decrease of the oscillating electrical output (ΔQ) and optical output (ΔA) at 480 nm. In Figure 6.24 panel b the ΔA is plotted in function of ΔQ. Notably, a linear correlation was observed, indicating that the electrons transferred to/from the hydrogel are associated with the switch of the redox state of the catechols systems. This slope seems to be the same with o without mediators, suggesting that the same number of electrons is required to switch the conducting and non-conducting catechols.

In addition, as illustrated in Figure 6.24 panel b, the addition of catechol to the Gr-Chit film further increase ΔQ in a scan-rate dependent manner, in agreement with the addition of a redox capacitance.

This redox capacitance is connected to the conducting catechols, when the Cat-Gr-Chit film was investigated without mediators. On the contrary, probably the redox capacitance includes both the conducting and non-conducting catechols when the Cat-Gr-Chit hydrogel was investigated with mediators. Importantly, mediators are required to switch the non-conducting catechols to allow significantly more electrons to be transferred to/from the hydrogel and corresponding increases in ΔQ and ΔA (480 nm).

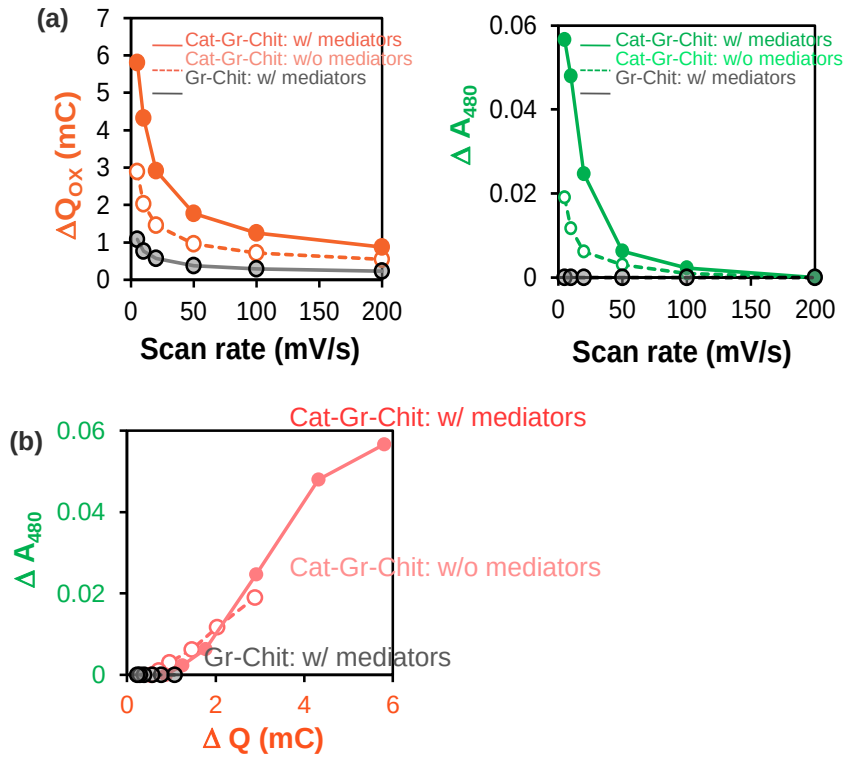

Figure 6.24. Molecular switching with mediators (detect the non-conducting catechols). (a) Dynamic analysis of the electrical and optical outputs as a function of scan rate (e.g., frequency); (b) cross-correlation illustrates the importance redox-state switching of the catechol (measured as ΔA) to the ability to transfer electrons into/from the composite (measured as ΔQ).

6.3.3.2 Electrochemical characterization of non-conducting catechol

In another series of experiments, CVs measurement were carried out with or without Fc ($E^{0,Fc}$=+0.25 V versus Ag/AgCl) and Ru^{3+} ($E^{0,Ru3+}$=–0.2 V versus Ag/AgCl) mediators. In the case of Gr-Chit hydrogel, small changes were observed with or without mediators, as result of their poor effect on the graphene conducting mechanism. On the contrary the Cat-Gr-Chit hydrogel

exhibited significant differences in presence of mediators, necessary to access to the redox-non-conducting catechols. Comparing the CVs of Cat-Gr-Chit hydrogel tested with or without mediators (Figure 6.25), three main observations from the CVs can be done:

i) in presence of mediators a large current peak was observed, consistent with the requirement for diffusible mediators to allow the non-conducting catechols to exchange electrons, and also illustrates the role of the mediators as voltage gates to allow electron flow to/from the non-conducting catechol population;

ii) the currents peak in presence of mediators was amplified: the mediators can transferred electrons from/to the non-conducting catechol population;

iii) Fc-oxidation (but not Fc-reduction) was amplified and Ru^{3+}- reduction (but not Ru^{3+}-oxidation) was amplified, features previously reported for redox-active but non-conducting films in bioelectronics applications.

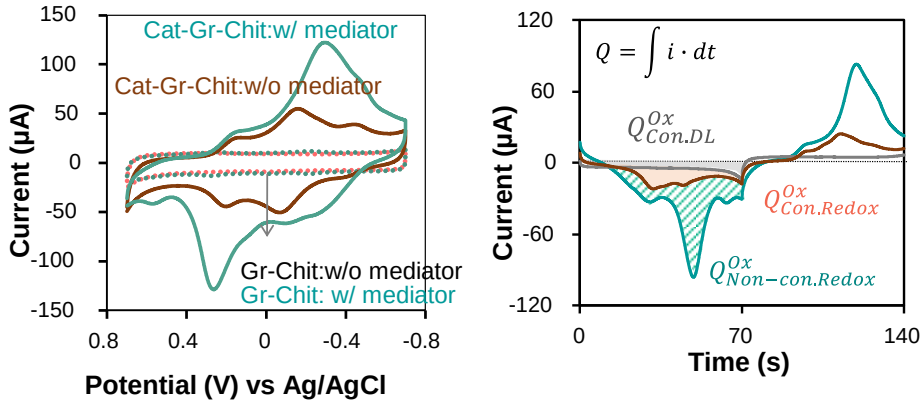

Figure 6.25. Electrochemical characterization with mediators. Cyclic voltammograms (CV) of graphene-containing composites when probed with or without mediators (0.1 mM Fc, 0.1 mM Ru^{3+}; scan rate of 10 mV s^{-1}).

Additionally, to estimate the relative contributions of the three electron transfer mechanisms, the integration of the current over time to calculate the charge was performed. Firstly, the Gr-Chit hydrogel was probed to evaluate the double layer charge conferred by graphene $Q^{Ox}_{Con.DL}$. Subsequently, the Cat-Gr-Chit hydrogel without mediators was probed to estimate the conductive redox charge conferred by the conducting catechol $Q^{Ox}_{Con.Redox}$, whereas when the Cat-Gr-Chit film was probed with mediators, the non-conducting catechol's $Q^{Ox}_{Non.Con-Redox}$ charged was estimated. The Q^{Ox}_{Total} is the sum of all these contributions.

$$Q^{Ox}_{Total} = Q^{Ox}_{Con.DL} + Q^{Ox}_{Con.Redox} + Q^{Ox}_{Non.Con-Redox}$$

Using the same thick hydrogels prepared as described before, the content of graphene and catechol systems were modified. Notably, the results shown in Figure 6.26 indicated that when the graphene content in the hydrogel increased, both the double layer charge and the conductive redox charge increased, whereas no difference for the non-conductive redox charge was observed. In contrast, when the catechol content increased, no changes was observed for the conducting double layer charge, while both the conductive redox charge and non-conductive redox charge increased. Notably, as evidente from Figure 6.26 panel b, increasing the catechol content, the non-conductive redox charge increased, whereas the conductive redox charge achieved a plateau, as result of a limitation in the graphene content. These results indicate that the ability of the mediators to access the non-conducting catechol population leads to a large increase in electron exchange in the hydrogel.

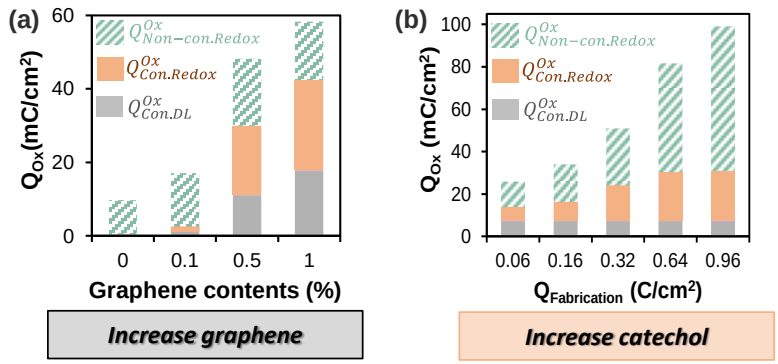

Figure 6.26. a) The effect of graphene on the oxidative charge-transfer mechanisms; b) the effect of catechol (qFab) on the oxidative charge-transfer mechanisms.

Different scan rates from 2 to 1000 mVs^{-1} on these thick hydrogels without mediators were applied. In addition, by dividing the output charge (Q) by the electrode surface area and scan rate as shown in the following equation, the CV data was transformed into area capacitances, allowing a comparison of the responses from various CVs using the same y-axis scale.

$$C(F/cm^2) = \frac{Q}{V \cdot A} = \frac{i \cdot t}{A \cdot V} = \frac{i}{A \cdot \upsilon}$$

The Gr-Chit hydrogel shape of CVs curves is largely independent on the scan rate, as result of an EDL capacitance, while in the case of Cat-Gr-Chit hydrogel exhibited changes in function of scan rate due to the contributions from both graphene double layer capacitance and the conducting-catechols redox capacitance. Finally, the Cat-Gr-Chit hydrogel were probed with mediators, which includes all three electron transfer mechanisms. These latter plots show that the total capacitance decreases with increasing scan rate which is consistent with a redox capacitance mechanism.

Additionally, to get more information, the peak current (i_p) was plotted versus the scan rate.

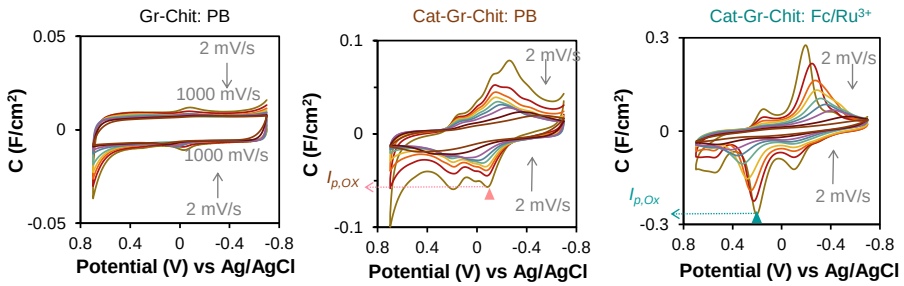

Figure 6.27. Dynamic analysis in which output currents are converted to area capacitance values (C, F cm^{-2}: CVs performed from 2 to 1000 mV s^{-1}).

As evident from the graph in Figure 6.27, the follow equations show a power-law dependence with the exponent (b) providing mechanistic insights: b approaches 1 for surface-controlled electrochemical processes, and 0.5 for

$$i(V) = a \cdot v^{b}$$

$$\log(i(V)) = b \cdot \log(v) + log(a)$$

diffusion-controlled processes.

Notably, as shown Figure 6.28. in absence of mediator for the Gr-Chit hydrogel, b approaches to 1(0.96), supporting the main hypothesis that the electron-transfer is associated with the surface controlled double layer formation (i.e., the capacitive charge), while in the case of Cat-Gr-Chit hydrogel without mediators the exponent b decreases to 0.82, indicating that maybe an additional surface-controlled redox reaction of conducting catechol is present. Interestingly, the lowest b value was obtained in the case of Cat-Gr-Chit probed in the presence of mediators (b = 0.65), supporting the hypothesis that mediator diffusion is required for electron-transfer of the non-conducting catechol.

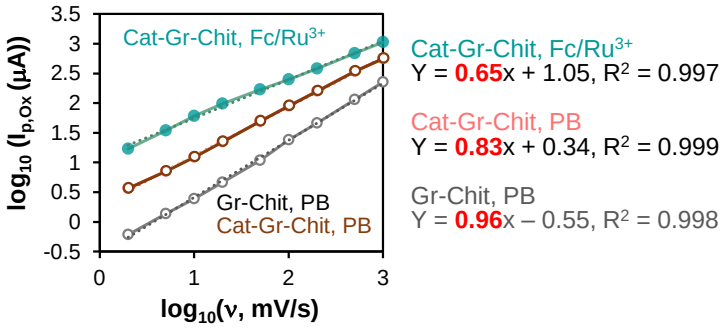

Figure 6.28. Dynamic analysis of oxidation peak currents as a function of the scan rate and related linear equations.

Overall, these findings provide evidence that the Cat-Gr-Chit probed the presence of a second non-conductive catechol populations. Specifically, it can be supposed that these "non-conducting" catechols are covalently grafted to the chitosan matrix but do not form the associations with Gr, not allowing a direct electron transfer (Figure 6.29).

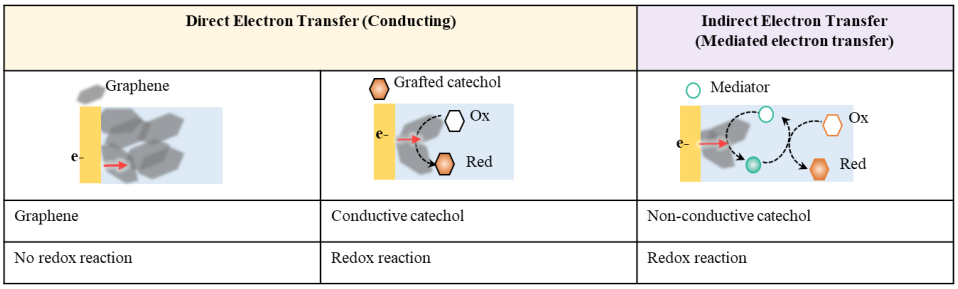

Figure 6.29. Representative scheme of the three main mechanism for the Cat-Gr-Chit hydrogel.

6.3.3.3 Stability of Redox-State Switching

Due to their ability to be repeatedly switched between two stable redox states, redox-active catechol-based hydrogels have been largely studied for biosensing and bioelectronics applications. In fact, these features confer unique molecular electronic properties (e.g., molecular memory). Of course, the

presence of graphene in the prepared hydrogel could affect the redox switching properties of catechols. Therefore, to evaluate the repeatability of switching over 10 cycles, an oscillating input potential was applied to this film.

In the case of the Cat-Gr-Chit hydrogel with mediators, the electrical output (ΔQ= 4.09 mC ± 0.12) and optical output (ΔA at 480 nm = 0.051±0.0036) remained relatively constant over 10 cycles. The same was observed in the case of the Cat-Gr-Chit hydrogel probed without mediators. This steady output indicates that the catechol moieties (both conducting and non-conducting) can be repeatedly switched. Then, a potential between -0.6 and +0.6 V was imposed. Repeatable response of both electrical and optical outputs for the Cat-Gr-Chit hydrogel (higher in presence of mediators) switching the redox-state was observed. When the step potential was maintained for 5 min, the absorbance remained stable (Figure 6.30). Based on these findings, it can be concluded that the redox states of both the conducting and non-conducting populations of catechol can be repeatedly switched.

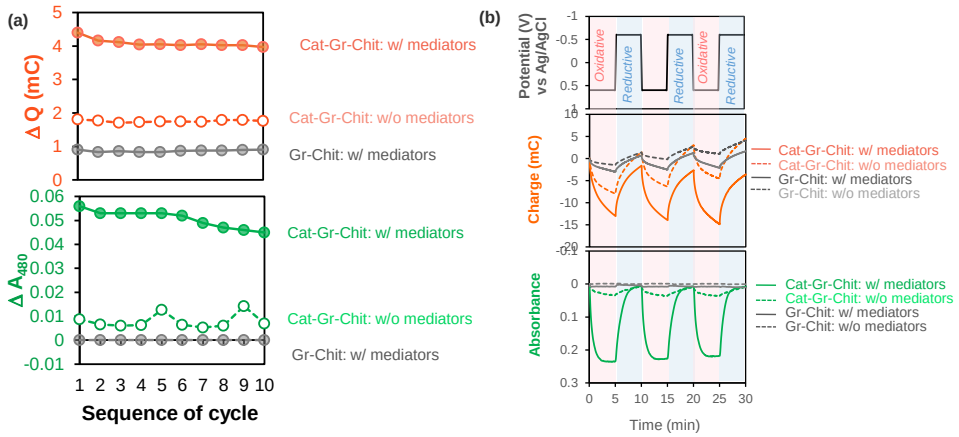

Figure 6.30. Stability of redox state switching. a) repeatable switching of catechol redox-states with and without mediators as measured from the optical output from multi-cycle CV measurements (scan rate of 10 mV s^{-1}). b) stability measurements of the reduced and oxidized redox-states of the catechol when a step potential was imposed.

As reported in the following scheme the incorporation of graphene within the hydrogel conferred charge-storage through a double layer and electron-transfer through a metal-like conductivity mechanism. Two catechol population were proved to exist. One population, the "conducting catechols", is believed to be in intimate contact with graphene and can directly exchange electrons with graphene, allowing charge-storage through a redox mechanism and can undergo direct electron-transfer with the graphene. The second population, the "non-conducting catechols", is believed to be grafted to the chitosan but physically separated from graphene and thus precluding direct electron exchange as previously demonstrated with the catechol-grafted chitosan, allowing the charge-storage through a redox mechanism but require mediators (diffusible electron shuttles) to allow electron-exchange (Figure 6.31).

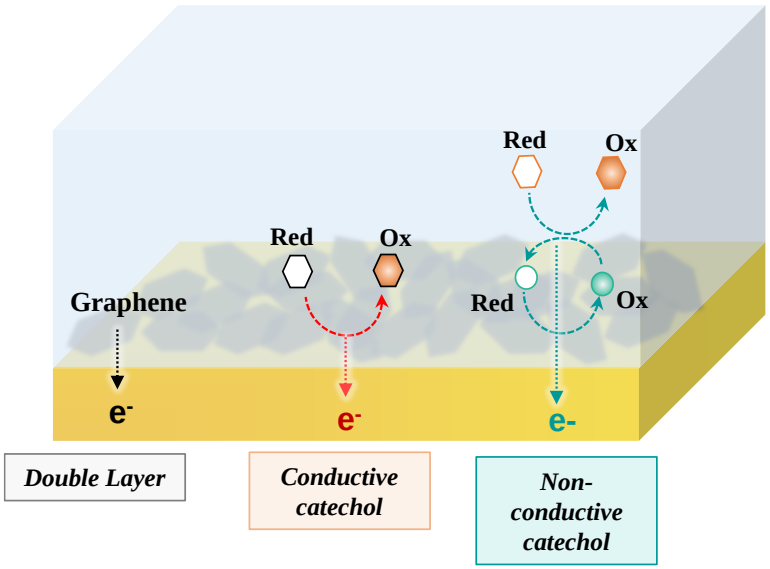

Figure 6.31. Representative scheme for the three-mechanism underlying the electron flow of the Cat-Gr-Chit hydrogels.

***Main Outcomes Of The Study*:**

- A chitosan hydrogel incorporating graphene and catechol was electrofabricated, showing synergistic properties.
  - The electron flow of the hydrogel was fully characterized by spectroelectrochemical reverse engineering approach.

6.4 Experimental section

Materials and Methods. Commercial-grade reagents and solvents were used without further purification, except where otherwise indicated. Poly-D,L-lactic acid (PDLLA, molecular weight: 126 kDa) was obtained from FormFutura, cellulose nanocrystals (CNCs, 88%) were purchased from CelluForce. 1,1,1,3,3,3-hexafluoro-2-propanol (HFP) was obtained from Iris Biotech GMBH. Chitosan (CS, molecular weight: 50-190 kDa, deacetylation ≥ 75%) was obtained from Sigma Aldrich. $Ru(NH_3)_6Cl_6$ (Ru^{3+}), catechol and Ferrocene dimethanol (Fc) were purchased from Alfa Chemistry. PNS was supplied by the Productora de Nuez S.P.R de R.I. (Mexico). Graphene (N002-PDR) was purchased from Angstron Materials. All reagents and solvents used were of analytical grade (Sigma-Aldrich). *Pseudomonas aeruginosa* PAO1 (ATCC® BAA-47), *Streptococcus mutans* (ATCC® 25175), *E.coli* were obtained from the American Type Culture Collection (ATCC) via a local distributor (LGC Standards S.r.l). Luria–Bertani (LB) agar, nutrient agar and BacTiter-Glo™ Microbial Cell Viability Assay Reagent were purchased from Promega. X'Pert Pro diffractometer, equipped with a PIXCel 1D detector, under CuKα radiation was used for XRD analysis of AgNP-PNS. Powder spectra were collected under ambient conditions in the range 5-80 °2θ, with a step size of 0.013 °2θ and counting time of 20 seconds per step. The PANalytical High-Score package, equipped with the ICDD PDF 2 database, was used to identify the crystalline phases in the samples. The amount of AgNP in the samples was evaluated by the RIR/Rietveld method (Chipera and Bish, 2013): a weighted amount (10% w/w) of corundum (NIST Standard Reference Material 676a) was added to each sample, the mixture was carefully homogenized, and the diffraction spectrum was acquired. Then, the relative mass percentage of corundum, Ag, and AgCl if present were calculated by a quantitative analysis carried out using the MAUD software. The results were rescaled accounting for the actual amount of corundum, obtaining the absolute weight percentage of each phase as the mean

value from three different samples. The structural information of each phase was acquired from the Crystallography Open Database (Crystallography Open Database, 2020).

ATR-FTIR spectra were recorded on the solid samples using a Nicolet 5700 Thermo Fisher Scientific instrument. Spectra were recorded as an average of 128 scans in the range 4000-450 cm^{-1} (resolution of 4 cm^{-1}). Background spectra were recorded each time and then subtracted from the sample spectra.

For SEM, TEM, and DLS characterization, 10 mg of sample was suspended in 3 mL of distilled water. The mixture was sonicated in a Labsonic Falc LBS1-0,6 ultrasonic bath for 30 min, then allowed to settle for another 30 min. The obtained supernatant was analyzed by TEM (FEI Tecnai G2 Spirit Twin device), SEM (FEI Quanta 200 FEG, 10-30 kV acceleration voltage, secondary electron detector) and DLS (Malvern NanoSizer ZS, 25 °C, with a wavelength of 633 nm and detection of backscattered light at an angle of 173°).

SEM images were acquired with a voltage of 20 kV and different magnifications, after gold sputter-coating on a Philips, FEI ESEM XL30 instrument. The diameter of the fibers was evaluated using ImageJ software supplied with the DiameterJ plug-in.

The images of Cat-Chit-Gr-hydrogel samples were obtained using a scanning electron microscope (SEM, SU-70). Uv-Vis spectroscopy (Evolution 60 spectrophotometer, Thermo Fisher Scientific), Raman spectroscopy (inVia Raman Microscopy, Renishaw Inc), and FourierTransform infrared spectroscopy (FT-IR, VERTEX 70 FT-IR, Bruker) were used to chemical characterized the prepared hydrogels.

A CHI6273C electrochemical analyzer (CH Instruments) was used for performing chrono-coulometry (CC, applying qFab), cyclic voltammetry (CV) and electrochemical impedance spectroscopy (EIS). A standard gold electrode was purchased from CH Instruments (Austin, TX) Instrumentation Electrochemical analysis. a DC power supply (2400 Sourcemeter, Keithley) was

used for the electrodeposition of chitosan (Chit) or graphene-chitosan (Gr-Chit) hydrogels.

AgNP-PNS were characterized by XRD, SEM, TEM, DLS and ATR-FTIR spectroscopy.

PNS milling and sieving. After being dried in an oven at 50 °C for 16 h, PNS were finely minced in a grinding mill (Retsch RM 200) for 15 min. 15 g of the sample thus obtained was then placed into a vibratory sieve shaker (Retsch AS 200), obtaining a material with homogeneous particle size distribution (75-125 μm).

Preparation of AgNP-PNS by the wet-chemical approach. To 20 mL of a 10 mM $AgNO_3$ water solution, 200 mg of PNS were added to 20 mL and stirred at room temperature for 24 h. Subsequently, the mixture was centrifuged (7000 rpm, 30 min), and the precipitate was washed three times with water. The final material was then lyophilized (yield of 75 % w/w).

Preparation of AgNP-PNS by the mechanochemical approach. PNS were extensively dried in a vacuum oven at 60 °C for 16 h. PNS in the presence of $AgNO_3$ 85:15 w/w ratio, respectively, were introduced into a vibratory ball mill (Retsch EMAX model) at 60 Hz for 90 min. To scale up the process, 10 g of sample constituted of 85:15 w/w PNS/$AgNO_3$ ratio were milled into a planetary ball mill (Fritsch Pulverisette 7 model) at 800 rpm for 30, 90, 120 and 180 min. In other experiments, a 55:45 w/w PNS/$AgNO_3$ ratio was used, with a milling time of 180 min, selected as the optimal experimental conditions to prepare the AgNP-PNS sample.

Preparation of AgNP-CLN. Lignin from chestnut shells was recovered as described before (see Chapter 5). 140 mg of lignin were added into a ball mill (Fritsch Pulverisette 23) with 25 mg of $AgNO_3$ (15 % w/w) at 50 osc/s. After 180 minutes, the recovered samples were washed three times with 50 mL of water and centrifuged to recover as precipitate AgNP-CLN.

Electrospinning. Polymer solution in the ratio percentages listed in Table 6.2 were prepared as follows. For scaffold **P (E)**, PDLLA (280.0 mg) was dissolved in HFP (2.0 mL) and kept under magnetic stirring overnight at 310 K. For scaffolds **PL01 (A)** and **PL03 (B),** chestnut lignin (2.0 and 6.0 mg, respectively) was suspended in HFP (2.0 mL), sonicated and left stirring at room temperature for 2 hours. Successively, PDLLA (280.0 mg) was added and all components were kept under magnetic stirring overnight at 310 K. For scaffolds **PA01 (C)** and **PA03 (D)**, AgNPs (2.0 and 6.0 mg, respectively) were suspended in HFP (2.0 mL), sonicated and left stirring at room temperature for 2 hours. Successively, PDLLA (280.0 mg) was added and the polymer solution was kept under magnetic stirring overnight at 310 K.

For scaffolds **PN (J)**, CNCs (8.2 mg) have been suspended in HFP (2.0 mL), sonicated and left stirring at room temperature for 2 hours. Successively, PDLLA (260.0 mg) was added and all kept under magnetic stirring overnight at 310 K. For scaffolds **PNL01 (F)** and **PNL03 (G)**, chestnut lignin (2.0 and 6.0 mg, respectively) was suspended in HFP (2.0 mL), sonicated and left stirring at room temperature for 2 hours. Afterward, CNCs (8.2 mg) were added and the suspension was left stirring at room temperature for 2 hours further. Successively, PDLLA (260.0 mg) was added and all kept under magnetic stirring overnight at 310 K.

For scaffolds **PNA01 (H)** and **PNA03 (I),** AgNPs (2.0 and 6.0 mg, respectively) were suspended in HFP (2.0 mL), sonicated and left stirring at room temperature for 2 hours. Afterward, CNCs (8.2 mg) were added and the suspension was left stirring at room temperature for further 2 hours. Successively, PDLLA (260.0 mg) was added and all components kept under magnetic stirring overnight at 310 K.

For scaffold **PC (O)**, CS (2.4 mg) has been suspended in HFP (2.0 mL), sonicated and left stirring at room temperature for 2 hours. Successively, PDLLA (260.0 mg) was added and all components were kept under magnetic

stirring overnight at 310 K. For scaffolds **PCL01 (K)** and **PCL03 (L),** chestnut lignin (2.0 and 6.0 mg, respectively) was suspended in HFP (2.0 mL), sonicated and left stirring at room temperature for 2 hours. Afterward, CS (2.4 mg) was added and the suspension was left stirring at room temperature for further 2 hours. Successively, PDLLA (260.0 mg) was added and all components kept under magnetic stirring overnight at 310 K. For scaffolds **PCA01 (M) and PCA03 (N),** AgNPs (2.0 and 6.0 mg, respectively) were suspended in HFP (2.0 mL), sonicated and left stirring at room temperature for 2 hours. Afterward, CS (2.4 mg) was added and the suspension was left stirring at room temperature for 2 hours further. Successively, PDLLA (260.0 mg) was added and all kept under magnetic stirring overnight at 310 K.

A Linari Engineering Gamma-High Voltage generator electrospinning system was used for the preparation of electrospin fibers. The polymer mixtures were loaded into a 10 mL glass syringe with an 18 G stainless-steel needle and then electrospun at 19 kV with a flow rate of 1.0 mL/h of the pump. The target was a round copper plate having 90 mm diameter coated with aluminium foils and the distance between the collector and the needle was set to 19 cm.

Antioxidant properties of AgNP-PNS

To a 200 μM DPPH ethanolic solution, AgNP-PNS or PNS (0.025-7.5 mg/mL) were added. After 10 min under stirring at room temperature, the absorbance at 515 nm was measured by Uv-Vis spectrophotometer. FRAP solution was prepared mixing 20 mM $FeCl_3$, 10 mM 2,4,6-tris(2-pirydyl)-s-triazine, and 0.3 M acetate buffer (pH 3.6) in a 1:1:10 v/v/v ratio. AgNP-PNS or PNS (0.03-0.15 mg/mL) were added to FRAP solution and stirred for 10 min at room temperature. The absorbance at 593 nm was measured. All the experiments were run in triplicate.

Antioxidant activity of the electrospun fibers. Electrospun fibers sections of ca. 1 cm^2 total surface area (corresponding to 7 mg of material) were deposited on the bottom of a vial containing 2,4 and 6 mL of a 200 μM ethanolic solution

of DPPH. A blank sample without the films was also prepared. The absorbance of each solution at 515 nm was periodically analysed. Experiments were run in triplicate. The same procedure was then applied for FRAP solution containing 1.7 mM $FeCl_3$ and 0.83 mM TPTZ in 0.3 M acetate buffer (pH 3.6) and the absorbance of each solution at 593 nm was periodically analysed. Experiments were run in triplicate.

Photocatalytic properties of AgNP-PNS

In a 60 mm cell-culture dish 10 mL of a methylene blue (MB) solution (30 mg/mL) in water was placed in presence of AgNP-PNS (4 mg). The suspension was irradiated with the aid of a solar simulator (Thermo Oriel 66902 model) at 60 W, with a UV-cutoff filter ($\lambda > 400$ nm) for 120 min. The MB absorbance was measured every 30 minutes by Uv-Vis spectroscopy, withdrawning 2 mL of the mixture and carefully replacing in the cell culture dish. Different control experiments were carried out: i) using PNS in place of AgNP-PNS; ii) in absence of AgNP-PNS; iii) in the dark. Each experiment was run in triplicate.

For the recycling of AgNP-PNS at the end of each experiment, the resulting mixture was centrifuged, washed extensively with water and lyophilized. Finally, AgNP-PNS were recovered and reused in the photodegradation experiment as above.

Antibacterial Activity of AgNP-PNS

Thermo Fisher Scientific, Waltham, Massachusetts, USA, provided the trypticase soy broth agar and trypticase soy yeast extract agar, which were used for the 18-hour cultures of P. aeruginosa PAO1 (ATCC® BAA-47) and S. mutans (ATCC® 25175), respectively. Then, one colony was reconstituted in liquid broth medium (5 mL), and it was incubated at 37 °C and 200 rpm for an overnight period. By observing the optical density (OD) at 600 nm of bacterial suspensions cultivated in the presence of the sample, AgNP-capacity PNS's to limit bacterial growth was determined. A 96-well polystyrene plate was used,

and AgNP-PNS was added at various concentrations (50, 100, 250, 500, and 1000 g/mL) in the presence of 200 L of liquid broth.

Then, the plates were incubated at 37 °C and 200 rpm in a microplate reader with bacteria injected at 0.5 MacFarland standard turbidity (about 1.5 108 CFU/mL) (Cytation 3, AHSI). Negative controls included liquid medium broth devoid of bacteria, whereas positive controls included 200 L of PAO1 (1.5 108 CFU/mL) or S. mutans (1.5 108 CFU/mL). The OD at 600 nm was measured at predetermined intervals (6 hours, 12 hours, and 24 hours). The tests were carried out three times. For the agar diffusion procedure, a solid broth medium measuring 10 mm by 150 mm was covered with 100 L of bacterial suspension containing around 1.5 108 CFU/mL and left to dry for about 10 minutes.

Agar bacterial plates were aseptically loaded with discs containing 250, 500, and 1000 g/mL of AgNP-PNS or 1000 g/mL of PNS. The discs were then incubated at 37 °C overnight either in the dark or with light illumination using a desk lamp fitted with an 11 W, 806 lumen, E27 ID60 LED bulb (Jedi Lighting). As a negative control, liquid medium broth devoid of microorganisms was utilized. The sizes of the inhibitory zones were measured at the conclusion of the incubation period. The tests were carried out three times.

Biofilm growth inhibition by AgNP-PNS

Biofilm was created, with a few alterations, as stated in [316]. In a 48-well polystyrene plate, various doses of AgNP-PNS (250, 500, and 1000 g/mL) were added in the presence of 750 L PAO1 or a suspension of *S. mutans* (1 107 CFU/mL) or both. For 6, 12, and 24 hours, the cultures were incubated statically at 37 °C in a humid environment in order to develop a mature biofilm. As a negative control, liquid medium broth devoid of bacteria was utilized; as a positive control, 750 L of PAO1 (1 107 CFU/mL) and *S. mutans* (1 107 CFU/mL) were employed.

The crystal violet (CV) test was used to measure the amount of surface-adhered biofilm [317]. Each well was carefully cleaned with sterile phosphate buffered

saline (PBS) before being allowed to air dry for 30 minutes. Then, a 0.1% w/v CV solution was applied to each well. Excess solution was drained after 30 minutes, and any remaining stain was washed off with PBS. The pigmented biofilms were dissolved in 96% ethanol and measured using a microplate reader to measure the OD at 570 nm (Cytation 3, AHSI). The tests were carried out in triplicate.

Catechol-graphene based hydrogel preparation for a spectro-electrochemical experiment. A transparent gold electrode (r = 0.2 cm) was dipped into a chitosan solution (1 % w/v) with/without a 0.2 % w/v graphene (low content) to obtain a Chit o Chit-Gr coeated electrode, respectively. Subsequently, a constant current density (0.6 $mA \cdot cm^{-2}$) was applied for 90 seconds. Then the coated electrode was immersed into 10 mM catechol solution (0.1 M phosphate buffer, pH 7.0) and a constant potential (0.6 V vs Ag/AgCl) was applied to reach the qFab of 0.3 $C \cdot cm^{-2}$. To remove the adsorbed not grafted catechol, the final electrode was extensively washed with water. Chit or Gr-Chit-hydrogel were electrodeposited on a standard gold electrode (r = 0.1 cm) or a gold coated silicon wafer (A = 1 cm^2). With this aim the electrode was immersed into a chitosan solution (1 w/v%) with various graphene contents using a constant current density of 0.6 $mA \cdot cm^{-2}$ for 3 min. Then, the Chit or Gr-Chit hydrogel coated electrode was dipped in 10 mM catechol solution and different catechol contents were electrodeposited using various qFab ($C \cdot cm^{-2}$). To remove the adsorbed catechol not grafted to the chitosan, the final electrode was extensively washed with water. After that, for SEM measurement, the hydrogel-coated electrode was freeze-dried. For FT-IR measurement, the hydrogel was suspended in water and dipped into 0.1 M NaOH. After 12 hours the hydrogel was peeled off from the electrode.

Spectroelectrochemical measurement of catechol-graphene based hydrogel. On a transparent gold electrode, a thin hydrogel film was electrodeposited. This latter was placed into a cuvette, filled with the phosphate buffer solution (0.1 M,

pH 7.0) in presence or in absence of 0.1 mM Fc and 0.1 mM Ru^{3+}. As a counter electrode, a platinum wire was used, while as reference electrode a Ag/AgCl was used. All three electrodes were connected to an electrochemical analyzer. The optical absorbance was followed at selected times by a Uv-Vis spectrophotometer. Simultaneously, the optical (absorbance) and electrochemical (current) output responses were individually recorded over time.

Electrochemical measurement of catechol-graphene based hydrogel. A thick hydrogel film was electrodeposited on a standard gold electrode. As a counter electrode, a platinum wire was used, while as reference electrode a Ag/AgCl was used. All three electrodes were connected to an electrochemical analyzer and placed into an electrochemical cell containing the phosphate buffer solution (0.1 M, pH 7.0) in presence or in absence of 0.1 mM Fc and 0.1 mM Ru^{3+} Air was excluded by purging N_2 during the experiment. A frequency range from 0.05 Hz to 10 kHz with a perturbation amplitude of 5 mV from the open circuit potential was used for the ElS measurement.

Mass measurement of composite hydrogel. To measure the mass of electrofabricated composite hydrogel, a quartz crystal microbalance (QCM) (CHI420, CH instruments, Inc., Austin, TX.) was used. The composite hydrogel was electrofabricated on a 8 MHz resonating, gold-coated crystal (working area: 0.205 cm^2). In an ex-situ QCM experiment, the initial frequency (f0) of a dried crystal was measured in the air. Subsequently, on the gold crystal the composite hydrogel was electrofabricated. To remove the water in the hydrogel the composite-hydrogel coated crystal was dried in the air for 2 hours. Then, the frequency (f1) of the dried hydrogelcoated crystal was measured. Δf was calculated as the difference between f0 and f1, used to estimate the mass change with a mass sensitivity of 1.34 $ng \cdot Hz^{-1}$.

Conclusions

The focus of this PhD thesis is represented by phenols and polyphenols, providing the main reactive unit in complex systems and biopolymers. These compounds have been finding increasing applications not only as food supplements, but also as additives for the implementation of functional materials. Notably, the use of green chemistry methodologies including solvent free conditions and mechanochemistry for functionalization or activation of phenolic compounds or their extraction from an easily accessible and low-cost sources, *i.e.* agri-food wastes, represented the central strategy applied in this thesis to improve their activities for various applications.

Among natural phenolic compounds, growing interest has been devoted to eumelanin, a family of heterogeneous and polymeric catechol pigments, ubiquitously found in nature, characterized by complex molecular and supramolecular structure with a wide spectrum of interesting properties such as antioxidant, photoprotective or redox activity. Thanks to their ability to give rise to multiple interactions including covalent and hydrogen bonding, cation-π and aromatic interactions, or binding of various metals, these pigments can be exploited for various applications. However, the poor solubility of melanin has so far limited the full characterization of their properties, that may hold the key of their biological role, and represents the major limitation in an electrochemical analysis, making difficult the exchange of electrons with the electrode surface. To overcome this limitation, recently an alternative top-down method, that hinges on an electrochemical reverse-engineering methodology, using soluble mediators (redox active species that can diffuse freely in solution), was developed. This innovative approach was applied to the synthetic model pigments obtained from an enzymatic promoted oxidation of DHI and DHICA monomers, probing their excellent redox and antioxidant active properties,

especially in the case of DHICA melanins. In addition, spectroelectrochemical analysis, allowing the simultaneous measurement of optical and electrochemical properties, highlighted the possibility to tune the redox properties of these pigments exploiting their metal binding abilities.

Furthermore, the possibility to use hexamethylenediamine (HMDA) to impart film forming ability to natural polymers including eumelanins has been recently explored with the aim to broaden the potential of polydopamine (PDA)-based films overcoming their inherent limitations. The detailed mechanism by which HMDA can mediate film deposition by catechol polymerization had remained so far little understood. In this context, the studies carried out in this PhD project led to deposition of a film from DHICA derivatives promoted by HMDA. This was yellowish in color, uniform and homogenous on different materials, and characterized by a moderate hydrophobicity. The main film components were shown to consist of dimers and small oligomers along with HMDA and monomeric MeDHICA, but no covalent conjugation products were observed. The proposed film deposition process is the spontaneous assembly of self-organized networks held together primarily by electrostatic interactions of deprotonated MeDHICA (anion species) and HMDA as the di-cation form.

Along this research line are also the studies aimed at developing new melanin precursors and melanins thereof. Nowadays, significant efforts have been devoted to the search of natural or naturally-derived products as functional ingredients of dermocosmetic formulations, in order to satisfy the increasing demand from consumers for products that might ensure high activity even at low doses without showing health risks. To this aim, a new type of amide/diamide melanin precursors were synthetized in satisfactory good yields. In contrast to the melanin obtained from other synthetic DHICA melanin derivatives, the DHICA amide melanins showed an absorption in the Uv-Vis region even higher than DHICA melanin and proved to be more active against radical and light-induced lipid peroxidation, indicating the potential of this pigment in preventing

the degradation of unsaturated fatty acid components of triglycerides and membrane phospholipids associated to inflammatory conditions and skin ageing. Hyperpigmentary disorders due to melanin overproduction or accumulation are among the most common skin disorders. Melasma and lentigo are two main examples of such disorders, but many other skin dyschromia phenomena caused by inflammatory reactions, or abnormal melanocyte activity are known. Tyrosinase is one of the key factor and enzyme related to these disorders. Therefore, the inhibition of this enzyme represents a straightforward strategy to regulate and control these syndromes.

Within this context, a green protocol based on eco-friendly solvent for the extraction of phenolic compounds from agri-food by-products after proper mechanical pre-treatment was developed, showing promising activity as in *vitro* inhibitors of tyrosinase. As an alternative strategy, a completely different approach, based on an *ad hoc* synthesis of an amide derivative of caffeic acid conjugated with dihydrolipoic acid, was implemented. Also in this case, promising results were obtained.

Among the possible uses of these phenolic compounds or their polymers, the extraction from agri-food by-products, chemical modification or incorporation in biopolymers are appealing strategies to exploit their properties for biomedical applications. Based on these considerations, selected phenolic acids such as caffeic acid, chlorogenic acid and gallic acid or extracts from different agri-food by-products were reacted with denatured soy or whey proteins, giving rise to materials with remarkable underwater resistance and mechanical properties together with optimal antioxidant and antibacterial activity, of interest for the development of surgical glues and wound treatment devices.

In this frame, the wide distribution of phenolic compounds in agri-food by-products has focused intense research work on the development and optimization of extraction methodologies. The conventional extraction protocols involve long extraction times, high costs, and use of organic solvents with

inherent drawbacks such as low boiling points, flammability, toxicity, and non-biodegradability. To overcome these limitations efforts have devoted to the development of recovery methods using low environmental impact solvents, such as deep eutectic solvent, showing strong extraction qualities, together with low cost and minimal environmental impact. In addition, to achieve a more efficient recovery and a more reproducible extraction procedure, the use of mechanical treatments, including a ball or a planetary mill grinding has been evaluated.

The research activity of the PhD project has led to the implementation a green procedure based on DES combined with proper mechanical pre-treatment for the recovery of lignin from shells of edible nuts. The developed approach allowed an efficient recovery and extraction in good yields of lignin-rich samples, characterized by great antioxidant properties, comparable or even higher than those reported in literature for other phenolic rich samples from the agri-food sector. Secondly, a sequential conventional/DES based extraction method for the recovery of low and high molecular weight phenolic compounds from agri-food by-products, including defatted spent coffee ground (dSCG) and pomegranate peels and seeds, was developed, allowing a rational and full exploitation of these agri-food by-products.

Another research topic presented in this thesis concerns the exploitation of polyphenols as organic components to be combined with inorganic materials to broaden the range of their properties.

Firstly, Pecan Nut Shells (PNS) as a source of phenolic compounds and as an efficient and low-cost agri-food by-product, were used for the *in-situ* synthesis of silver nanoparticles AgNP, AgNP-PNS. In particular, a mechanochemical, green and scalable approach was used to create multifunctional AgNPs. The developed method looks appropriate for large-scale implementation of antimicrobial devices for healthcare applications, such as in bone tissue

engineering as a topical antibacterial agent or wound dressing material with antibiotic action, as well as for uses in catalysis.

In addition, due to the encouraging results of the AgNP-PNS, the same approach was extended to other phenolic compounds. In particular, the lignin recovered from chestnut shells (CLN) using DES with the aid of a ball mill, were employed as efficient reducing agent for the *in-situ* synthesis of AgNPs. The final AgNP-CLN were then incorporated into electrospun fibers, giving rise to valuable materials with interesting antioxidant, antibacterial activity and good cytocompatibility. Finally, a composite hydrogel film composed of graphene and catechol was electrofabricated, offering synergistic properties due to the presence of the well-known conductor graphene with catechol systems. A full characterization of the electron flow of the final materials was carried out using also in this case an electrochemical analysis.

Overall, the present PhD thesis provides significant contributions of the diverse functional materials that can be prepared from phenolic building blocks, bridging the most intriguing fields nowadays studied. Herein, the intrinsic properties of phenolic compounds were fully exploited, giving rise to materials retaining the unique properties of phenolic compounds, such as redox potentials, metal binding, antioxidant activity, polymerization and Uv-Vis absorbance. In addition, materials prepared combining phenolic compounds with inorganic materials such as silver nanoparticles or graphene hold many of their useful properties with synergistic effects in applications ranging from photocatalysis to biomedicine, making them a distinct class of structural motifs for the preparation of functional materials.

References

1. Rasouli, H.; Farzaei, M.H.; Khodarahmi, R. Polyphenols and their benefits: A review. *Int. J. Food Prop.* **2017**, *20*, 1700–1741, doi:10.1080/10942912.2017.1354017.

2. Karim, F.; Fakhruddin, A.N.M. Recent advances in the development of biosensor for phenol: A review. *Rev. Environ. Sci. Biotechnol.* **2012**, *11*, 261–274, doi:10.1007/s11157-012-9268-9.

3. Zhang, Y.; Naebe, M. Lignin: A Review on Structure, Properties, and Applications as a Light-Colored UV Absorber. *ACS Sustain. Chem. Eng.* **2021**, *9*, 1427–1442, doi:10.1021/acssuschemeng.0c06998.

4. Zevallos Torres, L.A.; Lorenci Woiciechowski, A.; de Andrade Tanobe, V.O.; Karp, S.G.; Guimarães Lorenci, L.C.; Faulds, C.; Soccol, C.R. Lignin as a potential source of high-added value compounds: a review. *J. Clean. Prod.* **2020**, *263*, 121499, doi:10.1016/j.jclepro.2020.121499.

5. Xie, C.; Wang, X.; He, H.; Ding, Y.; Lu, X. Mussel-Inspired Hydrogels for Self-Adhesive Bioelectronics. *Adv. Funct. Mater.* 2020, *30*.

6. Barclay, T.G.; Hegab, H.M.; Clarke, S.R.; Ginic-Markovic, M. Versatile Surface Modification Using Polydopamine and Related Polycatecholamines: Chemistry, Structure, and Applications. *Adv. Mater. Interfaces* **2017**, *4*, 1–38, doi:10.1002/admi.201601192.

7. Xie, W.; Pakdel, E.; Liang, Y.; Kim, Y.J.; Liu, D.; Sun, L.; Wang, X. Natural Eumelanin and Its Derivatives as Multifunctional Materials for Bioinspired Applications: A Review. *Biomacromolecules* **2019**, *20*, 4312–4331, doi:10.1021/acs.biomac.9b01413.

8. Rahim, M.A.; Kristufek, S.L.; Pan, S.; Richardson, J.J.; Caruso, F. Phenolic Building Blocks for the Assembly of Functional Materials. *Angew. Chemie - Int. Ed.* **2019**, *58*, 1904–1927, doi:10.1002/anie.201807804.

9. Almeida, A.C.; Vale, A.C.; Pires, R.A.; Reis, R.L.; Alves1, N.M. - Layer-by-layer films based on catechol-modified polysaccharides produced by dip- and spin-coating onto different substrates. *J. Biomed. Mater. Res. Part B* **2020**, *108B*, 1412–1427, doi:10.1002/jbm.b.34489.

10. Hong, S.H.; Ryu, J.H.; Lee, H. Effect of charge on in vivo adhesion stability of catechol-conjugated polysaccharides. *J. Ind. Eng. Chem.* **2019**, *79*, 425–430, doi:10.1016/j.jiec.2019.07.017.

11. Ryu, J.H.; Hong, S.; Lee, H. Bio-inspired adhesive catechol-conjugated chitosan for biomedical applications: A mini review. *Acta Biomater.* **2015**, *27*, 101–115, doi:10.1016/j.actbio.2015.08.043.

12. Moro, K.I.B.; Bender, A.B.B.; da Silva, L.P.; Penna, N.G. Green Extraction Methods and Microencapsulation Technologies of Phenolic Compounds From Grape Pomace: A Review. *Food Bioprocess Technol.* **2021**, *14*, 1407–1431, doi:10.1007/s11947-021-02665-4.

13. Ali Redha, A. Review on Extraction of Phenolic Compounds from Natural Sources Using Green Deep Eutectic Solvents. *J. Agric. Food Chem.* **2021**, *69*, 878–912, doi:10.1021/acs.jafc.0c06641.

14. Gao, X.; Xu, Z.; Liu, G.; Wu, J. Polyphenols as a versatile component in tissue engineering. *Acta Biomater.* **2021**, *119*, 57–74, doi:10.1016/j.actbio.2020.11.004.

15. Zhang, X.; Li, Z.; Yang, P.; Duan, G.; Liu, X.; Gu, Z.; Li, Y. Polyphenol scaffolds in tissue engineering. *Mater. Horizons* **2021**, *8*, 145–167, doi:10.1039/d0mh01317j.

16. Shahidi, F.; Yeo, J.D. Bioactivities of phenolics by focusing on suppression of chronic diseases: A review. *Int. J. Mol. Sci.* **2018**, *19*, 1–16, doi:10.3390/ijms19061573.

17. Dai, J.; Mumper, R.J. Plant phenolics: Extraction, analysis and their antioxidant and anticancer properties. *Molecules* **2010**, *15*, 7313–7352, doi:10.3390/molecules15107313.

18. Działo, M.; Mierziak, J.; Korzun, U.; Preisner, M.; Szopa, J.; Kulma, A. The potential of plant phenolics in prevention and therapy of skin disorders. *Int. J. Mol. Sci.* **2016**, *17*, 1–41, doi:10.3390/ijms17020160.

19. Wu, D.; Zhou, J.; Creyer, M.N.; Yim, W.; Chen, Z.; Messersmith, P.B.; Jokerst, J. V. Phenolic-enabled nanotechnology: Versatile particle engineering for biomedicine. *Chem. Soc. Rev.* **2021**, *50*, 4432–4483, doi:10.1039/d0cs00908c.

20. Ignat, I.; Volf, I.; Popa, V.I. A critical review of methods for characterisation of polyphenolic compounds in fruits and vegetables. *Food Chem.* **2011**, *126*, 1821–1835, doi:10.1016/j.foodchem.2010.12.026.

21. Khoddami, A.; Wilkes, M.A.; Roberts, T.H. Techniques for analysis of plant phenolic compounds. *Molecules* **2013**, *18*, 2328–2375, doi:10.3390/molecules18022328.

22. Kumar, N.; Goel, N. Phenolic acids: Natural versatile molecules with promising therapeutic applications. *Biotechnol. Reports* **2019**, *24*, e00370, doi:10.1016/j.btre.2019.e00370.

23. Saibabu, V.; Fatima, Z.; Khan, L.A.; Hameed, S. Therapeutic potential of

dietary phenolic acids. *Adv. Pharmacol. Pharm. Scinces* **2015**, *2015*, 823539.

24. Kiokias, S.; Proestos, C.; Oreopoulou, V. Phenolic acids of plant origin - a review on their antioxidant activity in vitro (O/W emulsion systems) along with their in vivo health. *Foods* **2020**, *9*, 534.

25. Oluwole, O.; Fernando, W.B.; Lumanlan, J.; Ademuyiwa, O.; Jayasena, V. Role of phenolic acid, tannins, stilbenes, lignans and flavonoids in human health – a review. *Int. J. Food Sci. Technol.* **2022**, *57*, 6326–6335, doi:10.1111/ijfs.15936.

26. Koroleva, O.; Torkova, A.; Nikolaev, I.; Khrameeva, E.; Fedorova, T.; Tsentalovich, M.; Amarowicz, R. Evaluation of the antiradical properties of phenolic acids. *Int. J. Mol. Sci.* **2014**, *15*, 16351–16380, doi:10.3390/ijms150916351.

27. Kang, J.; Thakali, K.M.; Jensen, G.S.; Wu, X. Phenolic Acids of the Two Major Blueberry Species in the US Market and Their Antioxidant and Anti-inflammatory Activities. *Plant Foods Hum. Nutr.* **2015**, *70*, 56–62, doi:10.1007/s11130-014-0461-6.

28. Vinayagam, R.; Jayachandran, M.; Xu, B. Antidiabetic effects of simple phenolic acids: a comprehensive review. *Phyther. Res.* **2016**, *30*, 184–199, doi:10.1002/ptr.5528.

29. Abotaleb, M.; Liskova, A.; Kubatka, P.; Büsselberg, D. Therapeutic potential of plant phenolic acids in the treatment of cancer. *Biomolecules* **2020**, *10*, 1–23, doi:10.3390/biom10020221.

30. Ishaque, S.; Arshad, A.; Haider, M.; Fatima, F. Phenolic acid profiling by RP-HPLC: evaluation of antibacterial and anticancer activities of Canocarpus Erectus plant extracts. *Biol. Clin. Sci. Res. J.* **2021**, 1–9.

31. Cueva, C.; Moreno-Arribas, M.V.; Martín-Álvarez, P.J.; Bills, G.; Vicente, M.F.; Basilio, A.; Rivas, C.L.; Requena, T.; Rodríguez, J.M.; Bartolomé, B. Antimicrobial activity of phenolic acids against commensal, probiotic and pathogenic bacteria. *Res. Microbiol.* **2010**, *161*, 372–382, doi:10.1016/j.resmic.2010.04.006.

32. Prajna, J.; Richa, J.; Dipjyoti, C. HPLC quantification of phenolic acids from Vetiveria zizanioides (L .) Nash and its antioxidant and antimicrobial activity. *J. Pharm.* **2013**, *2013*, 270472.

33. Ordoñez, R.; Atarés, L.; Chiralt, A. Biodegradable active materials containing phenolic acids for food packaging applications. *Compr. Rev. Food Sci. Food Saf.* **2022**, *21*, 3910–3930, doi:10.1111/1541-4337.13011.

34. Balasundram, N.; Sundram, K.; Samman, S. Phenolic compounds in plants and agri-industrial by-products: antioxidant activity, occurrence, and potential uses. *Food Chem.* **2006**, *99*, 191–203, doi:10.1016/j.foodchem.2005.07.042.

35. Mujtaba, M.; Lipponen, J.; Ojanen, M.; Puttonen, S.; Vaittinen, H. Trends and challenges in the development of bio-based barrier coating materials for paper/cardboard food packaging; a review. *Sci. Total Environ.* **2022**, *851*, 158328, doi:10.1016/j.scitotenv.2022.158328.

36. Panzella, L.; Napolitano, A. Natural phenol polymers: Recent advances in food and health applications. *Antioxidants* **2017**, *6*, 1–24, doi:10.3390/antiox6020030.

37. García Ibarra, V.; Sendón, R.; Rodríguez-Bernaldo De Quirós, A. *Antimicrobial Food Packaging Based on Biodegradable Materials*; Elsevier Inc., 2016; ISBN 9780128007235.

38. Gupta, V.; Biswas, D.; Roy, S. A Comprehensive Review of Biodegradable Polymer-Based Films and Coatings and Their Food Packaging Applications. *Materials (Basel).* **2022**, *15*, doi:10.3390/ma15175899.

39. Lisitsyn, A.; Semenova, A.; Nasonova, V.; Polishchuk, E.; Revutskaya, N.; Kozyrev, I.; Kotenkova, E. Approaches in animal proteins and natural polysaccharides application for food packaging: Edible film production and quality estimation. *Polymers (Basel).* **2021**, *13*, doi:10.3390/polym13101592.

40. Liu, J.; Yong, H.; Yao, X.; Hu, H.; Yun, D.; Xiao, L. Recent advances in phenolic-protein conjugates: Synthesis, characterization, biological activities and potential applications. *RSC Adv.* **2019**, *9*, 35825–35840, doi:10.1039/c9ra07808h.

41. Zink, J.; Wyrobnik, T.; Prinz, T.; Schmid, M. *Physical, chemical and biochemical modifications of protein-based films and coatings: An extensive review*; 2016; Vol. 17; ISBN 8161491526.

42. Orlien, V.; Rinnan, Å. Processing Effects on Protein Structure and Physicochemical Properties. *Foods* **2022**, *11*, 0–3, doi:10.3390/foods11111607.

43. Byette, F.; Marcotte, I.; Pellerin, C. Covalently crosslinked mussel byssus protein-based materials with tunable properties. *Pept. Sci.* **2019**, *111*, 1–8, doi:10.1002/pep2.24053.

44. Anand, P.P.; Vardhanan, Y.S. Computational modelling of wet adhesive mussel foot proteins (Bivalvia): Insights into the evolutionary convolution in diverse perspectives. *Sci. Rep.* **2020**, *10*, 1–24, doi:10.1038/s41598-020-

59169-y.

45. Wang, Z.; Yang, H.C.; He, F.; Peng, S.; Li, Y.; Shao, L.; Darling, S.B. Mussel-Inspired Surface Engineering for Water-Remediation Materials. *Matter* **2019**, *1*, 115–155, doi:10.1016/j.matt.2019.05.002.

46. Shao, C.; Wang, M.; Meng, L.; Chang, H.; Wang, B.; Xu, F.; Yang, J.; Wan, P. Mussel-Inspired Cellulose Nanocomposite Tough Hydrogels with Synergistic Self-Healing, Adhesive, and Strain-Sensitive Properties. *Chem. Mater.* **2018**, *30*, 3110–3121, doi:10.1021/acs.chemmater.8b01172.

47. Kord Forooshani, P.; Lee, B.P. Recent approaches in designing bioadhesive materials inspired by mussel adhesive protein. *J. Polym. Sci. Part A Polym. Chem.* **2017**, *55*, 9–33, doi:10.1002/pola.28368.

48. Ryu, J.H.; Messersmith, P.B.; Lee, H. Polydopamine Surface Chemistry: A Decade of Discovery. *ACS Appl. Mater. Interfaces* **2018**, *10*, 7523–7540, doi:10.1021/acsami.7b19865.

49. Liu, H.; Qu, X.; Tan, H.; Song, J.; Lei, M.; Kim, E.; Payne, G.F.; Liu, C. Role of polydopamine's redox-activity on its pro-oxidant, radical-scavenging, and antimicrobial activities. *Acta Biomater.* **2019**, *88*, 181–196, doi:10.1016/j.actbio.2019.02.032.

50. Ball, V. Polydopamine nanomaterials: Recent advances in synthesis methods and applications. *Front. Bioeng. Biotechnol.* **2018**, *6*, 109, doi:10.3389/fbioe.2018.00109.

51. Della Vecchia, N.F.; Avolio, R.; Alfè, M.; Errico, M.E.; Napolitano, A.; D'Ischia, M. Building-block diversity in polydopamine underpins a multifunctional eumelanin-type platform tunable through a quinone control point. *Adv. Funct. Mater.* **2013**, *23*, 1331–1340, doi:10.1002/adfm.201202127.

52. Guo, Y.; Baschieri, A.; Mollica, F.; Valgimigli, L.; Cedrowski, J.; Litwinienko, G.; Amorati, R. Hydrogen Atom Transfer from HOO. to ortho-Quinones Explains the Antioxidant Activity of Polydopamine. *Angew. Chemie - Int. Ed.* **2021**, *60*, 15220–15224, doi:10.1002/anie.202101033.

53. Fu, Y.; Ren, P.; Wang, F.; Liang, M.; Hu, W.; Zhou, N.; Lu, Z.; Zhang, T. Mussel-inspired hybrid network hydrogel for continuous adhesion in water. *J. Mater. Chem. B* **2020**, *8*, 2148–2154, doi:10.1039/c9tb02863c.

54. Cheng, W.; Zeng, X.; Chen, H.; Li, Z.; Zeng, W.; Mei, L.; Zhao, Y. Versatile Polydopamine Platforms: Synthesis and Promising Applications for Surface Modification and Advanced Nanomedicine. *ACS Nano* **2019**, *13*, 8537–8565, doi:10.1021/acsnano.9b04436.

55. Paez, J.I.; Ustahüseyin, O.; Serrano, C.; Ton, X.A.; Shafiq, Z.; Auernhammer, G.K.; D'Ischia, M.; Del Campo, A. Gauging and Tuning Cross-Linking Kinetics of Catechol-PEG Adhesives via Catecholamine Functionalization. *Biomacromolecules* **2015**, *16*, 3811–3818, doi:10.1021/acs.biomac.5b01126.

56. Mei, S.; Xu, X.; Priestley, R.D.; Lu, Y. Polydopamine-based nanoreactors: Synthesis and applications in bioscience and energy materials. *Chem. Sci.* **2020**, *11*, 12269–12281, doi:10.1039/d0sc04486e.

57. Suárez-García, S.; Sedó, J.; Saiz-Poseu, J.; Ruiz-Molina, D. Copolymerization of a catechol and a diamine as a versatile polydopamine-like platform for surface functionalization: The case of a hydrophobic coating. *Biomimetics* **2017**, *2*, 22.

58. Lyu, Q.; Zhang, J.; Neoh, K.G.; Li Lin Chai, C. A one step method for the functional and property modification of DOPA based nanocoatings. *Nanoscale* **2017**, *9*, 12409–12415, doi:10.1039/c7nr05293f.

59. Alfieri, M.L.; Panzella, L.; Oscurato, S.L.; Salvatore, M.; Avolio, R.; Errico, M.E.; Maddalena, P.; Napolitano, A.; D'Ischia, M. The chemistry of polydopamine film formation: The amine-quinone interplay. *Biomimetics* **2018**, *3*, 26.

60. Panzella, L.; Gentile, G.; D'Errico, G.; Della Vecchia, N.F.; Errico, M.E.; Napolitano, A.; Carfagna, C.; D'Ischia, M. Atypical structural and π-electron features of a melanin polymer that lead to superior free-radical-scavenging properties. *Angew. Chemie - Int. Ed.* **2013**, *52*, 12684–12687, doi:10.1002/anie.201305747.

61. Micillo, R.; Panzella, L.; Koike, K.; Monfrecola, G.; Napolitano, A.; D'Ischia, M. "Fifty shades" of black and red or how carboxyl groups fine tune eumelanin and pheomelanin properties. *Int. J. Mol. Sci.* **2016**, *17*, 746, doi:10.3390/ijms17050746.

62. d'Ischia, M.; Napolitano, A.; Pezzella, A.; Meredith, P.; Buehler, M. Melanin Biopolymers: Tailoring Chemical Complexity for Materials Design. *Angew. Chemie - Int. Ed.* **2020**, *59*, 11196–11205, doi:10.1002/anie.201914276.

63. Panzella, L.; Napolitano, A.; D'Ischia, M. Is DHICA the key to dopachrome tautomerase and melanocyte functions? *Pigment Cell Melanoma Res.* **2011**, *24*, 248–249, doi:10.1111/j.1755-148X.2010.00771.x.

64. Palumbo, A.; d'Ischia, M.; Misuraca, G.; Prota, G.; Schultz, T.M. Structural modifications in biosynthetic melanins induced by metal ions. *BBA - Gen. Subj.* **1988**, *964*, 193–199, doi:10.1016/0304-4165(88)90166-3.

65. Ito, S.; Wakamatsu, K. Chemistry of mixed melanogenesis - Pivotal roles of dopaquinone. *Photochem. Photobiol.* **2008**, *84*, 582–592, doi:10.1111/j.1751-1097.2007.00238.x.

66. Corani, A.; Huijser, A.; Gustavsson, T.; Markovitsi, D.; Malmqvist, P.Å.; Pezzella, A.; D'Ischia, M.; Sundström, V. Superior photoprotective motifs and mechanisms in eumelanins uncovered. *J. Am. Chem. Soc.* **2014**, *136*, 11626–11635, doi:10.1021/ja501499q.

67. Gauden, M.; Pezzella, A.; Panzella, L.; Neves-Petersen, M.T.; Skovsen, E.; Petersen, S.B.; Mullen, K.M.; Napolitano, A.; D'Ischia, M.; Sundström, V. Role of solvent, pH, and molecular size in excited-state deactivation of key eumelanin building blocks: Implications for melanin pigment photostability. *J. Am. Chem. Soc.* **2008**, *130*, 17038–17043, doi:10.1021/ja806345q.

68. Bernardus Mostert, A.; Davy, K.J.P.; Ruggles, J.L.; Powell, B.J.; Gentle, I.R.; Meredith, P. Gaseous adsorption in melanins: Hydrophilic biomacromolecules with high electrical conductivities. *Langmuir* **2010**, *26*, 412–416, doi:10.1021/la901290f.

69. Cavallini, C.; Vitiello, G.; Adinolfi, B.; Silvestri, B.; Armanetti, P.; Manini, P.; Pezzella, A.; D'ischia, M.; Luciani, G.; Menichetti, L. Melanin and melanin-like hybrid materials in regenerative medicine. *Nanomaterials* **2020**, *10*, 1–32, doi:10.3390/nano10081518.

70. Khanbabaee, K.; van Ree, T. Tannins: Classification and definition. *Nat. Prod. Rep.* **2001**, *18*, 641–649, doi:10.1039/b101061l.

71. KoLeckar, K.; Kubikova, K.; Rehakova, Z.; Kuca, K.; Jun, D.; Jahodar, L.; Opletal, L. Condensed and hydrolysable tannins as antioxidants influencing the health. *Mini-Reviews Med. Chem.* **2008**, *8*, 436–447.

72. Peng, S.; Scalbert, A.; Monties, B. Insoluble ellagitannins in Castanea sativa and Quercus petraea woods. *Phytochemistry* **1991**, *30*, 775–778, doi:https://doi.org/10.1016/0031-9422(91)85250-4.

73. Comandini, P.; Lerma-García, M.J.; Simó-Alfonso, E.F.; Toschi, T.G. Tannin analysis of chestnut bark samples (Castanea sativa Mill.) by HPLC-DAD-MS. *Food Chem.* **2014**, *157*, 290–295, doi:10.1016/j.foodchem.2014.02.003.

74. Pizzi, A. Tannins: Major sources, properties and applications. In *Monomers, Polymers and Composites from Renewable Resources*; Belgacem, M.N., Gandini, A., Eds.; Elsevier, 2008; pp. 179–199 ISBN 9780080453163.

75. Ma, S.; Qin, H.; Jiang, M.; Wang, J.; Wang, W.; Guo, G.; Zhou, L.; Chen, W.; Han, B. Identification and comparison of tannins in gall of Rhus

chinensis Mill. and gall of Quercus infectoria Oliv. by High-Performance Liquid Chromatography-Electrospray Mass Spectrometry. *J. Chromatogr. Sci.* **2020**, *58*, 403–410, doi:10.1093/chromsci/bmz096.

76. Haslam, E. Natural polyphenols (vegetable tannins) as drugs: possible modes of action. *J. Nat. Prod.* **1996**, *59*, 205–215, doi:10.1021/np960040+.

77. Zalacain, A.; Prodanov, M.; Carmona, M.; Alonso, G.L. Optimisation of extraction and identification of gallotannins from sumac leaves. *Biosyst. Eng.* **2003**, *84*, 211–216, doi:10.1016/S1537-5110(02)00246-5.

78. Scalbert, A. Antimicrobial properties of tannins. *Phytochemistry* **1991**, *30*, 3875–3883, doi:10.1016/0031-9422(91)83426-L.

79. Unusan, N. Proanthocyanidins in grape seeds: an updated review of their health benefits and potential uses in the food industry. *J. Funct. Foods* **2020**, *67*, 103861, doi:10.1016/j.jff.2020.103861.

80. Reid, D.G.; Bonnet, S.L.; Kemp, G.; Van Der Westhuizen, J.H. Analysis of commercial proanthocyanidins. Part 4: solid state 13C NMR as a tool for in situ analysis of proanthocyanidin tannins, in heartwood and bark of quebracho and acacia, and related species. *Phytochemistry* **2013**, *94*, 243–248, doi:10.1016/j.phytochem.2013.06.007.

81. Haslam, E.; Cai, Y. Plant polyphenols (vegetable tannins): gallic acid metabolism. *Nat. Prod. Rep.* **1994**, *11*, 41–66, doi:10.1039/NP9941100041.

82. Buzzini, P.; Arapitsas, P.; Goretti, M.; Branda, E.; Turchetti, B.; Pinelli, P.; Ieri, F.; Romani, A. Antimicrobial and antiviral activity of hydrolysable tannins. *Mini-Reviews Med. Chem.* **2008**, *8*, 1179–1187, doi:10.2174/138955708786140990.

83. Hussain, G.; Huang, J.; Rasul, A.; Anwar, H.; Imran, A.; Maqbool, J.; Razzaq, A.; Aziz, N.; Makhdoom, E. ul H.; Konuk, M.; et al. Putative roles of plant-derived tannins in neurodegenerative and neuropsychiatry disorders: an updated review. *Molecules* **2019**, *24*, 2213, doi:10.3390/molecules24122213.

84. Porter, L.J. Tannins. *Methods Plant Biochem.* **1989**, *1*, 389–419, doi:10.1016/B978-0-12-461011-8.50017-2.

85. Chung, K.-T.; Wong, T.Y.; Wei, C.-I.; Huang, Y.-W.; Lin, Y.; Chung, T.; Johnson, M.G. Critical Reviews in Food Science and Nutrition Tannins and Human Health: A Review Tannins and Human Health: A Review. *Crit. Rev. Food Sci. Nutr.* **1998**, *386*, 37–41.

86. Kleinert, M.; Barth, T. Phenols from lignin. *Chem. Eng. Technol.* **2008**, *31*,

736–745, doi:10.1002/ceat.200800073.

87. Chio, C.; Sain, M.; Qin, W. Lignin utilization: A review of lignin depolymerization from various aspects. *Renew. Sustain. Energy Rev.* **2019**, *107*, 232–249, doi:10.1016/j.rser.2019.03.008.

88. Boerjan, W.; Ralph, J.; Baucher, M. Lignin biosynthesis. *Annu. Rev. Plant Biol.* **2003**, *54*, 519–546, doi:10.1146/annurev.arplant.54.031902.134938.

89. Tribot, A.; Amer, G.; Alio, M.A.; de Baynast, H.; Delattre, C.; Pons, A.; Mathias, J.-D.; Callois, J.-M.; Vial, C.; Michaud, P.; et al. Wood-lignin: supply, extraction processes and use as bio-based material. *Eur. Polym. J.* **2019**, *112*, 228–240, doi:10.1016/j.eurpolymj.2019.01.007.

90. Liu, Q.; Luo, L.; Zheng, L. Lignins: biosynthesis and biological functions in plants. *Int. J. Mol. Sci.* **2018**, *19*, 335, doi:10.3390/ijms19020335.

91. Baurhoo, B.; Ruiz-Feria, C.A.; Zhao, X. Purified lignin: nutritional and health impacts on farm animals-A review. *Anim. Feed Sci. Technol.* **2008**, *144*, 175–184, doi:10.1016/j.anifeedsci.2007.10.016.

92. Spiridon, I. Extraction of lignin and therapeutic applications of lignin-derived compounds. A review. *Environ. Chem. Lett.* **2020**, *18*, 771–785, doi:10.1007/s10311-020-00981-3.

93. Iravani, S.; Varma, R.S. Greener synthesis of lignin nanoparticles and their applications. *Green Chem.* **2020**, *22*, 612–636, doi:10.1039/c9gc02835h.

94. Wang, H.-M.; Yuan, T.-Q.; Song, G.-Y.; Sun, R.-C. Advanced and versatile lignin-derived biodegradable composite film materials toward a sustainable world. *Green Chem.* **2021**, *23*, 3790–3817, doi:10.1039/D1GC00790D.

95. Lizundia, E.; Sipponen, M.H.; Greca, L.G.; Balakshin, M.; Tardy, B.L.; Rojas, O.J.; Puglia, D. Multifunctional lignin-based nanocomposites and nanohybrids. *Green Chem.* **2021**, *23*, 6698–6760, doi:10.1039/d1gc01684a.

96. Fermoso, F.G.; Serrano, A.; Alonso-Fariñas, B.; Fernández-Bolaños, J.; Borja, R.; Rodríguez-Gutiérrez, G. Valuable compound extraction, anaerobic digestion, and composting: a leading biorefinery approach for agricultural wastes. *J. Agric. Food Chem.* **2018**, *66*, 8451–8468, doi:10.1021/acs.jafc.8b02667.

97. Xia, H.; Houghton, J.A.; Clark, J.H.; Matharu, A.S. Potential utilization of unavoidable food supply chain wastes-valorization of pea vine wastes. *ACS Sustain. Chem. Eng.* **2016**, *4*, 6002–6009, doi:10.1021/acssuschemeng.6b01297.

98. Zuin, V.G.; Ramin, L.Z. Green and sustainable separation of natural products

from agro-industrial waste: challenges, potentialities, and perspectives on emerging approaches. *Top. Curr. Chem.* **2018**, *376*, 3, doi:10.1007/s41061-017-0182-z.

99. Macias-Corral, M.; Samani, Z.; Hanson, A.; Smith, G.; Funk, P.; Yu, H.; Longworth, J. Anaerobic digestion of municipal solid waste and agricultural waste and the effect of co-digestion with dairy cow manure. *Bioresour. Technol.* **2008**, *99*, 8288–8293, doi:10.1016/j.biortech.2008.03.057.

100. Fierascu, R.C.; Sieniawska, E.; Ortan, A.; Fierascu, I.; Xiao, J. Fruits by-products – a source of valuable active principles. A short review. *Front. Bioeng. Biotechnol.* **2020**, *8*, 319, doi:10.3389/fbioe.2020.00319.

101. Torres-León, C.; Ramírez-Guzman, N.; Londoño-Hernandez, L.; Martinez-Medina, G.A.; Díaz-Herrera, R.; Navarro-Macias, V.; Alvarez-Pérez, O.B.; Picazo, B.; Villarreal-Vázquez, M.; Ascacio-Valdes, J.; et al. Food waste and byproducts: an opportunity to minimize malnutrition and hunger in developing countries. *Front. Sustain. Food Syst.* **2018**, *2*, 52, doi:10.3389/fsufs.2018.00052.

102. Mourtzinos, I.; Goula, A. Polyphenols in agricultural byproducts and food waste. In *Polyphenols in Plants*; Ronald Ross Watson, Ed.; Elsevier Inc., 2019; pp. 23–44 ISBN 9780128137680.

103. Panzella, L.; Moccia, F.; Nasti, R.; Marzorati, S.; Verotta, L.; Napolitano, A. Bioactive Phenolic Compounds From Agri-Food Wastes: An Update on Green and Sustainable Extraction Methodologies. *Front. Nutr.* **2020**, *7*, 1–27, doi:10.3389/fnut.2020.00060.

104. Teixeira, A.; Baenas, N.; Dominguez-Perles, R.; Barros, A.; Rosa, E.; Moreno, D.A.; Garcia-Viguera, C. Natural bioactive compounds from winery by-products as health promoters: a review. *Int. J. Mol. Sci.* **2014**, *15*, 15638–15678, doi:10.3390/ijms150915638.

105. Panwar, D.; Panesar, P.S.; Chopra, H.K. Recent trends on the valorization strategies for the management of citrus by-products. *Food Rev. Int.* **2021**, *37*, 91–120, doi:10.1080/87559129.2019.1695834.

106. Dassoff, E.S.; Guo, J.X.; Liu, Y.; Wang, S.C.; Li, Y.O. Potential development of non-synthetic food additives from orange processing by-products - a review. *Food Qual. Saf.* **2021**, *5*, 1–14, doi:10.1093/fqsafe/fyaa035.

107. Shahidi, F.; Ambigaipalan, P. Phenolics and polyphenolics in food, beverages and spices: antioxidant activity and health effects - a review. *J. Funct. Foods* **2015**, *18*, 820–897, doi:10.1016/j.jff.2015.06.018.

108. Tortora, K.; Femia, A. Pietro; Romagnoli, A.; Sineo, I.; Khatib, M.; Mulinacci, N.; Giovannelli, L.; Caderni, G. Pomegranate by-products in colorectal cancer chemoprevention: effects in Apc-mutated pirc rats and mechanistic studies in vitro and ex vivo. *Mol. Nutr. Food Res.* **2018**, *62*, 1700401, doi:10.1002/mnfr.201700401.

109. Fourati, M.; Smaoui, S.; Hlima, H. Ben; Elhadef, K.; Braïek, O. Ben; Ennouri, K.; Mtibaa, A.C.; Mellouli, L. Bioactive compounds and pharmacological potential of pomegranate (Punica granatum) seeds - a review. *Plants Foods Hum. Nutr.* **2020**, *75*, 477–486, doi:10.1007/s11130-020-00863-7.

110. Fazio, A.; Iacopetta, D.; La Torre, C.; Ceramella, J.; Muià, N.; Catalano, A.; Carocci, A.; Sinicropi, M.S. Finding solutions for agricultural wastes: antioxidant and antitumor properties of recovery. *Foods Funct.* **2018**, *9*, 6618–6631, doi:10.1039/c8fo01394b.

111. Alexandre, E.M.C.; Silva, S.; Santos, S.A.O.; Silvestre, A.J.D.; Duarte, M.F.; Saraiva, J.A.; Pintado, M. Antimicrobial activity of pomegranate peel extracts performed by high pressure and enzymatic assisted extraction. *Food Res. Int.* **2019**, *115*, 167–176, doi:10.1016/j.foodres.2018.08.044.

112. Eberhardt, M. V.; Lee, C.Y.; Liu, R.H. Antioxidant activity of fresh apples. *Nature* **2000**, *405*, 903–904, doi:10.1038/35016151.

113. Panzella, L.; Petriccione, M.; Rega, P.; Scortichini, M.; Napolitano, A. A reappraisal of traditional apple cultivars from Southern Italy as a rich source of phenols with superior antioxidant activity. *Food Chem.* **2013**, *140*, 672–679, doi:10.1016/j.foodchem.2013.02.121.

114. Murthy, P.S.; Naidu, M.M. Recovery of phenolic antioxidants and functional compounds from coffee industry by-products. *Food Bioprocess Technol.* **2012**, *5*, 897–903, doi:10.1007/s11947-010-0363-z.

115. Barba, F.J.; Soto, E.R.; Brncic, M.; Lorenzo, J.M. *Green extraction and valorization of by-products from food processing*;

116. Moreira, A.S.P.; Nunes, F.M.; Domingues, M.R.; Coimbra, M.A. Coffee melanoidins: structures, mechanisms of formation and potential health impacts. *Food Funct.* **2012**, *3*, 903–915, doi:10.1039/c2fo30048f.

117. Panzella, L.; Cerruti, P.; Ambrogi, V.; Agustin-Salazar, S.; D'Errico, G.; Carfagna, C.; Goya, L.; Ramos, S.; Martín, M.A.; Napolitano, A.; et al. A superior all-natural antioxidant biomaterial from spent coffee grounds for polymer stabilization, cell protection, and food lipid preservation. *ACS Sustain. Chem. Eng.* **2016**, *4*, 1169–1179, doi:10.1021/acssuschemeng.5b01234.

118. Panusa, A.; Zuorro, A.; Lavecchia, R.; Marrosu, G.; Petrucci, R. Recovery of natural antioxidants from spent coffee grounds. *J. Agric. Food Chem.* **2013**, *61*, 4162–4168, doi:10.1021/jf4005719.

119. Monente, C.; Ludwig, I.A.; Irigoyen, A.; De Peña, M.P.; Cid, C. Assessment of total (Free and Bound) phenolic compounds in spent coffee extracts. *J. Agric. Food Chem.* **2015**, *63*, 4327–4334, doi:10.1021/acs.jafc.5b01619.

120. Okur, I.; Soyler, B.; Sezer, P.; Halil, M.; Alpas, H. Improving the recovery of phenolic compounds from spent coffee grounds (SCG) by environmentally friendly extraction techniques. *Molecules* **2021**, *26*, 613, doi:10.3390/ molecules26030613.

121. Rochín-Medina, J.J.; Ramírez, K.; Rangel-Peraza, J.G.; Bustos-Terrones, Y.A. Increase of content and bioactivity of total phenolic compounds from spent coffee grounds through solid state fermentation by Bacillus clausii. *J. Food Sci. Technol.* **2018**, *55*, 915–923, doi:10.1007/s13197-017-2998-5.

122. Mussatto, S.I.; Ballesteros, L.F.; Martins, S.; Teixeira, J.A. Extraction of antioxidant phenolic compounds from spent coffee grounds. *Sep. Purif. Technol.* **2011**, *83*, 173–179, doi:10.1016/j.seppur.2011.09.036.

123. Pujol, D.; Liu, C.; Gominho, J.; Olivella, M.À.; Fiol, N.; Villaescusa, I.; Pereira, H. The chemical composition of exhausted coffee waste. *Ind. Crops Prod.* **2013**, *50*, 423–429, doi:10.1016/j.indcrop.2013.07.056.

124. de Melo Pereira, G. V.; de Carvalho Neto, D.P.; Magalhães Júnior, A.I.; do Prado, F.G.; Pagnoncelli, M.G.B.; Karp, S.G.; Soccol, C.R. *Chemical composition and health properties of coffee and coffee by-products*; 1st ed.; Elsevier Inc., 2020; Vol. 91; ISBN 9780128204702.

125. Bresciani, L.; Calani, L.; Bruni, R.; Brighenti, F.; Del Rio, D. Phenolic composition, caffeine content and antioxidant capacity of coffee silverskin. *Food Res. Int.* **2014**, *61*, 196–201, doi:10.1016/j.foodres.2013.10.047.

126. Salazar-López, N.J.; López-Rodríguez, C.V.; Hernández-Montoya, D.A.; Campos-Vega, R. Health benefits of spent coffee grounds Coffea Arabica L. In *Food Waste and by-products*; 2020; pp. 327–351.

127. García-Gutiérrez, N.; Maldonado-Celis, M.E.; Rojas-López, M.; Loarca-Piña, G.F.; Campos-Vega, R. The fermented non-digestible fraction of spent coffee grounds induces apoptosis in human colon cancer cells (SW480). *J. Funct. Foods* **2017**, *30*, 237–246, doi:10.1016/j.jff.2017.01.014.

128. López-Barrera, D.M.; Vázquez-Sánchez, K.; Loarca-Piña, M.G.F.; Campos-Vega, R. Spent coffee grounds, an innovative source of colonic fermentable compounds, inhibit inflammatory mediators in vitro. *Food Chem.* **2016**, *212*,

282–290, doi:10.1016/j.foodchem.2016.05.175.

129. Fernandez-Gomez, B.; Lezama, A.; Amigo-Benavent, M.; Ullate, M.; Herrero, M.; Martín, M.Á.; Mesa, M.D.; del Castillo, M.D. Insights on the health benefits of the bioactive compounds of coffee silverskin extract. *J. Funct. Foods* **2016**, *25*, 197–207, doi:10.1016/j.jff.2016.06.001.

130. Iriondo-Dehond, A.; Rios, M.B.; Herrera, T.; Rodriguez-Bertos, A.; Nuñez, F.; Andres, M.I.S.; Sanchez-Fortun, S.; Del Castillo, M.D. Coffee silverskin extract: nutritional value, safety and effect on key biological functions. *Nutrients* **2019**, *11*, 2693, doi:10.3390/nu11112693.

131. Rodrigues, F.; Palmeira-de-Oliveira, A.; Das Neves, J.; Sarmento, B.; Amaral, M.H.; Oliveira, M.B.P.P. Coffee silverskin: a possible valuable cosmetic ingredient. *Pharm. Biol.* **2015**, *53*, 386–394, doi:10.3109/13880209.2014.922589.

132. Robles, E.; Izaguirre, N.; Martin, A.; Moschou, D.; Labidi, J. Assessment of bleached and unbleached nanofibers from pistachio shells for nanopaper making. *Molecules* **2021**, *26*, 1371, doi:10.3390/molecules26051371.

133. Erşan, S.; Üstündağ, O.G.; Carle, R.; Schweiggert, R.M. Identification of phenolic compounds in red and green pistachio (Pistacia vera L.) hulls (Exo- and Mesocarp) by HPLC-DAD-ESI-(HR)- MS. *J. Agric. Food Chem.* **2016**, *64*, 5334−5344, doi:10.1021/acs.jafc.6b01745.

134. Sonmezdag, A.S.; Kelebek, H.; Selli, S. Characterization and comparative evaluation of volatile, phenolic and antioxidant properties of pistachio (Pistacia vera L.) hull. *J. Essent. oil Res.* **2016**, *29*, 262–270, doi:10.1080/10412905.2016.1216899.

135. Qiu, J.; Chen, L.; Zhu, Q.; Wang, D.; Wang, W.; Sun, X.; Liu, X.; Du, F. Screening natural antioxidants in peanut shell using DPPH – HPLC – DAD – TOF/MS methods. *Food Chem.* **2012**, *135*, 2366–2371, doi:10.1016/j.foodchem.2012.07.042.

136. Bobet, O.; Nassio, S.; Seynou, M.; Remy, B.; Zerbo, L.; Sanou, I.; Sawadogo, M.; Millogo, Y.; Gilles, E.; Faso, B. Characterization of peanut shells for their valorization in earth brick. *J. Miner. Mater. Charact. Eng.* **2020**, *8*, 301–315, doi:10.4236/jmmce.2020.84018.

137. Silva, V.; Falco, V.; Dias, M.I.; Barros, L.; Silva, A.; Capita, R.; Alonso-Calleja, C.; Amaral, J.S.; Igrejas, G.; Ferreira, I.C.F.R.; et al. Evaluation of the phenolic profile of Castanea sativa Mill. by-products and their antioxidant and antimicrobial activity against multiresistant bacteria. *Antioxidants* **2020**, *9*, 87, doi:10.3390/antiox9010087.

138. Domingos, I.; Esteves, B. Chemical composition and study on liquefaction optimization of chestnut shells. *Open Agric.* **2020**, *5*, 905–911, doi:10.1515/opag-2020-0089.

139. Hu, M.; Yang, X.; Chang, X. Bioactive phenolic components and potential health effects of chestnut shell: a review. *J. Food Biochem.* **2021**, *45*, e13696, doi:10.1111/jfbc.13696.

140. Alvarez-Parrilla, E.; Urrea-Lopez, R.; de la Rosa, L.A. View of bioactive components and health effects of pecan nuts and their byproducts: a review. *J. Food Bioact.* **2018**, *1*, 56–92, doi:10.31665/JFB.2018.1127.

141. Villasante, J.; Pérez-carrillo, E.; Heredia-olea, E.; Metón, I.; Almajano, M.P. In vitro antioxidant activity optimization of nut shell (Carya illinoinensis) by extrusion using response surface methods. *Biomolecules* **2019**, *9*, 883, doi:10.3390/biom9120883.

142. Yuan, B.; Lu, M.; Eskridge, K.M.; Isom, L.D.; Hanna, M.A. Extraction, identification, and quantification of antioxidant phenolics from hazelnut (Corylus avellana L.) shells. *Food Chem.* **2018**, *244*, 7–15, doi:10.1016/j.foodchem.2017.09.116.

143. Shahidi, F.; Varatharajan, V.; Oh, W.Y.; Peng, H. Phenolic compounds in agri-food by-products, their bioavailability and health effects. *J. Food Bioact.* **2019**, *5*, 57–119, doi:10.31665/jfb.2019.5178.

144. Szabo, K.; Dulf, F.V.; Diaconeasa, Z.; Vodnar, D.C. Antimicrobial and antioxidant properties of tomato processing byproducts and their correlation with the biochemical composition. *Lwt* **2019**, *116*, 108558, doi:10.1016/j.lwt.2019.108558.

145. Kiassos, E.; Mylonaki, S.; Makris, D.P.; Kefalas, P. Implementation of response surface methodology to optimise extraction of onion (Allium cepa) solid waste phenolics. *Innov. Food Sci. Emerg. Technol.* **2009**, *10*, 246–252, doi:10.1016/j.ifset.2008.10.004.

146. Wiltshire, E.J.; Eady, C.C.; Collings, D.A. Induction of anthocyanin in the inner epidermis of red onion leaves by environmental stimuli and transient expression of transcription factors. *Plant Cell Rep.* **2017**, *36*, 987–1000, doi:10.1007/s00299-017-2132-1.

147. Lovrić, V.; Putnik, P.; Bursać Kovačević, D.; Jukić, M.; Dragović-Uzelac, V. The Effect of Microwave-Assisted Extraction on the Phenolic Compounds and Antioxidant Capacity of Blackthorn Flowers. *Food Technol. Biotechnol.* **2017**, *55*, 243–250, doi:10.17113/ftb.55.02.17.4687.

148. Ran, X. li; Zhang, M.; Wang, Y.; Adhikari, B. *Novel technologies applied for*

recovery and value addition of high value compounds from plant byproducts: A review; 2019; Vol. 59; ISBN 5108580797.

149. Talmaciu, A.I.; Volf, I.; Popa, V.I. A Comparative Analysis of the "Green" Techniques Applied for Polyphenols Extraction from Bioresources. *Chem. Biodivers.* **2015**, *12*, 1635–1651, doi:10.1002/cbdv.201400415.

150. Garcia-Salas, P.; Morales-Soto, A.; Segura-Carretero, A.; Fernández-Gutiérrez, A. Phenolic-compound-extraction systems for fruit and vegetable samples. *Molecules* **2010**, *15*, 8813–8826, doi:10.3390/molecules15128813.

151. Do, J.L.; Friščić, T. Mechanochemistry: A Force of Synthesis. *ACS Cent. Sci.* **2017**, *3*, 13–19, doi:10.1021/acscentsci.6b00277.

152. Stalikas, C.D. Extraction, separation, and detection methods for phenolic acids and flavonoids. *J. Sep. Sci.* **2007**, *30*, 3268–3295, doi:10.1002/jssc.200700261.

153. Ikeda, M. Public health problems of organic solvents. *Toxicol. Lett.* **1992**, *64–65*, 191–201, doi:10.1016/0378-4274(92)90189-Q.

154. Paiva, A.; Craveiro, R.; Aroso, I.; Martins, M.; Reis, R.L.; Duarte, A.R.C. Natural deep eutectic solvents - Solvents for the 21st century. *ACS Sustain. Chem. Eng.* **2014**, *2*, 1063–1071, doi:10.1021/sc500096j.

155. Ruesgas-Ramón, M.; Figueroa-Espinoza, M.C.; Durand, E. Application of deep eutectic solvents (DES) for phenolic compounds extraction: overview, challenges, and opportunities. *J. Agric. Food Chem.* **2017**, *65*, 3591–3601, doi:10.1021/acs.jafc.7b01054.

156. Abbott, A.P.; Capper, G.; Davies, D.L.; Rasheed, R.K.; Tambyrajah, V. Novel solvent properties of choline chloride/urea mixtures. *Chem. Commun.* **2003**, *9*, 70–71, doi:10.1039/B210714G.

157. Radošević, K.; Bubalo, C.M.; Srček, V.G.; Grgas, D.; Dragičević, T.L.; Redovniković, R.I. Evaluation of toxicity and biodegradability of choline chloride based deep eutectic solvents. *Ecotoxicol. Environ. Saf.* **2015**, *112*, 46–53, doi:10.1016/j.ecoenv.2014.09.034.

158. Smith, E.L.; Abbott, A.P.; Ryder, K.S. Deep eutectic solvents (DESs) and their applications. *Chem. Rev.* **2014**, *114*, 11060–11082, doi:10.1021/cr300162p.

159. Zhang, Q.; De Oliveira Vigier, K.; Royer, S.; Jérôme, F. Deep eutectic solvents: syntheses, properties and applications. *Chem. Soc. Rev.* **2012**, *41*, 7108–46, doi:10.1039/c2cs35178a.

160. Francisco, M.; Van Den Bruinhorst, A.; Kroon, M.C. Low-transition-

temperature mixtures (LTTMs): a new generation of designer solvents. *Angew. Chemie - Int. Ed.* **2013**, *52*, 3074–3085, doi:10.1002/anie.201207548.

161. Choi, Y.H.; van Spronsen, J.; Dai, Y.; Verberne, M.; Hollmann, F.; Arends, I.W.C.E.; Witkamp, G.J.; Verpoorte, R. Are natural deep eutectic solvents the missing link in understanding cellular metabolism and physiology? *Plant Physiol.* **2011**, *156*, 1701–1705, doi:10.1104/pp.111.178426.

162. Dai, Y.; van Spronsen, J.; Witkamp, G.J.; Verpoorte, R.; Choi, Y.H. Natural deep eutectic solvents as new potential media for green technology. *Anal. Chim. Acta* **2013**, *766*, 61–68, doi:10.1016/j.aca.2012.12.019.

163. Abbott, A.P.; Barron, J.C.; Ryder, K.S.; Wilson, D. Eutectic-Based Ionic Liquids with Metal-Containing Anions and Cations. *Chem. - A Eur. J.* **2007**, *13*, 6495 – 6501, doi:10.1002/chem.200601738.

164. Tang, B.; Zhang, H.; Row, K.H. Application of deep eutectic solvents in the extraction and separation of target compounds from various samples. *J. Sep. Sci.* **2015**, *38*, 1053–1064, doi:10.1002/jssc.201401347.

165. Sołoducho, J.; Cabaj, J. Phenolic Compounds Hybrid Detectors. *J. Biomater. Nanobiotechnol.* **2013**, *04*, 17–27, doi:10.4236/jbnb.2013.43a003.

166. Saveleva, M.S.; Eftekhari, K.; Abalymov, A.; Douglas, T.E.L.; Volodkin, D.; Parakhonskiy, B. V.; Skirtach, A.G. Hierarchy of hybrid materials-the place of inorganics-in-organics in it, their composition and applications. *Front. Chem.* **2019**, *7*, 1–21, doi:10.3389/fchem.2019.00179.

167. Gomez-Romero, P. Hybrid Organic-Inorganic Materials—In Search of Synergic Activity. *Adv. Mater.* **2001**, *13*, 163–174, doi:10.1002/1521-4095(200102)13:3<163::AID-ADMA163>3.0.CO;2-U.

168. Jung, Y.; Kim, D. Recent advances in hybrid system of porous silicon nanoparticles and biocompatible polymers for biomedical applications. *Biomed. Eng. Lett.* **2021**, *11*, 171–181, doi:10.1007/s13534-021-00194-9.

169. Ferreira Soares, D.C.; Domingues, S.C.; Viana, D.B.; Tebaldi, M.L. Polymer-hybrid nanoparticles: Current advances in biomedical applications. *Biomed. Pharmacother.* **2020**, *131*, 110695, doi:10.1016/j.biopha.2020.110695.

170. Su, S.; Kang, P.M. Recent advances in nanocarrier-assisted therapeutics delivery systems. *Pharmaceutics* **2020**, *12*, 1–27, doi:10.3390/pharmaceutics12090837.

171. Khursheed, R.; Dua, K.; Vishwas, S.; Gulati, M.; Jha, N.K.; Aldhafeeri, G.M.; Alanazi, F.G.; Goh, B.H.; Gupta, G.; Paudel, K.R.; et al. Biomedical

applications of metallic nanoparticles in cancer: Current status and future perspectives. *Biomed. Pharmacother.* **2022**, *150*, 112951, doi:10.1016/j.biopha.2022.112951.

172. Drobota, M.; Ursache, S.; Aflori, M. Surface Functionalities of Polymers for Biomaterial Applications. *Polymers (Basel).* **2022**, *14*, doi:10.3390/polym14122307.

173. Macchione, M.A.; Biglione, C.; Strumia, M. Design, synthesis and architectures of hybrid nanomaterials for therapy and diagnosis applications. *Polymers (Basel).* **2018**, *10*, 1–34, doi:10.3390/polym10050527.

174. De Leo, V.; Milano, F.; Agostiano, A.; Catucci, L. Recent advancements in polymer/liposome assembly for drug delivery: From surface modifications to hybrid vesicles. *Polymers (Basel).* **2021**, *13*, doi:10.3390/polym13071027.

175. Sivadasan, D.; Sultan, M.H.; Madkhali, O.; Almoshari, Y.; Thangavel, N. Polymeric lipid hybrid nanoparticles (Plns) as emerging drug delivery platform—a comprehensive review of their properties, preparation methods, and therapeutic applications. *Pharmaceutics* **2021**, *13*, doi:10.3390/pharmaceutics13081291.

176. Mukherjee, A.; Waters, A.K.; Kalyan, P.; Achrol, A.S.; Kesari, S.; Yenugonda, V.M. Lipid-polymer hybrid nanoparticles as a nextgeneration drug delivery platform: State of the art, emerging technologies, and perspectives. *Int. J. Nanomedicine* **2019**, *14*, 1937–1952, doi:10.2147/IJN.S198353.

177. Bayda, S.; Adeel, M.; Tuccinardi, T.; Cordani, M.; Rizzolio, F. The history of nanoscience and nanotechnology: From chemical-physical applications to nanomedicine. *Molecules* **2020**, *25*, 1–15, doi:10.3390/molecules25010112.

178. Baig, N.; Kammakakam, I.; Falath, W.; Kammakakam, I. Nanomaterials: A review of synthesis methods, properties, recent progress, and challenges. *Mater. Adv.* **2021**, *2*, 1821–1871, doi:10.1039/d0ma00807a.

179. Nikolova, M.P.; Chavali, M.S. Metal oxide nanoparticles as biomedical materials. *Biomimetics* **2020**, *5*, doi:10.3390/BIOMIMETICS5020027.

180. Yaqoob, A.A.; Ahmad, H.; Parveen, T.; Ahmad, A.; Oves, M.; Ismail, I.M.I.; Qari, H.A.; Umar, K.; Mohamad Ibrahim, M.N. Recent Advances in Metal Decorated Nanomaterials and Their Various Biological Applications: A Review. *Front. Chem.* **2020**, *8*, 1–23, doi:10.3389/fchem.2020.00341.

181. Shejale, K.P.; Krishnapriya, R.; Patil, H.; Laishram, D.; Rawal, P.; Sharma, R.K. Recent advances in ultra-low temperature (sub-zero to 100 °c) synthesis, mechanism and applications of titania (TiO2) nanoparticles.

Mater. Adv. **2021**, *2*, 7502–7529, doi:10.1039/d1ma00942g.

182. Shi, H.; Magaye, R.; Castranova, V.; Zhao, J. Titanium dioxide nanoparticles: a review of current toxicological data. *Part. Fibre Toxicol.* **2013**, *10*, doi:10.1186/1743-8977-10-15.

183. Baig, N.; Kammakakam, I.; Falath, W.; Kammakakam, I. Nanomaterials: a review of synthesis methods, properties, recent progress, and challen. *Mater. Adv.* **2012**, *2*, 1821–1871, doi:10.1039/d0ma00807a.

184. Samuel, M.S.; Ravikumar, M.; John, A.; Selvarajan, E.; Patel, H.; Chander, P.S.; Soundarya, J.; Vuppala, S.; Balaji, R.; Chandrasekar, N. A Review on Green Synthesis of Nanoparticles and Their Diverse Biomedical and Environmental Applications. *Catalysts* **2022**, *12*, doi:10.3390/catal12050459.

185. Mohamed, A.; Shafey, E. Shafey2020.Pdf. **2020**, 304–339.

186. Gebre, S.H.; Sendeku, M.G. New frontiers in the biosynthesis of metal oxide nanoparticles and their environmental applications: an overview. *SN Appl. Sci.* **2019**, *1*, 1–28, doi:10.1007/s42452-019-0931-4.

187. Amini, S.M.; Akbari, A. Metal nanoparticles synthesis through natural phenolic acids. *IET Nanobiotechnology* **2019**, *13*, 771–777, doi:10.1049/iet-nbt.2018.5386.

188. Ying, S.; Guan, Z.; Ofoegbu, P.C.; Clubb, P.; Rico, C.; He, F.; Hong, J. Green synthesis of nanoparticles: Current developments and limitations. *Environ. Technol. Innov.* **2022**, *26*, 102336, doi:10.1016/j.eti.2022.102336.

189. Patra, J.K.; Baek, K.H. Comparative study of proteasome inhibitory, synergistic antibacterial, synergistic anticandidal, and antioxidant activities of gold nanoparticles biosynthesized using fruit waste materials. *Int. J. Nanomedicine* **2016**, *11*, 4691–4705, doi:10.2147/IJN.S108920.

190. Gubitosa, J.; Rizzi, V.; Lopedota, A.; Fini, P.; Laurenzana, A.; Fibbi, G.; Fanelli, F.; Petrella, A.; Laquintana, V.; Denora, N.; et al. One pot environmental friendly synthesis of gold nanoparticles using Punica Granatum Juice: A novel antioxidant agent for future dermatological and cosmetic applications. *J. Colloid Interface Sci.* **2018**, *521*, 50–61, doi:10.1016/j.jcis.2018.02.069.

191. Jiménez, Z.; Kim, Y.J.; Mathiyalagan, R.; Seo, K.H.; Mohanan, P.; Ahn, J.C.; Kim, Y.J.; Yang, D.C. Assessment of radical scavenging, whitening and moisture retention activities of Panax ginseng berry mediated gold nanoparticles as safe and efficient novel cosmetic material. *Artif. Cells, Nanomedicine Biotechnol.* **2018**, *46*, 333–340, doi:10.1080/21691401.2017.1307216.

192. Jiménez-Pérez, Z.E.; Singh, P.; Kim, Y.J.; Mathiyalagan, R.; Kim, D.H.; Lee, M.H.; Yang, D.C. Applications of Panax ginseng leaves-mediated gold nanoparticles in cosmetics relation to antioxidant, moisture retention, and whitening effect on B16BL6 cells. *J. Ginseng Res.* **2018**, *42*, 327–333, doi:10.1016/j.jgr.2017.04.003.

193. Jiménez Pérez, Z.E.; Mathiyalagan, R.; Markus, J.; Kim, Y.J.; Kang, H.M.; Abbai, R.; Seo, K.H.; Wang, D.; Soshnikova, V.; Yang, D.C. Ginseng-berry-mediated gold and silver nanoparticle synthesis and evaluation of their in vitro antioxidant, antimicrobial, and cytotoxicity effects on human dermal fibroblast and murine melanoma skin cell lines. *Int. J. Nanomedicine* **2017**, *12*, 709–723, doi:10.2147/IJN.S118373.

194. Dhayalan, M.; Denison, M.I.J.; Ayyar, M.; Gandhi, N.N.; Krishnan, K.; Abdulhadi, B. Biogenic synthesis, characterization of gold and silver nanoparticles from Coleus forskohlii and their clinical importance. *J. Photochem. Photobiol. B Biol.* **2018**, *183*, 251–257, doi:10.1016/j.jphotobiol.2018.04.042.

195. Kaya, B.; Darendelioğlu, E.; Dervişoğlu, G.; Tartik, M. Determination of comparative biological activities of silver nanoparticles formed by biological synthesis using Achillea Vermicularis. *Pakistan J. Bot.* **2018**, *50*, 1423–1432.

196. Saratale, R.G.; Saratale, G.D.; Ghodake, G.; Cho, S.K.; Kadam, A.; Kumar, G.; Jeon, B.H.; Pant, D.; Bhatnagar, A.; Shin, H.S. Wheat straw extracted lignin in silver nanoparticles synthesis: Expanding its prophecy towards antineoplastic potency and hydrogen peroxide sensing ability. *Int. J. Biol. Macromol.* **2019**, *128*, 391–400, doi:10.1016/j.ijbiomac.2019.01.120.

197. Panzella, L.; Cerruti, P.; Aprea, P.; Paolillo, R.; Pellegrino, G.; Moccia, F.; Condorelli, G.G.; Vollaro, A.; Ambrogi, V.; Catania, M.R.; et al. Silver nanoparticles on hydrolyzed spent coffee grounds (HSCG) for green antibacterial devices. *J. Clean. Prod.* **2020**, *268*, 122352, doi:10.1016/j.jclepro.2020.122352.

198. Novoselov, K.S.; Geim, A.K.; Morozov, S. V.; Jiang, D.; Zhang, Y.; Dubonos, S. V.; Grigorieva, I. V.; Firsov, A.A. Electric field in atomically thin carbon films. *Science (80-.).* **2004**, *306*, 666–669, doi:10.1126/science.1102896.

199. Armano, A.; Agnello, S. Two-Dimensional Carbon: A Review of Synthesis Methods, and Electronic, Optical, and Vibrational Properties of Single-Layer Graphene. *C — J. Carbon Res.* **2019**, *5*, 67, doi:10.3390/c5040067.

200. Yang, G.; Li, L.; Lee, W.B.; Ng, M.C. Structure of graphene and its disorders: a review. *Sci. Technol. Adv. Mater.* **2018**, *19*, 613–648,

doi:10.1080/14686996.2018.1494493.

201. Magne, T.M.; de Oliveira Vieira, T.; Alencar, L.M.R.; Junior, F.F.M.; Gemini-Piperni, S.; Carneiro, S. V.; Fechine, L.M.U.D.; Freire, R.M.; Golokhvast, K.; Metrangolo, P.; et al. *Graphene and its derivatives: understanding the main chemical and medicinal chemistry roles for biomedical applications*; Springer Berlin Heidelberg, 2022; Vol. 12; ISBN 0123456789.

202. Sontakke, A.D.; Purkait, M.K. A brief review on graphene oxide Nanoscrolls: Structure, Synthesis, characterization and scope of applications. *Chem. Eng. J.* **2021**, *420*, 129914, doi:10.1016/j.cej.2021.129914.

203. Trikkaliotis, D.G.; Christoforidis, A.K.; Mitropoulos, A.C.; Kyzas, G.Z. Graphene oxide synthesis, properties and characterization techniques: A comprehensive review. *ChemEngineering* **2021**, *5*, doi:10.3390/chemengineering5030064.

204. Ikram, R.; Jan, B.M.; Ahmad, W. An overview of industrial scalable production of graphene oxide and analytical approaches for synthesis and characterization. *J. Mater. Res. Technol.* **2020**, *9*, 11587–11610, doi:10.1016/j.jmrt.2020.08.050.

205. Han, X.M.; Zheng, K.W.; Wang, R.L.; Yue, S.F.; Chen, J.; Zhao, Z.W.; Song, F.; Su, Y.; Ma, Q. Functionalization and optimization-strategy of graphene oxide-based nanomaterials for gene and drug delivery. *Am. J. Transl. Res.* **2020**, *12*, 1515–1534.

206. Kang, S.M.; Park, S.; Kim, D.; Park, S.Y.; Ruoff, R.S.; Lee, H. Simultaneous reduction and surface functionalization of graphene oxide by mussel-inspired chemistry. *Adv. Funct. Mater.* **2011**, *21*, 108–112, doi:10.1002/adfm.201001692.

207. Graphene, D.C. Strong Integrated Strength and Toughness Artificial Nacre Based on. *ACS Nano* **2014**, 9511–9517.

208. Han, K.; Bai, Q.; Wu, W.; Sun, N.; Cui, N.; Lu, T. Gelatin-based adhesive hydrogel with self-healing, hemostasis, and electrical conductivity. *Int. J. Biol. Macromol.* **2021**, *183*, 2142–2151, doi:10.1016/j.ijbiomac.2021.05.147.

209. Cao, W.; Zhou, X.; McCallum, N.C.; Hu, Z.; Ni, Q.Z.; Kapoor, U.; Heil, C.M.; Cay, K.S.; Zand, T.; Mantanona, A.J.; et al. Unraveling the structure and function of melanin through synthesis. *J. Am. Chem. Soc.* **2021**, *143*, 2622–2637, doi:10.1021/jacs.0c12322.

210. Raper, H.S. The Tyrosinase-tyrosine Reaction. *Biochem. J.* **1927**, *21*, 89–96, doi:10.1042/bj0210089.

211. Panzella, L.; Gentile, G.; D'Errico, G.; Della Vecchia, N.F.; Errico, M.E.; Napolitano, A.; Carfagna, C.; D'Ischia, M. Atypical structural and π-electron features of a melanin polymer that lead to superior free-radical-scavenging properties. *Angew. Chemie* **2013**, *125*, 12916–12919, doi:10.1002/ange.201305747.

212. Panzella, L.; Ebato, A.; Napolitano, A.; Koike, K. The late stages of melanogenesis: Exploring the chemical facets and the application opportunities. *Int. J. Mol. Sci.* **2018**, *19*, doi:10.3390/ijms19061753.

213. Micillo, R.; Iacomino, M.; Perfetti, M.; Panzella, L.; Koike, K.; D'Errico, G.; d'Ischia, M.; Napolitano, A. Unexpected impact of esterification on the antioxidant activity and (photo)stability of a eumelanin from 5,6-dihydroxyindole-2-carboxylic acid. *Pigment Cell Melanoma Res.* **2018**, *31*, 475–483, doi:10.1111/pcmr.12689.

214. Liberti, D.; Alfieri, M.L.; Monti, D.M.; Panzella, L.; Napolitano, A. A melanin-related phenolic polymer with potent photoprotective and antioxidant activities for dermo-cosmetic applications. *Antioxidants* **2020**, *9*, 270, doi:10.3390/antiox9040270.

215. Kim, E.; Panzella, L.; Napolitano, A.; Payne, G.F. Redox Activities of Melanins Investigated by Electrochemical Reverse Engineering: Implications for their Roles in Oxidative Stress. *J. Invest. Dermatol.* **2020**, *140*, 537–543, doi:10.1016/j.jid.2019.09.010.

216. Kang, M.; Kim, E.; Temoçin, Z.; Li, J.; Dadachova, E.; Wang, Z.; Panzella, L.; Napolitano, A.; Bentley, W.E.; Payne, G.F. Reverse Engineering to Characterize Redox Properties: Revealing Melanin's Redox Activity through Mediated Electrochemical Probing. *Chem. Mater.* **2018**, *30*, 5814–5826, doi:10.1021/acs.chemmater.8b02428.

217. Kim, E.; Kang, M.; Tschirhart, T.; Malo, M.; Dadachova, E.; Cao, G.; Yin, J.J.; Bentley, W.E.; Wang, Z.; Payne, G.F. Spectroelectrochemical Reverse Engineering DemonstratesThat Melanin's Redox and Radical Scavenging Activities Are Linked. *Biomacromolecules* **2017**, *18*, 4084–4098, doi:10.1021/acs.biomac.7b01166.

218. d'Ischia, M.; Napolitano, A.; Prota, G. Peroxidase as an alternative to tyrosinase in the oxidative polymerization of 5,6-dihydroxyindoles to melanin(s). *BBA - Gen. Subj.* **1991**, *1073*, 423–430, doi:10.1016/0304-4165(91)90152-7.

219. Xu, R.; Prontera, C.T.; Di Mauro, E.; Pezzella, A.; Soavi, F.; Santato, C. An electrochemical study of natural and chemically controlled eumelanin. *APL Mater.* **2017**, *5*, doi:10.1063/1.5000161.

220. Tu, L.H.; Tseng, N.H.; Tsai, Y.R.; Lin, T.W.; Lo, Y.W.; Charng, J.L.; Hsu, H.T.; Chen, Y.S.; Chen, R.J.; Wu, Y.T.; et al. Rationally designed divalent caffeic amides inhibit amyloid-β fibrillization, induce fibril dissociation, and ameliorate cytotoxicity. *Eur. J. Med. Chem.* **2018**, *158*, 393–404, doi:10.1016/j.ejmech.2018.08.084.

221. Albericio, F. Developments in peptide and amide synthesis. *Curr. Opin. Chem. Biol.* **2004**, *8*, 211–221, doi:10.1016/j.cbpa.2004.03.002.

222. Pezzella, A.; Napolitano, A.; D'Ischia, M.; Prota, G. Oxidative polymerisation of 5,6-dihydroxyindole-2-carboxylic acid to melanin: A new insight. *Tetrahedron* **1996**, *52*, 7913–7920, doi:10.1016/0040-4020(96)00362-6.

223. Panzella, L.; Benning, K.; Nesbeth, D.N.; Setaro, B.; D'Errico, G.; Napolitano, A.; d'Ischia, M. Identification of black sturgeon caviar pigment as eumelanin. *Food Chem.* **2022**, *373*, 131474, doi:10.1016/j.foodchem.2021.131474.

224. Muñoz-García, A.B.; Sannino, F.; Vitiello, G.; Pirozzi, D.; Minieri, L.; Aronne, A.; Pernice, P.; Pavone, M.; D'Errico, G. Origin and electronic features of reactive oxygen species at hybrid zirconia-acetylacetonate interfaces. *ACS Appl. Mater. Interfaces* **2015**, *7*, 21662–21667, doi:10.1021/acsami.5b06988.

225. Mostert, A.B.; Hanson, G.R.; Sarna, T.; Gentle, I.R.; Powell, B.J.; Meredith, P. Hydration-controlled X-band EPR spectroscopy: a tool for unravelling the complexities of the solid-state free radical in eumelanin. *J. Phys. Chem. B* **2013**, *117*, 4965–4972, doi:10.1021/jp401615e.

226. Edge, R.; D'Ischia, M.; Land, E.J.; Napolitano, A.; Navaratnam, S.; Panzella, L.; Pezzella, A.; Ramsden, C.A.; Riley, P.A. Dopaquinone redox exchange with dihydroxyindole and dihydroxyindole carboxylic acid. *Pigment Cell Res.* **2006**, *19*, 443–450, doi:10.1111/j.1600-0749.2006.00327.x.

227. Goupy, P.; Dufour, C.; Loonis, M.; Dangles, O. Quantitative kinetic analysis of hydrogen transfer reactions from dietary polyphenols to the DPPH radical. *J. Agric. Food Chem.* **2003**, *51*, 615–622, doi:10.1021/jf025938l.

228. Benzie, I.F.F.; Strain, J.J. The Ferric Reducing Ability of Plasma (FRAP) as a Measure of "'Antioxidant Power"': The FRAP Assay. *Anal. Biochem.* **1996**, *239*, 70–76, doi:10.1039/c6ay01739h.

229. Re, R.; Pellegrini, N.; Proteggente, A.; Pannala, A.; Yang, M.; Rice-Evans, C. Antioxidant activity applying an improved ABTS radical cation decolorization assay. *Free Radic. Biol. Med.* **1999**, *26*, 1231–1237, doi:10.1016/S0891-5849(98)00315-3.

230. d'Ischia, M.; Wakamatsu, K.; Cicoira, F.; Di Mauro, E.; Garcia-Borron, J.C.; Commo, S.; Galván, I.; Ghanem, G.; Kenzo, K.; Meredith, P.; et al. Melanins and melanogenesis: From pigment cells to human health and technological applications. *Pigment Cell Melanoma Res.* **2015**, *28*, 520–544, doi:10.1111/pcmr.12393.

231. Slominski, A.; Tobin, D.J.; Shibahara, S.; Wortsman, J. Melanin pigmentation in mammalian skin and its hormonal regulation. *Physiol. Rev.* **2004**, *84*, 1155–1228, doi:10.1152/physrev.00044.2003.

232. VIRADOR1, V.; MATSUNAGA, N.; MATSUNAGA, J.; VALENCIA, J.; OLDHAM, R.J.; KAMEYAMA, K.; GARY L., P.; FERRANS, V.J.; VIEIRA, W.D.; ABDEL-MALEK6, Z.A.; et al. Production of Melanocyte-Specific Antibodies to Human Melanosomal Proteins: Expression Patterns in Normal Human Skin and in Cutaneous Pigmented Lesions. *Pigment CELL RES* **2001**, *14*, 289–296.

233. A, G.-K.; J, P.; H, M. Melanogenesis Inhibitors: Strategies for Searching for and Evaluation of Active Compounds. *Curr. Med. Chem.* **2016**, *23*, 3548–3574, doi:10.2174/0929867323666160.

234. Ebanks, J.P.; Wickett, R.R.; Boissy, R.E. Mechanisms regulating skin pigmentation: The rise and fall of complexion coloration. *Int. J. Mol. Sci.* **2009**, *10*, 4066–4087, doi:10.3390/ijms10094066.

235. Hearing, V.J.; Tsukamoto, K. Enzymatic control of pigmentation in mammals. *FASEB J.* **1991**, *5*, 2902–2909, doi:10.1096/fasebj.5.14.1752358.

236. Land, E.J.; Ramsden, C.A.; Riley, P.A. Tyrosinase autoactivation and the chemistry of ortho-quinone amines. *Acc. Chem. Res.* **2003**, *36*, 300–308, doi:10.1021/ar020062p.

237. Riley, P.A. Tyrosinase kinetics: A semi-quantitative model of the mechanism of oxidation of monohydric and dihydric phenolic substrates. *J. Theor. Biol.* **2000**, *203*, 1–12, doi:10.1006/jtbi.1999.1061.

238. Micillo, R.; Pistorio, V.; Pizzo, E.; Panzella, L.; Napolitano, A.; D'Ischia, M. 2-S-Lipoylcaffeic Acid, a natural product-based entry to tyrosinase inhibition via catechol manipulation. *Biomimetics* **2017**, *2*, 15, doi:10.3390/biomimetics2030015.

239. Pezzella, A.; Lista, L.; Napolitano, A.; D'Ischia, M. An expedient one-pot entry to catecholestrogens and other catechol compounds via IBX-mediated phenolic oxygenation. *Tetrahedron Lett.* **2005**, *46*, 3541–3544, doi:10.1016/j.tetlet.2005.03.060.

240. Magdziak, D.; Rodriguez, A.A.; Van De Water, R.W.; Pettus, T.R.R.

Regioselective Oxidation of Phenols to o-Quinones with o- Iodoxybenzoic Acid (IBX). *Org. Lett.* **2002**, *4*, 285–288., doi:10.1021/ol017068j.

241. Gunsalus, I.C.; Barton, L.S.; Gruber, W. Biosynthesis and Structure of Lipoic Acid Derivatives. *J. Am. Chem. Soc.* **1956**, *78*, 1763–1766, doi:10.1021/ja01589a079.

242. Panzella, L.; De Lucia, M.; Napolitano, A.; d'Ischia, M. The first expedient entry to the human melanogen 2-S-cysteinyldopa exploiting the anomalous regioselectivity of 3,4-dihydroxycinnamic acid-thiol conjugation. *Tetrahedron Lett.* **2007**, *48*, 7650–7652, doi:10.1016/j.tetlet.2007.08.098.

243. Panzella, L.; Napolitano, A.; D'Ischia, M. Oxidative conjugation of chlorogenic acid with glutathione: Structural characterization of addition products and a new nitrite-promoted pathway. *Bioorganic Med. Chem.* **2003**, *11*, 4797–4805, doi:10.1016/S0968-0896(03)00460-7.

244. Zhu, J.; Zhou, H.; Gerhard, E.M.; Zhang, S.; Parra Rodríguez, F.I.; Pan, T.; Yang, H.; Lin, Y.; Yang, J.; Cheng, H. Smart bioadhesives for wound healing and closure. *Bioact. Mater.* **2023**, *19*, 360–375, doi:10.1016/j.bioactmat.2022.04.020.

245. Guo, Q.; Chen, J.; Wang, J.; Zeng, H.; Yu, J. Recent progress in synthesis and application of mussel-inspired adhesives. *Nanoscale* 2020, *12*, 1307–1324.

246. Saiz-Poseu, J.; Mancebo-Aracil, J.; Nador, F.; Busquè, F.; Ruiz-Molina, D. The Chemistry behind Catechol-Based Adhesion. *Angew. Chemie - Int. Ed.* **2019**, *58*, 696–714, doi:10.1002/anie.201801063.

247. Yu, W.; Cui, Y.; Han, M.; Jia, P.; Zhao, Y.; Zhang, M.; Sun, Y.; Nian, R. Mussel-inspired chemistry in producing mechanically robust and bioactive hydrogels as skin dressings. *Mater. Today Chem.* **2023**, *27*, doi:10.1016/j.mtchem.2022.101272.

248. Deng, X.; Huang, B.; Wang, Q.; Wu, W.; Coates, P.; Sefat, F.; Lu, C.; Zhang, W.; Zhang, X. A Mussel-Inspired Antibacterial Hydrogel with High Cell Affinity, Toughness, Self-Healing, and Recycling Properties for Wound Healing. *ACS Sustain. Chem. Eng.* **2021**, *9*, 3070–3082, doi:10.1021/acssuschemeng.0c06672.

249. Kim, M.H.; Lee, J.; Lee, J.N.; Lee, H.; Park, W.H. Mussel-inspired poly(γ-gl utamic acid)/nanosilicate composite hydrogels with enhanced mechanical properties, tissue adhesive properties, and skin tissue regeneration. *Acta Biomater.* **2021**, *123*, 254–262, doi:10.1016/j.actbio.2021.01.014.

250. Guo, J.; Sun, W.; Kim, J.P.; Lu, X.; Li, Q.; Lin, M.; Mrowczynski, O.; Rizk,

E.B.; Cheng, J.; Qian, G.; et al. Development of tannin-inspired antimicrobial bioadhesives. *Acta Biomater.* **2018**, *72*, 35–44, doi:10.1016/j.actbio.2018.03.008.

251. Gan, D.; Xing, W.; Jiang, L.; Fang, J.; Zhao, C.; Ren, F.; Fang, L.; Wang, K.; Lu, X. Plant-inspired adhesive and tough hydrogel based on Ag-Lignin nanoparticles-triggered dynamic redox catechol chemistry. *Nat. Commun.* **2019**, *10*, doi:10.1038/s41467-019-09351-2.

252. Cholewinski, A.; Yang, F.; Zhao, B. Algae-mussel-inspired hydrogel composite glue for underwater bonding. *Mater. Horizons* **2019**, *6*, 285–293, doi:10.1039/c8mh01421c.

253. Mortier, C.; Costa, D.C.S.; Oliveira, M.B.; Haugen, H.J.; Lyngstadaas, S.P.; Blaker, J.J.; Mano, J.F. Advanced hydrogels based on natural macromolecules: chemical routes to achieve mechanical versatility. *Mater. Today Chem.* **2022**, *26*, 101222, doi:10.1016/j.mtchem.2022.101222.

254. Friedman, M.; Brandon, D.L. Nutritional and health benefits of soy proteins. *J. Agric. Food Chem.* 2001, *49*, 1069–1086.

255. Lamaming, S.Z.; Lamaming, J.; Rawi, N.F.M.; Hashim, R.; Kassim, M.H.M.; Hussin, M.H.; Bustami, Y.; Sulaiman, O.; Amini, M.H.M.; Hiziroglu, S. Improvements and limitation of soy protein-based adhesive: A review. *Polym. Eng. Sci.* **2021**, *61*, 2393–2405, doi:10.1002/pen.25782.

256. Friedman, M.; Brandon, D.L. Nutritional and health benefits of soy proteins. *J. Agric. Food Chem.* **2001**, *49*, 1069–1086, doi:10.1021/jf0009246.

257. Liu, J.; Li, Z.; Lin, Q.; Jiang, X.; Yao, J.; Yang, Y.; Shao, Z.; Chen, X. A Robust, Resilient, and Multi-Functional Soy Protein-Based Hydrogel. *ACS Sustain. Chem. Eng.* **2018**, *6*, 13730–13738, doi:10.1021/acssuschemeng.8b01450.

258. Luo, Y.; Wang, Y.; Xia, C.; Ahmad, A.; Yang, R.; Li, X.; Shi, S.Q.; Li, J.; Guo, M.; Nadda, A.K.; et al. Eco-friendly soy protein isolate-based films strengthened by water-soluble glycerin epoxy resin. *Prog. Org. Coatings* **2022**, *162*, doi:10.1016/j.porgcoat.2021.106566.

259. Pang, H.; Ma, C.; Zhang, S. Conversion of soybean oil extraction wastes into high-performance wood adhesives based on mussel-inspired cation-π interactions. *Int. J. Biol. Macromol.* **2022**, *209*, 83–92, doi:10.1016/j.ijbiomac.2022.03.152.

260. Wang, Z.; Kang, H.; Liu, H.; Zhang, S.; Xia, C.; Wang, Z.; Li, J. Dual-Network Nanocross-linking Strategy to Improve Bulk Mechanical and Water-Resistant Adhesion Properties of Biobased Wood Adhesives. *ACS*

Sustain. Chem. Eng. **2020**, *8*, 16430–16440, doi:10.1021/acssuschemeng.0c04913.

261. Kang, H.; Wang, Z.; Zhang, W.; Li, J.; Zhang, S. Physico-chemical properties improvement of soy protein isolate films through caffeic acid incorporation and tri-functional aziridine hybridization. *Food Hydrocoll.* **2016**, *61*, 923–932, doi:10.1016/j.foodhyd.2016.07.009.

262. Li, Y.; Huang, X.; Xu, Y.; Ma, C.; Cai, L.; Zhang, J.; Luo, J.; Li, J.; Li, J.; Shi, S.Q.; et al. A bio-inspired multifunctional soy protein-based material: From strong underwater adhesion to 3D printing. *Chem. Eng. J.* **2022**, *430*, 133017, doi:10.1016/j.cej.2021.133017.

263. Wang, Z.; Kang, H.; Zhang, W.; Zhang, S.; Li, J. Improvement of Interfacial Adhesion by Bio-Inspired Catechol-Functionalized soy protein with Versatile Reactivity: Preparation of fully utilizable Soy-Based Film. *Polymers (Basel).* **2017**, *9*, doi:10.3390/polym9030095.

264. Wang, L.; Liu, J.; Zhang, W.; Zhang, D.; Li, J.; Zhang, S. Biomimetic soy protein-based exterior-use films with excellent UV-blocking performance from catechol derivative Acacia mangium tannin. *J. Appl. Polym. Sci.* **2021**, *138*, doi:10.1002/app.50185.

265. Podlena, M.; Böhm, M.; Saloni, D.; Velarde, G.; Salas, C. Tuning the adhesive properties of soy protein wood adhesives with different coadjutant polymers, nanocellulose and lignin. *Polymers (Basel).* **2021**, *13*, 1–16, doi:10.3390/polym13121972.

266. Huang, W.; Sun, X. Adhesive properties of soy proteins modified by urea and guanidine hydrochloride. *JAOCS, J. Am. Oil Chem. Soc.* **2000**, *77*, 101–104, doi:10.1007/s11746-000-0016-6.

267. Iacomino, M.; Weber, F.; Gleichenhagen, M.; Pistorio, V.; Panzella, L.; Pizzo, E.; Schieber, A.; D'Ischia, M.; Napolitano, A. Stable Benzacridine Pigments by Oxidative Coupling of Chlorogenic Acid with Amino Acids and Proteins: Toward Natural Product-Based Green Food Coloring. *J. Agric. Food Chem.* **2017**, *65*, 6519–6528, doi:10.1021/acs.jafc.7b00999.

268. Ghahri, S.; Chen, X.; Pizzi, A.; Hajihassani, R.; Papadopoulos, A.N. Natural tannins as new cross-linking materials for soy-based adhesives. *Polymers (Basel).* **2021**, *13*, 1–15, doi:10.3390/polym13040595.

269. Kocheva, L.S.; Karmanov, A.P.; Mironov, M.V.; Belyy, V.A.; Polina, I.N.; Pokryshkin, S.A. Characteristics of chemical structure of lignin biopolymer from Araucaria relict plant. Questions and answers of evolution. *Int. J. Biol. Macromol.* **2020**, *159*, 896–903, doi:10.1016/j.ijbiomac.2020.05.150.

270. Panzella, L.; D'Errico, G.; Vitiello, G.; Perfetti, M.; Alfieri, M.L.; Napolitano, A.; D'Ischia, M. Disentangling structure-dependent antioxidant mechanisms in phenolic polymers by multiparametric EPR analysis. *Chem. Commun.* **2018**, *54*, 9426–9429, doi:10.1039/c8cc05989f.

271. Boatright, W.L.; Jahan, M.S.; Walters, B.M.; Miller, A.F.; Cui, D.; Hustedt, E.J.; Lei, Q. Carbon-centered radicals in isolated soy proteins. *J. Food Sci.* **2008**, *73*, doi:10.1111/j.1750-3841.2008.00693.x.

272. Boatright, W.L.; Qingxin, L.; Jahan, M.S. Effect of storage conditions on carbon-centered radicals in soy protein products. *J. Agric. Food Chem.* **2009**, *57*, 7969–7973, doi:10.1021/jf900087v.

273. Iacomino, M.; Weber, F.; Gleichenhagen, M.; Pistorio, V.; Panzella, L.; Pizzo, E.; Schieber, A.; D'Ischia, M.; Napolitano, A. Stable Benzacridine Pigments by Oxidative Coupling of Chlorogenic Acid with Amino Acids and Proteins: Toward Natural Product-Based Green Food Coloring. *J. Agric. Food Chem.* **2017**, *65*, 6519–6528, doi:10.1021/acs.jafc.7b00999.

274. Iacomino, M.; Paez, J.I.; Avolio, R.; Carpentieri, A.; Panzella, L.; Falco, G.; Pizzo, E.; Errico, M.E.; Napolitano, A.; Del Campo, A.; et al. Multifunctional Thin Films and Coatings from Caffeic Acid and a Cross-Linking Diamine. *Langmuir* **2017**, *33*, 2096–2102, doi:10.1021/acs.langmuir.6b04079.

275. Gökmen, V.; Serpen, A.; Fogliano, V. Direct measurement of the total antioxidant capacity of foods: the "QUENCHER" approach. *Trends Food Sci. Technol.* **2009**, *20*, 278–288, doi:10.1016/j.tifs.2009.03.010.

276. Zhou, S.D.; Huang, L.; Meng, L.; Lin, Y.F.; Xu, X.; Dong, M.S. Soy protein isolate -(-)-epigallocatechin gallate conjugate: Covalent binding sites identification and IgE binding ability evaluation. *Food Chem.* **2020**, *333*, doi:10.1016/j.foodchem.2020.127400.

277. Villiou, M.; Paez, J.I.; Del Campo, A. Photodegradable Hydrogels for Cell Encapsulation and Tissue Adhesion. *ACS Appl. Mater. Interfaces* **2020**, *12*, 37862–37872, doi:10.1021/acsami.0c08568.

278. Gaglione, R.; Dell'Olmo, E.; Bosso, A.; Chino, M.; Pane, K.; Ascione, F.; Itri, F.; Caserta, S.; Amoresano, A.; Lombardi, A.; et al. Novel human bioactive peptides identified in Apolipoprotein B: Evaluation of their therapeutic potential. *Biochem. Pharmacol.* **2017**, *130*, 34–50, doi:10.1016/j.bcp.2017.01.009.

279. Moccia, F.; Agustin-Salazar, S.; Verotta, L.; Caneva, E.; Giovando, S.; D'Errico, G.; Panzella, L.; D'Ischia, M.; Napolitano, A. Antioxidant properties of agri-food byproducts and specific boosting effects of hydrolytic

treatments. *Antioxidants* **2020**, *9*, 438, doi:10.3390/antiox9050438.

280. Han, H.; Lee, K. Systematic approach to mimic phenolic natural polymers for biofabrication. *Polymers (Basel).* **2022**, *14*, 1282, doi:10.3390/polym14071282.

281. Liu, J.; Li, X.; Row, H.K. Development of deep eutectic solvents for sustainable chemistry. *J. Mol. Liq.* **2022**, *362*, 119654, doi:10.1016/j.molliq.2022.119654.

282. Ling, J.K.U.; Hadinoto, K. Deep eutectic solvent as green solvent in extraction of biological macromolecules: a review. *Int. J. Mol. Sci.* **2022**, *23*, 3381, doi:10.3390/ijms23063381.

283. Ijardar, S.P.; Singh, V.; Gardas, R.L. Revisiting the physicochemical properties and applications of deep eutectic solvents. *Molecules* **2022**, *27*, 1368, doi:10.3390/molecules27041368.

284. Chen, Z.; Ragauskas, A.; Wan, C. Lignin extraction and upgrading using deep eutectic solvents. *Ind. Crops Prod.* **2020**, *147*, 112241, doi:10.1016/j.indcrop.2020.112241.

285. Dheyab, A.S.; Abu Bakar, M.F.; AlOmar, M.; Sabran, S.F.; Hanafi, A.F.M.; Mohamad, A. Deep eutectic solvents (DESs) as green extraction media of beneficial bioactive phytochemicals. *Separation* **2021**, *8*, 176, doi:10.3390/separations8100176.

286. Moccia, F.; Gallucci, N.; Giovando, S.; Zuorro, A.; Lavecchia, R.; Errico, G.D.; Panzella, L.; Napolitano, A. A tunable deep eutectic solvent-based processing for valorization of chestnut wood fiber as a source of ellagic acid and lignin. *J. Environ. Chem. Eng.* **2022**, *10*, 107773, doi:10.1016/j.jece.2022.107773.

287. Yang, G.; An, X.; Yang, S. The effect of ball milling time on the isolation of lignin in the cell wall of different biomass. *Front. Bioeng. Biotechnol.* **2022**, *9*, 807625, doi:10.3389/fbioe.2021.807625.

288. Guo, X.; Junna, X.; Wolcott, M.P.; Zhang, J. Mechanochemical oleation of lignin through ball milling and properties of its blends with PLA. *Sustain. Chem.* **2016**, *1*, 3449–3454, doi:10.1002/slct.201600633.

289. Zinovyev, G.; Sumerskii, I.; Rosenau, T.; Balakshin, M.; Potthast, A. Ball milling's effect on pine milled wood lignin's structure and molar mass. *Molecules* **2018**, *23*, 2223, doi:10.3390/molecules23092223.

290. Dabral, S.; Wotruba, H.; Hernandez, J.G.; Bolm, C. Mechanochemical oxidation and cleavage of lignin β-O-4 model compounds and lignin. *ACS*

Sustain. Chem. Eng. **2018**, *6*, 3242−3254, doi:10.1021/acssuschemeng.7b03418.

291. Schiavi, D.; Ronchetti, R.; Di Lorenzo, V.; Salustri, M.; Petrucci, C.; Vivani, R.; Giovagnoli, S.; Camaioni, E.; Balestra, G.M. Circular hazelnut protection by lignocellulosic waste valorization for nanopesticides development. *Appl. Sci.* **2022**, *12*, 2604, doi:10.3390/app12052604.

292. Gordobil, O.; Olaizola, P.; Banales, J.M.; Labidi, J. Lignins from agroindustrial by-products as natural ingredients for cosmetics: chemical structure and in vitro sunscreen and cytotoxic activities. *Molecules* **2020**, *25*, 1131, doi:10.3390/molecules25051131.

293. Du, B.; Wang, X.; Chai, L.; Wang, X.; Pan, Z.; Chen, X.; Zhou, J.; Sun, R.-C. Fabricating lignin-based carbon nanofibers as versatile supercapacitors from food wastes. *Int. J. Biol. Macromol.* **2022**, *194*, 632–643, doi:10.1016/j.ijbiomac.2021.11.107.

294. Sogut, E.; Seydim, A.C. Utilization of chestnut shell lignin in alginate films. *J. Sci. Food Agric.* **2022**, doi:10.1002/jsfa.11785.

295. Panzella, L.; D'Errico, G.; Vitiello, G.; Perfetti, M.; Alfieri, M.L.; Napolitano, A.; D'Ischia, M. Disentangling structure-dependent antioxidant mechanisms in phenolic polymers by multiparametric EPR analysis. *Chem. Commun.* **2018**, *54*, 9426–9429, doi:10.1039/c8cc05989f.

296. Patil, S. V.; Argyropoulos, D.S. Stable organic radicals in lignin: a review. *ChemSusChem* **2017**, *10*, 3284–3303, doi:10.1002/cssc.201700869.

297. Bährle, C.; Nick, T.U.; Bennati, M.; Jeschke, G.; Vogel, F. High-field electron paramagnetic resonance and density functional theory study of stable organic radicals in lignin: influence of the extraction process, botanical origin, and protonation reactions on the radical g tensor. *J. Phys. Chem. A* **2015**, *119*, 6475–6482, doi:10.1021/acs.jpca.5b02200.

298. Piccinino, D.; Capecchi, E.; Tomaino, E.; Gabellone, S.; Gigli, V.; Avitabile, D.; Saladino, R. Nano-structured lignin as green antioxidant and uv shielding ingredient for sunscreen applications. *Antioxidants* **2021**, *10*, 274, doi:10.3390/antiox10020274.

299. Panzella, L.; Pérez-Burillo, S.; Pastoriza, S.; Martín, M.Á.; Cerruti, P.; Goya, L.; Ramos, S.; Rufián-Henares, J.Á.; Napolitano, A.; D'Ischia, M. High antioxidant action and prebiotic activity of hydrolyzed spent coffee grounds (HSCG) in a simulated digestion-fermentation model: toward the development of a novel food supplement. *J. Agric. Food Chem.* **2017**, *65*, 6452–6459, doi:10.1021/acs.jafc.7b02302.

300. Miki, K.; Kamitakahara, H.; Yoshinaga, A.; Tobimatsu, Y.; Takano, T. Methylation-triggered fractionation of lignocellulosic biomass to afford cellulose-, hemicellulose-, and lignin-based functional polymers: via click chemistry. *Green Chem.* **2020**, *22*, 2909–2928, doi:10.1039/d0gc00451k.

301. Goriparti, S.; Harish, M.N.K.; Sampath, S. Ellagic acid – a novel organic electrode material for high capacity lithium ion batteries. *Chem. Commun.* **2013**, *49*, 7234–7236, doi:10.1039/c3cc43194k.

302. González-Rivera, J.; Mero, A.; Husanu, E.; Mezzetta, A.; Ferrari, C.; D'andrea, F.; Bramanti, E.; Pomelli, C.S.; Guazzelli, L. Combining acid-based deep eutectic solvents and microwave irradiation for improved chestnut shell waste valorization †. **2021**, doi:10.1039/d1gc03450b.

303. Husanu, E.; Mero, A.; Rivera, J.G.; Mezzetta, A.; Ruiz, J.C.; D'andrea, F.; Pomelli, C.S.; Guazzelli, L. Exploiting deep eutectic solvents and ionic liquids for the valorization of chestnut shell waste. *ACS Sustain. Chem. Eng.* **2020**, *8*, 18386–18399, doi:10.1021/acssuschemeng.0c04945.

304. Panzella, L.; Napolitano, A. Condensed tannins, a viable solution to meet the need for sustainable and effective multifunctionality in food packaging: structure, sources, and properties. *J. Agric. Food Chem.* **2022**, *70*, 751–758.

305. Garcia-Villalba, R.; Espín, J.C.; Kroon, P.A.; Alasalvar, C.; Heinonen, M.; Voorspoels, S.; Tomas-Barberan, F. A validated method for the characterization and quantification of extractable and non-extractable ellagitannins after acid hydrolysis in pomegranate fruits, juices, and extracts. *J. Agric. Food Chem.* **2015**, *63*, 6555–6566, doi:10.1021/acs.jafc.5b02062.

306. Panzella, L.; Eidenberger, T.; Napolitano, A.; D'Ischia, M. Black sesame pigment: DPPH assay-guided purification, antioxidant/ antinitrosating properties, and identification of a degradative structural marker. *J. Agric. Food Chem.* **2012**, *60*, 8895–8901, doi:10.1021/jf2053096.

307. Moccia, F.; Agustin-Salazar, S.; Berg, A.; Setaro, B.; Micillo, R.; Pizzo, E.; Weber, F.; Gamez-Meza, N.; Schieber, A.; Cerruti, P.; et al. Pecan (Carya illinoinensis (Wagenh .) K . Koch) nut shell as an accessible polyphenol source for active packaging and food colorant stabilization. *ACS Sustain. Chem. Eng.* **2020**, *8*, 6700–6712, doi:10.1021/acssuschemeng.0c00356.

308. Seifzadeh, N.; Ali Sahari, M.; Barzegar, M.; Ahmadi Gavlighi, H.; Calani, L.; Del Rio, D.; Galaverna, G. Evaluation of polyphenolic compounds in membrane concentrated pistachio hull extract. *Food Chem.* **2019**, *277*, 398–406, doi:10.1016/j.foodchem.2018.10.001.

309. Herald, T.J.; Gadgil, P.; Perumal, R.; Bean, S.R.; Wilson, J.D. High-throughput micro-plate HCl-vanillin assay for screening tannin content in

sorghum grain. *J. Sci. Food Agric.* **2014**, *94*, 2133–2136, doi:10.1002/jsfa.6538.

310. Panzella, L.; Eidenberger, T.; Napolitano, A. Anti-Amyloid aggregation activity of black sesame pigment: toward a novel Alzheimer's disease preventive agent. *Molecules* **2018**, *23*, 676, doi:10.3390/molecules23030676.

311. Faustini, M.; Nicole, L.; Ruiz-Hitzky, E.; Sanchez, C. History of Organic–Inorganic Hybrid Materials: Prehistory, Art, Science, and Advanced Applications. *Adv. Funct. Mater.* **2018**, *28*, doi:10.1002/adfm.201704158.

312. Choudhary, M.K.; Kataria, J.; Sharma, S. Evaluation of the kinetic and catalytic properties of biogenically synthesized silver nanoparticles. *J. Clean. Prod.* **2018**, *198*, 882–890, doi:10.1016/j.jclepro.2018.09.015.

313. Rawal, S.; Patel, M.M. Threatening cancer with nanoparticle aided combination oncotherapy. *J. Control. Release* **2019**, *301*, 76–109, doi:10.1016/j.jconrel.2019.03.015.

314. Guerrini, A.; Burlini, I.; Lorenzo, B.H.; Grandini, A.; Vertuani, S.; Tacchini, M.; Sacchetti, G. Antioxidant and antimicrobial extracts obtained from agricultural by-products: Strategies for a sustainable recovery and future perspectives. *Food Bioprod. Process.* **2020**, *24*, 397–407 Contents, doi:10.1016/j.fbp.2020.10.003.

315. Ferrari, A.C.; Bonaccorso, F.; Fal'ko, V.; Novoselov, K.S.; Roche, S.; Bøggild, P.; Borini, S.; Koppens, F.H.L.; Palermo, V.; Pugno, N.; et al. Science and technology roadmap for graphene, related two-dimensional crystals, and hybrid systems. *Nanoscale* **2015**, *7*, 4598–4810, doi:10.1039/c4nr01600a.

316. Bonadies, I.; Di Cristo, F.; Valentino, A.; Peluso, G.; Calarco, A.; Salle, A. Di Ph-responsive resveratrol-loaded electrospun membranes for the prevention of implant-associated infections. *Nanomaterials* **2020**, *10*, 1–18, doi:10.3390/nano10061175.

317. Salle, A. Di; Viscusi, G.; Cristo, F. Di; Valentino, A.; Gorrasi, G.; Lamberti, E.; Vittoria, V.; Calarco, A.; Peluso, G. Antimicrobial and Antibiofilm Activity of Curcumin-Loaded. *Assoc. Infect. Mol.* **2021**, *26*, 4866.

List of abbreviations

ABTS 2,2-azino-bis-(3-ethyl- benzthiazoline-6-sulfonic acid)

AFM Atomic Force Microscopy

AAPH 2,2'-azobis(2- midinopropane) dihydrochloride

AgNPs AgNanoParticles

AR Amplification Ratio

ATR-FTIR Attenuated Total Reflectance Fourier Transform Infrared

CA Caffeic Acid

CAME Caffeic Acid Methyl Ester

CGA Chlorogenic Acid

CLN Chestnut Lignin

CS Coffee Silverskin

CTRL Control

CV Cyclic Voltammetry

DA Dopamine

DAICA 5,6-diacetoxyindole-2-carboxylic acid

DES Deep Eutectic Solvent

DFT Density-Functional Theory

DHI 5,6-dihydroxyindole

DHICA 5,6-dihydroxyindole-2-carboxylic acid

DHLA Dihydrolipoic Acid

DIPEA N,N-diisopropylethylamine

DLS Dynamic Light Scattering

DMF N,N- dimethylformamide

DMSO dimethyl sulfoxide

DPPH 2,2-diphenyl-1-picryl-hydrazyl-hydrate

dSCG defatted Spent Coffee Ground

EA Ellagic Acid

EDC 1-Ethyl-3-(3-dimethylaminopropyl)carbodiimide

EDL Electrical Double Layer

EDTA Ethylenediaminetetraacetic acid

EIS Electrochemical Impedance Spectroscopy

Fc 1,1'-ferrocenedimethanol

FRAP Ferric Reducing/Antioxidant Power

FWHM Full Width at Half Maximum

GA Gallic Acid

GO Graphene Oxide

H2DCFDA 2′,7′-dichlorodihydrofluorescein diAcetate

HaCat Human Keratinocytes

HATU 1-[Bis(dimethylamino)methylene]-1H-1,2,3-triazolo[4,5-b]pyridinium 3-oxide hexafluorophosphate, Hexafluorophosphate Azabenzotriazole Tetramethyl Uronium)

HBA Hydrogen Bond Acceptor

HBD Hydrogen Bond Donor

HDF Human Dermal Fibroblasts

HFP 1,1,1,3,3,3-HexaFluoro-2-Propanol

HMDA Hexamethylenediamine

HOBt Hydroxybenzotriazole

HPLC High Pressure Liquid Chromatography

IBX 2-Iodoxybenzoic acid

LA Lipoic Acid

MAE Microwave Assisted Extraction

MALDI Maldi Assisted Laser Desorption Ionization

MB Methylene Blue

MeDHICA Methyl ester of 5,6-dihydroxyindole-2-carboxylic acid

MLNP MelaninLikeNanoParticles

MNP MelaninNanoParticles

MTT 3-(4,5-dimethyl-2-thiazolyl)-2,5-diphenyl-2H-tetrazolium bromide

NMR Nuclear Magnetic Resonance

ODS OctaDecylSilane

OPA o-phthalaldehyde

PB Phosphate Buffer

PCA Phenazine-1-carboxylic acid

PDA Polydopamine

PDLLA D,L-Polylactic Acid

PNS Pecan Nut Shell

QCM Quartz Crystal Microbalance

RNS Reactive Nitrogen Species

ROS Reactive Oxygen Species

RR Rectification Ratio

Rt Retention Time

SCG Spent Coffee Ground

SDS Sodium Dodecyl Sulfate

SEM Scanning Electron Microscopy

s/l Solid to Liquid ratio

SPI Soy Protein Isolate

TEA Triethylamine

TEG Thromboelastography

TEM Transmission Electron Microscopy

TFC Total Flavonoids Content

TLC Thin Layer Chromatography

TPC Total Phenol Content

TPTZ 2,4,6-tris(2-pyridyl)-s-triazine

UAE Ultrasound Assisted Extraction

UV Ultraviolet

Vis Visible

WCA Water Contact Angle

WPI Whey Protein Isolate

WVP Water Vapour Permeability

XRD X-Ray Diffraction

WVP Water Vapour Permeability

XRD X-Ray Diffraction